HAL
open science

Data-driven fault diagnosis for PEMFC systems

Zhongliang Li

To cite this version:

Zhongliang Li. Data-driven fault diagnosis for PEMFC systems. Automatic. UNIVERSITE D'AIX-MARSEILLE, 2014. English. NNT : . tel-01275281

HAL Id: tel-01275281

https://theses.hal.science/tel-01275281

Submitted on 17 Feb 2016

HAL is a multi-disciplinary open access archive for the deposit and dissemination of scientific research documents, whether they are published or not. The documents may come from teaching and research institutions in France or abroad, or from public or private research centers.

L'archive ouverte pluridisciplinaire **HAL**, est destinée au dépôt et à la diffusion de documents scientifiques de niveau recherche, publiés ou non, émanant des établissements d'enseignement et de recherche français ou étrangers, des laboratoires publics ou privés.

UNIVERSITÉ AIX-MARSEILLE

École Doctorale en Mathématiques et Informatique de Marseille ED 184

PHD THESIS

presented by

Zhongliang LI

to obtain the degree of

Doctor of the Aix-Marseille University

Discipline: Automatic

Data-driven fault diagnosis for PEMFC systems

Will be defended in September 2014

Jury :

Pr. Eric BIDEAUX	INSA of Lyon	Reviewer
Pr. Maurice FADEL	ENSEEIHT/INPT	Reviewer
Pr. Mohamed BOUTAYEB	University of Lorraine	Examinator
Pr. Yongdong LI	Tsinghua University, China	Examinator
M. Ulf GROOS	Fraunhofer-ISE, Germany	Examinator
Dr. Stefan GIURGEA	UTBM	Co-director
Pr. Daniel HISSEL	University of Franche Comté	Co-director
Pr. Rachid OUTBIB	Aix-Marseille University	Director

Thesis prepared at the laboratory LSIS (UMR CNRS 7296) in Marseille, FCLAB (CNRS 3539) & FEMTO-ST/Energy Lab (UMR CNRS 6174) in Belfort

Cette oeuvre est mise à disposition selon les termes de la Licence Creative Commons Attribution - Pas d'Utilisation Commerciale - Pas de Modification 3.0 France.

Acknowledgments

This work was done while the author was with the laboratory LSIS in Aix-Marseille University and with the laboratory FCLAB in Belfort. First and foremost, I would like to give the most sincere thanks to Prof. Dr. Rachid OUTBIB and Prof. Dr. Daniel HISSEL, who are respectively my supervisor in LSIS and FCLAB. I am grateful for their guidance and support in my research work and the preparation of this dissertation. I would also like to express my deepest appreciation to Dr. Stefan GIURGEA, who is also my thesis supervisor, for his insightful discussion about this work and constructive comments on the dissertation.

I would also thank the partners within the project DIAPASON 2 for their working on the experiments corresponding to this work.

Many thanks should go to the colleagues in LSIS and FCLAB and the friends in Marseille and Belfort, who have made my time spent at the two French cities both substantial and pleasurable.

Finally, I would like to give my gratitude to my family members for their persistent and unconditional understanding and supporting.

RÉSUMÉ

Cette thèse est consacrée à l'étude de diagnostic de pannes pour les systèmes pile à combustible de type PEMFC. Le but est d'améliorer la fiabilité et la durabilité de la membrane électrolyte polymère afin de promouvoir la commercialisation de la technologie des piles à combustible. Afin d'assurer un diagnostic précis et applicable en temps réel, les approches explorées dans cette thèse sont celles du diagnostic guidé par les données.

Parmi les méthodes dédiées au diagnostic guidé par les données, les techniques basées sur la reconnaissance de forme sont les plus utilisées. Dans ce travail, les variables considérées sont les tensions des cellules et la démarche adoptée se compose de deux étapes. La première étape consiste à extraire les caractéristiques, et la deuxième étape permet d'établir une classification. Les résultats établis dans le cadre de la thèse peuvent être regroupés en trois contributions principales.

La première contribution est constituée d'une étude comparative. Plus précisément, plusieurs méthodes sont explorées puis comparées en vue de déterminer une stratégie précise et offrant un coût de calcul optimal.

La deuxième contribution concerne le diagnostic online sans connaissance complète des défauts au préalable. Il s'agit d'une technique adaptative qui permet d'appréhender l'apparition de nouveaux types de défauts. Cette technique est fondée sur la méthodologie SSM-SVM et les règles de détection et de localisation ont été améliorées pour répondre au problème du diagnostic en temps réel.

La troisième contribution est obtenue à partir méthodologie fondée sur l'utilisation partielle de modèles dynamiques. Le principe de détection et localisation de défauts est fondé sur des techniques d'identification et sur la génération de résidus directement à partir des données d'exploitation.

Toutes les stratégies proposées dans le cadre de la thèse ont été testées à travers des données expérimentales et validées sur un système embarqué.

Mots clés: système PEMFC, diagnostic en ligne, des tensions cellulaires, classification de modèle, l'extraction d'entité, la précision du diagnostic, le coût de calcul, systèmes embarqués, la détection des défauts roman, adaptation en ligne, l'identification du modèle, l'espace de parité, conception résiduelle, dynamique processus.

ABSTRACT

Aiming at improving the reliability and durability of Polymer Electrolyte Membrane Fuel Cell (PEMFC) systems and promote the commercialization of fuel cell technologies, this thesis work is dedicated to the fault diagnosis study for PEMFC systems. In consideration of the sophistication in establishing the accurate and diagnosis-friendly model for PEMFC systems, data-driven fault diagnosis is the main focus in this thesis.

As a main branch of data-driven fault diagnosis, the methods based on pattern classification techniques are firstly studied. Taking individual fuel cell voltages as original diagnosis variables, fault detection and isolation (FDI) is achieved through a two-step procedure. The first step is for feature extraction, while the second one is for classification. According to this framework, several representative methodologies in each step are investigated and compared from the perspectives of diagnosis accuracy and computational cost.

Specific to the defects on novel class detection and online adaptation capability of conventional classification based diagnosis methods, a novel diagnosis strategy is proposed for PEMFC system diagnosis. A new classifier named Sphere-shaped Multi-class Support Vector Machine (SSM-SVM) and modified diagnostic rules are utilized to realize the novel fault recognition. While an incremental learning method is extended to achieve the online adaptation.

Apart from the pattern classification based diagnosis approach, a so-called partial model-based data-driven approach is introduced to handle PEMFC diagnosis in dynamic processes. With the aid of a subspace identification method (SIM), the model-based residual generation is designed directly from the normal and dynamic operating data. Then, fault detection and isolation are further realized by evaluating the generated residuals.

The proposed diagnosis strategies have been verified using the experimental data

which cover a set of representative faults and different PEMFC stacks. The preliminary online implementation results with an embedded system are also supplied.

Key words: PEMFC system, Online diagnosis, Cell voltages, Pattern classification, Feature extraction, Diagnosis accuracy, Computational cost, Embedded system, Novel fault detection, Online adaptation, Model identification, Parity space, Residual design, Dynamic process.

Contents

General introduction **1**

1 Generalities on PEMFC systems and diagnosis **7**

1.1 Principle of PEMFC functioning 8

1.2 PEMFC system 12

1.2.1 Air supply subsystem 13

1.2.2 Hydrogen supply subsystem 14

1.2.3 Humidification/water management subsystem 14

1.2.4 Heat management subsystem 15

1.2.5 Power conditioning subsystem 15

1.2.6 Control/supervision subsystem 16

1.3 Status and challenges of PEMFC development 16

1.3.1 Status of PEMFC development 17

1.3.2 Challenges of PEMFC development 18

1.4 Degradations of PEMFC system 20

1.4.1 Degradations related to ageing effect 20

1.4.2 Degradations related to system operations 21

1.4.2.1 Faults inside fuel cells 21

1.4.2.2 Faults on reactants supply 21

1.4.2.3 Faults on heat management 22

1.4.2.4 Faults on water management 22

1.4.2.5 Faults on electric circuit 23

1.4.2.6 Remarks 23

1.5 Fault diagnosis for PEMFC systems 24
1.5.1 Model-based diagnostic methods 26
1.5.1.1 Analytical model based 26
1.5.1.2 Black box model based 29
1.5.2 Data-driven diagnostic methods 31
1.5.2.1 Variables can be used 31
1.5.2.2 Multivariate analysis 34
1.5.2.3 Classification based 36
1.5.3 Challenges of online PEMFC system fault diagnosis 39
1.6 Conclusion 40

2 Experimental PEMFC stacks and experimentation framework 43
2.1 Test benches and stacks 43
2.1.1 Two test benches 43
2.1.2 Three PEMFC stacks 46
2.2 Experiments and database 48
2.2.1 Experiments and database of 20-cell stack 48
2.2.1.1 Normal operating (Nl) 48
2.2.1.2 Flooding (F_f) and membrane drying (F_d) 50
2.2.2 Experiments and databases of 8-cell stack and 40-cell stack . . 50
2.2.2.1 High current pulse (F_1) 51
2.2.2.2 Stop cooling water (F_2) 51
2.2.2.3 High air stoichiometry (F_3) and low air stoichiometry (F_4) 53
2.2.2.4 CO poisoning (F_5) 58
2.3 Role of individual cell voltages for diagnosis 58
2.4 Conclusion 63

3 Pattern classification tools for diagnosis: a comparative study 65
3.1 Approach principle 65
3.2 Data labeling methodologies 67

3.2.1 Pressure drop model 67
3.2.2 A statistical method for identification F_f and F_d 68
3.2.3 Data labeling result 70
3.3 Feature extraction 71
3.3.1 PCA 72
3.3.2 FDA 74
3.3.3 KPCA 76
3.3.4 KFDA 80
3.3.5 Remarks on feature extraction methods 81
3.4 Classification 82
3.4.1 GMM 82
3.4.1.1 Bayesian decision theory 83
3.4.1.2 GMM for modeling class-conditional probability function 84
3.4.2 kNN 84
3.4.3 SVM 86
3.5 Comparative results of different methodologies 89
3.5.1 Results on feature extraction and classification 89
3.5.2 Discussion about computation costs 95
3.6 Conclusion 97

4 Pattern classification for diagnosis: multi-fault FDI 99
4.1 DAGSVM for multi-fault FDI 100
4.2 Implementations of the diagnostic approach 101
4.2.1 Data labeling 102
4.2.2 FDA procedure 103
4.2.3 DAGSVM procedure 107
4.3 Results and discussion 109
4.4 Online implementation in an embedded system 111
4.4.1 Embedded system designed for PEMFC system diagnosis . . . 111

4.4.2 Implementation results 112
4.4.2.1 Online fault diagnosis developing process 112
4.4.2.2 Algorithm integration test results 115
4.5 Conclusion 115

5 Pattern classification for diagnosis: novel fault recognition and online adaptation 117
5.1 Framework of the strategy 118
5.2 FDI and novel fault recognition 119
5.2.1 Problem mathematical description 119
5.2.2 SSM-SVM 120
5.2.3 Diagnostic rules 124
5.3 Online adaptation method 126
5.3.1 Incremental learning method for SSM-SVM 127
5.3.1.1 Incremental procedure 127
5.3.1.2 Upper limit on $\Delta\alpha_s^i$ 130
5.3.1.3 Recursive update of the inverse matrix 130
5.3.1.4 Incremental learning algorithm 131
5.3.1.5 Initialization procedure 131
5.3.2 Improvement of real-time learning performance 133
5.4 Results and discussion 134
5.4.1 Experiments and database 134
5.4.2 Multi-fault detection and isolation 135
5.4.3 Online adaptation 138
5.4.4 Detection a novel failure mode 140
5.4.5 Real-time capability 142
5.5 Conclusion 142

6 Partially model-based methodology for data-driven diagnosis 145
6.1 Background knowledge 146
6.1.1 Model description 146

6.1.2 Parity space model based fault diagnosis 147
6.1.3 Subspace model identification method 150
6.1.3.1 Identification of the intermediate matrices 152
6.1.3.2 Identification of system matrices 154
6.2 Description of the diagnostic strategy 155
6.2.1 Fault detection 155
6.2.2 Fault isolation in residual space 156
6.2.3 Overall framework of the strategy 157
6.3 Application of PEMFC diagnosis 158
6.3.1 Experiments and data acquisition 158
6.4 Results and discussion 160
6.4.1 Parity space identification 160
6.4.2 Fault detection 160
6.4.3 Fault isolation 168
6.5 Conclusion 168

Conclusion and Perspectives **171**

Bibliography **174**

A Derivation processes of some methodologies **185**
A.1 Formulation of KPCA 185
A.2 Centering in high-dimension space 187
A.3 Formulation of KFDA 188
A.4 Proof of EM process 190
A.5 Extension linear separable SVM to nonlinear non-separable case . . . 191
A.6 SMO training 193
A.6.1 Solving for two Lagrange multipliers 193
A.6.2 Choosing multipliers to optimize 194
A.7 Determination of system order 196
A.8 Proof of (5.32) 197

Personal publications **199**

List of Figures

1-1 The basic principle of PEMFC operation 9
1-2 Various voltage losses and polarization curve of an operating PEMFC 11
1-3 Schematic of PEMFC stack [8] 12
1-4 PEMFC system structure 13
1-5 Powertrain layout of Honda's next generation FCX fuel cell vehicle [11] 16
1-6 Fuel cell shipped in recent years [12] 17
1-7 MW of fuel cell shipped in recent years [12] 18
1-8 Fuel cell targets versus status [13] 19
1-9 Projected fuel cell transportation system costs per kW, assuming high volume production (500,000 units per year) [14] 19
1-10 Analytical model-based fault diagnosis scheme [24] 26
1-11 PEMFC equivalent circuit developed by Hernandez et al. [31] 27
1-12 Diagram of fault diagnosis based on model observer [33] 28
1-13 A typical EIS curve 32
1-14 LSV test result obtained on a 3-cell stack [46] 33
1-15 Voltage against time in a current interrupt process 34
1-16 Schematic of multivariate analysis 36
1-17 Flowchart of a classification based diagnosis process 37

2-1 Overall view of the 1 kW testbench 44
2-2 Overall view of the 10kW test bench 44
2-3 Schematic of the used 10 kW test bench [61] 46
2-4 Current evolution in normal experiment 49

2-5 Measurements in F_1 process 52
2-6 Measurements in F_2 process 54
2-7 Measurements in F_3 process 56
2-8 Measurements in F_4 process 57
2-9 Measurements in F_5 process 59
2-10 Cell voltages in a normal experiment. 61
2-11 Cell voltages in a fault experiment 61
2-12 The evolution of cell voltages in different processes 62

3-1 The framework of the diagnosis approach 66
3-2 Three kinds of flow field structures. (a) Parallel flow field. (b) Serpentine flow field. (c) interdigitated flow field 67
3-3 Training data labeling process 69
3-4 Values of parameter W in normal condition and their limits 70
3-5 Parameter W of data in fault process 71
3-6 SVM schematic diagram 86
3-7 Features obtained by adopting PCA 90
3-8 Features obtained by adopting FDA 91
3-9 Features obtained by adopting KPCA 91
3-10 Features obtained by adopting KFDA 92
3-11 Classification results in FDA feature space by GMM 93
3-12 Classification results in FDA feature space by kNN 93
3-13 Classification results in FDA feature space by SVM 94

4-1 DAGSVM structure 101
4-2 Flowchart of the diagnosis strategy 102
4-3 Eigenvalues and ACR values of FDA result for 8-cell stack 104
4-4 Eigenvalues and ACR values of FDA result for 40-cell stack 105
4-5 Data projected to the 2-dimensional space 8-cell stack 105
4-6 Data projected to the 3-dimensional space for 8-cell stack 106
4-7 Data projected to the 2-dimensional space for 40-cell stack 106

4-8 Data projected to the 3-dimensional space for 40-cell stack 107
4-9 Structure of a general embedded system [98] 112
4-10 Embedded system designed for PEMFC system diagnosis [100] 113
4-11 Flowchart of online fault diagnosis developing process 114

5-1 Flowchart of the proposed diagnostic strategy 118
5-2 Schematic diagrams of conventional binary SVM based multi-class classifier and SSM-SVM. 120
5-3 Schematic diagram of SSM-SVM 122
5-4 Schematic of incremental learning 127
5-5 Principle of discarding useless data 134
5-6 Evolution of cell voltages in different states. (a) Nl_1, (b) F_1, (c) F_2, (d) F_3, (e) F_4 136
5-7 First 3 features of the *projecting vectors* from 5 different health states 137
5-8 Evolution of stack voltage over time 139
5-9 First 3 features of the *projecting vectors* from 8 different health states 139

6-1 Schematic of parity space based fault detection 147
6-2 Objective of the model identification 150
6-3 Parity space designed from data 155
6-4 Procedure of fault data preparation 157
6-5 Flow chart of the diagnosis strategy 158
6-6 Input and output variables used for fault diagnosis strategy 159
6-7 Input variables in normal operating state 161
6-8 Output variables in normal operating state 162
6-9 Values of AIC for different system order 162
6-10 Residuals and R in normal state 163
6-11 Residuals and R in the experiment of F_1 fault 164
6-12 Residuals and R in the experiment of F_2 fault 165
6-13 Residuals and R in the experiment of F_3 fault 166
6-14 Residuals and R in the experiment of F_4 fault 167

List of Tables

1.1 Different fuel cell types [5] 8

1.2 Variables can be used for PEMFC system diagnosis 35

2.1 Measured variables 47

2.2 The parameters of the investigated fuel cell stack [56] 47

2.3 Nominal conditions of the stacks 48

2.4 Experiments of various health states carried out on different PEMFC stacks 49

3.1 Representative kernel functions 79

3.2 Results of varied classifications in different feature spaces 94

3.3 Computation costs of the feature extraction methodologies 96

3.4 Computation costs of the classification methodologies 96

3.5 Computation costs using general computer 96

4.1 Sample numbers of the training and test data 103

4.2 Comparative results of classification in various feature spaces for 8-cell stack 108

4.3 Comparative results of classification in various feature spaces for 40-cell stack 108

4.4 Confusion matrix of the test data after classification for 8-cell stack . 109

4.5 Confusion matrix of the test data after classification for 40-cell stack 110

4.6 Comparative results from embedded system and from PC 115

5.1 Bookkeeping conditions 130
5.2 Concerned states (classes) 135
5.3 Confusion matrix (%) with new fault detection 138
5.4 Confusion matrix (%) without new fault detection 138
5.5 Classification accuracy (%) of normal datasets using the models updated at different times 140
5.6 Confusion matrix (%) with F_1 as new fault class 141
5.7 Confusion matrix (%) with F_2 as new fault class 141
5.8 Confusion matrix (%) with F_3 as new fault class 141
5.9 Confusion matrix (%) with F_4 as new fault class 141
5.10 Occupied memory and computing time 142

Nomenclature

Abreviation

ACR Accumulation Contribution Rate

AI Artificial intelligent

AIC Akaike Information Criterion

ANFIS Adaptive neuro-fuzzy inference system

BP Bipolar plate

BS Bayesian networks

CHP Combined heat and power

CL Catalyst layer

CP Collector plate

CV Cyclic voltammetry

DA Diagnosis accuracy

DOE Department of Energy

EDR Error diagnosis rate

EIS Electrochemical impedance spectroscopy

EIV Error in variable

FD Fault detection

FDA Fisher Discriminative Analysis

FDI Fault detection and isolation

FDIA Fault detection, isolation and analysis

FFT Fast Fourier transform

GDL Gas diffusion layer

GFC Gas flow channel

GMM Gaussian mixture model

HNN Hamming neural network

KFDA Kernel Fisher Discriminative Analysis

kNN k nearest neighbor

KPCA Kernel Principal Component Analysis

LPV Linear parameter varying

LSV Linear sweep voltammetry

LTI Linear time invariant

MEA Membrane electrolyte assembly

NNS Neural networks

PCA Principal component analysis

PEMFC Polymer Electrolyte Membrane Fuel Cell or Proton Exchange Membrane Fuel Cell

QP Quadratic problem

SIM Subspace identification method

SMO Sequential Minimal Optimization

SSM-SVM Spherical-Shaped Multiple-class Support Vector Machine

SV Support vector

SVM Support vector machine

Symbol

α Vector coefficient or Lagrange multiplier

$\boldsymbol{\mu}_j$ Mean vector of jth Gaussian component

$\boldsymbol{C}$ Covariance matrix in high dimension space

$\boldsymbol{K}$ Kernel matrix

$\boldsymbol{S}$ Covariance matrix of the training dataset

$\boldsymbol{S}_b$ Between class scatter matrix

$\boldsymbol{S}_t$ Total scatter matrix

$\boldsymbol{S}_w$ Within class scatter matrix

$\boldsymbol{v}$ Vector composed by cell voltages

$\boldsymbol{w}$ Projecting vector, coefficient vector

$\boldsymbol{z}$ Projected vector

λ Lagrange multiplier, eigenvalue

$\mu_i(.)$ Membership of a sample to ith class

ω_i	Set composed by sample indexes in ith class
Ω_{novel}	Class constructed by new fault samples
σ	Parameter in Gaussian kernel
Σ_j	Covariance matrix of jth Gaussian component
$\tilde{\boldsymbol{K}}$	Modified kernel matrix
$\Phi(.)$	Nonlinear mapping
ξ	Slack variable
ζ_i	Parameter set of Gaussian mixture model for ith class
C	Number of classes
D	Flow rate
$d_i(.)$	Distance from a sample to ith sphere center
F_5	CO poisoning fault
g	Class label for binary SVM; Partial derivative in SSM-SVM
h	Class index
I	Current
$k(.,.)$	Kernel function
L	Dimension of feature space; Objective optimizing function after introducing Lagrange multipliers
L_{GDL}	Rib length of bipolar plate
L_{GFC}	Length of gas flow channel
N_i	Sample number of ith class

P	Pressure
Q	Defined as $Q^i_{n,m} = c^i_n c^i_m k(\boldsymbol{z}_n, \boldsymbol{z}_m)$ in SSM-SVM
R_i	Gaussian component number in ith class; Radius of ith sphere in Chapter 5.
V_i	Set composed by original data in ith class
β	Coefficient sensitivity in SSM-SVM
$\boldsymbol{\alpha}_i$	Center of ith sphere
$\boldsymbol{a}$	Vector composed by Lagrange coefficients
$\boldsymbol{Q}_J$	Jacobian matrix in SSM-SVM
$\boldsymbol{R}_J$	Inverse matrix of $\boldsymbol{Q}_J$ in SSM-SVM
ΔG	Difference between the Gibbs free energy of products and reactants
ΔP	pressure drop of the air inlet and outlet
γ	Margin sensitivity in SSM-SVM
$\langle ., . \rangle$	Inner product
$\mathbb{F}$	High-dimentional space
$\mathbb{R}^M$	M-dimentional space
$\mathcal{E}$	Set of error vector sample indexes
$\mathcal{R}$	Set of reserve vector sample indexes
$\mathcal{S}$	Set of margin vector sample indexes
$\mathcal{T}$	Set of all sample indexes
$\mathcal{U}$	Set of unlearned sample indexes
μ	Viscosity

b	Offset of hyperplane
c	Class label for SSM-SVM
d	Partial derivative in SSM-SVM
d_0	Diameter of pore in gas diffusion layer
E	Ideal voltage
F	Faraday's constant
F_1	High current pulse
F_2	Stop cooling water
F_3	High S_c
F_4	Low S_c
F_d	Membrane drying fault
F_f	Flooding fault
K_{C_0}	Permeability
M	Original data dimension
N	Training sample number
Nl	Normal operating
RH	Relative humidity
S	Support vector number
s	Volume fraction occupied by water
S_c	Cathode stoichiometry
T	Temperature

Th	Threshold
$v(n)$	Voltage of nth cell
W	Water indicator variable; function to optimize in SSM-SVM

Subscript

air	Air
E	Error vector
H_2	Hydrogen
H_2O	Water
in	Inlet
out	Outlet
R	Reserve vector
S	Margin vector

Supscript

Φ	With nonlinear mapping
k	k nearest neighbors
s	Support vector

General introduction

Environment and resource issues are drawing increasing attention of the world. On the one hand, according to the report of U.S. Energy Information Administration (EIA) [1], worldwide energy-related carbon dioxide (CO_2) emissions are predicted to rise from about 31 billion metric tons in 2010 to 45 billion metric tons in 2040, a 46-percent increase, if the current policies and regulations limiting fossil fuel use is given. Considering the global warming caused by the greenhouse effect has already appeared, the increase of anthropogenic carbon dioxide emissions, which are considered as the main factors of greenhouse effect, is becoming intolerable. Apart from the carbon dioxide emissions, the air pollution caused by energy-related activities is another unavoidable environment issue. On the other hand, fossil fuels supply almost 80 percent of world energy use. Since they are non-renewable resources whose reserves are limited, improving energy structure is the common motif of all over the world.

The hydrogen energy, which can be produced from diverse sources, can be transformed to electric energy by using fuel cells. The development of fuel cell technologies is drawing increasing attention, since it is demonstrated to be an effective solution to improve the energy source structure and remit the consuming of nonrenewable resources. Among different types of fuel cells, Proton Exchange Membrane Fuel Cell (PEMFC) is one of the most used types, especially in transportation applications. However, cost, reliability and durability are still the barriers which have to be overcome to realize the commercialization of PEMFC. For instance, the current announced lifetime of PEMFC in transportation applications is about 2500 h. This value is still far away from the target of 5000 h given by U. S. Department of Energy (DOE) [2].

To improve the reliability and durability of PEMFC systems, the faults related to system operations should be detected, isolated, and corrected in time to avoid severe damages to the systems. To do so, fault diagnosis should be equipped to the PEMFC systems. Concerning fault diagnosis strategies, two categories can be formulated generally with model based diagnosis approaches and data-driven ones. Both two types of approaches possess both advantages and disadvantages, and the suitable diagnosis approach should be selected according to the specific applications. On account of PEMFC, the sufficient accurate, generalized and diagnosis-oriented models are usually difficult to obtain. In this case, data-driven fault diagnosis seems to be more relevant for practical use of PEMFC systems. The objective of this thesis is to develop the efficient data-driven fault diagnosis strategies which are suitable for PEMFC systems.

Among the different data-driven approaches, the pattern classification based ones have shown their superiors in fault diagnosis in the last two decades. The principle of classification based diagnosis can be summarized as follows. An empirical classifier is firstly established from history data. This is considered as the training phase. Then, by using the trained classifier, the real-time data can be classified into certain classes that correspond to the health states, namely normal state or various fault states. This is considered as the performing phase. Thus, fault detection and isolation can be achieved with these two phases.

The application of the pattern classification techniques for PEMFC fault diagnosis is mainly studied in this thesis. The experimental data from several different PEMFC stacks are concerned. The data are obtained in the experiments involving not only the normal operating state, but also the fault states. The concerned faults are related to the different parts of PEMFC systems, such as the air supply subsystem, hydrogen supply subsystem, water management subsystem, heat management subsystem, etc. The objective of this work is to diagnose these faults efficiently. To evaluate the performance of the fault diagnosis approaches, two criteria, namely diagnosis accuracy and computational cost, are considered through this work. Sufficiently high diagnosis accuracy and low computational cost make an diagnosis approach reliable and suitable

for online implementation.

More precisely, in this thesis, several pattern classification methodologies will firstly be compared from the perspectives of diagnosis accuracy and computational cost. Then, some procedures are proposed to improve the conventional classification methods in the aspects of novel fault recognition and online adaptation. In addition to the pattern classification based approaches, a novel data-driven partially model-based diagnosis method, which is dedicated to fault diagnosis in dynamic processes, will be explored. All the obtained results are based on the experimental data sampled from real testbenches.

Overview of the thesis is as follows:

In the first chapter, the technologies of PEMFC and PEMFC systems are introduced. The state-of-art of the fault diagnosis strategies for PEMFC is also reviewed. The challenges of online fault diagnosis for PEMFC systems are listed at the end of this chapter.

Chapter 2 is dedicated to present the test benches, the PEMFC stacks, and the experiments which have been carried out. The experimental databases which are used in the thesis work are also described.

In chapter 3, pattern classification based diagnosis approach is proposed. In the approach, the two water management faults named flooding and membrane drying, are firstly concerned. Individual cell voltages are selected as the original variables for diagnosis. Feature extraction techniques, namely PCA, FDA, KPCA and KFDA, and classification techniques, namely GMM, kNN and SVM, are used successively to extract diagnosis-oriented features and classify the features into different classes related to the health states. Fault detection and isolation can therefore be achieved. The performances of several feature extraction and classification methodologies are compared from the perspectives of diagnosis precision and computational cost. Since the classification based diagnosis approach belongs to supervised learning methods, a strategy, which combines the pressure drop model and statistical analysis, is proposed to identify the water management faults and used for labeling the training data.

Experimental data of a 20-cell stack is used to verify this part of the work.

Following the work in chapter 3, chapter 4 is dedicated to further verify the multi-fault detection and isolation performance of the proposed diagnosis strategy. The data from more fault types and more PEMFC stacks are used for this test. Still, cell voltages serve as the variables for diagnosis. The methodologies FDA and SVM are used for feature extraction and classification. To further decrease the online performing time, the method Directed Acyclic Graph SVM is adopted for multi-class classification. The data that cover five fault types of two different PEMFC stacks (an 8-cell stack and a 40-cell stack) are used for this verification work. The results show that multiple faults can be detected and isolated with high accuracy rate. Moreover, this classification based diagnosis strategy was successfully integrated to a specially designed embedded system, the preliminary results are also presented in the thesis.

Chapter 5 is devoted to conquering two defects of conventional classification based fault diagnosis approaches. One defect is that the conventional classification based approach fails to detect a novel fault type. The other one is the absence of the online adaptation capability when the ageing effect of PEMFC is taken into account. Specific to the first defect, a classification method named *Spherical-Shaped Multiple-class Support Vector Machine* (SSM-SVM), as well as the new diagnostic rules are proposed is proposed instead of the traditional SVM classifier. With the proposed approach, not only the data from the known health states can be detected, but the data from the potential failure mode can also be recognized. Aiming at the second defect, an online adaptation procedure called incremental learning is proposed to update the diagnosis models in real time. The diagnostic performance can be maintained through this procedure. Then, the experimental data are used to justify the capabilities of the novel fault type recognition and online adaptation of the proposed approach.

Chapter 6 is dedicated to figuring out the PEMFC diagnosis in dynamic processes. The diagnostic strategy relying on a dynamic model, such as state space model, can usually do better than the classification based diagnosis in the aspects of diagnosis in dynamic processes and robustness to unseen data. Based on this observation, a so-called partial model-based data-driven approach is introduced to achieve the PEMFC

system diagnosis in dynamic processes. In the approach, the model-based residual generation procedure can be designed directly from a set of the normal operating data. Fault detection can therefore be realized. Moreover, SVM classification is carried out in the residual space to realize the fault isolation aim. This new fault diagnosis strategy is also verified using the experimental data.

To end the thesis, an independent chapter is added to summarize the contributions of the thesis work, and highlight the directions of the future work.

Chapter 1

Generalities on PEMFC systems and diagnosis

*A **fuel cell** is a device that converts the chemical energy from a fuel (hydrogen is the most common fuel) into electricity, heat and byproducts (generally water) through a chemical reaction with oxygen or another oxidizing agent* [3]. Hydrogen and fuel cells offer a broad range of benefits for the environment and the balance of the energy structure. Due to their high efficiency and in-situ near zero-emission operation, fuel cells have the potential to drastically reduce greenhouse gas emissions in many applications. Since hydrogen can be produced from diverse sources such as renewable resources, biomass-based fuels, and natural gas, large-scale using of fuel cells can slack the dependence to the fossil fuels, and advance the renewable power development [4].

A variety of fuel cell types, which are distinguished by the electrolyte that is used, have been proposed since the last century. Basic information about these fuel cell types is summarized in Table 1.1 [5].

Among the variety types, owing to its simplicity, viability, quick start-up and wide application range, Proton Exchange Membrane Fuel Cell (PEMFC[1]) has drawn the most attention from both academic and industrial institutions.

[1]PEM in PEMFC can stand for either Proton Exchange Membrane or Polymer Electrolyte Membrane

Table 1.1: Different fuel cell types [5]

Fuel Cell Type	Mobile Ion	Operating Temperature	Application and notes
Alkaline AFC	OH^-	50-200 ℃	Used in space vehicles. e.g. Apollo Shuttle
Proton exchange membrane PEMFC	H^+	50-100 ℃	Especially suitable for vehicles and mobile applications, but also for lower power CHP system
Phosphoric acid PAFC	H^+	220 ℃	Large numbers of 200 kW CHP systems in use.
Molten carbonate MCFC	CO_3^{2-}	650 ℃	Suitable for medium to large scale CHP systems, up to MW capability.
Solid oxide SOFC	O^{2-}	500-1000 ℃	Suitable for all sizes of CHP systems, 2kW to multi MW

1.1 Principle of PEMFC functioning

As Fig. 1-1 shows, from the middle to the both sides, a typical PEMFC consists the following components [5]:

- Membrane

  Polymer membrane, which acts as the electrolyte, is the heart of PEMFC. It is impermeable to gases but it conducts protons.

- Catalyst layers (CL)

  At the two interfaces of the polymer membrane there are the layers with catalyst particles. The best catalyst for both the anode and the cathode is platinum. The catalyst particles are supported on larger carbon particles.

- Gas diffusion layers (GDL)

  The polymer membrane, with catalyst layers settled on the two sides, is sandwiched between two sheets of porous layers, which are called GDLs. These layers are typically made out of carbon cloth or carbon fiber paper. One of the functions of GDLs is to allow diffuse of both the reactant gases and product water. Besides, GDLs also perform as the electrically conductive electrodes and the heat-conducting mediums. The membrane, CLs, GDLs are usually combined

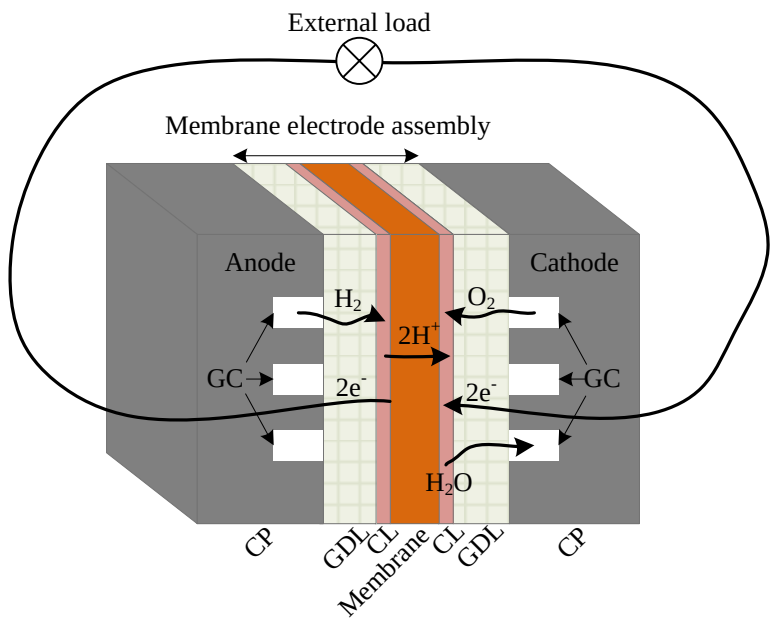

Figure 1-1: The basic principle of PEMFC operation

together as the membrane electrode assembly (MEA).

- Collector plates (CP)

  The CPs are settled on the two external sides of a PEMFC. Gas flow channels (GFCs) are grooved on the one side or the both sides for gas flow (one-side channels are shown in the figure). The CPs can not only house the GFCs, but also act as the electrically conductors and heat conductors. Moreover, they provide structural support for fuel cells.

A running PEMFC is usually fed continuously with hydrogen on the anode side and with air on the cathode side. Electrochemical reactions occur at the surface of the CLs. On the anode side, hydrogen is oxidized:

$$H_2 \rightarrow 2H^+ + 2e^-$$

Protons travel through the membrane, while the electrons travel through the CLs, the GDLs, and the external electric circuit where they perform electrical work and return to the cathode side.

With the protons transferred through the membrane and the electrons through the external circuit, the oxygen is reduced on the cathode side:

$$\frac{1}{2}O_2 + 2H^+ + 2e^- \rightarrow H_2O$$

Combined the reactions on the anode and cathode sides, the global reaction is

$$\frac{1}{2}O_2 + H_2 \rightarrow H_2O \tag{1.1}$$

With the conversion of chemical energy to electrical energy and heat, the by-product water is generated and expelled mostly with the unreacted air from the cathode side.

The maximum amount of electrical energy generated in a PEMFC corresponds to *Gibbs free energy*[2]. In the reaction (1.1), denoting the difference between the Gibbs free energy of the products and the that of reactants as ΔG (expressed in (eV) for one mole H_2O), the theoretical potential (ideal voltage) of the fuel cell corresponding ΔG is

$$E = \frac{-\Delta G}{2F} \tag{1.2}$$

where F is the Faraday's constant. This gives a value of about 1.2 V for a fuel cell operating below 100 ℃[5]. However the voltage of a practical PEMFC is usually less than this value. Voltage losses in an operational fuel cell are caused by several factors.

As Fig. 2-10 shows, the distance between the real open circuit voltage and the ideal output voltage is caused by the factors such as the crossover of the reactants. The curve that characterize the relationship between the voltage and the current is named *polarization curve*. Three main factors that impact the voltage losses are [5] [6]:

1. **Activation losses**. This part of voltage is lost in driving the chemical reaction. These losses depend on the catalyst material and the micro-structure of MEA,

[2]Gibb free energy can be defined as the "energy available to do external work, neglecting any work done by changes in pressure and/or volume". In a fuel cell the external work involves moving electrons round an external circuit

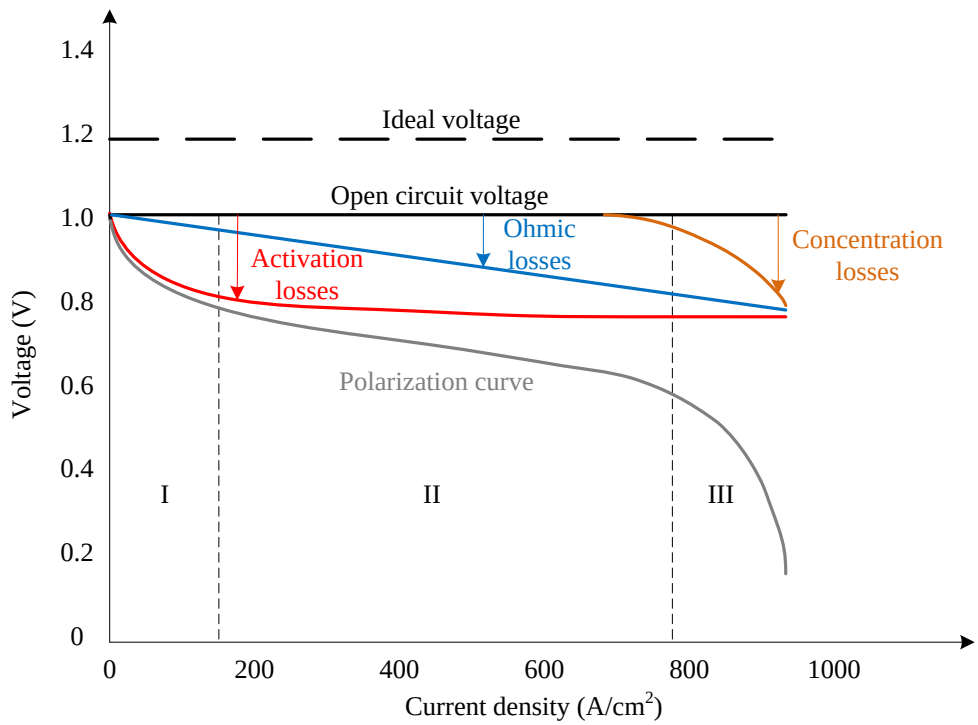

Figure 1-2: Various voltage losses and polarization curve of an operating PEMFC

reactant activities, and on current density.

2. **Ohmic losses**. This category of voltage losses is caused by the resistance associated to the electrodes, the electrolyte, and other interconnections. Ohmic losses are proportional to the current density. Besides, the material and the structure of the fuel cell, and the temperature can impact this kind of losses.

3. **Concentration losses**. These losses result from the drop in concentration of the reactants at the surface of the electrodes, and depend strongly on the current density, reactant activity, and electrode structure.

The effects of the three factors are easy to distinguish. Activation losses, ohmic losses, and concentration losses predominate respectively in the zones I, II, III shown in Fig. 1-2 [7].

When drawing a useful current, the voltage of a single PEMFC is about 0.7 V, which is too small in most cases. In order to produce a more useful voltage or power, many cells have to be connected in series, which functions as a fuel cell stack. In

practice, the cell interconnection is usually achieved by using the bipolar configuration. As Fig. 1-3 shows [8], bipolar plates (BPs) are the CPs installed inside the stack. GFCs are grooved on the both sides of BPs. This makes connections all over one cathode and the anode of the next cell. Meanwhile, the air and hydrogen can be fed to the cathode side and anode side of two neighbored cells.

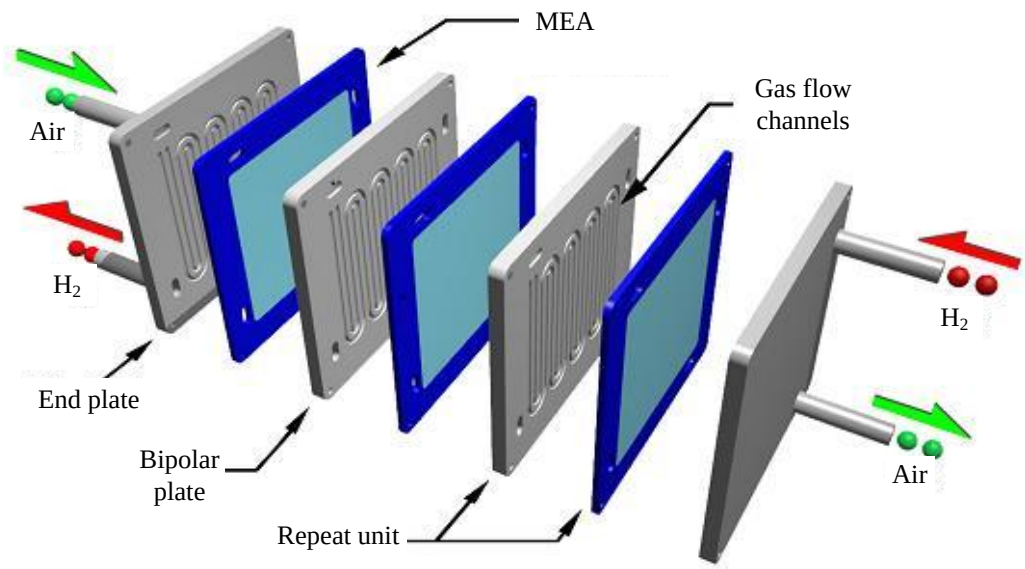

Figure 1-3: Schematic of PEMFC stack [8]

1.2 PEMFC system

A fuel cell stack is obviously the heart of a PEMFC system, however, the stack itself would not be useful without auxiliary supporting subsystems. As Fig. 1-4 shows, apart from the stack, the practical PEMFC systems involve the following subsystems:

- Air supply subsystem
- Hydrogen supply subsystem
- Humidification/water management subsystem
- Heat management subsystem
- Power conditioning subsystem

- Control/supervision subsystem

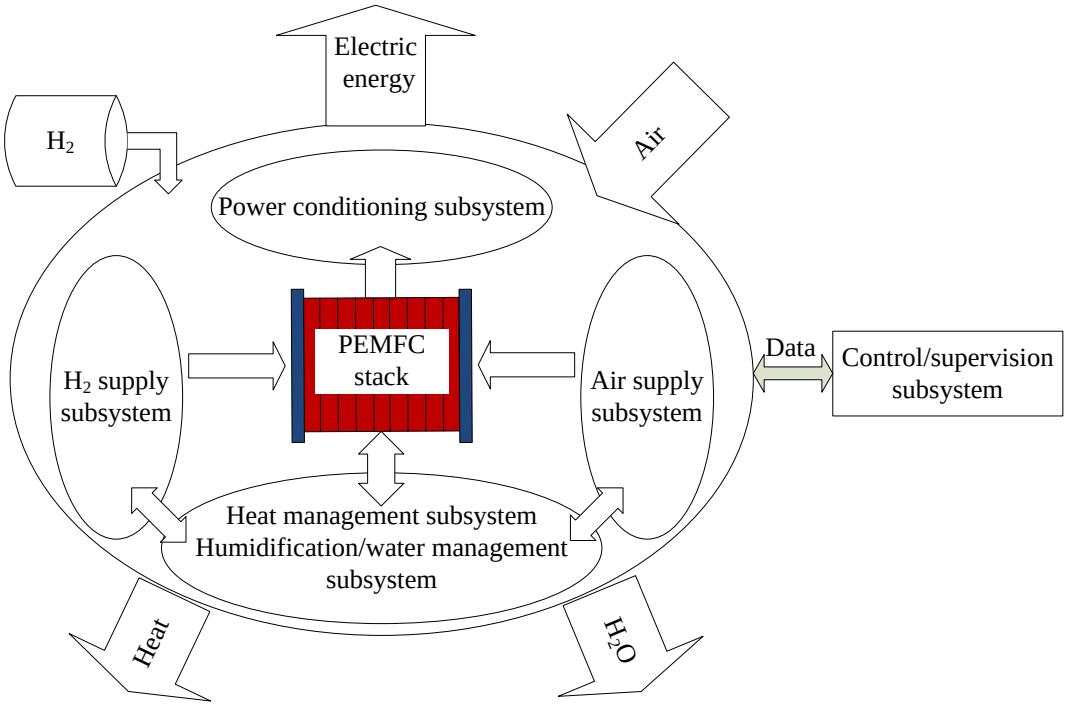

Figure 1-4: PEMFC system structure

1.2.1 Air supply subsystem

The objective of the air supply subsystem is to supply air with proper flow rate and/or pressure to the cathode of fuel cells. Air is usually provided by a blower or a compressor, which is located at the air inlet. By regulating the blower or compressor, sufficient air can be maintained to keep the desired cathode stoichiometry flow rate (S_c) over the full power range. The proper S_c can make the stack operate in an optimal and efficient state; while insufficient air flow cause degradations or even damage the stack in severe cases.

Another function of air supply subsystem is to supply a proper air pressure for the fuel cell stacks. The pressure at the air inlet is generally pressurized from slightly above atmospheric pressure to 2.5 bar [9]. In fact, it is found that running a fuel cell at higher pressure will increase the output power of the fuel cell stacks. However, since the high pressure determines a higher energy consumption associated to the

compressor, a trade-off is supposed to be maintained between increasing efficiency at stack level and reducing the power losses at the system level. The pressure regulation requires a variable downstream pressure valve (nozzle) utilization at the reactants outlet. The controls of S_c and air pressure are usually coupled.

1.2.2 Hydrogen supply subsystem

Hydrogen is usually supplied from a tank, where hydrogen is compressedly stored. Thanks to the valves, as well as the pressure regulator and the flow regulator, the hydrogen pressure and flow rate can be controlled. Hydrogen can be supplied either in dead-end or in a flow-through mode. In the dead-end mode, the hydrogen outlet is closed and the hydrogen is consumed in the fuel cells. Since the impurities, water vapor, and nitrogen diffused from the cathode side may accumulate as operating, periodic purging of the hydrogen compartment is usually required [10]. In the flow-through mode, excess hydrogen is flowed though the stack, which means that the anode stoichiometry flow rate (S_a) is more than 1. The unused hydrogen is returned to the inlet side either by an ejector or pump device. Separating and collecting any liquid water that may be present at the anode outlet is usually required for flow-through mode operation.

1.2.3 Humidification/water management subsystem

A strong relationship between proton conductivity and water content of the membrane exists in PEMFC, thus the membranes need to be maintained properly humidified to guarantee a satisfactory ion conductivity during stack operation. The water produced at cathode side and the air moisture is usually not sufficient to maintain properly the membrane humidification [9]. One common way to solve this problem is to add humidifiers which can humidify the air, the hydrogen, or both, before they enter the stack. Various humidification schemes could be employed such as bubbling of gas through water, direct water or steam injection, exchange of water through a water permeable medium, etc [10].

1.2.4 Heat management subsystem

In converting the chemical energy into electricity, the efficiencies of PEMFCs are normally less than 60 % [4]. This means that more than 40 % of the chemical energy would be disposed as heat. It is found that running PEMFCs between 60 ℃ and 80 ℃ can obtain higher efficiency [10]. To make the PEMFC stack operate in this favorable temperature interval, components for cooling must be employed. Several cooling methods have been studied, such as using highly thermal conductive material as heat spreaders, air flow cooling, liquid cooling, etc [5].

Notice that water and heat are considered as the byproducts of fuel cell operation. In some practical systems, they can be partially re-used, for instance, for humidification of the reactant gases.

1.2.5 Power conditioning subsystem

The electrical output voltage of a PEMFC stack is not constant when the stack is employed in a load-varying situation. Moreover, the output power of the stack is not often at the suitable voltage for the load. A DC/DC converter is used to regulate the stack voltage to a fixed value, which can be higher or lower than the output stack voltage [5]. Notice that, depending on the application objects, more than one DC/DC converters may be needed to generate different output voltages. For instance, in the fuel cell vehicles, there are DC/DC converters used for auxiliary subsystems and the ones used for main power chain. The output power of the converter, which is designed for auxiliary subsystems, can be supplied to the components in auxiliary subsystems, such as compressors, cooling fans and start-up batteries. Following the DC/DC converter in the main power chain, the power inverter and electric motor are usually the main components. Fig. 1-5 shows the powertrain layout of Honda's concept fuel cell vehicle [11].

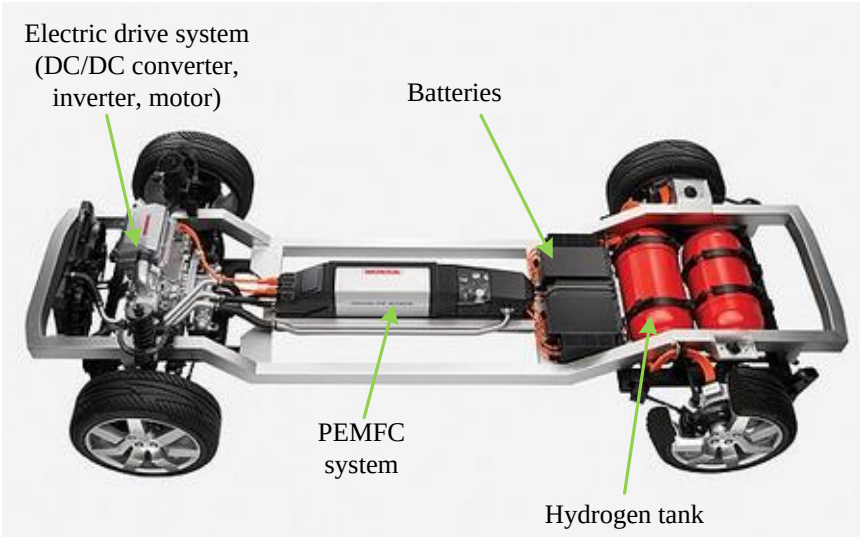

Figure 1-5: Powertrain layout of Honda's next generation FCX fuel cell vehicle [11]

1.2.6 Control/supervision subsystem

To make the PEMFC system operate in the efficient and safe state, various subsystems should function and cooperate properly. Control/supervision subsystem play an important role in achieving these goals. On the one hand, by synthesizing the operating information from the sampled data, the commands can be given to control the different subsystems efficiently; on the other hand, the abnormal states are supposed to be detected with the supervision function.

1.3 Status and challenges of PEMFC development

PEMFCs are potentially beneficial for many applications, however, PEMFC systems were always known to be "five years away from commercial exploitation" [5]. Sometimes, this disappointing sentence makes the people suspect the possibility of the final applications of PEMFCs. Meanwhile, this means that although there are still some bottle necks for PEMFC technologies to be overcome, the distance from widely use seems to be not very long.

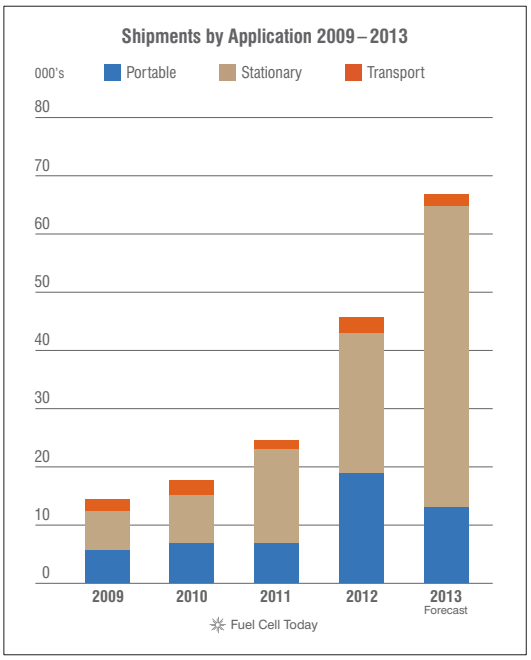

(a) Shipments by application

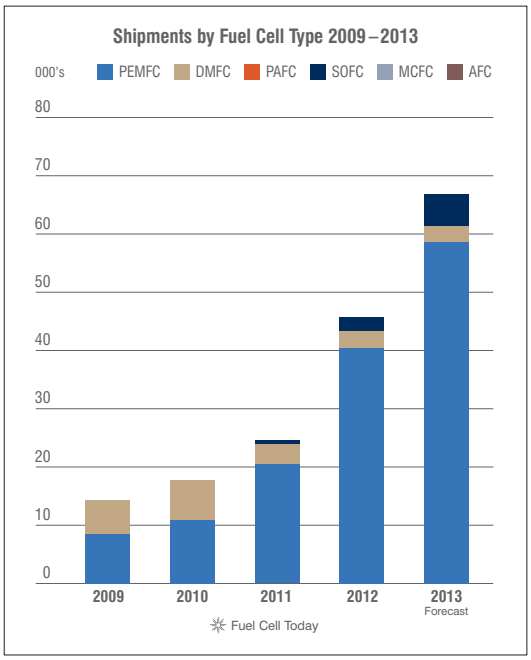

(b) Shipments by fuel cell type

Figure 1-6: Fuel cell shipped in recent years [12]

1.3.1 Status of PEMFC development

During the last two decades, the increasing environment and resource concerns drive many countries and organizations to accelerate the researching and developing the fuel cell technologies. And we have seen the use of fuel cells in the commercial markets and demonstrations has considerably increased in recent years. Fig. 1-6(a) and 1-6(b) give the fuel cell systems shipped by application and by fuel cell type in recent years [12]. The number in 2012 is about 40,000 units, which roughly doubles the one in 2011 and a 400 % increase over the one in 2009. And the increase still trends to continue.

Significant power growth of the shipped fuel cell systems can be seen from Fig.1-7. From Fig.1-7(b), it is revealed that a dip in PEMFC capacity shipped occurred in 2011. By comparing these two charts, it is inferred that this dip is caused primarily by a reduction in transportation deployments. Fortunately, the shipments for transportation applications recovered in 2012 from the disappointing year 2011 [12].

Actually, in the transportation sector, several car manufacturers, including Gen-

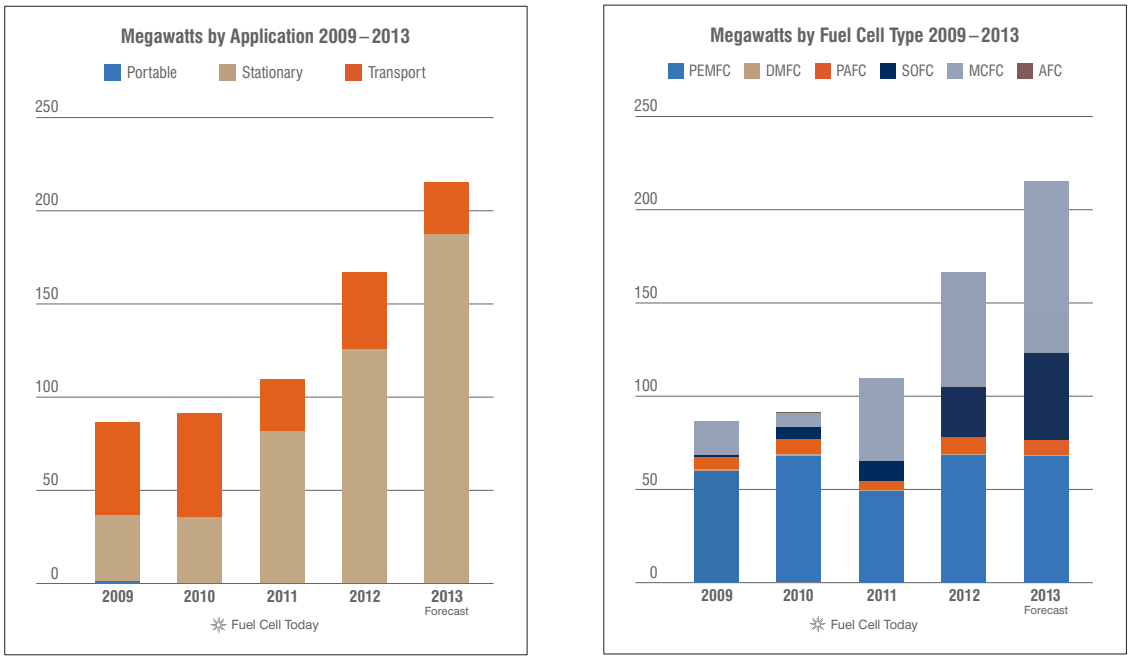

(a) Shipments by application

(b) Shipments by fuel cell type

Figure 1-7: MW of fuel cell shipped in recent years [12]

eral Motors, Daimler, Toyota, Honda, and Hyundai have re-affirmed near-term commercialization goals for fuel cell electric vehicles [4]. For instance, Toyota and Honda have pledged to offer next-generation fuel cell vehicles set to launch in 2015.

1.3.2 Challenges of PEMFC development

Although considerable effort has been devoted to advancing the PEMFC technologies, and significant progress has been achieved over the last decades, such as the mild improvement in overall system efficiency, some challenges still need to be overcome. For the fuel cell system itself, as shown in Fig. 1-8, cost and durability are always two key barriers.

On the one hand, the cost of manufacturing needs to be further lowered. For instance, in the transportation sector which PEMFC is most used, the manufacturing cost is still too high. As Fig. 1-9, the current (projected high-volume manufacturing) fuel cell transportation system cost announced in 2012 has been lowered to \$47 kW^{-1} [14]. It is still higher than the target value of \$30 kW^{-1}, which is considered as a

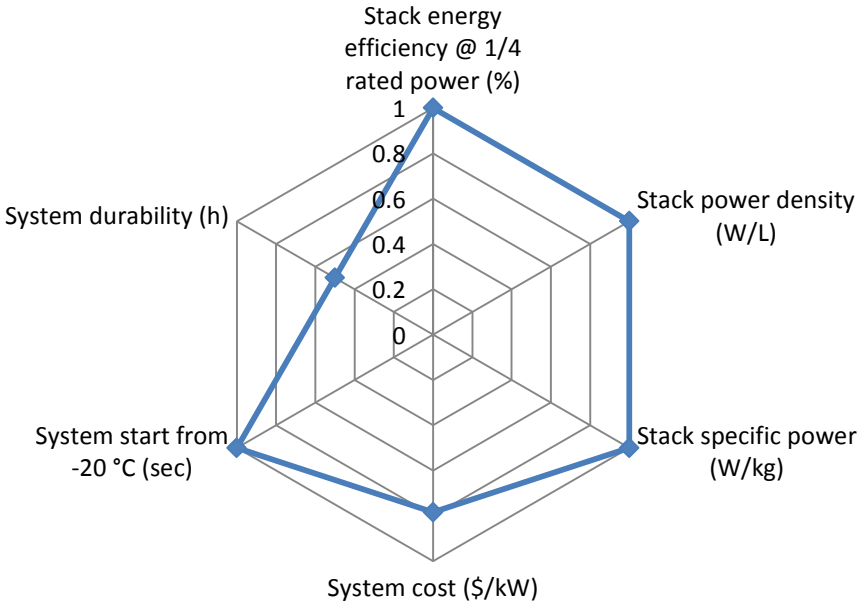

Figure 1-8: Fuel cell targets versus status [13]

competitive value in the mainstream transportation sector [4].

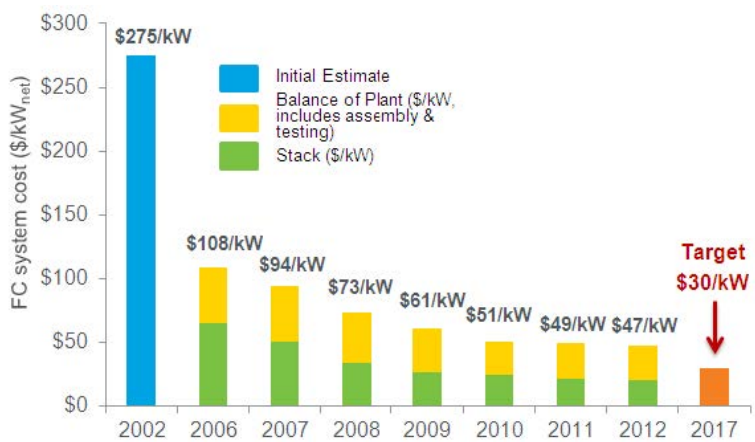

Figure 1-9: Projected fuel cell transportation system costs per kW, assuming high volume production (500,000 units per year) [14]

On the other hand, to achieve large scale market penetration, durability is another technical hurdle. For instance, the lifetime of no less than 40,000 h for stationary applications and 5000 h for electric vehicles is the target in the strategic Plan of the U. S. Department of Energy (DOE) [2]. Substantial progress has been made

in lengthening the lifetime of fuel cells, and the highest demonstrated durability of stationary and automotive fuel cells can currently reach to 20,000 h and 2,500 h [4] respectively. However, the distance to target is still great.

Other than the challenges with the fuel cells, the technical challenges associated with producing, delivering, and storing hydrogen also exist.

1.4 Degradations of PEMFC system

It should be noticed that the cost related to PEMFC systems could be significantly decreased by large-scale manufacturing. Nevertheless, the durability problems have to be worked out from the technological perspective. Even more, decreasing the quality of the materials (catalysts) may be needed to further reduce the costs, the durability could therefore be lowered in such cases. To improve the PEMFC system durability performance, a good knowledge of the its degradation mechanism is necessary.

The stack is the heart of a PEMFC system, and the auxiliary subsystems serve for the stack to make it operate efficiently and safely. The performance of the stack usually reflect the condition of the whole system. Performance degradations of the stack can be impacted by various factors. Based on the influencing factors, we can classify the degradations into two categories: the degradations related to ageing effect and the ones related to system operations.

1.4.1 Degradations related to ageing effect

The degradations related to ageing effect usually do not lead to catastrophic failure that makes the system quickly lose the efficiency, but simply to a gradual decrease in performance. The degradations are not recoverable or reversible, such as the membrane degradation due to loss of electrochemical surface area, the corrosion of the catalyst layer [15]. This kind of degradations can be affected by many internal and external factors, such as fuel cell design and assembly, the quality of materials, operational conditions, etc. The improvement of material durability characteristic can

essentially mitigate these degradations. A lot of researchers in chemical and mechanical domains are working on mitigation the ageing effect related degradations.

1.4.2 Degradations related to system operations

The degradations related to system operations can be called as "faults". The faults could be associated to different components or functioning parts of the systems.

1.4.2.1 Faults inside fuel cells

Apart from the degradations related to ageing effect, some faults could occur inside the fuel cells even within the ageing limit. These faults are usually resulted from uncorrected operations or from fuel cell fabrication processes. The faults could cover the different internal components, such as membrane, CLs, GDLs, BPs, and are usually the irreversible ones [15].

1.4.2.2 Faults on reactants supply

- Contamination

  Impurities, such as CO, CO_2, H_2S, and NH_3 can cause the contamination fault at the anode side; while air pollutants, such as NO_x, SO_x, CO, CO_2 can cause the contamination at the cathode side. The contaminants of the reactants are mainly from the hydrogen manufacturing process and the exhausts of industrial processes and vehicles. The contaminants can be adsorbed on the catalyst surface. In this situation, the reaction sites are partially blocked, which reduces the membrane proton conductivity. Such that PEMFC performance is degraded even permanently [16].

- Improper pressures

  Usually, higher output power can be generated by operating the PEMFC with a higher reactant pressures. However, higher pressure means higher power loss in the air compression, and the size, weight and cost of the compressor increase accordingly [5]. Hence, to obtain the most efficient operating state, the pressures

of the hydrogen and air must be controlled in a range. It is considered as a fault that the pressures exceed this range.

To avoid the strike caused by the pressure difference between cathode side and anode side, the pressure of the hydrogen should be kept equal to that of the air. Improper pressure (too high or too low) can accelerate the degradation of the MEAs [15].

- Improper gas flow rates

  Too low hydrogen or/and air flow rate will cause the starvation fault. The main consequences of fuel cell starvation are loss catalyst active surface area and carbon-support corrosion [17]. Moreover, low air flow rate could be an incentive factor that leads to cathode water flooding [18].

  An excessively high oxygen flow could result in membrane drying, decreasing the conductivity of the membrane. In addition, more power is consumed to get a higher air stoichiometry, which will lower the overall system efficiency [19].

1.4.2.3 Faults on heat management

In practice, PEMFC voltages are usually enhanced at higher temperatures. Besides, some heat generated in the operation could be utilized without being expelling to the environment [20]. The faults on heat management could lead to a too low temperature or too high temperature. On the one hand, too low temperature would be a factor that lower the PEMFC output voltage, and thus lower the system efficiency. Besides, too low temperature helps the condensation of water vapor, and probably cause flooding inside the fuel cells. On the other hand, a too high temperature due to ineffective cooling can cause membrane dehydration and thus lower the conductivity of the membrane. Additionally and more severely, the increased temperature might cause overheating damage to the membrane [21].

1.4.2.4 Faults on water management

Inadequate water management may cause the degradation of the PEMFC.

- Membrane drying

  Membrane drying fault results from the inadequate humidified membrane. The dry membrane not only increases significantly the resistance of membrane, but also conductivity hinders the access of protons to the catalyst surface. Thus, the activation losses and the ohmic losses are both increased. In addition, severe drying fault has been proved to lead to irreversible membrane damage. The membrane drying fault preferentially takes place at the anode side when water is produced at the cathode side [7].

- Flooding

  The accumulation of liquid water in the GCs and/or gas porosities of GDLs and CLs, results in a "flooding" fault. Excessive liquid water will block the reactant pathways, thus making the fuel cell stack degraded. As water is generated and expelled mostly at the cathode side, flooding happens generally at the cathode side [7].

1.4.2.5 Faults on electric circuit

The PEMFC should be operated in a suitable load range. Both the cases in which the load is too low or too high can be seen as the faults. On the one hand, it is found that the ageing related degradation could be accelerated when the PEMFC is operated under the too high voltage caused by low current in the long term [22]. On the other hand, too high load current will cause the concentration voltage loss. In the special cases such as short circuit or high current pulse, the irreversible degradation such as melting the electrodes could be caused [23].

1.4.2.6 Remarks

1. Since the functions of the auxiliary subsystems and the stack are coupled, it is always the case that the occurrence of a specific fault results in other faults. For instance, the water management faults are usually leaded by the faults of the reactant supply faults or/and the heat management faults; the short circuit

can cause the temperature increasing fault.

2. At the early stage of their evolutions, the faults related to operations are usually considered as "reversible" or "recoverable" ones, which can be corrected through appropriate correcting operations. Nevertheless, these faults could evolute to the irreversible faults without adequate actions, such as the structural damages to the fuel cell.

1.5 Fault diagnosis for PEMFC systems

To minimize the fuel cell performance degradation, much effort is being made on the research on degradation mechanisms of materials, and the design and assembly of fuel cells. These are considered as the essential solutions to mitigate the degradations related to ageing effect. Apart from these internal improvements, making PEMFCs and the stacks operate in an optimal condition can certainly mitigate the performance degradation. Especially, the faults related to operations should be detected, isolated, and corrected in time to avoid severe damage to the systems. To do this, fault diagnosis should be equipped to the PEMFC systems.

Fault diagnosis, considered as a crucial component of various industrial systems, is currently receiving considerably increasing attention. The overall concept of fault diagnosis covers three essential tasks [24]:

- Fault detection: detection of the occurrence of faults.
- Fault isolation: localization of different faults.
- Fault analysis or identification: determination of the type, magnitude and cause of the fault.

According to different performance requirements, a fault diagnosis system is called fault detection (FD) system, fault detection and isolation (FDI) system or fault detection, isolation, and analysis (FDIA) system [25]. It has been found that the efficient fault diagnosis approaches can considerably reduce the incident rates and economic

costs [26]. Actually, fault diagnosis is playing an increasingly important role in some kinds of modern industrial systems [27].

As for PEMFC systems, through efficient diagnosis, more serious faults can be avoided thanks to an early fault alarm. Based on the diagnostic results, operating conditions can be adjusted to make the fuel cell operate efficiently and safely. Moreover, the precise diagnosis information can speed up the development of new technologies and reduce the downtime (repair time) [28]. During the last decade, fault diagnosis for PEMFC has been receiving increasing attention from both academic and industrial communities.

Normally, the fault diagnosis could be realized by using hardware redundancy or/and software redundancy. Hardware redundancy is realized by reconstructing the crucial components using identical hardware, thus a fault can be diagnosed directly by the deviation between the actual component output and the one of its redundancy [24]. Due to the high cost of the hardware components, this strategy is rarely considered. Versus hardware redundancy, software redundancy is to replace the hardware components by a software model, which can reconstruct the process behavior. Since fault diagnosis using software redundancy is more efficient, most studies are carried out in this direction. Usually, fault diagnosis refers to the software redundancy by default.

In the literature, some approaches have been proposed to address the PEMFC system diagnosis problems. Depending on whether an input-to-output process model is needed, the proposed approach can be generally categorized to two classes: model based diagnosis methods and data-driven diagnosis methods[3]. In the following, the proposed approaches in these two categories are reviewed. The representative papers are selected to give the hints of each method. For more detailed reviews of these two categories methods, the review papers [29] [30] can be referred.

[3]Note that in some literature, the definitions and categories of the diagnosis approaches are different.

1.5.1 Model-based diagnostic methods

Model-based diagnosis is a traditional way to realize the aim of FDI. As shown in Fig. 1-10, when a process model is obtained, the diagnosis starts by a *residual generation* procedure, which is to create the estimates of the process outputs and to build the difference between the process outputs and their estimates. *Residual evaluation* procedure proceeds following the *residual generation*. This can be considered as the post-processing of residuals, which can extract the diagnosis oriented information from the residual signals and make the diagnostic decision [24]. The process models used for diagnosis can be sorted to analytical models and "black-box" models.

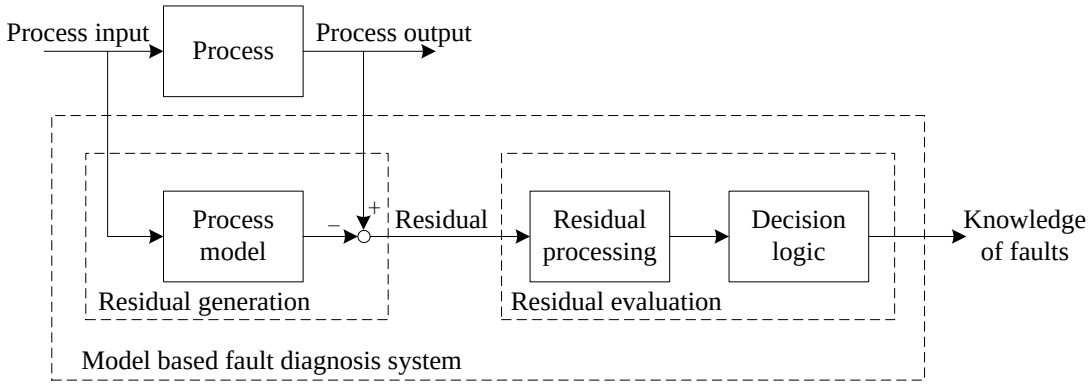

Figure 1-10: Analytical model-based fault diagnosis scheme [24]

1.5.1.1 Analytical model based

Most of the analytical model-based approach are based on general input-output or state space model, which is usually developed based on the physics and mathematics knowledge of the process [24]. According to the residual generation mechanism, it is possible to classify the analytical model based diagnosis methods into three main categories: (i) parameter identification based; (ii) observer-based; (iii) parity space methods.

Strategies have been proposed in these three categories. For the parameter identification based methods, the values of some parameters in the models are related to the behavior of the PEMFC system operations. When the variation of these parameters exceeds a certain limit, the correlated fault can be detected and isolated. In

[31], the authors developed an electrical equivalent circuit for charge matter and energy conservation laws simulation. Gas fluid dynamics is taken into account through the analogies between the pneumatic elements and the electrical components. The electrical equivalent could be seen as an analytical model (see Fig. 1-11). The component parameters are identified through a recurrent least squared method, and the variation of the specific electrical component values can be seen as the indicator of the corresponding faults. As shown in Fig. 1-11, three faults, flooding, membrane drying, and membrane deterioration are related to the corresponding components in the equivalent circuit. Therefore, the occurrence of the faults can be detected by checking the values of these components.

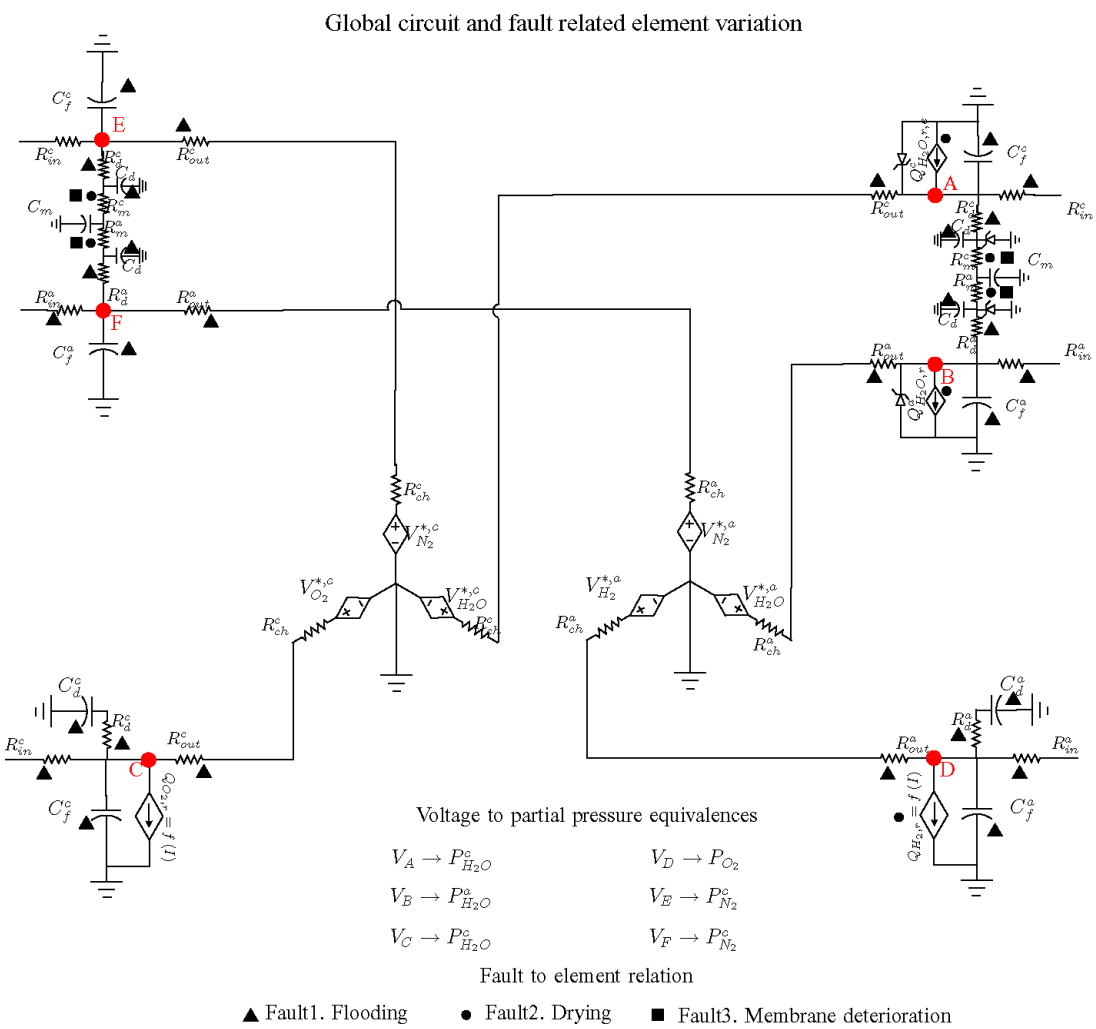

Figure 1-11: PEMFC equivalent circuit developed by Hernandez et al. [31]

In the framework of observer based methods, the residuals are generated by using a designed observer. In [32] and [33], a observer based diagnosis method is proposed. Specific to the a commercial PEMFC system (Ballard 1.2 kW Nexa), a linear parameter varying (LPV) model is built through linearization of a previously calibrated non-linear PEMFC model. As shown in Fig. 1-12, based on the proposed LPV model, a observer for state estimation with *Luenberger observer* structure is designed. Then, the residuals can be computed through compare the process outputs and the estimated outputs using the observer. The diagnosis strategy is verified using a simulator developed using the experimentally calibrated nonlinear model. Some faults emulated using the simulator can be satisfactorily detected.

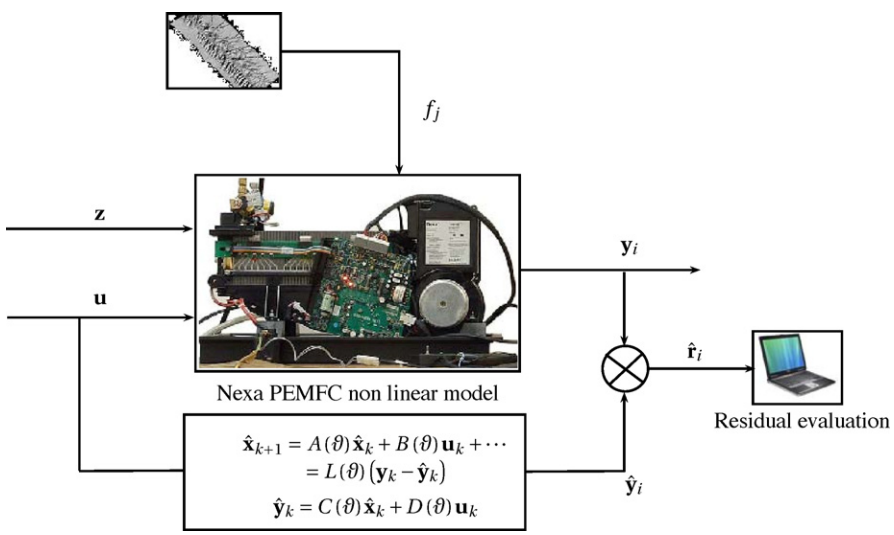

Figure 1-12: Diagram of fault diagnosis based on model observer [33]

Parallel to the observer-based methods, and associated to the state space models, the so-called parity space methods are another group of model based methods. The parity relation, instead of an observer, is used for residual generation procedure. The design of parity space based methods can be achieved in a straightforward manner [25]. In [34], the approach is proposed for PEMFC system diagnosis. The parity relations are extracted from an eight state equations representation. Some faults such as flooding, drying, compressor over-voltage could be detected and isolated.

To carry out the above mentioned three kinds of analytical model based approaches, an accurate process model of PEMFC systems is necessary. To construct

such a model, a high degree of competence is needed in different areas of knowledge such as thermodynamics, fluid dynamics, electrochemistry, and thus the model is usually a complex physical multidimensional model. Sometimes, the complex mathematical equations can be replaced by the empirical laws supported by prior knowledge. These models are named "grey-box" models. However, modeling the PEMFC systems either to an analytical model or a "grey-box" one, is a rather difficult task. Especially, identification of fuel cell inner parameters concerning the operation, the geometries as well as materials is difficult to obtain [35]. For instance, the knowledge air inlet flow rate , stack temperature and dew point temperature that usually need a special monitoring system and a specifically adapted fuel cell geometry. This might be difficult and even impossible in many fuel cell stacks [36]. Moreover, the composition and component parameters of PEMFC system usually vary among different PEMFC systems, it is therefore hard to construct a general model.

1.5.1.2 Black box model based

To avoid the difficulties of constructing an analytical model or "grey-box" model, "black-box" models are proposed. Essentially, the black-box models are based on statistical theory. The relationships between the system inputs and outputs are not based on physical equations, but are deduced through suitable experimental databases [29].

In the black-box model based methods, the complex non-linear PEMFC systems can be imitated by a topology of artificial intelligent (AI) models. As conventional model-based operation, the residuals can be generated by comparing the real system outputs and the model outputs, and fault diagnosis is then realized via a residual evaluation procedure.

In [36], the authors proposed a "black-box" model based on neural networks (NNS) method for PEMFC systems. In the model, four variables: current, stack temperature, dew point temperature, and air flow rate, are considered as model inputs; stack voltage and cathode side pressure drop are considered as model outputs. The NNS model is constructed by using the data in normal operation. A diagnosis decision can

be made to discriminate flooding, drying and normal operations by comparing the model outputs and real time outputs.

In [37], a fuzzy model with stack voltage and current as inputs, and a virtual output named satisfaction rate is built for the diagnosis of a 500 W PEMFC system. An experimental polarization curve under nominal operating conditions is obtained and support the data for tuning the model. Two types of faults, nitrogen or water accumulation and membrane drying, could be detected and discriminated by evaluate the variation of the output value.

Adaptive neuro-fuzzy inference systems (ANFIS) is another "black-box" model, which combine NNS and fuzzy logic together. This method is receiving more and more attention in recent years, especially in the diagnosis domain. In an ANFIS model, the advantages of both NNS and fuzzy logic can be somehow gained at the same time. In [38], the ANFIS model is used for performance prediction of a PEMFC. Cell temperature, anode and cathode humidification temperature and pressure are used as the model inputs; cell voltage is considered as model output. The model shows good agreement with the experimental data and this indicates that ANFIS is capable of predicting fuel cell performance.

Actually, much more effort has been made to modeling PEMFC systems with the "black-box" models. Other than the aforementioned three. In [39] [40], the models based on NNS are proposed respectively. Modeling a PEMFC by a support vector machine (SVM) is proposed in [41] and [42]. However, these modeling methods are not dedicated to the fault diagnosis objectives.

Although the AI models can offer good ability of modeling the complex process of PEMFC system, the residual generation and evaluation of AI models are not so well established as the conventional analytical models. For instance, if only stack voltage or cell voltage is considered as the output variable for most "black-box" models, it is hard to discriminate different faults by comparing this single output value with real time sample. Additionally, as AI models belongs to "black-box" models, the difficulty of explaining the causal relationship among variables exists.

1.5.2 Data-driven diagnostic methods

In contrast to model based diagnosis approach, which requires a process model, the data-driven approach makes use of the information from the history data. Some data-driven methods have also been proposed for PEMFC diagnosis.

1.5.2.1 Variables can be used

The data-driven diagnosis can be done based on different variables, and the choice of the variables is usually crucial, and can impact the performance of diagnosis performance. For PEMFC systems, the regular variables that can be easily measured on a real system, such as stack temperature, the air pressure and stack voltage or cell voltages, can be considered as the variables for diagnosis. Besides, the variables can come from some specific measurements or experiments rather than the ones from regular measurements. Electroanalytical methods, polarization curve, electrochemical impedance spectroscopy (EIS), linear sweep voltammetry (LSV) and cyclic voltagmmetry (CV) are four most used ones to obtain the useful variables for diagnosis. However, it should be emphasized that without the special EIS test instrument, the EIS measurement can still be partially obtained through the control power converter and processing of the measured current and voltage signals [43].

- **Polarization curve**: A plot of cell voltage or stack voltage vs. current density is known as a polarization curve. As Fig. 1-2 shows, the output voltage decreases with the increasing of current due to various voltage losses. Polarization curves are one of the most common used method to characterize the electrochemical performance of the fuel cell stack [44].

- **EIS**: EIS is a powerful experimental technique that compares the electrical response of a test system to a time varying electrical excitation in order to delineate interfacial and bulk material parameters [45]. As Fig. 1-13 shows, a typical EIS curve consists a high frequency arc and a low frequency arc. EIS can provide the impedance values at different frequencies. Usually, the cross points of the EIS with real axis are respectively express the internal resistance

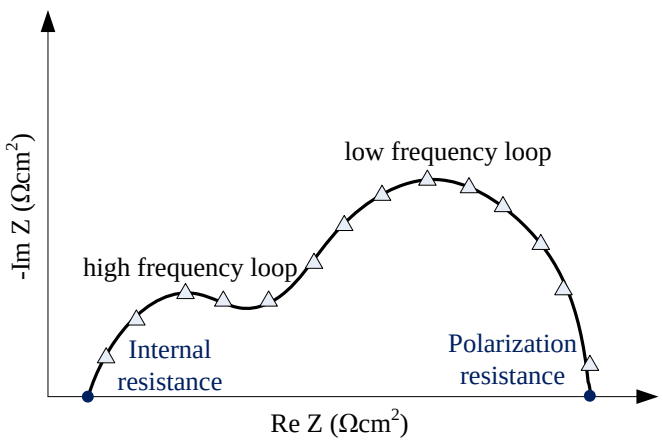

Figure 1-13: A typical EIS curve

and the polarization resistance. Information on the operating states, as well as the fuel cell internal parameters of the operated electrochemical systems could be drawn [44]. To measure the EIS of a PEMFC or stack, an AC current signal with various frequencies is generated and added to a DC current as charge current. The voltage with different frequency components is measured, and the impedance at different frequency can be calculated by using the measured voltage and current. Other than the galvanostatic mode, EIS can also be measured in the potentiostatic mode.

- **LSV**: LSV is a powerful tool to estimate hydrogen crossover and detect internal electronic short between anode and cathode. In LSV experiments, the anode is usually fed with hydrogen while the cathode is supplied with nitrogen. A potential between the working electrode and a pseudo-reference electrode (at cathode) is swept linearly in time, while the electrons flow at the working electrode is measured as current [46]. An example of LSV record obtained from a 3-cell stack is displayed in Fig. 1-14 [46]. Crossover current and short-circuit resistance are two crucial variables extracted from the LSV measurement.

- **CV**: CV is dedicated to the evaluation of the electrocatalytic performances. As for LSV experiments, the FC is fed with hydrogen at the working electrode (anode) and inert gas (nitrogen, helium) at the counter/pseudo-reference elec-

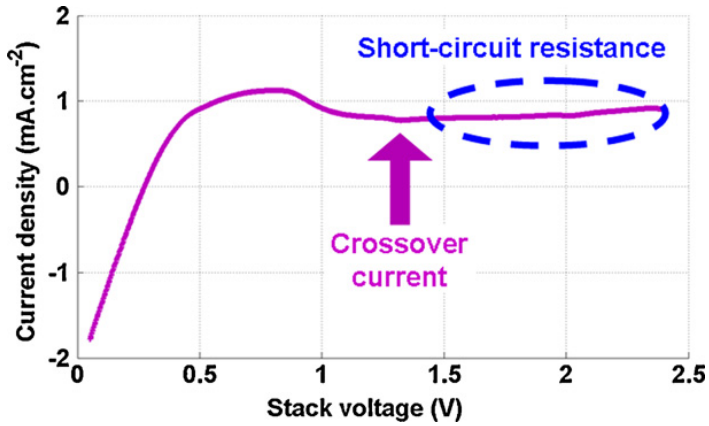

Figure 1-14: LSV test result obtained on a 3-cell stack [46]

trode (cathode), respectively. Compared to LSV experiments, the voltage of the working electrode is swept not only from low value to high value, but an additional reverse voltage scan is also performed during a CV measuring experiment [46].

- **Current interruption method**: The current interruption test can give both accurate quantitative results and quick qualitative indications. In this method, a current provided by a cell or stack is suddenly cut off. The profile of the voltage in the process is shown in Fig. 1-15. The ohmic losses will immediately reduce to zero, while the activation losses will take some time to vanish [5]. Hence, from the voltage profile, the ohmic losses and activation losses could be extracted.

The characters of variables that are potential for PEMFC system diagnosis are summarized in Table 1.2. The variables that can be sampled through regular measurements are usually used for diagnosis of the degradations related to system operations or "faults"; while the variables obtained by special measurements are usually used to diagnose the degradations related to the ageing effect and the faults occurs inside the fuel cells. Most of the special measurements must be carried out offline, which means that the normal operating needs to be stopped to launch the measurements. EIS measurement can be considered to be online which can be measured during the system operating. However, the traditional instruments for EIS test are usually costly,

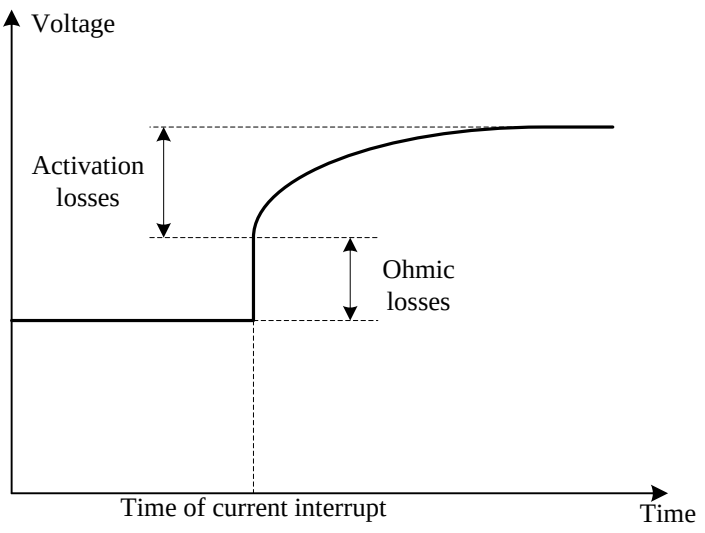

Figure 1-15: Voltage against time in a current interrupt process

especially for high-power cases. In addition, a completed EIS takes more than ten minutes, which lowers its online performance. In [43], the possibility of online obtaining the partial EIS curves through the control of DC/DC converters has been demonstrated. Such an EIS measurement method is so interesting that an European project named D-CODE[4], whose objective is to realize the integration of DC/DC converter based EIS measurement and EIS based diagnosis was launched in 2011 [47]. It could therefore be considered that the variables got from regular measurements and the power converter based EIS measurement are considered more relevant for online system diagnosis. The variables can be used for PEMFC system diagnosis are summarized in Table 1.2.

It should be noticed that other than the above mentioned variables that could be used as the ones for diagnosis, the open current voltage is used to detect the leakage fault in [48].

1.5.2.2 Multivariate analysis

Multivariate analysis[5] methods aim to remove the often-observed high degree of redundancy in the data by defining a reduced set of statistically uncorrelated variable.

[4]D-CODE: DC/DC Converter-based Diagnostics for PEM systems
[5]Multivariate analysis is also called multivariate statistical process control (MSPC)

Table 1.2: Variables can be used for PEMFC system diagnosis

Measurement type	Variable	Online/Offline	Cost
Regular measurement	Stack voltage	Online	Low
	Cell voltages	Online	Medium/high
	Current	Online	Low
	Temperatures	Online	Low
	Pressures	Online	Medium
	Flow rates	Online	High
	Humidities	Online	Medium
	EIS (Power converter based)	Online	Low
Special measurement	Polarization curves	Offline	Low
	EIS (Traditional)	Online (limited)	High
	LSV	Offline	Medium
	CV	Offline	Medium

Here, Fig. 1-16 can show the principle of the multivariate analysis. Suppose that the two variables x and y are monitored, and the fault diagnosis is based on them. The samples in normal state are distributed in the zone colored gray. If the individual variables are investigated independently, the upper and lower limits of the two variables $[x_1, x_2]$, $[y_1, y_2]$ could be found by considering the distribution each variables in normal operation state. With these limits, whether a point is in normal state can be told by judge whether it is within the variable limits. However, for some points, such as point 1 and point 2, they will be misdiagnosed to the normal state, although they are outside the normal zone. Comparatively, by using multivariate analysis, the data can be projected to a new space composed by x', y', and the normal zone obtained in the new space can rejected point 1 and point 2 successfully.

In [49], multivariate analysis technique, PCA (principal component analysis), is used for PEMFC diagnosis. PCA is used here mainly for fault detection. The theory of PCA is to build a principal component model under normal working conditions by using the relevance of process variables, and to find the fault by testing the divergence of samples from the principal component model [49]. To achieve this, dataset of 17 parameters were used for building the PCA model offline, and the faults can be detedted through the PCA model.

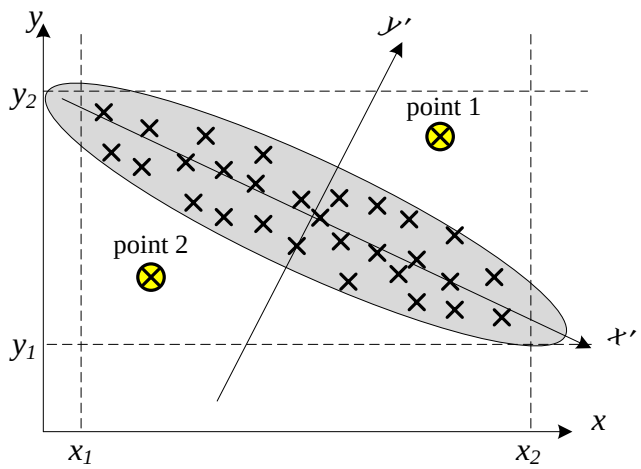

Figure 1-16: Schematic of multivariate analysis

Although multivariate analysis methods are thought to be simple and efficiency to realize fault detection, they seems only efficient in dealing with the diagnosis problems in steady state. In addition, the fault isolation performance of multivariate analysis methods is usually weak. Moreover, many variables are required, which means that many sensors need to be installed to the system.

1.5.2.3 Classification based

Another data-driven diagnosis branch is the pattern classification based approach. The classification based diagnostic procedure usually proceeds in two steps. Firstly, an empirical classifier is established from prior knowledge and history data. This is considered as the training process. Then, by using the classifier obtained, the real-time data are classified into certain classes that correspond to the health states, namely normal state or various fault states. Thus, fault detection and isolation can be achieved.

It has also been noticed that the classification performance can be improved by combining some signal analysis and/or feature extraction, as well as the feature selection methods [50]. Therefore, a general classification based diagnosis procedure can be summarized in Fig.1-17.

In [51], a kind of NNS named hamming neural network (HNN) is used to monitor

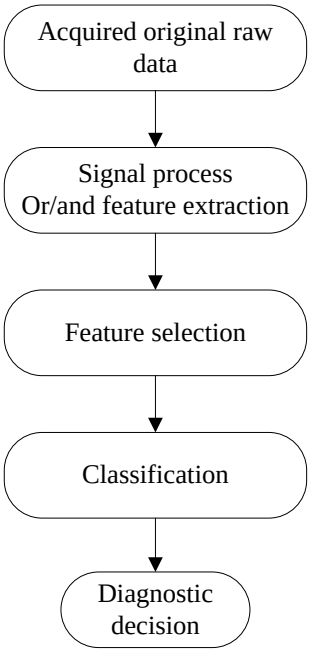

Figure 1-17: Flowchart of a classification based diagnosis process

the health state of a PEMFC. In this approach, a designed pulse current profile is performed on 20 single PEMFCs that were in different ageing stages. Four statistical features were extracted from each output voltage, and used for training HNN. Thus, HNN can classify the features of an arbitrary operating cell to one of the 20 different classes. The operating status, which was defined from fresh to aged, could be determined consequently. However, the proposed approach can only support the ageing information. The diagnosis of operating faults seems to be weak. Furthermore, a special current profile must be used to get the features.

In [35], the authors propose a PEMFC system durability diagnosis tool. Two values have then been extracted from EIS curves. Evolution over time of these two values is then considered. Fuzzy-clustering methodology is applied to identify clusters in this 2-D space; each of them relates to a specific behavior or ageing process of the concerned stack. Although this methodology gives some initial guidelines within the framework of embedded fuel cell system durability diagnosis, its function on fault diagnosis aspect is still not explored. Recently, authors of [52] extend the fuzzy clustering method further to the fault diagnosis of a commercial PEMFC system.

With feature extraction and selection step, two features, named maximal magnitude and occurring frequency of maximal phase, are used. The fault oxygen starvation and flooding could be identified. However, the fuzzy-clustering method is utilized on the obtained dataset. To diagnose the durability of an arbitrary sample, a classification procedure seems to be necessary following the clustering.

In [53], Bayesian networks (BS) classification is used for the PEMFC diagnosis. By using it, the cause-effect relationship among the variables of the process can be qualified and quantified. Four types of faults, including faults in the reactant supply subsystem, faults in the heat management subsystem, and faults inside the fuel cell, were diagnosed based on monitoring the easy-measured variables, such as current, stack voltage, temperature. However, the database for training the BS was still coming from a physical model. Similarly and more recently, another BS based fault diagnosis is proposed in [54]. Different from the former approach, the diagnosis variables are from the EIS measurement. More specifically, Bayesian classifier is implemented based on the impedance values at six different frequency points. Six operating modes can be discriminated by using this approach. However, these six operating modes involve just the status of water management.

The authors of [55] used Fast Fourier Transform (FFT) to correlate the stack voltage evolution with the pressure drop signal across the cathode/anode. The dominant frequency of cathode pressure drop signal was found to be an indicator of cathode flooding and a predictor of stack voltage increase and decrease. However, even if the FFT based methods lead to fine frequency resolution, they are not adapted to non-stationary signals which are typically extracted from the fuel cell during operation [30].

In [56], a classification based diagnosis strategy is proposed. A signal processing procedure, called wavelet transformation, is used to extract features from the stack voltage signal. Then, classification is used to identify whether flooding fault happens. Although this diagnosis approach is proven to be promising for the detection of flooding fault, the detection of other fault types and the fault isolation needs to be further investigated. A similar diagnosis approach is proposed recently in [57].

Wavelet transform combined with multifractal formalism is used to analyze the stack voltage, and the features which are sensitive to faults can be extracted. Similarly, the extracted features serve as the diagnostic symbols for classification. Several abnormal operation states in air supply subsystem can be detected. The approach seems to be promising for it needs only the regular stack voltage measurement. Nevertheless, more fault cases and more operating data should be tested to verify its performance and robustness.

The classification based diagnosis usually requires the data in normal state and in various fault classes. To do this, experiments in concerned fault situations should be carried out. This is considered to be hard even impossible missions in consideration of the hidden dangers. Moreover, these methods might suffer from lacking the robustness against unseen data [58].

1.5.3 Challenges of online PEMFC system fault diagnosis

Although much work has been done towards efficient and reliable PEMFC system diagnosis, the development of the diagnosis approach for fuel cell systems is still comparatively lagging behind the other development areas in fuel cell technology. Some challenges still exist, which motivate us to take more efforts on this topic.

1. Because model based fault diagnosis offers a physical significance of faults and the model based diagnosis theory seems to be well built [59]. If a diagnosis friendly process model, such as state space model, is available, a number of standard methods are available for diagnosis design. However, the model, which is accurate enough and adapted for diagnosis, is still absent. Hence, more efforts should be taken to model the fuel cell systems.

2. The available approaches mainly focus on the capability of the detection of some specific faults. Less attention is paid to the fault isolation and analysis. To make the diagnosis procedure more completed and more efficient, fault isolation and analysis should be attached more importance. To do this, amount of experiments under fault operations should be investigated.

3. To implement the diagnosis, the costs must also be taken into account, especially in the case of high-volume production. The costly sensors or instruments should be avoided if possible. For instance, the sensors for measuring gas flow rate, and the special instruments for EIS measurements.

4. Until now, the diagnosis strategies are mostly in the test stage. To really apply and verify these strategies, real-time implementation should be carried out. Especially, for the mobile applications, the diagnosis strategies should be coded in an embedded system, which deserves more efforts.

5. The fault diagnosis usually involves the faults that are related to the system operations. Note that the system degradations can also be caused by the ageing effects, which is considered as the normal evolution. Hence, the diagnosis strategy should be capable to discriminate the degradations caused by faults from that caused be ageing effects. In other word, the diagnosis strategy should do self-adaption in long-time operation.

6. When the faults are correctly diagnosed in time, suitable actions should be taken to eliminate these faults. Reasonable suggestions orders should be given to aid the system control or reparation. These tasks are actually in the scope of the fault tolerance control.

Motivated by the above mentioned challenges, this Ph.D. work is dedicated to advancing the PEMFC system diagnosis. Especially, the data-driven diagnosis is focused on. It should be emphasized that the study launched is not only useful for PEMFC system diagnosis, but it can also support some hints and inspiring thinking for the diagnosis of other industrial system.

1.6 Conclusion

In this chapter, the principles of the PEMFC functioning, the composition of PEMFC stack and PEMFC systems are generally introduced. The two main challenges for the

wide applications and commercialization, cost and durability, are given and discussed. The necessity of fault diagnosis for PEMFC systems is emphasized. The current available diagnosis approaches are reviewed, and the existing challenges are listed.

Chapter 2

Experimental PEMFC stacks and experimentation framework

This Ph.D. work places emphasis on the data-driven diagnosis, undoubtedly, the preparation of experimental data from real PEMFC systems are thus necessary. To make the presentation of the diagnostic strategy more clear, he experimental methodology to observe and measure the PEMFC operating parameters in normal and fault conditions been used will be introduced in this chapter. To do this, the test benches and PEMFC stacks investigated are firstly presented. After that, the experiments that were carried out to generate databases are introduced. Finally, the obtained datasets are described.

2.1 Test benches and stacks

2.1.1 Two test benches

A 1 kW and a 10 kW test benches, which had been developed in-lab, were employed respectively to fulfill the experimental requirements. Fig. 2-1 and Fig. 2-2 show the overall view of these two test benches.

Both test benches can be divided into several subsystems. Taking the 10 kW test bench as example, the schematic of the whole system is shown in Fig. 2-3, and the

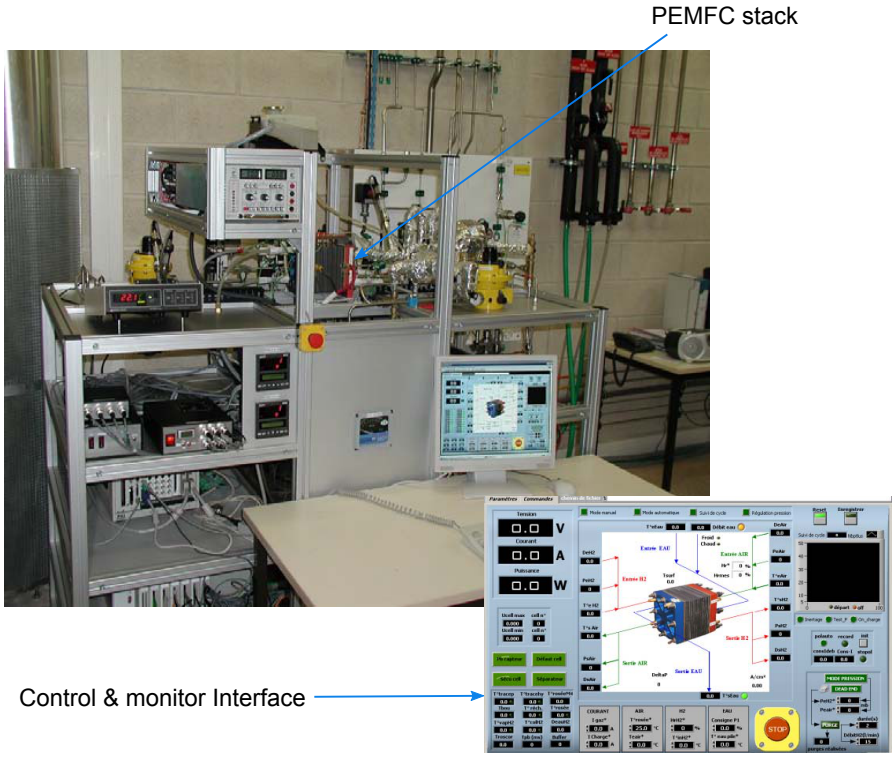

Figure 2-1: Overall view of the 1 kW testbench

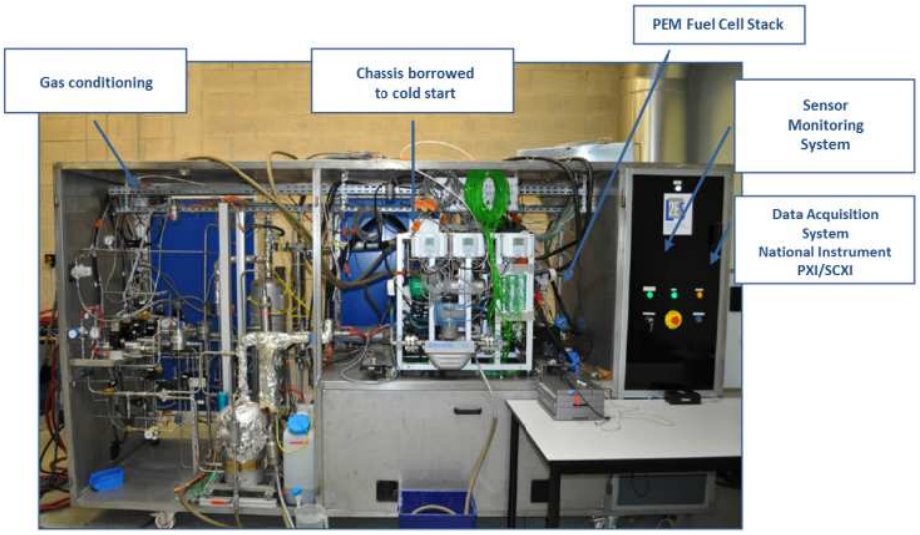

Figure 2-2: Overall view of the 10kW test bench

functions of each subsystem are as follows:

- Air supply subsystem: The air supply subsystem allows the regulation of air flow rate and air pressure on the cathode side of the fuel cells. The laboratory air network provides an elevated pressure of the air. Upstream and downstream valves as well as a mass flow rate regulator were been used to regulate air flow rate and air pressure in the stack. An automatic adjustment of air flow rate according to current can achieve a constant air stoichiometry (S_c). The hygrometry level at the air inlet can be regulated to the required conditions by using a humidifier located upstream of the stack.

- Hydrogen supply subsystem: Hydrogen is supplied from a high pressure tank. The pressure at the hydrogen inlet can be controlled to equal value with the air pressure through pressure regulator. An automatic adjustment of hydrogen flow rate according to current can achieve a constant stoichiometry (S_a). Hydrogen flow rate is set through the regulator downstream of the stack. Similarly as the air supply subsystem, hygrometry level at the hydrogen inlet can also be regulated thanks to the humidifier for hydrogen. The control of the humidifying of reactant gases is realized through regulation of the dew point temperatures of the upstream humidifiers.

- Temperature subsystem: The test bench is equipped with a thermal-regulated water circuit which ensures the control of the stack temperature. The value measured by the temperature sensor placed at the water circuit outlet is considered as the average stack temperature.

- Electronic load: The load current can be flexibly varied through an electronic load.

- Control/supervision unit: The controls of the test bench and the parameter monitoring are fulfilled using National Instruments Materials and Labview software. The variables that can be measured or monitored are summarized in Table

2.1. Other than these regular variables, EIS test instruments were installed on the two systems to measure EIS curves.

The composition of the 1 kW test bench is similar to that of 10 kW test bench. Except that the positions of gas flow rate regulators and gas pressure regulators are exchanged, and the component models with the same function are not completely same. More details about the two test benches, for instance the specific component models, can be found respectively in [60] and [61].

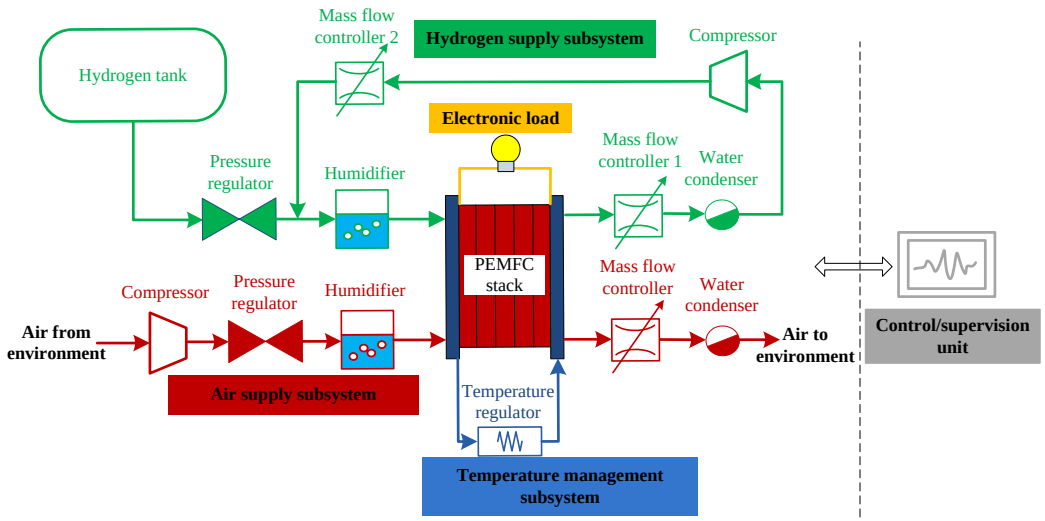

Figure 2-3: Schematic of the used 10 kW test bench [61]

2.1.2 Three PEMFC stacks

Three PEMFC stacks, which own respectively 20 cells, 8 cells and 40 cells, were used to carry out the various experiments. All these tests were in the framework French ANR DIAPASON project[1], which consisted two phases. Among the three stacks, the 20-cell stack was provided by a stack manufacturer. The stack was assembled with commercial MEAs marked Gore MESGA Primea Series 5510 and graphite distribution collector plates. The parameters of this stack is summarized in Table 2.2. The 8-cell stack and the 40-cell stacks were fabricated by the French research organization

[1]DIAPASON means "DIAgnostic de Pile à combustible Pour Applications automobiles et Stationaires sans instrumentatiON", and in English it means "Diagnosis of Fuel Cells for stationary and automotive applications".

Table 2.1: Measured variables

Variable	Notation
Flow rate at the H_2 inlet	D_{in,H_2}
Pressure at the H_2 inlet	P_{in,H_2}
Pressure at the H_2 outlet	P_{out,H_2}
Temperature at the H_2 inlet	T_{in,H_2}
Temperature at the H_2 outlet	T_{out,H_2}
Relative humidity at the H_2 outlet	RH_{in,H_2}
Flow rate at the *air* inlet	$D_{in,air}$
Pressure at the *air* inlet	$P_{in,air}$
Pressure at the *air* outlet	$P_{out,air}$
Temperature at the *air* inlet	$T_{in,air}$
Temperature at the *air* outlet	$T_{out,air}$
Relative humidity at the *air* outlet	$RH_{in,air}$
Temperature at the cooling water inlet	$T_{in,water}$
Temperature at the cooling water outlet	$T_{out,water}$
Current	I
Stack voltage	V_s
nth cell voltage (from anode side)	$v(n)$

CEA specially for automotive application[2]. Both stacks have the same technology parameters except the number of cells. The nominal operating conditions of the two stacks are summarized in Table 2.3. Actually, the 20-cell stack was used to fulfill the experimental requirements of the first-phase project; while the 8-cell stack and 40-cell stack were used for the second-phase tests.

Table 2.2: The parameters of the investigated fuel cell stack [56]

Cell area	100 cm^2
Cell number	20
Flow field structure	serpentine
Electrode surface area	100 cm^2
Nominal output power	500 W
Operating temperature region	20-65 ℃
Maximum operating pressures	1.5 bar
Anode stoichiometry	2
Cathode stoichiometry	4

[2]CEA: Alternative Energies and Atomic Energy Commission

Table 2.3: Nominal conditions of the stacks

Parameter	Value
Stoichiometry H_2	1.5
Stoichiometry Air	2
Pressure at H_2 inlet	150 kPa
Pressure at Air inlet	150 kPa
Differential of anode pressure and cathode pressure	30 kPa
Temperature (exit of cooling circuit)	80 °C
Anode relative humidity	50%
Cathode relative humidity	50%
Current	110 A
Voltage per cell	0.7 V
Electrical power of 8-cell stack	616 W
Electrical power of 40-cell stack	3080 W

2.2 Experiments and database

A variety of experiments including the ones under normal operating condition and different fault conditions were carried out on the three stacks. Note that different fault types are concerned over the two phases of project. The experiments carried out on the different stacks are summarized in Table 2.4. The faults, caused by the abnormal operations of the water management subsystem, the electric circuit, temperature subsystem, air supply subsystem and hydrogen supply subsystem, were taken into consideration. In fact, the failures of the different subsystems or auxiliary components usually result in the abnormal or non-optimal operations suffered by the stack. The faults studied are usually considered as ”reversible” or ”recoverable”, which can be corrected through appropriate operations. The efficient FDI of such kind of faults is the key focus of system diagnosis. In the following, these experiments and the obtained databases are presented respectively.

2.2.1 Experiments and database of 20-cell stack

2.2.1.1 Normal operating (Nl)

Based on the 1 kW experimental test bench, experiments in normal conditions were firstly carried out. In the experiments, stack temperature is set at T_{fc} = 40℃, the

Table 2.4: Experiments of various health states carried out on different PEMFC stacks

Stack	Health state description	Location	Notation
20-cell stack	Normal operating	Whole system	Nl
	Flooding	Water management subsystem	F_f
	Membrane drying	Water management subsystem	F_d
8-cell stack & 40-cell stack	Normal operating	Whole system	Nl
	High current pulse	Electric circuit	F_1
	Stop cooling water	Temperature subsystem	F_2
	High S_c	Air supply subsystem	F_3
	Low S_c	Air supply subsystem	F_4
8-cell stack	CO poisoning	H_2 supply subsystem	F_5

stoichiometries of hydrogen and air were set at the nominal values as in Table 2.2, relative humidity RH was been situated between 75% and 98%, which is considered as a normal region. The output current was configured from 40A to 2A. As Fig. 2-4 shows, current was set at 20 discrete points, for every current point, 100 samples were collected to one group.

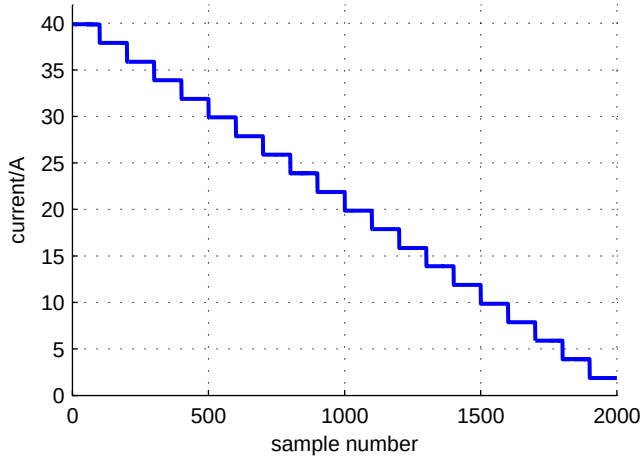

Figure 2-4: Current evolution in normal experiment

2.2.1.2 Flooding (F_f) and membrane drying (F_d)

Fault experiments of F_f and F_d were carried out to obtain the data in faulty states. In the fault experiments, the output current was fixed at 40 A; stack temperature is set at $T_{fc} = 40$ ℃; the stoichiometries of hydrogen and air were set at the nominal values as table 2.2. Relative humidity RH was been situated between 85% and 110%. The value of RH exceeds unity means that some liquid water vapour is presented in combination with the completely saturated air at inlet. The data acquired from a fault experiment was used for training procedure. Several independent fault experiments were done to further test and verify the approach.

It is considered in our study that a certain amount liquid water exists in the air paths of a normal operating fuel cell stack. At the beginning of each fault experiment, some time was needed to construct the necessary water environment, and the stack showed membrane drying state during this period. After this period, with the help of high humidified inlet air, the liquid water accumulated in the air paths. The flooding is therefore induced after a period of normal state. Hence, during the fault experiments, the stack went through three successive states: membrane drying fault state, normal state, and flooding fault state. The variables exposed in Table 2.1 were measured and saved in each experiment. Each fault experiment lasted about 15 min, and the sample time is set as 150 ms.

2.2.2 Experiments and databases of 8-cell stack and 40-cell stack

Experiments on the 8-cell stack and 40-cell stack were carried out over the 1 kW and 10 kW test benches respectively. Five faulty states other than fault free operating state were concerned. In order to test the robustness of the diagnosis strategies, experiments were carried out several times in each condition. Similarly, the variables in Table 2.1 were measured and saved in each experiment. The sample time is set as 100 ms for the tests of the two stacks. In the normal operating experiments, namely Nl, the two systems were both set to the nominal conditions. As for fault experiments,

taking one experiment as example for each fault, some intuitive and visualized results are presented to give a preliminary and qualitative analysis in the following content.

2.2.2.1 High current pulse (F_1)

At the system level, this is a fault which can occur at the electric circuit, such as electrical power converter. In the faulty experiments, high current pulse or short circuit was imposed between the two electrodes of the fuel cell stacks. Fig. 2-5 (a)-(b) show the electrical behavior of the stack in a short circuit process. It can be seen that a current impact appeared at the beginning of the short circuit. The current then decreased to stabilize at a fixed value which is about 2 times the nominal value. Here the current was limited by the mass transfer losses and by the hydrogen flow [62].

Fig. 2-5 (c)-(d) show the temperatures and humidities of the two stacks in the F_1 process. The short circuit occurred from 19 s to 27 s for the 8-cell stack, and from 83 s to 94 s for the 40-cell stack approximately. The high current pulse in the process caused a rise in the stack temperature, which is reflected by the temperature increase at the outlet of cooling water. The temperature was brought down with the help of the cooling circuit after the short circuit was eliminated. Since the saturation pressure of the fuel cell increased with the increasing of stack temperature, the relative humidities showed the inverted evolution of the stack temperature.

The pressures and gas flow rates in the process are shown in Fig. 2-5 (d)-(e). It can be observed that the cathode pressure varied little, while the anode pressure decreased with the abrupt consumption of the hydrogen in the fault process. After the fault was eliminated, the anode pressure was recovered thanks to a pressure regulator. The flow rates of the gases did not vary basically.

2.2.2.2 Stop cooling water (F_2)

At the system level, the F_2 fault happens at the temperature subsystem. It was caused by stopping the cooling water for some time. Fig. 2-6 shows the experimental measurements in the F_2 process. The disconnection of the cooling water circuit oc-

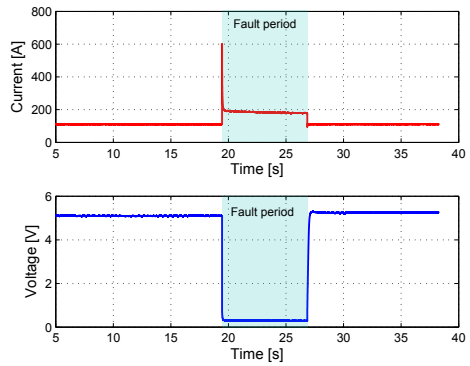

(a) Stack voltage and current of 8-cell stack

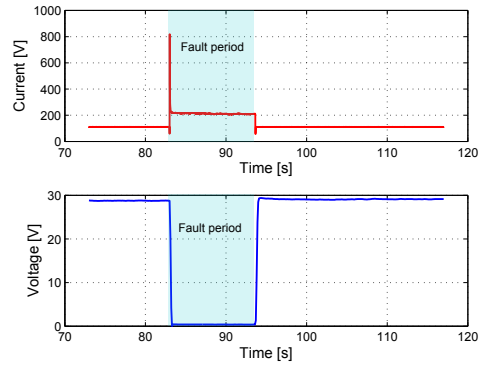

(b) Stack voltage and current of 40-cell stack

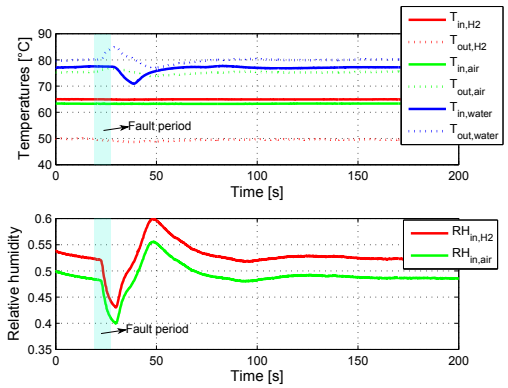

(c) Temperatures and relative humidities of 8-cell stack

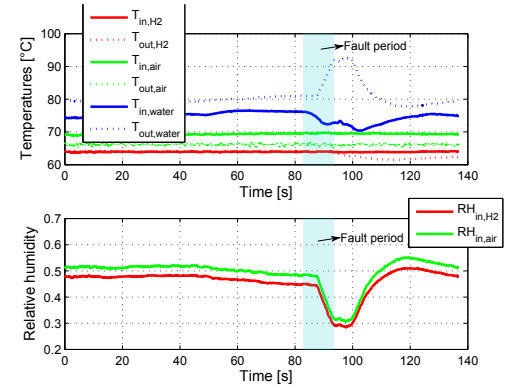

(d) Temperatures and relative humidities of 40-cell stack

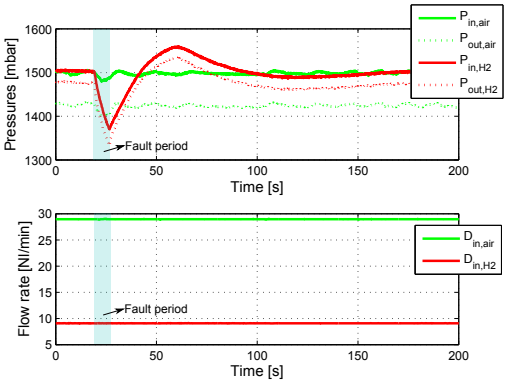

(e) Pressures and flow rates of 8-cell stack

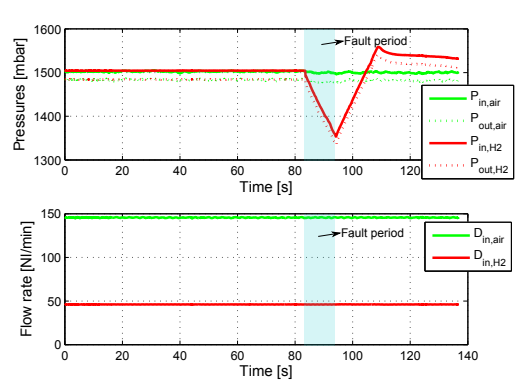

(f) Pressures and flow rates of 40-cell stack

Figure 2-5: Measurements in F_1 process

curred from 33 s to 76 s for the 8-cell stack, and from 8 s to 86 s for the 40-cell stack approximately. Temperatures and relative humidities in this process are shown in Fig. 2-6 (c)-(d). For the 8-cell stack, the temperatures of hydrogen inlet and outlet, inlet of air, inlet and outlet of cooling water showed little variation, while the temperature of air outlet increased in the process. For the 40-cell stack, the temperature at hydrogen outlet rose (from about 35 s to 100 s), while other temperatures showed no evident variations. Based on this observation, it is the reasonable to say that $T_{out,air}$ of the 8-cell stack and $T_{out,H2}$ of the 40-cell stack can better reflect the temperature variation of the stack than $T_{out,water}$ in the F_2 fault process. After the water circuit was reconnected, the $T_{out,water}$ was increased firstly under the influence of the internal temperature of the stack. Then, it decreased by regulation of the temperature subsystem. Concerning the relative humidities, an inverted evolution of $T_{out,water}$ could be observed for the humidities of both stacks.

Fig. 2-6 (a)-(b) show the electrical behavior of the stack in the process. With the constant current, the stack voltage decreased in this period. After that, the cooling water circuit was reconnected and the stack voltage rose up to the nominal value with the function of temperature regulation. It should be noticed that no marked decrease in the voltage was observed in the first phase. More precisely, it decreased about 0.25 V from 8 s to 60 s. A fast decline happened from 60 s to 92 s. A decrease of 8 V can be observed. For the 8-cell stack, voltage started decreasing when the cooling circuit was disconnected. The drops in the stack voltages could be connected to the membrane drying phenomenon. Actually, excessive temperature due to ineffective cooling can cause membrane dehydration and thus lower the conductivity of the membrane.

Fig. 2-6 (e)-(f) show the pressures and flow rates in the F_2 fault process. It can be said that there were no evident variations on these variables during the experiment.

2.2.2.3 High air stoichiometry (F_3) and low air stoichiometry (F_4)

At the system level, these two faults occur at the air supply subsystem. In the experiments of F_3 (respectively F_4), air stoichiometry was set to values that are higher (respectively lower) than the nominal value. Actually, a fuel cell can operate within

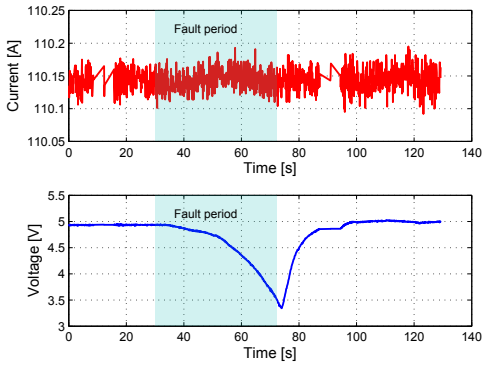

(a) Stack voltage and current of 8-cell stack

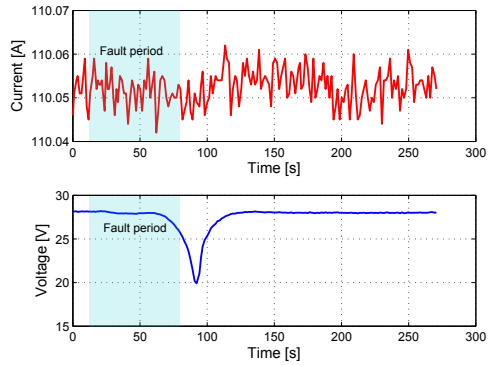

(b) Stack voltage and current of 40-cell stack

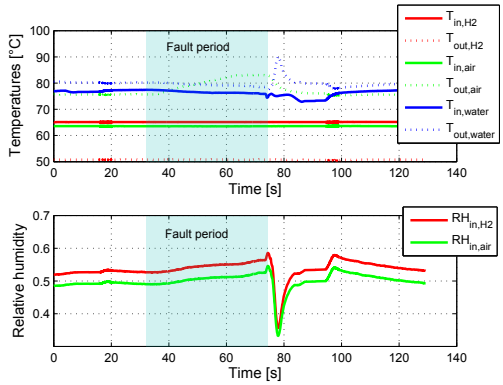

(c) Temperatures and relative humidities of 8-cell stack

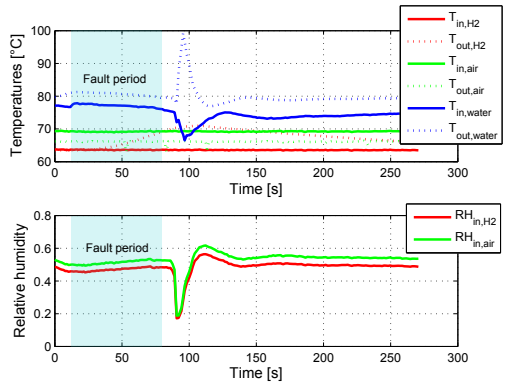

(d) Temperatures and relative humidities of 40-cell stack

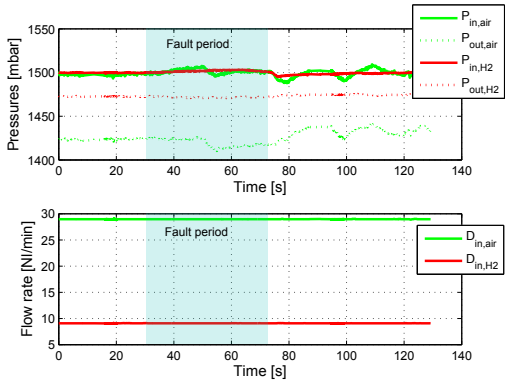

(e) Pressures and flow rates of 8-cell stack

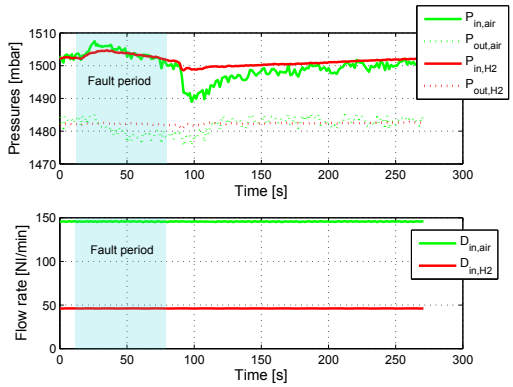

(f) Pressures and flow rates 40-cell stack

Figure 2-6: Measurements in F_2 process

a range of air stoichiometry values without the appearance of severe degradation. Technically, the air stoichiometry shift from nominal value to a certain degree causes rather a non-optimal operating state than a ”fault”.

The electrical, thermal, and fluidic variables in a F_3 fault experiment are shown in Fig. 2-7. The air stoichiometry was set respectively at 4 for the 8-cell stack and 5 for the 40-cell stack. From the experimental results, it can be seen that the stack reached to a stable state. The temperatures of gases and cooling water did not markedly vary in the process. $P_{in,air}$ was maintained to be the nominal value, while $P_{out,air}$ was smaller compared to the value in a normal operating process. In fact, the difference in the pressures at the air inlet and air outlet corresponds to the air flow rate. A larger flow rate usually results in a larger pressure difference [63]. With the nominal load, the stack voltages varied little from the nominal values. Note that during the F_3 and F_4 processes, EIS tests were also carried out for the 8-cell stack. Some light-magnitude signals of various frequencies could be seen for both currents and stack voltages.

The electrical, thermal, and fluidic variables in the F_4 fault experiment are shown in Fig. 2-8. The air stoichiometry was set at 1.2 for the 8-cell stack and 1.4 for the 40-cell stack. As in the case of F_3, it can be seen that the stack reached to a stable state. The temperatures of various positions did not show obvious variations in the process. The pressure at the air inlet was maintained at the nominal value, while the pressure at the air outlet reached to a higher value, which was contrary to the case of F_3. Little variations are seen in the currents and stack voltages.

Although the obvious degradation did not appear during the F_3 and F_4 faults, these faults should be avoided in the long term run. On the one hand, low air stoichiometry could be an incentive factor that leads to cathode water flooding and cathode starvation, which are considered as severer faults that can lead to very sharp degradation or even damage to the stack. On the other hand, an excessively high air flow could result in membrane drying, decreasing the conductivity of the membrane. In addition, more power is consumed to get a higher air stoichiometry, which will lower the overall system efficiency [19].

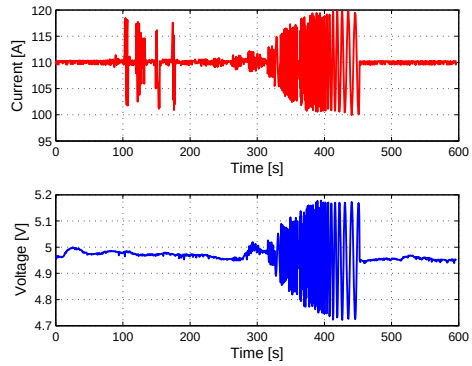

(a) Stack voltage and current of 8-cell stack

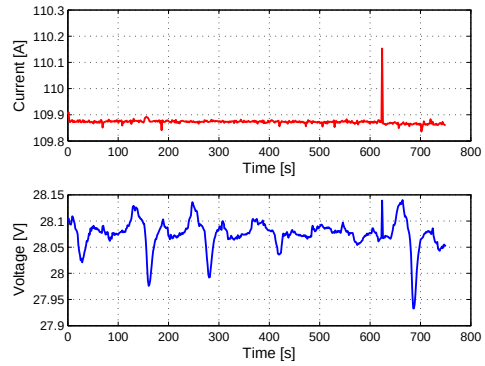

(b) Stack voltage and current of 40-cell stack

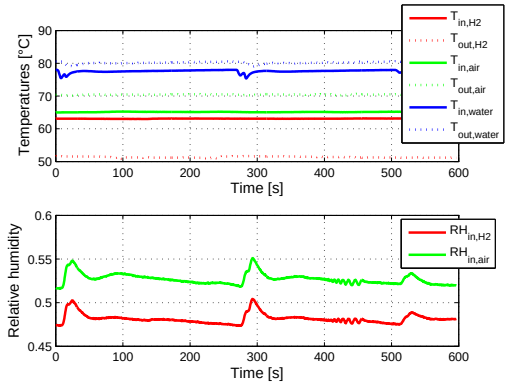

(c) Temperatures and relative humidities of 8-cell stack

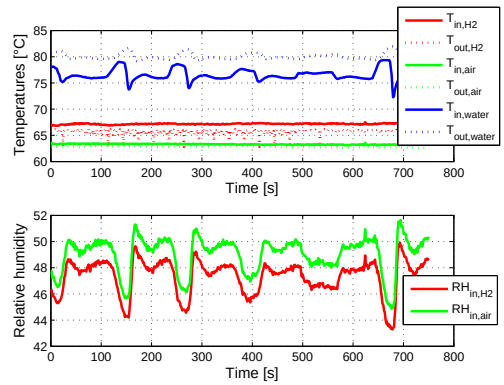

(d) Temperatures and relative humidities of 40-cell stack

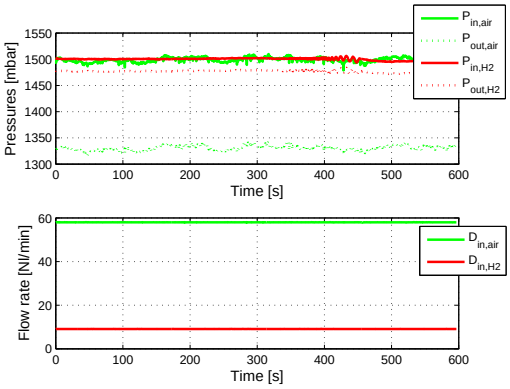

(e) Pressures and flow rates of 8-cell stack

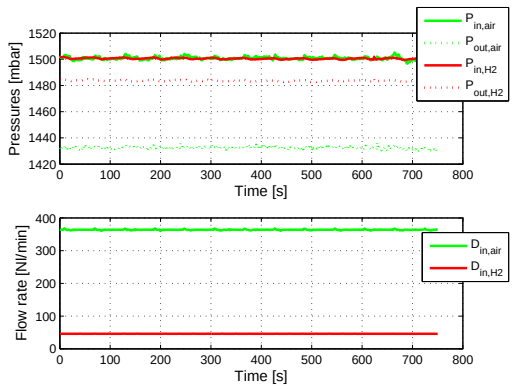

(f) Pressures and flow rates of 40-cell stack

Figure 2-7: Measurements in F_3 process

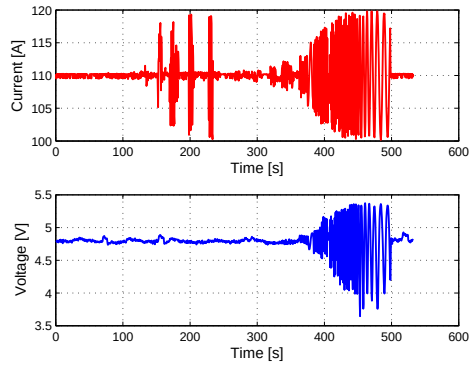

(a) Stack voltage and current of 8-cell stack

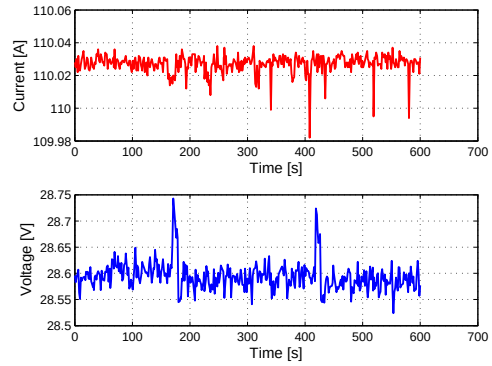

(b) Stack voltage and current of 40-cell stack

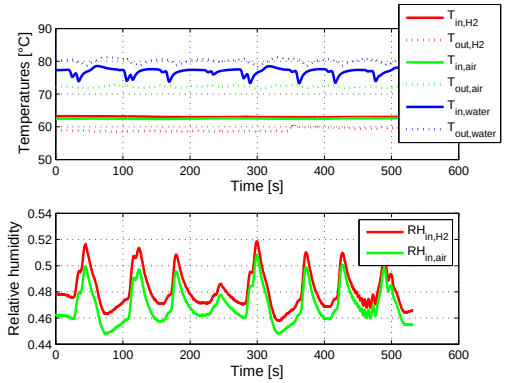

(c) Temperatures and relative humidities of 8-cell stack

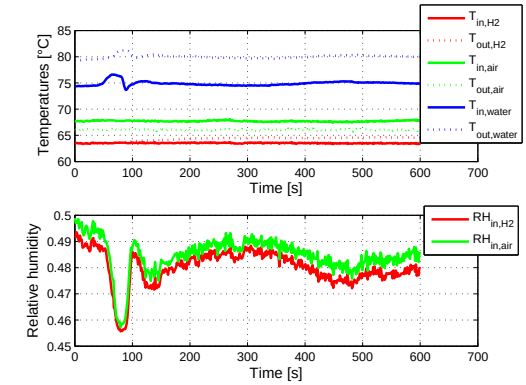

(d) Temperatures and relative humidities of 40-cell stack

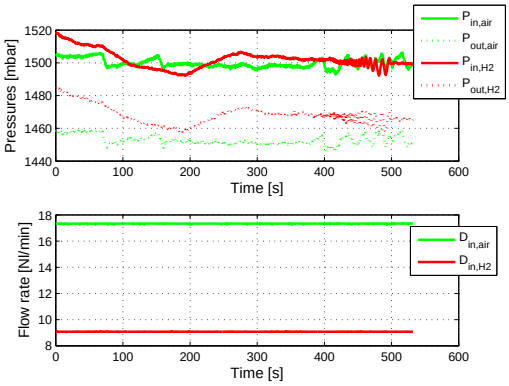

(e) Pressures and flow rates of 8-cell stack

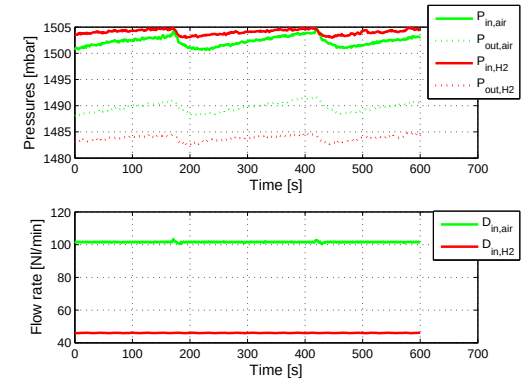

(f) Pressures and flow rates of 40-cell stack

Figure 2-8: Measurements in F_4 process

2.2.2.4 CO poisoning (F_5)

At the system level, CO poisoning occurs at the hydrogen supply subsystem. Actually, this fault has been considered one of the most common faults for PEMFC. The presence of carbon monoxide can block or limit the active sites of the platinum catalyst, and thus decrease the fuel cell performance [64]. The experiment of fault F_5 was carried out over the 8-cell stack by feeding the hydrogen with 10 ppm CO for 1.5 h, and then pure hydrogen was supplied instead of poisoned gas. In the process, EIS tests were performed several times.

The measurements are shown in Fig. 2-9. From a global point of view, the output stack voltage gradually decreased in the fault process and increased in the recovery process. The change rate of stack voltage decreased in both stages. The temperatures at the hydrogen outlet increased at the beginning of the fault process until 1100 s approximately , and then decreased. The temperature rise could be correlated to the increase in the anodic impedance [64]. From Fig. 2-9 (c), the pressure waves at the hydrogen inlet and outlet correspond to the current waveform, while the pressures at the air inlet and outlet varied little in the process. Based on the above preliminary analysis, the faults concerned include the severe faults, which could cause the rapid degradation of the system performance, such as F_1, F_2, F_5, and the slight faults, such as F_3, F_4.

2.3 Role of individual cell voltages for diagnosis

It is observed that different faults result in the different variations of the measurements. From a practical perspective, the "on-board" instrumentation has to be minimized, and using a minimal number of low-cost sensors is usually desirable. In order to realize FDI of these faults, stack voltage is usually considered as an efficient variable since it is the output of the system. However, only stack voltage seems to be feeble to achieve fault isolation aim, because a number of faults can cause the voltage drop.

Fuel cell voltage signals are highly dependent to the current, electrochemical char-

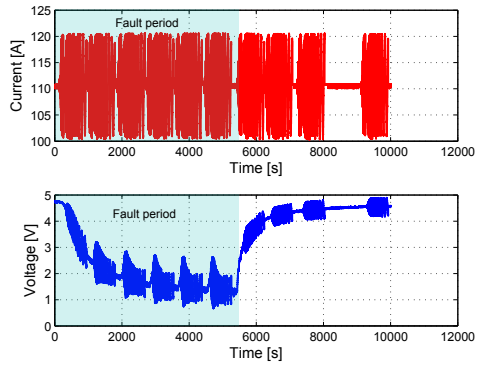

(a) Stack voltage and current of 8-cell stack

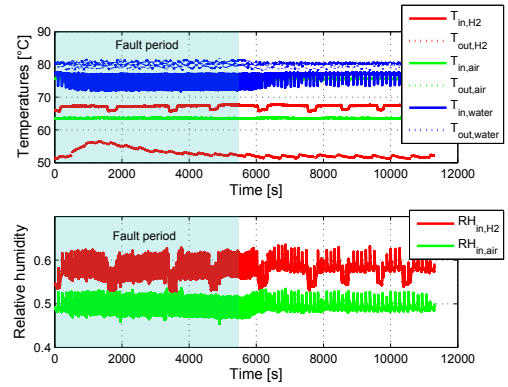

(b) Temperatures and relative humidities of 8-cell stack

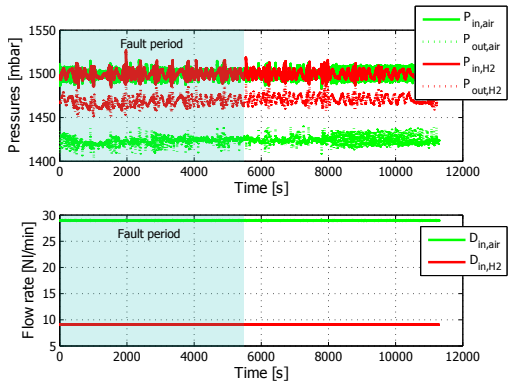

(c) Pressures and flow rates of 8-cell stack

Figure 2-9: Measurements in F_5 process

acteristics, temperature, and aging effect. So the cell voltage can reflect the local situation of a stack. In other words, the individual cell voltage can be seen as sensors inside the fuel cell stack. Without doubt, the individual cell voltages can supply more information for diagnosis than mere stack voltages. The importance of monitoring individual cell voltages is also stressed, since the cell with the lowest cell voltage in the stack restricts the maximum power output of the stack [65], it is necessary to monitor every single (or several) cell voltage(s) to some degree. Moreover, the cost of measurement of voltage signal is relatively low. Based on the above points, vectors constructed by individual cell voltages are considered as the original data for diagnosis. However, it should be noticed that a multi-channel voltage measurement system must be added for acquiring all the single cell voltages. This could lead to an increase of the overall system cost.

The individual behavior cell voltages of 20-cell stack in normal experiment and fault experiment are respectively depicted by Fig. 2-10 and 2-11. From the figures, it can be observed that the amplitudes of cell voltages in a normal experiment are more homogeneous than in a fault experiment from an overall point of view. In fault experiment, the cell voltages decrease with different speeds in the second half stage.

Fig. 2-12 shows the evolution of the cell voltages in the aforementioned processes. It should be noted that the individual cell voltages are distributed more evenly in certain states, e.g. Nl, F_3, F_4, than that in others e.g. F_1, F_2, F_5. The spacial distribution of individual cell voltages varies with the type of fault. Essentially, different faults can lead to different spatial distributions of temperature, humidity, and gas fluids and thus result in the different spatial distributions of individual cell voltages.

It seems that the individual cell voltages are the variables with the discriminative capability of different health states. Thus, they can be chosen as the original diagnosis-oriented variables for carrying out fault diagnosis.

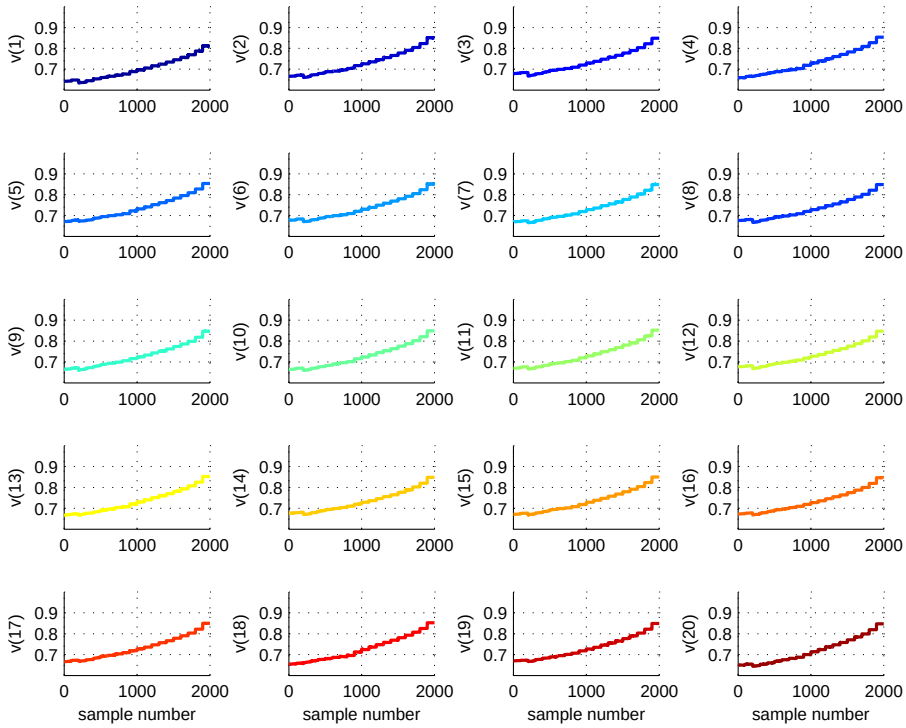

Figure 2-10: Cell voltages in a normal experiment.

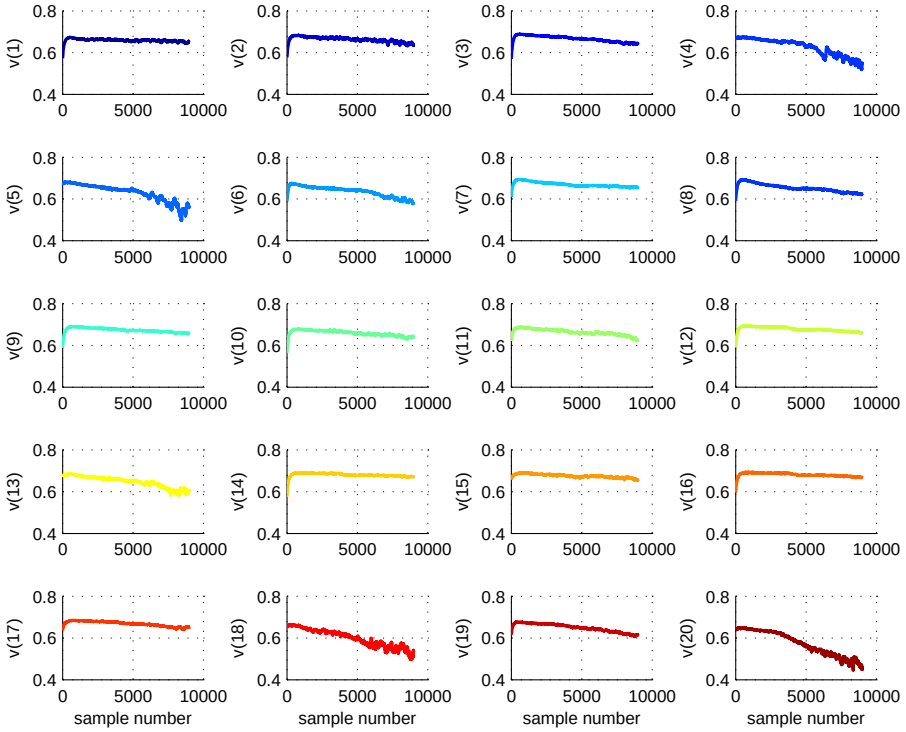

Figure 2-11: Cell voltages in a fault experiment

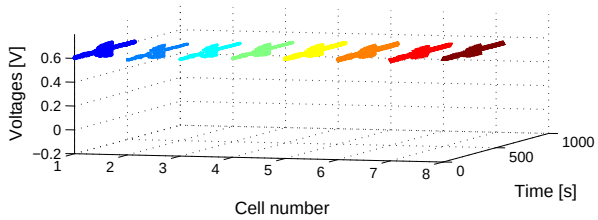

(a) Nl state (8-cell stack)

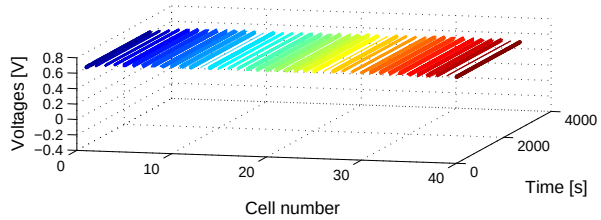

(b) Nl state (40-cell stack)

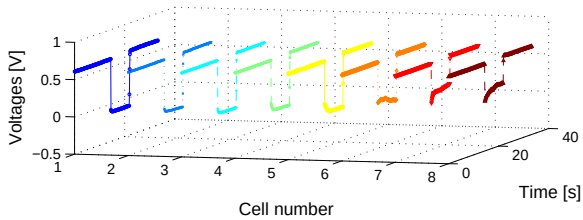

(c) F_1 state (8-cell stack)

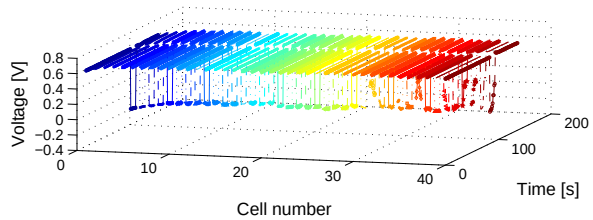

(d) F_1 state (40-cell stack)

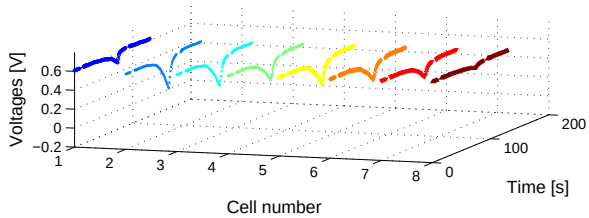

(e) F_2 state (8-cell stack)

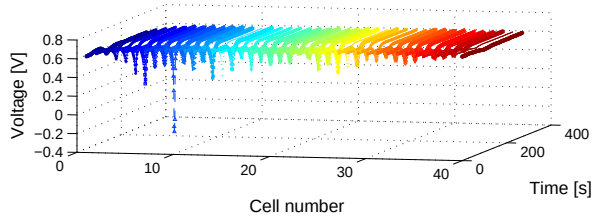

(f) F_2 state (40-cell stack)

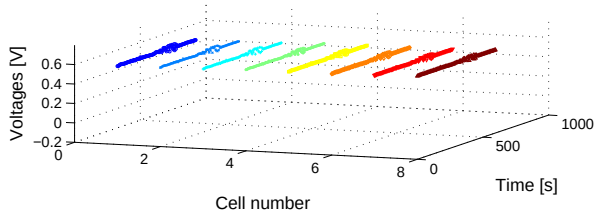

(g) F_3 state (8-cell stack)

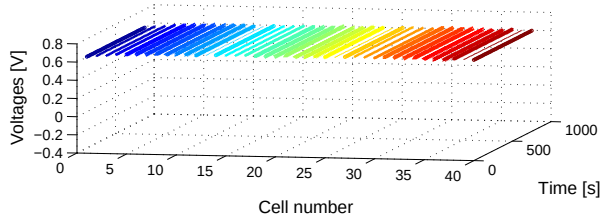

(h) F_3 state (40-cell stack)

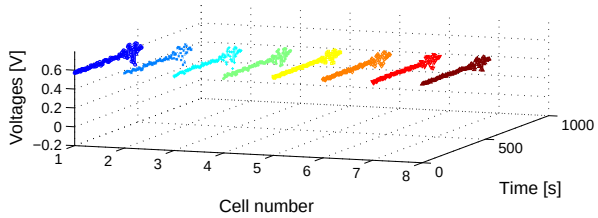

(i) F_4 state (8-cell stack)

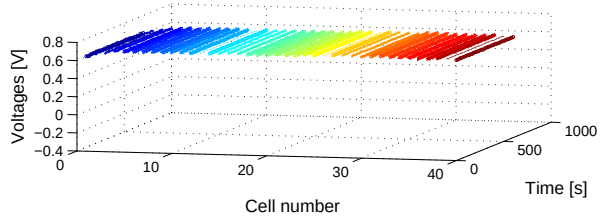

(j) F_4 state (40-cell stack)

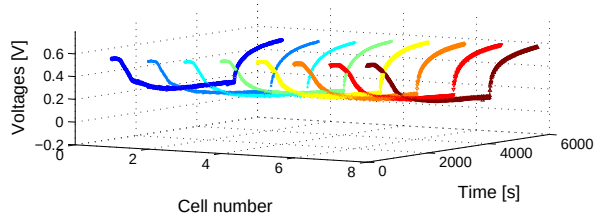

(k) F_5 state (8-cell stack)

Figure 2-12: The evolution of cell voltages in different processes

2.4 Conclusion

In this chapter, the two test benches and three stacks used to carry out the experiments are introduced. The experiments done for the three stacks are described. The databases sampled from the experiments are also presented and discussed preliminarily. At the end of this chapter, the role that single-cell voltages can play in fault diagnosis is discussed. It is found that several advantages can be obtained when the individual cell voltages are used as the variables for diagnosis.

Chapter 3

Pattern classification tools for diagnosis: a comparative study

Based on the discussion of last chapter, it have been acknowledged that individual cell voltages are very promising variables for PEMFC system diagnosis. Taking individual cell voltages as diagnostic variables, the classification based fault diagnostic methodologies will be studied in this chapter. The methodologies in each stage of the strategy will be compared. The database obtained from the experiments on 20-cell stack will be dedicated for this comparative study, and the faults F_f and F_d will serve as the faults to diagnose.

3.1 Approach principle

The approach proposed in this chapter is based on experimental data of 20-cell stack and contains three steps (see Fig. 3-1) : data labeling process, model training process, and diagnosis process. The first two processes are off-line, while the third one is on-line.

The pattern classification methods used belong to supervised ones. In supervised learning, the samples for training should be provided with their category labels before the training procedure. Consequently, it is necessary to define the classes and label the training data. In the labeling stage, a two-phase pressure drop model combined with

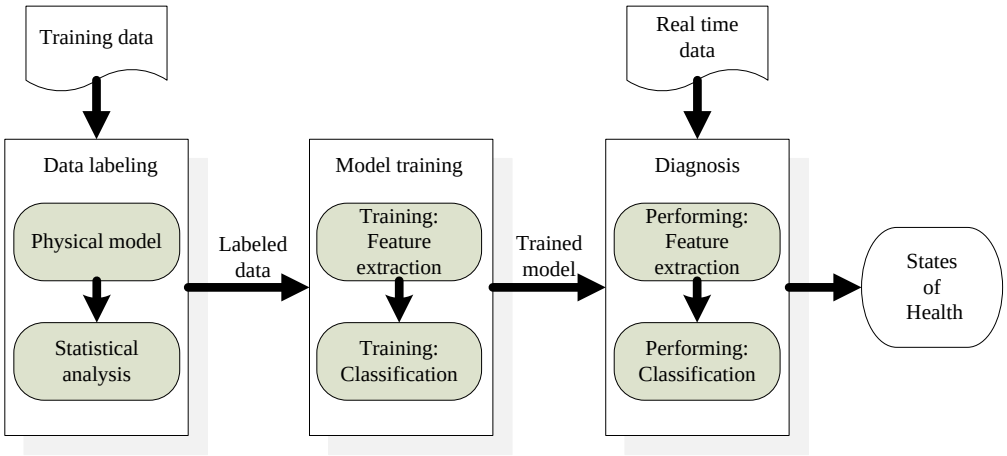

Figure 3-1: The framework of the diagnosis approach

statistical analysis is used to achieve this [66] [67]. After the data labeling process, the training data can be labeled to three classes: normal state, flooding fault state, and membrane drying state.

In the model training process, two kinds of actions, which are feature extraction and classification, need to be realized. In feature extraction, the goal is to find certain projecting vectors to map the original high-dimensional vectors to feature space, which is of low-dimension. Notice that in the classification, the classifiers will be trained in the feature space. By the trained classifiers, a new point in feature space can be fixed to one of the three predefined classes. In the literature, there are various kinds of methodologies for feature extraction and classification. Hence, this work present several relevant and representative methodologies that can be used to compare their performances on the PEMFC diagnosis.

In the diagnosis process, the real-time cell voltages are sampled and represented by vectors. Then, the feature extraction and classification procedures are respectively carried out by using the models obtained in the training process. The real-time data can thus be classified into three classes, and the diagnosis is realized accordingly after these two procedures.

3.2 Data labeling methodologies

For most cases, the data from different health states can be prepared by carrying out the specific experiments. However, in some cases, historical data that serve as training data often contains both normal and abnormal data, and cannot be intuitively labeled with the knowledge in hand. A data labeling procedure seems to be needful in such situations [68]. Here, in the fault experiments on 20-cell stack, the data of different health states are mixed. In order to label the training data to the three classes: "Nl", "F_f", and "F_d", the normal range of liquid water inside the fuel cell must be evaluated. Here, pressure drop model and statistical analysis are combined to achieve this goal.

3.2.1 Pressure drop model

The pressure drop between inlet and outlet channels is significant of the gases removal out of the fuel cell, and it is relevant to the content of liquid water in the flow fields [7]. Since the generated water is mostly expelled from the cathode side, it is more relevant to the water management issues. Hence, the pressure drop model in the cathode side will be considered.

GFCs are grooved on both sides of BPs for gas flow and different structures can be used. Fig. 3-2 depicts three classic structures: parallel, serpentine and interdigitated flow fields. Notice that the pressure drop model is dependent on the considered structures.

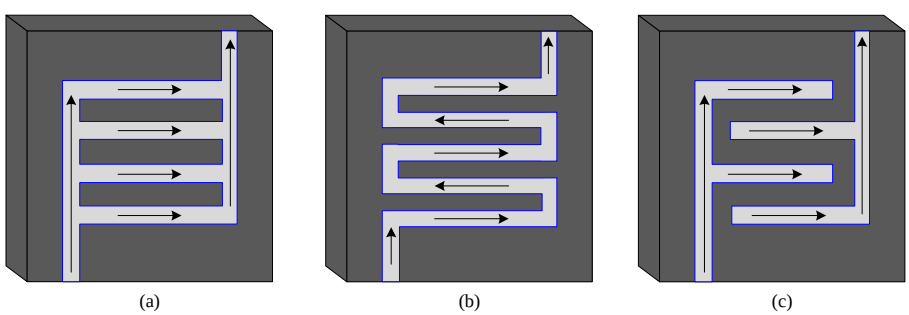

Figure 3-2: Three kinds of flow field structures. (a) Parallel flow field. (b) Serpentine flow field. (c) interdigitated flow field

For the parallel and serpentine flow fields, the air passes from the GFCs, and the

pressure drops throughout the GFCs. The major part of pressure loss is associated with the frictional losses along the channel pipe [69]. In this case, the pressure drop model based on Darcy law is given by [66]

$$\Delta P = \frac{\mu}{K_{C_0}(1-s)^{n_k}} D_{air} L_{GFC} \tag{3.1}$$

where D_{air} is the average air flow rate, K_{C_0} is permeability, which is impacted by the sizes and the structures of flow fields. μ denotes viscosity of air and L_{GFC} is the length of the channel. $s \in [0, 1)$ is defined as the volume fraction of GFC occupied by liquid water, which is a key parameter characterizing the water quantity. n_k is a constant between 4.5 and 5.0 (see [66]).

For the interdigitated flow field, the pressure drop mainly occurs in the GDL. In this case, the pressure drop can be denoted as [67]

$$\Delta P = \frac{150(1-\varepsilon(1-s))^2\mu}{\varepsilon^3(1-s)^3 d_0^2} D_{air} L_{GDL} \tag{3.2}$$

where d_0 is the representative diameter of pore in GDL, L_{GDL} is the rib length of the BP. ε is constant that reflects the porosity of GDL. $s \in [0, 1)$ quantifies the portion of pores (in GDL) occupied by liquid water. Undoubtedly, in (3.1) and (3.2), s can be considered as a criteria to quantify the water content inside the fuel cells.

3.2.2 A statistical method for identification F_f and F_d

From (3.1) and (3.2), the quantity $\Delta P / D_{air}$ can be considered as a function depending on s:

$$W(s) = \frac{\Delta P}{D_{air}}$$

where

$$W^{(1)}(s) = \frac{\alpha}{(1-s)^{n_k}} \quad \text{and} \quad W^{(2)}(s) = \beta \frac{(1-\varepsilon(1-s))^2}{(1-s)^3} \tag{3.3}$$

with

$$\alpha = \frac{\mu L_{GFC}}{K_{C_0}} \quad \text{and} \quad \beta = 150 \frac{\mu L_{GDL}}{\varepsilon^3 d_0^2}$$

Clearly, $W^{(1)}$ and $W^{(2)}$ defined by (3.3) are increasing function for $s \in [0, 1)$. Thus, W can replace s to express water quantity. In normal state, it is considered that the fuel cell can operate in a range of s, so the values of W also distribute in a normal range. If the values of W follow a normal distribution, which is the case in our study, a common statistical method "3-sigma" can be used in order to evaluate the limits of W in normal state:

$$W_{max} = \bar{W} + 3\sigma(W), W_{min} = \bar{W} - 3\sigma(W) \tag{3.4}$$

where $\bar{W}$ and $\sigma(W)$ are respectively the average value and standard deviation of W samples in normal state.

In the labeling process, W_{max} is the threshold for flooding diagnosis while W_{min} is the one for drying fault diagnosis. The flow chart of the training data labeling procedure can be depicted as Fig. 3-3.

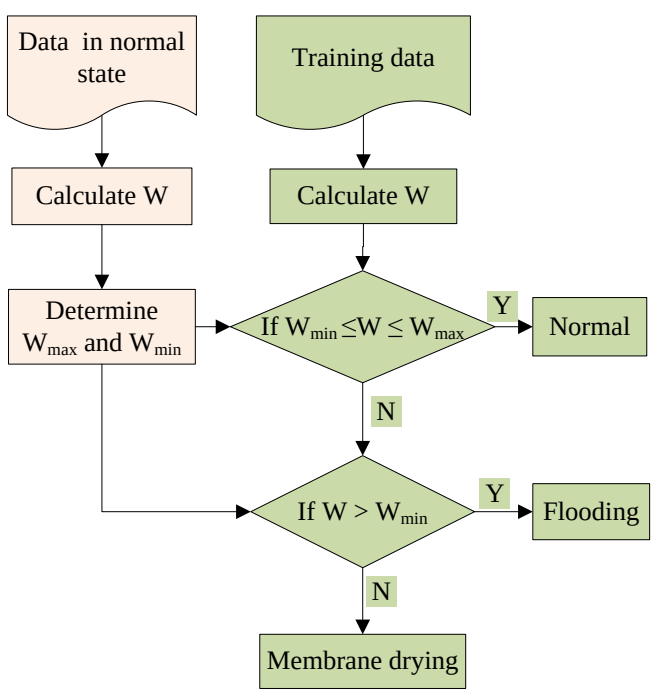

Figure 3-3: Training data labeling process

3.2.3 Data labeling result

The experimental data of 20-cell stack that were presented in the last chapter are used to verify the methodologies.

In the normal state experiments, water indicator W was calculated for every sample. The Lilliefors tests were used to test the null hypothesis that W follows a normally distributed population for each group [70]. The null hypotheses were not rejected with significance level 0.05 for all the 20 groups. Hence, it was reasonable to define the up and down limits as (3.4).

The values W of normal condition in different current points are as in Fig. 3-4. The up limit W_{max} and down limit W_{min} are also shown in this figure. It can be seen that W_{max} and W_{min} increase globally with current increasing. This could be because water volume generated increases with the rise of the current. Other phenomena could produce the nonlinear property of W for a compressible fluid flow, such as the flow regime (laminar flow, turbulent flow, or transition flow between laminar and turbulent) [71].

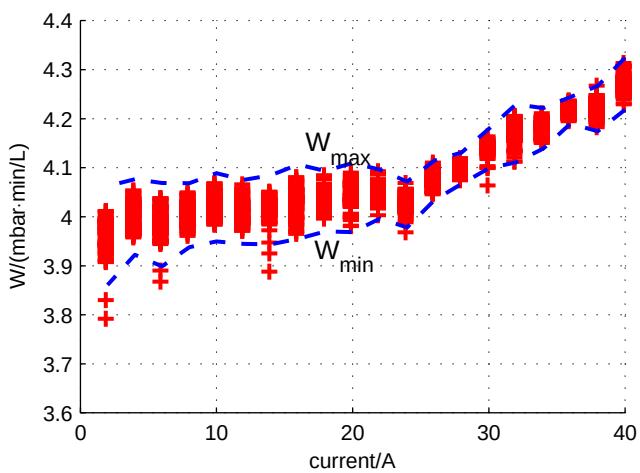

Figure 3-4: Values of parameter W in normal condition and their limits

The values of W in the fault experiments were compared with the corresponding limits W_{max} and W_{min}. The parameter W in a fault experiment was shown in Fig. 3-5.

It seems that the variable W deduced from the pressure drop model is able to be used for monitoring the the water management faults F_f and F_d. However, it should also be noticed that pressure sensors and the instruments for air flow measurement must be settled at both sides of the air stream. These sensors would increase the cost of the fuel cell system. This motivates us to make an effort to realize the fault diagnosis by analyzing only cell voltages.

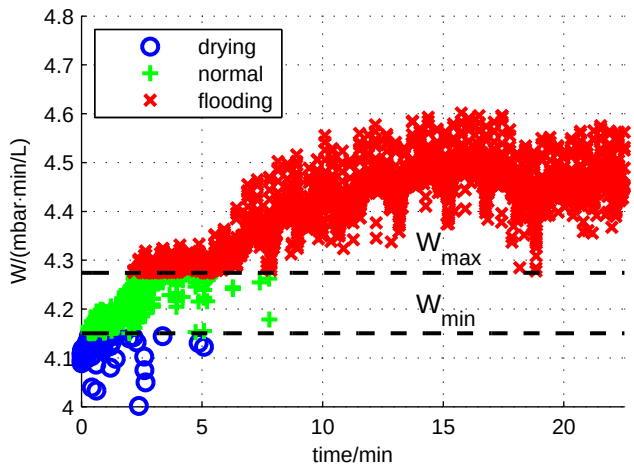

Figure 3-5: Parameter W of data in fault process

3.3 Feature extraction

For high power applications, for instance vehicles, a large number of fuel cells are usually stacked in series to meet the power requirement. Hence, large dimension data has to be handled when individual cell voltages serve as the variables for diagnosis. In order to reduce the complexities of computations, it is necessary to lower the data dimension by some means of feature extraction. At the same time, the feature extraction procedure is motivated to draw useful features for diagnosis. Based on the above considerations, four representative feature extraction methodologies, which can meet these two needs, are presented in this subsection. More precisely, two typical unsupervised and supervised methodologies: Principal Component Analysis (PCA), Fisher

Discriminant Analysis (FDA), and their nonlinear forms Kernel Principal Component Analysis (KPCA) and Kernel Principal Component Analysis (KFDA), are considered.

The feature extraction problem can be described as follows: Collect N training samples $\boldsymbol{v}_1,\ \boldsymbol{v}_2,\ \ldots,\ \boldsymbol{v}_N \in \mathbb{R}^M$, which are distributed in C classes $V_1, V_2, \ldots, V_C$. Sample indexes in ith class are collected as set ω_i. Sample $\boldsymbol{v}_n$ is a vector constructed by M cell voltages (cell number is M):

$$\boldsymbol{v}_n = [v_n(1), v_n(2), \ldots, v_n(M)]^T \tag{3.5}$$

The sample number of ith class is N_i, which satisfies $\sum_{i=1}^{C} N_i = N$. The class index of $\boldsymbol{v}_n$ is denoted by h_n, $h_n \in \{1, 2, \ldots, C\}$. The objective of the training process is to find L $(L < M)$ M-dimension unit projecting vectors: $\{\boldsymbol{w}_1, \boldsymbol{w}_2, ..., \boldsymbol{w}_L\}$. With these vectors, a real-time sample $\boldsymbol{v}$ can be projected to a L-dimension feature space, the projected vector $\boldsymbol{z}$ is expressed:

$$\boldsymbol{z} = [\boldsymbol{w}_1^T \boldsymbol{v}, \boldsymbol{w}_2^T \boldsymbol{v}, \ldots, \boldsymbol{w}_L^T \boldsymbol{v}]^T \tag{3.6}$$

3.3.1 PCA

PCA is an unsupervised dimensionality reduction and feature extraction technique that preserves the significant variability information in the original data set. It changes more relevant variables into seldom uncorrelated variables according to the lowest data missing rule [49].

Without loss of generality, it is considered that the original data are firstly projected to into a 1-dimension space with projecting vector $\boldsymbol{w}$:

$$z_n = \boldsymbol{w}^T \boldsymbol{v}_n \tag{3.7}$$

where $\{z_n\}$ are the projected points corresponding to $\{\boldsymbol{v}_n\}$, the variance of $\{z_n\}$ is[1]

$$s_z = \frac{1}{N}\sum_{n=1}^{N}(\boldsymbol{w}^T\boldsymbol{v}_n - \boldsymbol{w}^T\bar{\boldsymbol{v}})^2 = \boldsymbol{w}^T\boldsymbol{S}\boldsymbol{w} \tag{3.8}$$

where $\bar{\boldsymbol{v}} = \frac{1}{N}\sum_{n=1}^{N}\boldsymbol{v}_n$, and $\boldsymbol{S} = \frac{1}{N}\sum_{n=1}^{N}(\boldsymbol{v}_n - \bar{\boldsymbol{v}})^2$.

The task is to find $\boldsymbol{w}$ which makes the s_y to be maximum, to do this, Lagrange multiplier denoted by λ is introduced as

$$L(\boldsymbol{w}, \lambda) = \boldsymbol{w}^T\boldsymbol{S}\boldsymbol{w} - \lambda(1 - \boldsymbol{w}^T\boldsymbol{w}) \tag{3.9}$$

By setting the derivative with respect to $\boldsymbol{w}$ equal to zero, it is obtained that

$$\boldsymbol{S}\boldsymbol{w} = \lambda\boldsymbol{w} \tag{3.10}$$

So the variance will be a maximum when we set $\boldsymbol{w}$ equal to the eigenvector corresponding to largest eigenvalue

$$\boldsymbol{w}^T\boldsymbol{S}\boldsymbol{w} = \lambda \tag{3.11}$$

Since the number of observations is usually much larger than dimension number of observations, i.e. $N \gg M$, matrix $\boldsymbol{S}$ is usually full rank, and there are M positive eigenvalues related to $\boldsymbol{S}$[2]. It can be imagined that when $\boldsymbol{v}_n$ is projected to a L dimensional space, the L eigenvectors $\boldsymbol{w}_1, \boldsymbol{w}_2, \ldots, \boldsymbol{w}_L$ with the L largest eigenvalues $\lambda_1, \lambda_2, \ldots, \lambda_L$ are the corresponding projecting vectors.

The Accumulation Contribution Rate (ACR) which is defined as

$$ACR = \frac{\sum_{i=1}^{L}\lambda_i}{\sum_{i=1}^{M}\lambda_i} \tag{3.12}$$

is used to describe the accumulation variance contribution rate of the principal components. When ACR is over a threshold, it will be regarded that the principal com-

[1]Here, the denotation $\{z_n\} = \{z_n | n = 1, \ldots, N\}$ is used. The denotation $\{\boldsymbol{v}_n\}$ is similarly defined.

[2]Because the covariance matrix is positive-semidefinite, of which the eigenvalues are all equal or greater than 0.

ponents can represent the information of original data sufficiently.

PCA procedure used in this study can be summarized by Algorithm 1.

Algorithm 1 PCA

Training:

1: Collect samples $\boldsymbol{v}_1, \boldsymbol{v}_2, \ldots, \boldsymbol{v}_N$.

2: Perform singular value decomposition on covariance matrix:

$$\frac{1}{N}\sum_{n=1}^{N}(\boldsymbol{v}_n - \bar{\boldsymbol{v}})(\boldsymbol{v}_n - \bar{\boldsymbol{v}})^T = \boldsymbol{P}\Lambda\boldsymbol{P}^T \tag{3.13}$$

where $\bar{\boldsymbol{v}} = \sum_{n=1}^{N}\boldsymbol{v}_n/N$, $\boldsymbol{P} = [\boldsymbol{w}_1, \ldots, \boldsymbol{w}_M]$, $\Lambda = diag(\lambda_1, \ldots, \lambda_M)$, $\lambda_1 \geq \lambda_2 \geq \cdots \geq \lambda_M$.

3: Determine the number of principal components L by respecting:

$$\frac{\sum_{i=1}^{L}\lambda_i}{\sum_{i=1}^{M}\lambda_i} \geq Th, \frac{\sum_{i=1}^{L-1}\lambda_i}{\sum_{i=1}^{M}\lambda_i} < Th \tag{3.14}$$

where Th is a pre-set threshold, whose value is near but less than 1 (here is set at 0.9).

4: Save vectors $\boldsymbol{w}_1, \ldots, \boldsymbol{w}_L$.

Performing:

Calculate the projected vector of a new sample $\boldsymbol{v}$ as (3.6).

3.3.2 FDA

FDA is a supervised technique developed to reduce the dimensions of the data in the hope of obtaining a more manageable classification problem. The objective of FDA is to find the mapping vectors that make the data in the same class concentrated while the data in different classes separated [72] [73].

Original vectors $\{\boldsymbol{v}_n\}$ are projected into the 1-dimension points $\{z_n\}$ with the same projecting procedure defined in (3.7). Within-class variance s_w is defined in the feature space:

$$s_w = \sum_{i=1}^{C}\sum_{n\in\omega_i}(z_n - \bar{z}_i)^2 \tag{3.15}$$

where $\bar{z}_i$ is the mean value of data in ith class: $\bar{z}_i = \sum_{n\in\omega_i} z_n/N_i$. s_w represents the variance of the data in the identical classes.

The between-class variance s_b which represents the variance between data in different classes is defined:

$$s_b = \sum_{i=1}^{C} N_i(\bar{z}_i - \bar{z})^2 \tag{3.16}$$

The Fisher criterion, which is large when the between-class covariance s_b is large and the within-class covariance s_w is small, is given by

$$J(\boldsymbol{w}) = \frac{s_b}{s_w} \tag{3.17}$$

Substituting (3.7) to (3.15) and (3.16), (3.17) can be rewritten under the form

$$J(\boldsymbol{w}) = \frac{\boldsymbol{w}^T \boldsymbol{S}_b \boldsymbol{w}}{\boldsymbol{w}^T \boldsymbol{S}_w \boldsymbol{w}} \tag{3.18}$$

where within class scatter matrix $\boldsymbol{S}_w$ and between class matrix $\boldsymbol{S}_b$ are defined

$$\boldsymbol{S}_w = \sum_{i=1}^{C} \sum_{n \in \omega_i} (\boldsymbol{v}_n - \bar{\boldsymbol{v}}_i)(\boldsymbol{v}_n - \bar{\boldsymbol{v}}_i)^T \tag{3.19}$$

and

$$\boldsymbol{S}_b = \sum_{i=1}^{C} N_i(\bar{\boldsymbol{v}}_i - \bar{\boldsymbol{v}})(\bar{\boldsymbol{v}}_i - \bar{\boldsymbol{v}})^T \tag{3.20}$$

where $\bar{\boldsymbol{v}}_i$ is the mean vector in class ω_i: $\bar{\boldsymbol{v}}_i = \sum_{\boldsymbol{v}_n \in \omega_i} \boldsymbol{v}_n / N_i$, and $\bar{\boldsymbol{v}}$ is the mean vector of the total dataset: $\bar{\boldsymbol{v}} = \sum_{n=1}^{N} \boldsymbol{v}_n / N$.

The *within class scatter matrix* $\boldsymbol{S}_w$ is proportional to the sample covariance matrix for the pooled M-dimensional data. It is symmetric and positive semidefinite, and is usually nonsingular if $N > M$. Likewise, $\boldsymbol{S}_b$ is also symmetric and positive semidefinite, but usually $\boldsymbol{S}_b$ is quite singular.

Another matrix named *total scatter matrix* $\boldsymbol{S}_t$ is also defined

$$\boldsymbol{S}_t = \sum_{n=1}^{N} (\boldsymbol{x}_n - \bar{\boldsymbol{x}})(\boldsymbol{x}_n - \bar{\boldsymbol{x}})^T \tag{3.21}$$

it is easy to verify that

$$\boldsymbol{S}_t = \boldsymbol{S}_b + \boldsymbol{S}_w \tag{3.22}$$

In (3.18), the problem seeking $\boldsymbol{w}$ that makes $J(\boldsymbol{w})$ be maximum can also be converted to seeking the equal $\boldsymbol{w}$ which makes either of the following criterion maximized:

$$J_1(\boldsymbol{w}) = J(\boldsymbol{w}) + 1 = \frac{\boldsymbol{w}^T(\boldsymbol{S}_b + \boldsymbol{S}_w)\boldsymbol{w}}{\boldsymbol{w}^T\boldsymbol{S}_w\boldsymbol{w}} = \frac{\boldsymbol{w}^T\boldsymbol{S}_t\boldsymbol{w}}{\boldsymbol{w}^T\boldsymbol{S}_w\boldsymbol{w}} \tag{3.23}$$

$$J_2(\boldsymbol{w}) = \frac{1}{1/J(\boldsymbol{w}) + 1} = \frac{\boldsymbol{w}^T\boldsymbol{S}_b\boldsymbol{w}}{\boldsymbol{w}^T(\boldsymbol{S}_b + \boldsymbol{S}_w)\boldsymbol{w}} = \frac{\boldsymbol{w}^T\boldsymbol{S}_b\boldsymbol{w}}{\boldsymbol{w}^T\boldsymbol{S}_t\boldsymbol{w}} \tag{3.24}$$

Maximization of $J(\boldsymbol{w})$ in (3.18) is straightforward [74]. The optimal projecting vector $\boldsymbol{w}_1$ is equal to the eigenvector of $\boldsymbol{S}_w^{-1}\boldsymbol{S}_b$ that corresponds to the largest eigenvalue. Similarly, $\boldsymbol{w}_1$, $\boldsymbol{w}_2$, $\ldots$, $\boldsymbol{w}_L$ can be obtained by seeking the L eigenvectors corresponding to the L largest eigenvalues (denoted by λ_1, λ_2, $\ldots$, λ_L, and $\lambda_1 \geq \lambda_2 \geq \ldots, \geq \lambda_L$).

Because $\boldsymbol{S}_b$ is the sum of C matrices of rank one or less, only $C-1$ of these are independent, $\boldsymbol{S}_b$ is of rank $C-1$ or less. Thus, no more than $C-1$ of the eigenvalues are nonzero, and the projecting vectors correspond to these nonzero eigenvalues [72]. Hence, the dimension of the feature space L should satisfy the constraint

$$L \leq C - 1 \tag{3.25}$$

The FDA procedure in this work can be briefly formulated by Algorithm 2.

3.3.3 KPCA

KPCA is an extension of PCA, which aims to solve nonlinear PCA. The key idea of KPCA is intuitive and generic. In general, the nonlinear correlated data can always be mapped to a higher-dimensional space in which they vary linearly via a nonlinear mapping [75]. After this nonlinear mapping, PCA procedure can be carried out in the new space. Actually, this two-step process can be realized by introducing kernel functions and playing "kernel trick" [76].

Algorithm 2 FDA

Training:

1: Collect labeled samples: $\boldsymbol{v}_1, \boldsymbol{v}_2, \ldots, \boldsymbol{v}_N$.

2: Calculate within-class-scatter matrix $\boldsymbol{S}_w$ and between-class-scatter matrix $\boldsymbol{S}_b$.

$$\boldsymbol{S}_w = \sum_{i=1}^{C} \sum_{n \in \omega_i} (\boldsymbol{v}_n - \bar{\boldsymbol{v}}_i)(\boldsymbol{v}_n - \bar{\boldsymbol{v}}_i)^T$$

$$\boldsymbol{S}_b = \sum_{i=1}^{C} N_i (\bar{\boldsymbol{v}}_i - \bar{\boldsymbol{v}})(\bar{\boldsymbol{v}}_i - \bar{\boldsymbol{v}})^T$$

where $\bar{\boldsymbol{v}} = \sum_{n=1}^{N} \boldsymbol{v}_n / N$, and $\bar{\boldsymbol{v}}_i = \sum_{\boldsymbol{v}_n \in V_i} \boldsymbol{v}_n / N_i$.

3: Set L that satisfies the condition $L \leq C - 1$, and find the L eigenvectors of $\boldsymbol{S}_w^{-1} \boldsymbol{S}_b$, $\boldsymbol{w}_1, \ldots, \boldsymbol{w}_L$ with non-zero eigenvalues.

Performing:

Calculate the projected vector of a new sample as (3.6).

We define a nonlinear mapping Φ as

$$\Phi : \mathbb{R}^M \to \mathbb{F} \tag{3.26}$$

where $\mathbb{R}^M$ denotes the M-dimentional space, $\mathbb{F}$ denotes a high-dimentianal space. The point $\boldsymbol{v}_n$ in space $\mathbb{R}^M$ is mapped to space $\mathbb{F}$. The corresponding mapped point is denoted as $\Phi(\boldsymbol{v}_n)$. The covariance matrix of $\{\Phi(\boldsymbol{v}_n)\}$ is given as

$$\boldsymbol{C} = \frac{1}{N} \sum_{n=1}^{N} \Phi(\boldsymbol{v}_n) \Phi(\boldsymbol{v}_n)^T \tag{3.27}$$

where it is assumed that $\sum_{n=1}^{N} \Phi(\boldsymbol{v}_n) = 0$[3]. The linear PCA in the new space $\mathbb{F}$ is to solve the eigenvalue problem

$$\boldsymbol{C}\boldsymbol{w} = \lambda \boldsymbol{w} \tag{3.28}$$

where eigenvalues $\lambda \geq 0$, $\boldsymbol{w}$ are the correlating eigenvector in space $\mathbb{F}$. As

$$\lambda \boldsymbol{w} = \boldsymbol{C}\boldsymbol{w} = \frac{1}{N} \sum_{n=1}^{N} \Phi(\boldsymbol{v}_n) \Phi(\boldsymbol{v}_n)^T \boldsymbol{w} = \frac{1}{N} \sum_{n=1}^{N} \langle \Phi(\boldsymbol{v}_n), \boldsymbol{w} \rangle \Phi(\boldsymbol{v}_n) \tag{3.29}$$

[3]We make such a hypothesis for it is easy to discuss, the general situation will be mentioned later.

from this equation, we can see all solutions $\boldsymbol{w}$ with $\lambda > 0$ must lie in the span of $\{\Phi(\boldsymbol{v}_n)\}$. So eigenvector $\boldsymbol{w}$ can be expressed as

$$\boldsymbol{w} = \sum_{n=1}^{N} \alpha_n \Phi(\boldsymbol{v}_n) \tag{3.30}$$

Define vector $\boldsymbol{\alpha} = [\alpha_1, \ldots, \alpha_N]^T$, $\boldsymbol{\alpha}$ is corresponding to $\boldsymbol{w}$. In order to find the $\boldsymbol{\alpha}$, the equation (3.28) can be converted to a new one [77] (see appendix A.1). As

$$\lambda N \boldsymbol{\alpha} = \boldsymbol{K}\boldsymbol{\alpha} \tag{3.31}$$

where $\boldsymbol{K}$ is an $N \times N$ matrix with the elements

$$K_{nm} = \langle \Phi(\boldsymbol{v}_n), \Phi(\boldsymbol{v}_m) \rangle = k(\boldsymbol{v}_n, \boldsymbol{v}_m) \tag{3.32}$$

where $k(\boldsymbol{v}_n, \boldsymbol{v}_m)$ is defined as kernel function corresponding to a given nonlinear mapping Φ. The introduction kernel function allows us to compute the value of the dot product in $\mathbb{F}$ without having to carry out the nonlinear mapping Φ. The general question is which function k does correspond to a dot product in some space $\mathbb{F}$. This question has been discussed in [78]. The following Mercer's theorem gives a solution to judge if a function is a valid kernel

Theorem 1. *(Mercer's theorem): Let function $k(\boldsymbol{v}_n, \boldsymbol{v}_m)$ be given, then $k(.,.)$ is a valid kernel function (i.e.$\exists$ nonlinear mapping Φ, s.t. $k(\boldsymbol{v}_n, \boldsymbol{v}_m) = \Phi(\boldsymbol{v}_n)^T \Phi(\boldsymbol{v}_m)$) if and only if for all set $\{\boldsymbol{v}_1, \boldsymbol{v}_2, \ldots, \boldsymbol{v}_N\}(N < \infty)$, the kernel matrix $\boldsymbol{K}$ satisfies the finitely positive semi-definite property*[4].

The proof of the Mercer's theorem is given for instance in [79]. Consequently, the requirement on the kernel function is that it satisfies Mercer's theorem. There exist a number of kernel functions [80]. Representative kernel functions are given by Table 3.1.

[4]In linear algebra, $\boldsymbol{K}$ is said to be positive semi-definite if $\boldsymbol{x}^T \boldsymbol{K} \boldsymbol{x}$ is non-negative for every non-zero N-dimensional column vector $\boldsymbol{x}$.

Table 3.1: Representative kernel functions

Name	Expression	Parameters
Linear kernel	$k(\boldsymbol{v}_n, \boldsymbol{v}_m) = \boldsymbol{v}_n^T \boldsymbol{v}_m$	Null
Polynomial kernel	$k(\boldsymbol{v}_n, \boldsymbol{v}_m) = (\boldsymbol{v}_n \boldsymbol{v}_m + 1)^d$	d
Sigmoid kernel	$k(\boldsymbol{v}_n, \boldsymbol{v}_m) = \tanh(\beta_0 \langle \boldsymbol{v}_n, \boldsymbol{v}_m \rangle + \beta_1)$	β_0, β_1
Gaussian kernel (Radial basis kernel)	$k(\boldsymbol{v}_n, \boldsymbol{v}_m) = \exp(-\frac{\|\|\boldsymbol{v}_n - \boldsymbol{v}_m\|\|^2}{\sigma})$	σ

The polynomial kernel and radial basis kernel always satisfy Mercer's theorem, whereas the sigmoid kernel satisfies it only for certain values of β_0 and β_1 [81]. Among various kernel functions, Gaussian kernel function is usually the first choice for its high performance in most cases [82]. Actually, it is found that Gaussian kernel can approximate most types of kernel functions if the kernel parameter *sigma* is chosen appropriately [83]. Hence, this popular kernel function is involved through our study.

For simplicity, the assumption that $\sum_{n=1}^{N} \Phi(\boldsymbol{v}_n) = 0$ is made previous. For a general situation, there is a way to do mean centering in space $\mathbb{F}$ by modifying $\boldsymbol{K}$ to $\tilde{\boldsymbol{K}}$, as

$$\tilde{\boldsymbol{K}} = \boldsymbol{K} - \boldsymbol{1}_N \boldsymbol{K} - \boldsymbol{K} \boldsymbol{1}_N + \boldsymbol{1}_N \boldsymbol{K} \boldsymbol{1}_N \tag{3.33}$$

where $\boldsymbol{1}_N$ is a $N \times N$ matrix of which each element is $1/N$ (see appendix A.2).

For an arbitrary M-dimension data $\boldsymbol{v}$, in order to map it to a lower L-dimension space, L eigenvectors $\boldsymbol{\alpha}_1, \boldsymbol{\alpha}_2, \ldots, \boldsymbol{\alpha}_L$ of $\tilde{\boldsymbol{K}}$ corresponding the first L maximum eigenvalues $\lambda_1, \lambda_2, \ldots, \lambda_L$ must be found. After finding the eigenvectors, the lth element of the mapped vector (i.e. feature vector) $\boldsymbol{z}$ can be calculated as following

$$z(l) = \langle \boldsymbol{w}_l, \Phi(\boldsymbol{v}) \rangle = \langle \sum_{n=1}^{N} \alpha_l(n) \Phi(\boldsymbol{v}_n), \Phi(\boldsymbol{v}) \rangle = \sum_{n=1}^{N} \alpha_l(n) k(\boldsymbol{v}_n, \boldsymbol{v}) \tag{3.34}$$

where $\boldsymbol{w}_l$ is the lth eigenvector of $\boldsymbol{C}$ corresponding to $\boldsymbol{\alpha}_l$, $\alpha_l(n)$ is the nth element of vector $\boldsymbol{\alpha}_l$.

The KPCA procedure is summarized by Algorithm 3.

Algorithm 3 KPCA

Training:

1: Collect $\boldsymbol{v}_1, \boldsymbol{v}_2, \ldots, \boldsymbol{v}_N$.
2: Get $\boldsymbol{K} \in \mathbb{R}^{N\times N} : \boldsymbol{K}_{ij} = k(\boldsymbol{v_i}, \boldsymbol{v_j})$, where $k(\boldsymbol{v_i}, \boldsymbol{v_j})$ is a kernal function.
3: Modify $\boldsymbol{K}$ to $\tilde{\boldsymbol{K}}$ as (3.33).
4: Find L eigenvectors of $\tilde{\boldsymbol{K}}$ with the largest eigenvalues, which are denoted as $\boldsymbol{\alpha}_1, \boldsymbol{\alpha}_2, \ldots, \boldsymbol{\alpha}_L \in \mathbb{R}^N$.

Performing:

Calculate the projected vector of a new sample $\boldsymbol{v}$. The lth ($l \in 1, 2, \ldots, L$) element of the projected vector $\boldsymbol{z}$ can be calculated using (3.34).

3.3.4 KFDA

The non-linear versions of FDA have been proposed over the last few years [84]. As KPCA, the key idea of KFDA is also to map the data to a new space by nonlinear mapping firstly, and then carry out FDA procedure in the new space. Kernel trick helps to realize the KFDA process in the similar way as KPCA [85].

With the nonlinear mapping as (3.26), the FDA procedure in the new space can be achieved by maxmizing the following Fisher criterion:

$$J^{\Phi}(\boldsymbol{w}) = \frac{\boldsymbol{w}^T \boldsymbol{S}_b^{\Phi} \boldsymbol{w}}{\boldsymbol{w}^T \boldsymbol{S}_t^{\Phi} \boldsymbol{w}} \tag{3.35}$$

where $\boldsymbol{S}_b^{\Phi}$ and $\boldsymbol{S}_t^{\Phi}$ are the *between-class scatter matrix* and *total scatter matrix* in the space $\mathbb{F}$. With the assumption that $\sum_{n=1}^{N} \Phi(\boldsymbol{v}_n) = 0$, these two matrices can be expressed as

$$\boldsymbol{S}_b^{\Phi} = \sum_{i=1}^{C} N_i \bar{\Phi}(\boldsymbol{x}_i) \bar{\Phi}(\boldsymbol{x}_i)^T \tag{3.36}$$

and

$$\boldsymbol{S}_t^{\Phi} = \sum_{i=1}^{C} \sum_{n\in\omega_i} \Phi(\boldsymbol{x}_n) \Phi(\boldsymbol{x}_n)^T \tag{3.37}$$

where $\bar{\Phi}(\boldsymbol{x}_i)$ is the mean value of samples in ith class. The eigenvector $\boldsymbol{w}$ can be also expressed by a linear combination of the observations in space $\mathbb{F}$ as (3.30). From (3.36), (3.37), (3.7), and (3.30), Fisher criterion (3.35) is converted to the following

expression (see appendix A.3) [85].

$$J^{\boldsymbol{K}}(\boldsymbol{\alpha}) = \frac{\boldsymbol{\alpha}^T(\boldsymbol{K}\boldsymbol{W}\boldsymbol{K})\boldsymbol{\alpha}}{\boldsymbol{\alpha}^T(\boldsymbol{K}\boldsymbol{K})\boldsymbol{\alpha}} \tag{3.38}$$

where $\boldsymbol{K}$ is defined by (3.32); $\boldsymbol{W} = diag(\boldsymbol{W}_1, \boldsymbol{W}_2 \ldots, \boldsymbol{W}_C)$, $\boldsymbol{W}_i$ $(i = 1, \ldots, C)$ is a $N_i \times N_i$ matrix with terms all equal to $1/N_i$. Like FDA, the problem (3.38) is to find the eigenvectors of $(\boldsymbol{K}\boldsymbol{K})^{-1}\boldsymbol{K}\boldsymbol{W}\boldsymbol{K}$, after L eigenvectors of with the largest eigenvalues $\boldsymbol{\alpha}_1, \boldsymbol{\alpha}_2, \ldots, \boldsymbol{\alpha}_L$ are obtained, (3.34) can be used for computing the feature vector $\boldsymbol{z}$ for a new data $\boldsymbol{v}$.

The KFDA procedure is summarized by Algorithm 4.

Algorithm 4 KFDA

Training:

1: Collect labeled samples: $\boldsymbol{v}_1, \boldsymbol{v}_2, \ldots, \boldsymbol{v}_N$.

2: Get kernel matrix $\boldsymbol{K}$.

3: Modify $\boldsymbol{K}$ to $\tilde{\boldsymbol{K}}$ as (3.33).

4: Get matrix $\boldsymbol{W}$:

$$\boldsymbol{W} = diag(\boldsymbol{W}_1, \boldsymbol{W}_2 \ldots, \boldsymbol{W}_C) \tag{3.39}$$

where $\boldsymbol{W}_i \in \mathbb{R}^{N_i \times N_i}$ with terms all equal to $1/N_i$.

5: Find L eigenvectors of $(\tilde{\boldsymbol{K}}\tilde{\boldsymbol{K}})^{-1}\tilde{\boldsymbol{K}}\boldsymbol{W}\tilde{\boldsymbol{K}}$ with the largest eigenvalues, which are denoted by $\boldsymbol{\alpha}_1, \boldsymbol{\alpha}_2, \ldots, \boldsymbol{\alpha}_L \in \mathbb{R}^N$

Performing:

Calculate the projected vector of a new sample $\boldsymbol{v}$. The lth $(l \in 1, 2, \ldots, L)$ element of the projected vector $\boldsymbol{z}$ can be calculated as (3.34).

3.3.5 Remarks on feature extraction methods

1. It was verified in [84] that KFDA is equivalent to KPCA plus FDA. That is, KPCA is performed first then FDA is carried out in the feature space obtained by KPCA.

2. PCA and FDA can be seen as the special situation of KPCA and KFDA using the linear kernel function $k(\boldsymbol{v}_n, \boldsymbol{v}_m) = \boldsymbol{v}_n^T \boldsymbol{v}_m$.

3. The performances of both KPCA and KFDA are highly related to the choice of kernel function and the parameters in the kernel function.

4. Both KPCA and KFDA have two drawbacks that the computation time may increase with the number of training samples, and the data patterns in the feature space are rather hard to interpret in the input data space [86].

3.4 Classification

The classification proceeds after feature extraction step. In this step, classifiers are trained in the feature space. Following the feature extraction, the classification procedure can be described as follows: Given N samples $\boldsymbol{z}_1, \boldsymbol{z}_2, \ldots, \boldsymbol{z}_N \in \mathbb{R}^L$, which are used for training, the sample indexes are distributed in C classes: $\omega_1, \omega_2, \ldots, \omega_C$. The sample number in ith class is N_i, which satisfies $\sum_{i=1}^{C} N_i = N$. The class index of $\boldsymbol{z}_n$ is denoted by h_n, $h_n \in \{1, 2, \ldots, C\}$. The objective of the training process is to get a classifier. With the classifier, the class index h of a real time sample $\boldsymbol{z}$ can be obtained.

In order to make a comparison among different classifiers, three representative classifiers: GMM, kNN, and SVM are under consideration. Without loss of generality, GMM is a preferable parametric classification method, while kNN and SVM are two typical non-parametric ones. kNN is a widely used method due to its simplicity and flexibility. The remarkable characteristics of SVM, such as good generalization performance, the absence of local minima and the sparse representation of solution, attract much attention in recent years [87].

3.4.1 GMM

GMM is a parametric classification methodology based on Bayes decision theory [88]. In this part, firstly, we introduce Bayesian decision theory, after that, Gaussian mixture model is recommended, a parameter estimation method named expectation-maximization algorithm is introduced finally.

3.4.1.1 Bayesian decision theory

Bayes' formula is given

$$p(\omega_i|\boldsymbol{z}) = \frac{p(\boldsymbol{z}|\omega_i)p(\omega_i)}{p(\boldsymbol{z})} \tag{3.40}$$

In this formula, as definition previous, ω_i $(i = 1, 2, \ldots, C)$ is the index set of ith class; $\boldsymbol{z}$ is an arbitrary sample; $p(\omega_i)$ (*prior probability*) is the probability of next sample belongs to ith class, which satisfies the following equation

$$\sum_{i}^{C} p(\omega_i) = 1 \tag{3.41}$$

$p(\boldsymbol{z}|\omega_i)$ is *class-conditional probability*; $p(\omega_i|\boldsymbol{z})$ is *posterior*. $p(\boldsymbol{z})$ is *evidence*, which satisfies

$$p(\boldsymbol{z}) = \sum_{i}^{C} p(\boldsymbol{z}|\omega_i)p(\omega_i) \tag{3.42}$$

To decide which class a data $\boldsymbol{z}$ belongs to, we should compare the probabilities $\boldsymbol{z}$ in different classes (*posterior*). It is resolved that $\boldsymbol{z}$ belongs to the class with the biggest posterior. In other words, we just need to compare $p(\boldsymbol{z}|\omega_i)p(\omega_i)$ with different i. The *prior probability* $p(\omega_i)$ is usually thought to be the frequency weight of data belongs to ith class, so the main object is to estimate the *class-conditional probability* $p(\boldsymbol{z}|\omega_i)$. Generally, there are two steps to accomplish the classification using Bayes decision theory:

1. **Training step**: Using training samples to estimate the parameters of a probability distribution function in individual classes (*class-conditional probability density* function).

2. **Prediction step**: For any unseen test sample, the method computes the posterior probability of that sample belonging to each class, and then classifies the test sample according the largest posterior probability [72].

3.4.1.2 GMM for modeling class-conditional probability function

Estimating the *class-conditional probability* functions is realized by GMM. In GMM, $p(\boldsymbol{z}|\omega_i), i = 1, \ldots, C$ is represented as a weighted sum of R_i component Gaussian densities in the following equation:

$$p(\boldsymbol{z}|\omega_i) = \sum_{j=1}^{R_i} p(c_j|\omega_i) p(\boldsymbol{z}|c_j, \omega_i) \tag{3.43}$$

where $p(c_j|\omega_i), j = 1, \ldots, R_i$ are the mixture weights, which satisfies $\sum_{j=1}^{R_i} p(c_j|\omega_i) = 1$, $p(\boldsymbol{z}|c_j, \omega_i)$ are the component Gaussian densities. Each component density is a L-variate Gaussian function of the form,

$$p(\boldsymbol{z}|c_j, \omega_i) = \frac{1}{(2\pi)^{M/2}|\Sigma_j|^{1/2}} \exp\left\{-\frac{1}{2}(\boldsymbol{z} - \boldsymbol{\mu}_j)^T \Sigma_j^{-1} (\boldsymbol{z} - \boldsymbol{\mu}_j)\right\} \tag{3.44}$$

with mean vector $\boldsymbol{\mu}_j$ and covariance matrix Σ_j. Parameters $\boldsymbol{\mu}_j$, Σ_j and $p(c_j)$ are collectively represented by the notation ζ_i:

$$\zeta_i = \{p(c_j), \boldsymbol{\mu}_j, \Sigma_j\} \quad j = 1, \ldots, R_i$$

The configuration of R_i is often determined by the complexity of the data distribution. A complex distribution could be described by a choice of a large R_i. A parameter estimation method, named Expectation-Maximization (EM) algorithm, is adopted to estimate ζ_i (see A.2) [89]. The GMM classification method is described by Algorithm 5.

3.4.2 kNN

kNN (see Algorithm 6) is a widely-used nonparametric classifier [73]. In the kNN procedure, the classification decision is based on the N training samples. An object is classified by a majority vote of its neighbors, with the object being assigned to the class most common among its k nearest neighbors, where k is a positive integer, typically small [90]. The training calculation is needless, and the procedure is given

Algorithm 5 GMM

Training:

1: Collect labeled samples $\boldsymbol{z}_1, \boldsymbol{z}_2, \ldots, \boldsymbol{z}_N$
2: Initial R_i for $i = 1, \ldots, C$.
3: **for** $i = 1$ to C
Estimate and save ζ_i by using EM algorithm.
end for

Performing:

1: For a new sample $\boldsymbol{z}$, calculate $p(\boldsymbol{z}|\omega_i, \zeta_i)$.
2: Class index h is assigned:

$$h = \arg\left\{\max_{i\in\{1,\ldots,C\}} N_i p(\boldsymbol{z}|\omega_i, \zeta_i)\right\} \tag{3.45}$$

by Algorithm 6.

Algorithm 6 kNN

Training:

1: Collect and save labeled samples: $\boldsymbol{z}_1, \boldsymbol{z}_2, \ldots, \boldsymbol{z}_N$.

Performing:

1: For a new sample $\boldsymbol{z}$, calculate its Euclidean distances to $\boldsymbol{z}_1, \boldsymbol{z}_2, \ldots, \boldsymbol{z}_N$.
2: Find the nearest k neighbors of $\boldsymbol{z}$ that are at the minimum Euclidean distances: $\boldsymbol{z}_1^k, \boldsymbol{z}_2^k, \ldots, \boldsymbol{z}_k^k$, whose class indexes are $h_1^k, h_2^k, \ldots, h_k^k$.
3: $\boldsymbol{z}$ is assigned to a class to which most of the neighbors belong:

$$h = \arg\left\{\max_{j\in\{1,\ldots,C\}} \sum_{i=1}^{k} \delta(h_i^k, j)\right\} \tag{3.46}$$

The number of neighbors k, the only free parameter in kNN, can be optimized using the *leave-one-out cross-validation* method. Specifically, *leave-one-out cross-validation* involves using a single observation from the training dataset as the validation data, and the remaining observations as the training data. This is repeated such that each observation in the sample is used once as the validation data. The error classification rate could be then obtained. The k that can minimize the error rate is considered as the final number of neighbors.

3.4.3 SVM

SVM is a classification method developed by V. Vapnik [91] and has been widely applied the last two decades. The basic theory comes from binary classification problem. As Fig. 3-6 shows, there are data samples distributed in two classes, suppose we have some hyperplane which separates the points. Then, SVM looks for the optimal hyperplane with the maximum distance from the nearest training samples. A subset of training samples that lie on the margin are called support vectors.

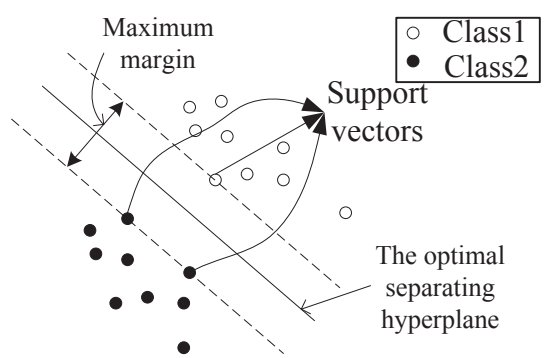

Figure 3-6: SVM schematic diagram

To explain the binary SVM more specifically, take $(N_1 + N_2)$ labeled sample $\boldsymbol{z}_1$, $\boldsymbol{z}_2, \ldots, \boldsymbol{z}_{N_1+N_2}$ from 1st and 2nd classes as training examples. $g_n \in \{-1, 1\}$ is defined as the class label of sample $\boldsymbol{z}_n$ (-1 for class 1, 1 for class 2).

Suppose the linear hyperplane is expressed as $\boldsymbol{w}\boldsymbol{z} + b = 0$, where $\boldsymbol{w}$ is normal to the hyperplane. For the linearly separable case, the training data satisfy

$$\begin{cases} \boldsymbol{w}\boldsymbol{z}_n + b \geq +1, \ \forall n \ s.t. \ g_n = 1 \\ \boldsymbol{w}\boldsymbol{z}_n + b \leq -1, \ \forall n \ s.t. \ g_n = -1 \end{cases} \tag{3.47}$$

which can be equally expressed as

$$g_n(\boldsymbol{w}\boldsymbol{z}_n + b - 1) \geq 1 \tag{3.48}$$

Let d_+ (respectively d_-) be the shortest distance from the separating hyperplane to the closest positive (respectively, negative) point. Define the margin of a separat-

ing hyperplane to be $d_+ + d_-$. The support vector algorithm simply looks for the separating hyperplane with largest margin [92].

The nearest points lie on the planes $\boldsymbol{w}\boldsymbol{z}+b=\pm 1$, so the margin is simply $2/||\boldsymbol{w}||$. Consequently, the problem is converted to the following quadratic program:

$$\begin{aligned} &\min_{\boldsymbol{w},b} \frac{1}{2}||\boldsymbol{w}||^2 \\ s.t. \quad & g_n(\boldsymbol{w}\boldsymbol{z}_n + b - 1) \geq 1 \quad \forall n \end{aligned} \tag{3.49}$$

To solve this quadratic programming problem, Lagrange multipliers $a_n \geq 0$ are introduced, the Lagrange function is

$$L(\boldsymbol{w}, b, \boldsymbol{a}) = \frac{1}{2}||\boldsymbol{w}||^2 - \sum_{n=1}^{N} a_n[g_n(\boldsymbol{w}\boldsymbol{z}_n + b - 1)] \tag{3.50}$$

where Lagrange coefficients are collectedly expressed as $\boldsymbol{a} = [a_1, \ldots, a_N]^T$. Setting the derivative of $L(\boldsymbol{w}, b, \boldsymbol{a})$ with respect to $\boldsymbol{w}$ and b equal to zero, we obtain the following condition

$$\boldsymbol{w} = \sum_{n=1}^{N} a_n g_n \boldsymbol{z}_n \tag{3.51}$$

$$0 = \sum_{n=1}^{N} a_n g_n \tag{3.52}$$

Using these conditions, (3.50) is converted to the following quadratic problem (QP)

$$\begin{aligned} &\min \tilde{L}(\boldsymbol{a}) = \frac{1}{2}\sum_{n=1}^{N}\sum_{m=1}^{N} a_n a_m g_n g_m \boldsymbol{z}_n \boldsymbol{z}_m - \sum_{n=1}^{N} a_n \\ s.t. \quad & a_n \geq 0 \quad \text{and} \quad \sum_{n=1}^{N} a_n g_n = 0 \quad \text{for } n = 1, 2, \ldots, N_1 + N_2 \end{aligned} \tag{3.53}$$

The above algorithm for separable data and the decision function is a linear. To make the SVM be applied to non-separable and nonlinear cases, the above QP can be adapted by modifying the constraint condition and introducing kernel functions

(see Appendix A.5), as

$$\min \tilde{L}(\boldsymbol{a}) = \frac{1}{2} \sum_{n=1}^{N_1+N_2} \sum_{m=1}^{N_1+N_2} a_n a_m g_n g_m k(\boldsymbol{z}_n, \boldsymbol{z}_m) - \sum_{n=1}^{N_1+N_2} a_n \tag{3.54}$$

subject to

$$\sum_{n=1}^{N_1+N_2} a_n g_n = 0 \tag{3.55}$$

$$0 \leq a_n \leq D \quad \text{for } n = 1, 2, \ldots, N_1 + N_2 \tag{3.56}$$

In our study, a practical approach, namely Sequential Minimal Optimization (SMO), is used solve the QP problem (3.54). For more details, the reader is referred to Appendix A.6 [91]. After solving the QP problem, the Lagrange multipliers a_1, a_2, $\ldots$, $a_{N_1+N_2}$ are obtained. The samples corresponding to positive Lagrange multipliers are SVs, which are denoted by $\boldsymbol{z}_1^s$, $\boldsymbol{z}_2^s$, $\ldots$, $\boldsymbol{z}_S^s$. S is the number of SVs. The corresponding a_n and g_n of SV $\boldsymbol{z}_n^s$ are denoted by a_n^s and g_n^s.

The class label g of an arbitrary data point $\boldsymbol{z}$ can be determined by the following equation:

$$g = sign\left(\sum_{n=1}^{S} a_n^s g_n^s k(\boldsymbol{z}_n^s, \boldsymbol{z}) + b\right) \tag{3.57}$$

where the bias b is given

$$b = \frac{1}{S} \sum_{j=1}^{S} \left(g_j^s - \sum_{n=1}^{S} a_n^s g_n^s k(\boldsymbol{z}_n^s, \boldsymbol{z}_j^s) \right) \tag{3.58}$$

From (3.57), it could be observed that the determination of the class label is depended on the SVs, and the corresponding parameters $\{a_n^s\}$ and $\{g_n^s\}$. This property is central to the practical applicability of SVM.

The training process and the performing procedure can be synthetically summarized as Algorithm 7.

The above mentioned SVM is a binary classifier. To extend the binary classifier to multi-classification situations, there are several ways. A method named "One-Against-One" is adopted in this chapter. Actually, $C(C-1)/2$ binary SVMs can

Algorithm 7 Binary SVM

Training:

1: Collect $(N_1 + N_2)$ labeled sample $\boldsymbol{z}_1$, $\boldsymbol{z}_2$, ..., $\boldsymbol{z}_{N_1+N_2}$ from classes Z_1 and Z_2. $g_n \in \{-1, 1\}$, is the class label of sample $\boldsymbol{z}_n$ (-1 for class 1, 1 for class 2). Initial D.

2: Solve the quadratic problem (3.54) by using SMO method.

3: Save support vectors: $\boldsymbol{z}_1^s, \boldsymbol{z}_2^s, \ldots, \boldsymbol{z}_S^s$ and corresponding g_n and a_n, which are denoted by $\{g_n^s\}$ and $\{a_n^s\}$.

Performing:

For a new sample $\boldsymbol{z}$, its class label is determined with respect to (3.57).

be constructed based on the training data in C classes. When an arbitrary sample comes, its classification results of all the binary SVMs are firstly obtained. The final classification is obtained by voting all binary classification results. The details can be found in [93].

3.5 Comparative results of different methodologies

3.5.1 Results on feature extraction and classification

After the samples in fault experiments were labeled, we got to the model training step. As aforementioned, the analytic targets were individual cell voltages in this step. The individual cell voltages in normal experiment and fault experiment are respectively as in Fig. 2-10 and 2-11.

As 20-cell stack is concerned here, the dimension of original data is $M = 20$, and the number of training samples is $N = 9000$. After labeling process, the training samples were labeled into three classes, so the class number $C = 3$. To evaluate the performance of the feature extraction methods and the different classifiers , A criterion Error Diagnosis Rate (EDR) is defined. The error diagnosis points refer to the points which are wrongly diagnosed. EDR means the proportion of the error diagnosis points to total data points.

With the training data set, the feature extraction models and the classification

models were trained successively. Some parameters were initialized first. The kernel functions used in KPCA, KFDA and SVM are all Gaussian kernels. From the similar experience in [84], the parameters of the kernel functions in KPCA and KFDA, i.e. σ in Table 3.1, were set as $0.5M$, where $M = 20$ is the data dimension of original data space in this study. The number of Gaussian components in GMM, i.e. R_i in (3.43), is set at 1 for all the feature extraction methods considering the distribution characteristics of data in feature spaces. In fact, from visualization point of view, it was found that the within-class data distributions in feature spaces (see respectively Fig. 3-7, 3-8, 3-9, 3-10) are not complex and one Gaussian component could describe the distributions with an acceptable precision. In kNN, the values of k were set at 5, 7, 1, 15 respectively for the methods PCA, FDA, KPCA, and KFDA, with respecting to the leave-one-out error [72]. In SVM, the values of kernel parameters (σ) and the parameter D in (3.56) were determined by trying a group of combinations (see for instance [93]). The pair of (σ, D) that achieved the lowest EDR for test data was chosen. Here the values of σ and D were set at 2 and 10000 respectively for all the feature extraction methods.

Through feature extraction, the original 20-dimensional data was projected to a 2-dimension space. Fig. 3-7, 3-8, 3-9 and 3-10 show the data of a fault experiment in feature spaces generated by PCA, FDA, KPCA, and KFDA respectively.

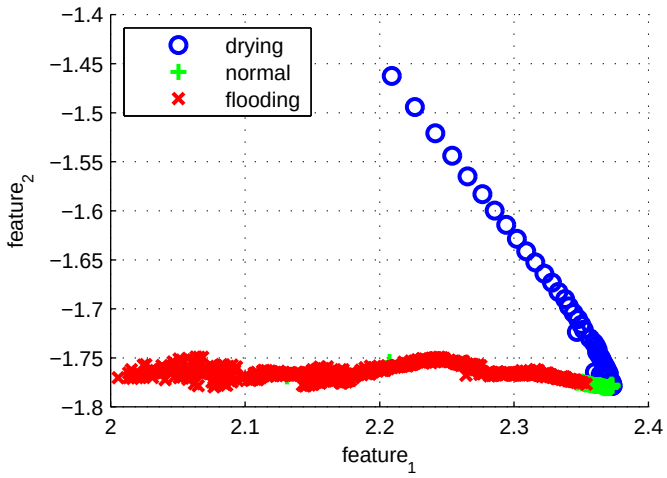

Figure 3-7: Features obtained by adopting PCA

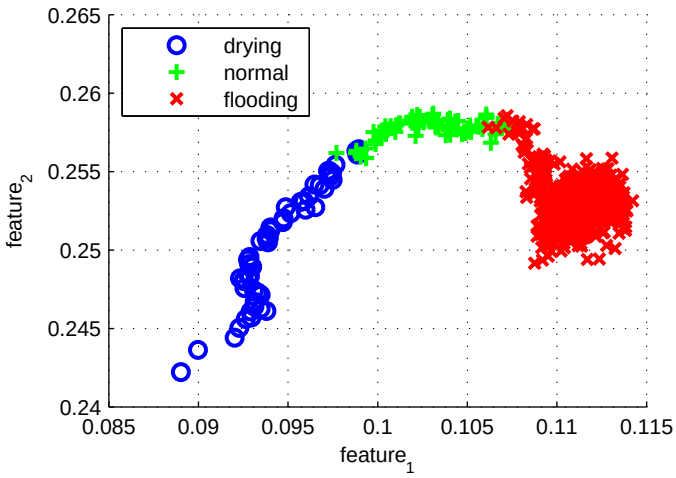

Figure 3-8: Features obtained by adopting FDA

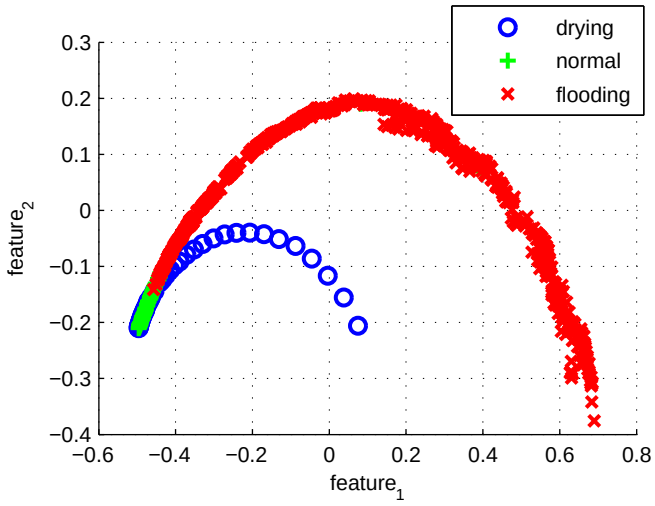

Figure 3-9: Features obtained by adopting KPCA

It can be seen that the data points in Fig. 3-7 and 3-9 disperse over the whole scale, whereas the overlap regions between data in the normal state and the other two fault states are large. In contrast, as for the results of FDA and KFDA (see respectively Fig. 3-8, 3-10), the points in the same class are more concentrated, and the amounts of overlapping points are small, which means points in different classes are decentralized.

Classification methods, GMM, kNN, and SVM were carried out in the different

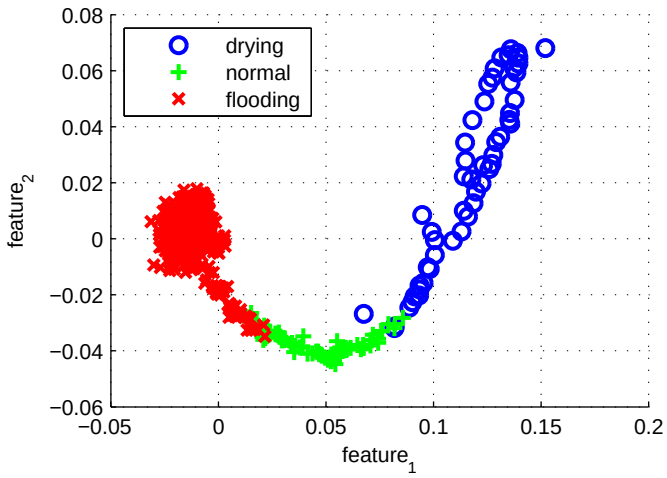

Figure 3-10: Features obtained by adopting KFDA

feature spaces. For instance, Fig. 3-11, 3-12 and 3-13 show the visualization results of GMM, kNN, SVM classifications in FDA feature space respectively. It can be seen that the feature space is divided into three zones, which denotes different states, and the boundaries determined by different classifiers are different.

Table 3.2 shows EDRs for different combinations of the feature extraction methods and classification methods. In order to evaluate the robustness of the approach, the data, which is acquired from the other fault experiments than the one for training, were handled as test data. The test data were firstly labeled. Then, the trained feature extraction and classification models were used to process the test data. The EDRs of test data were thus obtained by comparing the diagnostic results with the labeling results.

From Table 3.2, the performances of the feature extraction methods can be compared. For each classification methodology, the error rates using FDA and KFDA as feature extraction tools are generally lower than that using PCA and KPCA. The reason is that PCA and KPCA are unsupervised methodologies, the training samples are treated equally without considering the label of each point, while FDA and KFDA are supervised methodologies, the labeling information is utilised sufficiently. Hence, we can consider that FDA and KFDA are more suitable for classification problems such as fault diagnosis.

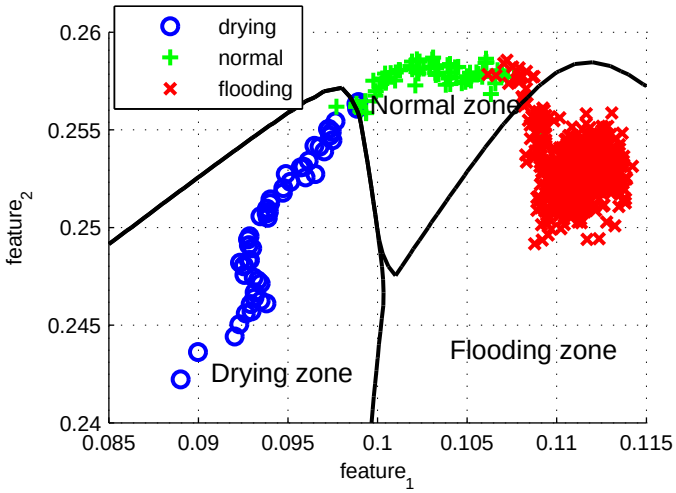

Figure 3-11: Classification results in FDA feature space by GMM

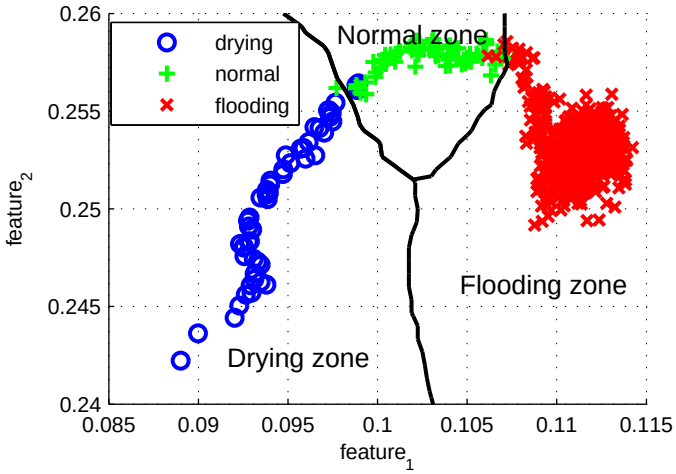

Figure 3-12: Classification results in FDA feature space by kNN

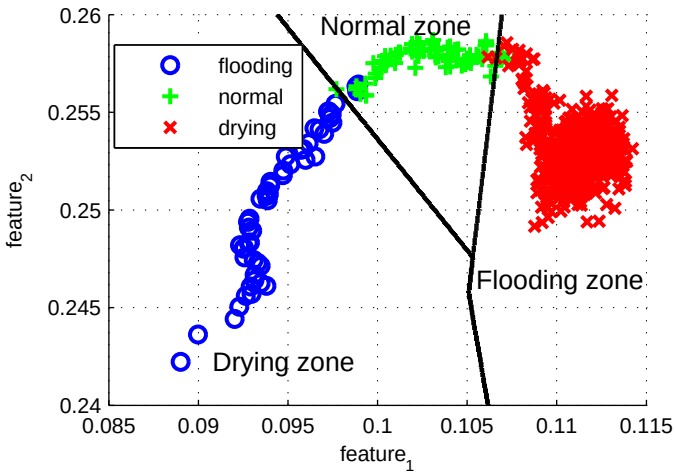

Figure 3-13: Classification results in FDA feature space by SVM

Table 3.2: Results of varied classifications in different feature spaces

Feature extraction	Classification	EDR of training data	EDR of test data
	GMM	0.051	0.110
	kNN	0.016	0.110
PCA	SVM	0.015	0.129
	GMM	0.032	0.087
	kNN	0.013	0.070
FDA	SVM	0.014	0.070
	GMM	0.089	0.058
	kNN	0.052	0.121
KPCA	SVM	0.058	0.113
	GMM	0.034	0.085
	kNN	0.014	0.082
KFDA	SVM	0.016	0.075

In practice, it is difficult to choose the highest performance classifier. Various problems may have different suitable classification solutions. Concerning our case, the choice of the proper classifier can be achieved firstly by comparing the EDRs of classifiers with FDA and KFDA as foregoing procedures. It can be observed that EDRs obtained using kNN and SVM are always lower than when using GMM.

3.5.2 Discussion about computation costs

Apart from EDR, computation cost is a crucial factor that needs to be taken into account for real-time implementation. For an online use, the diagnosis approach will be coded in an embedded chip (for instance a DSP), whose computing capability and storage capacity are much lower than that of a standard computer. The computation complexity is really a strict constraint for implementation. In our approach, the training process is usually out of consideration, since it is completed off-line. Concerning the online diagnosis process, feature extraction methodologies and classification methodologies are considered respectively. The order notation $O()$ is used here to describe the computation cost. $f(x) = O\left(h(x)\right)$ denotes that there are x_0 and c_0, such that $|f(x)| \leq c_0|h(x)|$ for all $x > x_0$. The order notation is used to give a bound on the limiting behavior of a function.

As in Table 3.3 and 3.4, different methodologies are evaluated from the perspectives of occupied memory and computation time. From this table, it can be seen that among different feature extraction methods, needed memory and computation time of KPCA and KFDA are in proportion to the number of training samples, and thus are usually large. While for classifiers, the needed memory and computation time of kNN are in proportion to the number of training samples. These methodologies are less suitable than the others for online diagnosis.

For reference here, the computation time and needed memory in a standard computer is given here. With a computer Dell (precision M4700, 2.7 G Processor, 8 G RAM) and with 64 bit Matlab R2010b, the needed memory and computation time are summarized in Table 3.5.

Considering synthetically the performances of EDR and feasibility of online im-

Table 3.3: Computation costs of the feature extraction methodologies

Methodologies	Feature extraction			
	PCA	FDA	KPCA	KFDA
Occupied memory	$O(ML)$	$O(ML)$	$O(MN+NL)$	$O(MN+NL)$
Computation time	$O(ML)$	$O(ML)$	$O(MN+NL)$	$O(MN+NL)$

Table 3.4: Computation costs of the classification methodologies

Methodologies	Classification		
	GMM	kNN	SVM
Occupied memory	$O\big(CR(\frac{(1+M)(M+2)}{2})\big)$	$O(MN)$	$O(MS+S)$
Computation time	$O\big(CR(\frac{(1+M)(M+2)}{2})\big)$	$O(MN)$	$O(MS+S)$

Table 3.5: Computation costs using general computer

Method	Needed memory	Computation time
PCA	1 kb	0.0070 s
FDA	1 kb	0.0070 s
KPCA	6.114 Mb	0.3700 s
KFDA	6.116 Mb	0.3800 s
GMM	1 kb	0.0003 s
kNN	160 kb	0.0800 s
SVM	2 kb	0.0007 s

plementation, FDA combined by SVM can be chosen as final solution in our case.

3.6 Conclusion

This chapter presents a strategy based on pattern recognition tools for the diagnosis of water management faults in PEMFC stacks. The procedure is realized by classifying the features that are extracted from the vectors constructed by individual cell voltages.

In this approach, the water indicator W, which is calculated using the measured values of ΔP and D_{air}, is defined to describe the quantity of water inside the fuel cell stack and label the training data. Individual cell voltages are chosen as original variables for diagnosis. Representative feature extraction methods: PCA, FDA, KPCA, KFDA, and classification methods: GMM, kNN, SVM, are employed and compared from the point of view of diagnosis precision and computation cost. The test results for a 20-cell stack show that FDA and SVM have higher performance and less computation costs comparing with other methods in our case. The EDR of diagnosis by using such an approach is always below 10%. It is therefore inferred that cell voltages can be considered as diagnostic variables at least for detection of water management faults. Additionally, the strategy, which combines FDA and SVM, is a very promising diagnostic proposal to diagnose the faults associated with water management for PEMFC.

To verify the generality of this strategy, FDI of multiple types of faults for different PEMFC stacks will be studied and discussed further in next chapter.

Chapter 4

Pattern classification for diagnosis: multi-fault FDI

In the last chapter, the pattern classification based fault diagnosis strategy is proposed. Taking cell voltages as the variables for diagnosis, FDA and SVM as feature extraction and classification tools, the water management faults F_f and F_d are diagnosed. In this chapter, in order to further verify this diagnostic strategy, more types of faults on more stacks will be concerned. The objective of this study is to verify that individual cell voltages could be considered as diagnostic variables for more fault types, and the strategy composed by FDA and SVM can obtain appropriate performance for multi-fault FDI. Specifically, the experimental data of the five fault types: F_1, F_2, F_3, F_4, F_5, and of two stacks 8-cell stack, 40-cell stack will be explored. The methods FDA and SVM still function respectively as the feature extraction and classification tools. To further reduce the online computational burden, a multi-class SVM called Directed Acyclic Graph SVM (DAGSVM) is adopted. To end this chapter, the embedded system, which is specially designed for implementing PEMFC diagnosis, is introduced, and the preliminary results of implementation with this system are then given.

4.1 DAGSVM for multi-fault FDI

Multi-fault FDI can be considered as a multi-class classification problem taking each health state as a class. With the diagnostic strategy proposed in the last chapter, the classification is carried out in the feature space generated using FDA. As a classification tool, SVM has attracted a lot of attention in the fault diagnosis domain in recent years (see for instance [94]). Its remarkable characteristics, such as good generalization performance, the absence of local minima and the sparse representation of solution, make it an attractive pattern classification tool [87].

The basic SVM is designed for binary classification. To extend the binary SVM to multiclass classification, several methods have been proposed. In [93], a comparison study of the performances of various multiclass SVM is given. The results indicate that the "one-against-one" and DAGSVM methods may be more suitable for practical use than the other methods. For instance, in the last chapter, the "one-against-one" method is used to achieve the three-class classification problem.

Both the methods "one-against-one" and DAGSVM are based on basic binary SVMs. When these two methods are compared, the advantage of using DAGSVM is that its performing time is less than the "one-against-one" method, especially in the situation that the class number is large. This characteristic makes DAGSVM more suitable for online diagnosis implementation.

DAGSVM was firstly presented in [95]. As "one-against-one" method, to solve a C-class classification problem, it is necessary to construct all possible binary classifiers from a training set of classes, each classifier being trained on only two out of C classes. There would thus be $C(C-1)/2$ binary classifiers trained in the training stage.

Actually, Directed Acyclic Graph (DAG) is used in the performing phase. A typical rooted binary DAG is shown in Fig. 4-1. It has C *layers*, $C(C-1)/2$ *internal nodes* and C *leaves*. The nodes are arranged in a triangle structure with the single *root node* at the top, two *nodes* in the second layer and so on, until the final layer of *leaves* [95].

For DAGSVM, each node represents a binary SVM of ith and jth classes ($i, j =$

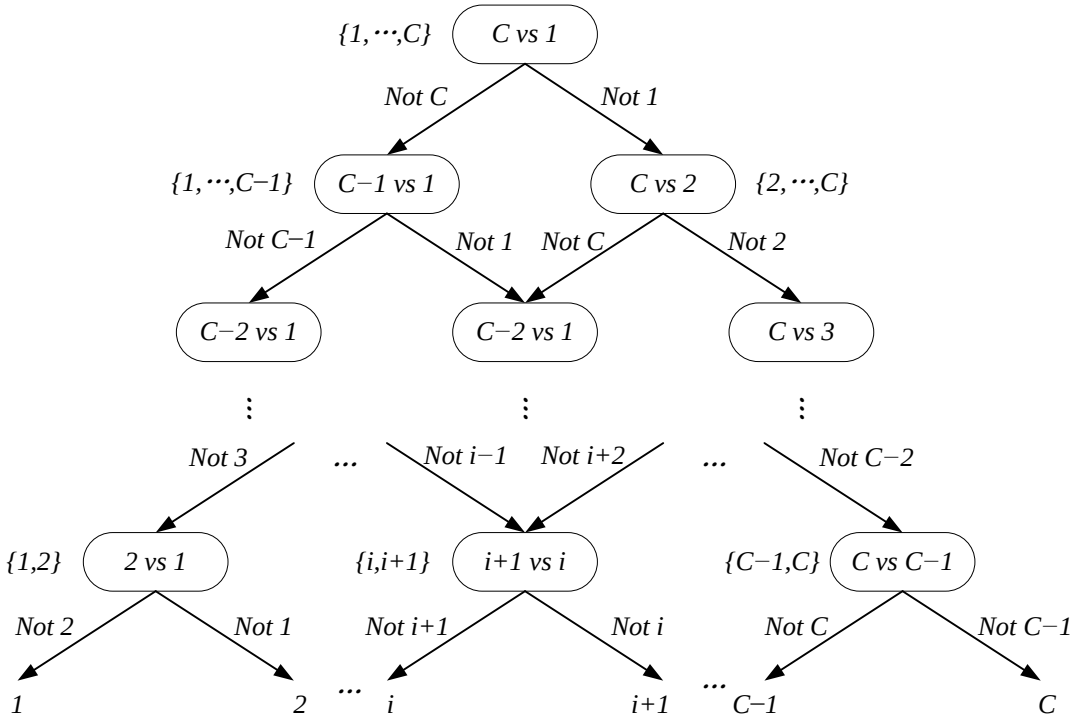

Figure 4-1: DAGSVM structure

$1, \ldots, C$). Given a test sample, starting from the *root node*, the binary classification function at a *node* is evaluated. Then it moves to the node in the next layer from either left or right path depending on the binary classification result. Then, the binary classification function of the next *node* is evaluated. Therefore, a path is taken before reaching a *leaf* which indicates the predicted class. The path is known as the *evaluation path* which goes through $C-1$ *nodes*. Hence, performing $C-1$ times of binary classifications is needed to derive the final class determination.

4.2 Implementations of the diagnostic approach

To remind the whole strategy, the flowchart used here for multi-fault FDI strategy is shown in Fig. 4-2. As stated in the last chapter, the strategy contains offline data labeling process, model training process, and online diagnosis process.

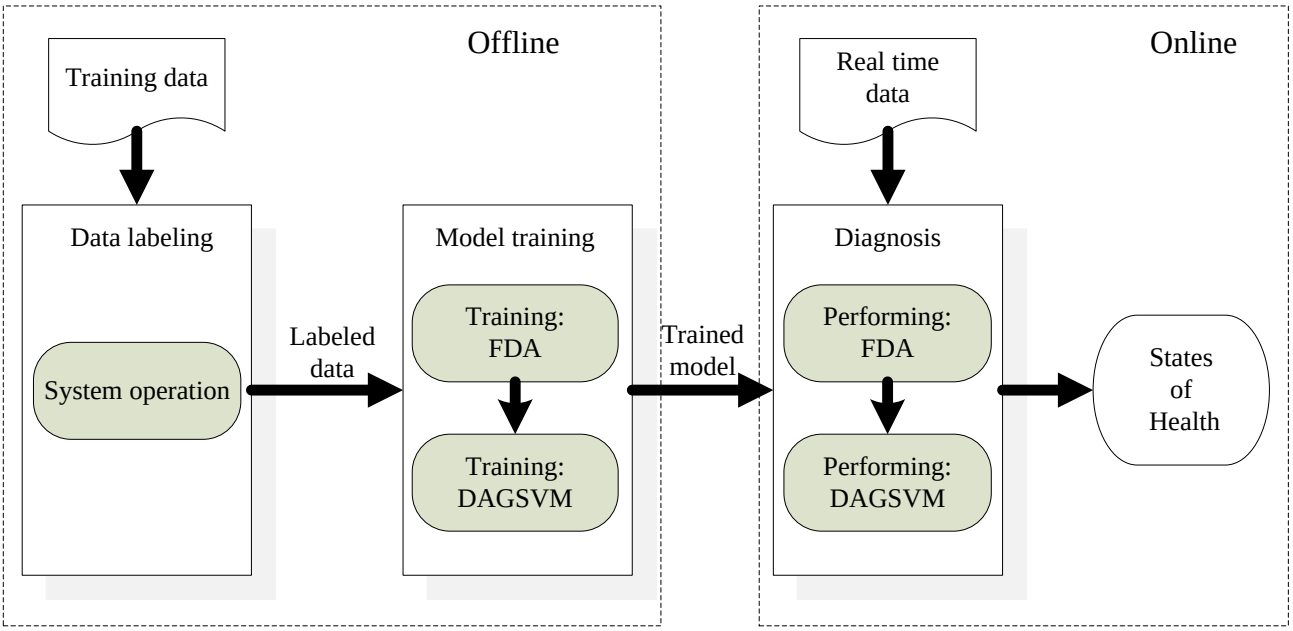

Figure 4-2: Flowchart of the diagnosis strategy

4.2.1 Data labeling

As described in chapter 2, the experimental datasets of 8-cell stack and 40-cell stack are taken into account. When the fault free dataset and the datasets of the concerned faults are obtained by carrying out the corresponding experiments, the FDI problem is considered as a classification problem. For the 8-cell stack, the class number is 6, i.e. the classes of Nl, F_1, F_2, F_3, F_4, F_5 are considered; while the one for the 40-cell stack is 5, i.e. the classes of Nl, F_1, F_2, F_3, F_4 are considered. At each time point, the vector composed by individual cell voltages is considered as the original variable for diagnosis. So 8-dimensional data and 40-dimensional data are processed respectively for the 8-cell stack and the 40-cell stack.

To implement and verify the approach, the datasets for training and test should firstly be prepared. As both FDA and SVM methods are supervised ones, the samples in different classes must be prepared and labeled to construct the datasets for training and test. For states Nl, F_3, and F_4, the corresponding experiments were carried out in constant conditions. The data sampled during the experiments can be labeled with the corresponding class labels easily. Differently, in the experiments of F_1, F_2 and F_5,

the faults occurred in the transition between the normal operating states. The samples in the faulty operating time intervals were collected. Since several experiments were done for each condition, the samples in one (or several) specific experiment(s) were employed as the training data, while the samples from other experiments were collected as test data. The sample numbers in different classes for training and testing are shown in Table 4.1. Notice that, in order to cover the fault zones, the dataset with longer duration is usually selected for training. Hence, the test data is less than training data for some classes, e.g. F_2 of 40-cell stack.

Table 4.1: Sample numbers of the training and test data

	Nl	F_1	F_2	F_3	F_4	F_5
Training data (8-cell stack)	2474	263	201	253	225	246
Test data (8-cell stack)	3633	239	301	253	180	541
Training data (40-cell stack)	2825	111	21	501	401	Null
Test data (40-cell stack)	5431	31	201	2500	2200	Null

4.2.2 FDA procedure

In this procedure, the cell voltage composed vectors are projected into the low-dimensional feature space by using FDA. In the FDA operation, the dimension of the projected space must satisfy the constraint (3.25). The maximum feature space dimension number is therefore 5 for the 8-cell stack and 4 for the 40-cell stack.

Through the training process, 5 projecting vectors are obtained for the 8-cell stack, while the number of the projecting vectors is 4 for the 40-cell stack. The eigenvalues can reflect the amount of discriminant information that the corresponding projecting vectors can preserve. To indicate the proportion of the eigenvalues corresponding to the projecting vectors in all non-zero eigenvalues, the criterion ACR is defined similarly:

$$ACR = \frac{\sum_{i=1}^{L} \lambda_i}{\sum_{i=1}^{C-1} \lambda_i} \tag{4.1}$$

After training process, the eigenvalues corresponding to the first 3 projecting vectors and ACRs when the feature dimension L is set at 1, 2, and 3, are shown in Fig.

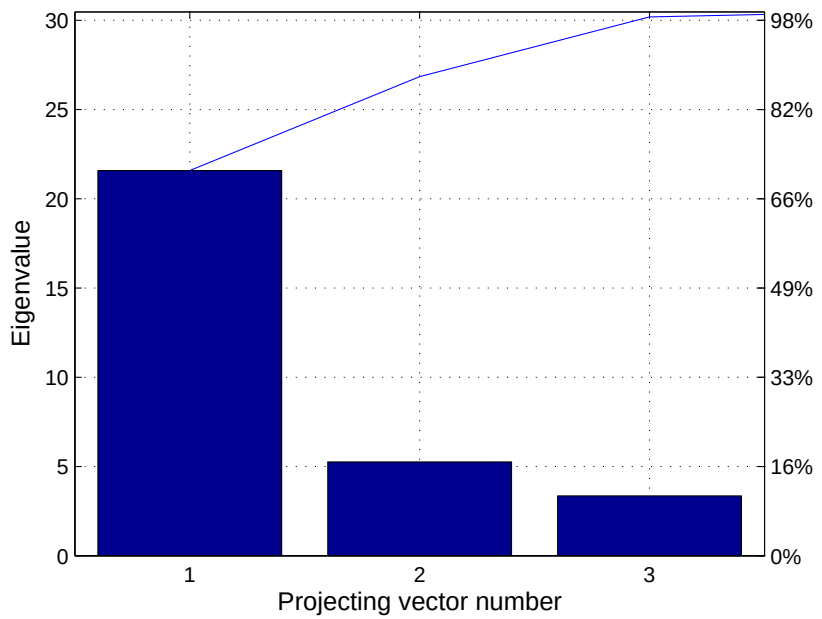

Figure 4-3: Eigenvalues and ACR values of FDA result for 8-cell stack

4-3 and Fig. 4-4 respectively for 8-cell stack and 40-cell stack. From the figures, for both stacks, it can be observed that the first 3 projecting vectors can preserve more than 95% of the discriminant information.

The first two and three features of the data in different classes can be observed visually. The data of 8-cell stack in 2-dimensional and 3-dimensional feature spaces are shown in Fig. 4-5 and Fig. 4-6; While the ones for 40-cell stack are shown in Fig. 4-7 and Fig. 4-8.

From these figures, it is observed that:

- The points of different classes are generally separated visually in either 2-dimensional or 3-dimensional feature space.
- The samples in F_3 and F_4 classes are near the ones in Nl. Comparatively, the samples in class F_1, F_2 and F_5 are mainly far away from the fault-free samples.
- Some overlaps exist between different classes. For instance, Nl and F_4 for both stacks; Nl and F_3 for 8-cell stack, can be observed from the figures.
- More discriminative information could be extracted from 3-dimensional feature

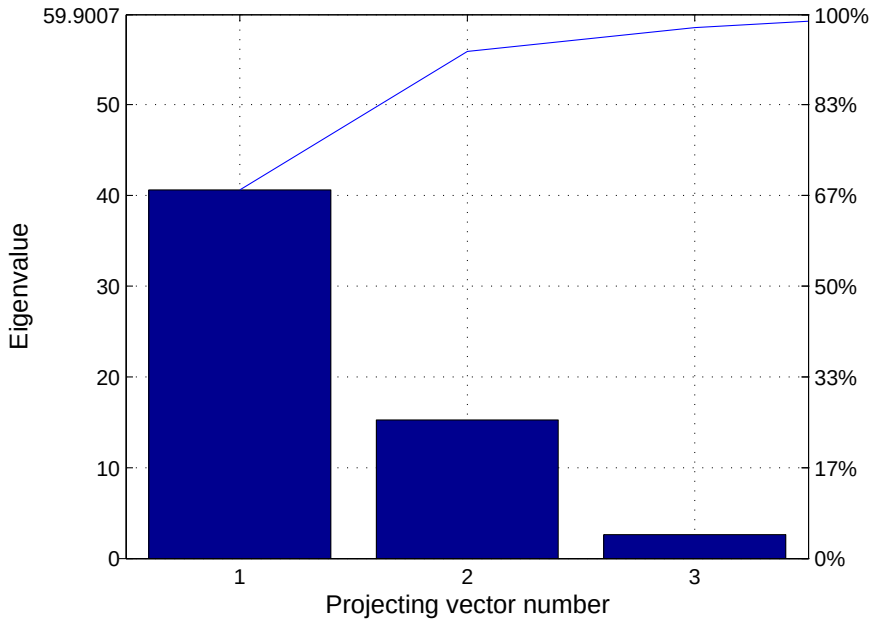

Figure 4-4: Eigenvalues and ACR values of FDA result for 40-cell stack

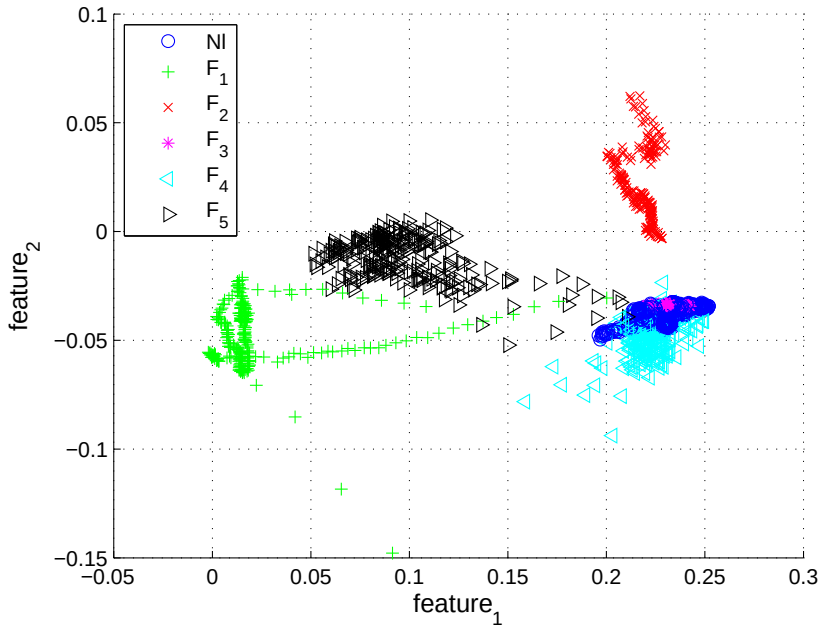

Figure 4-5: Data projected to the 2-dimensional space 8-cell stack

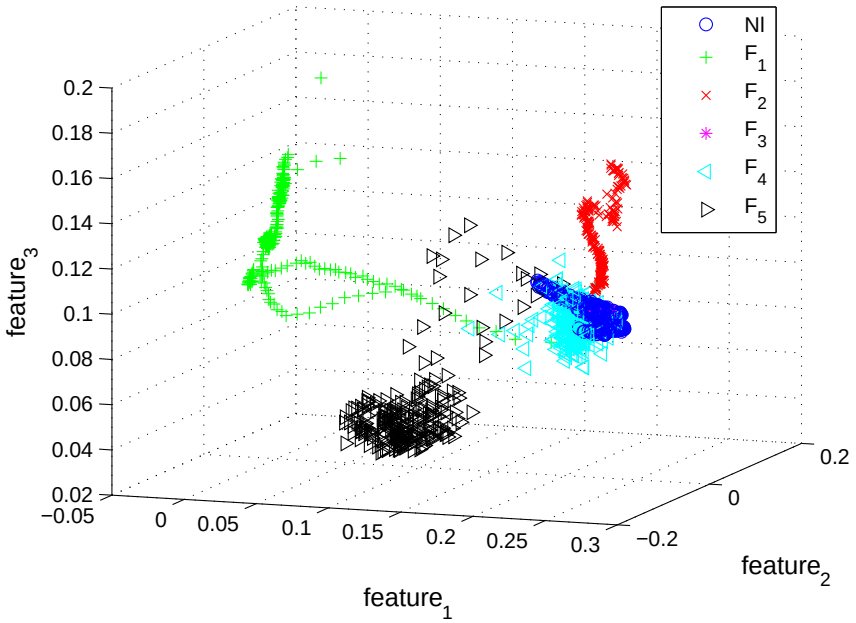

Figure 4-6: Data projected to the 3-dimensional space for 8-cell stack

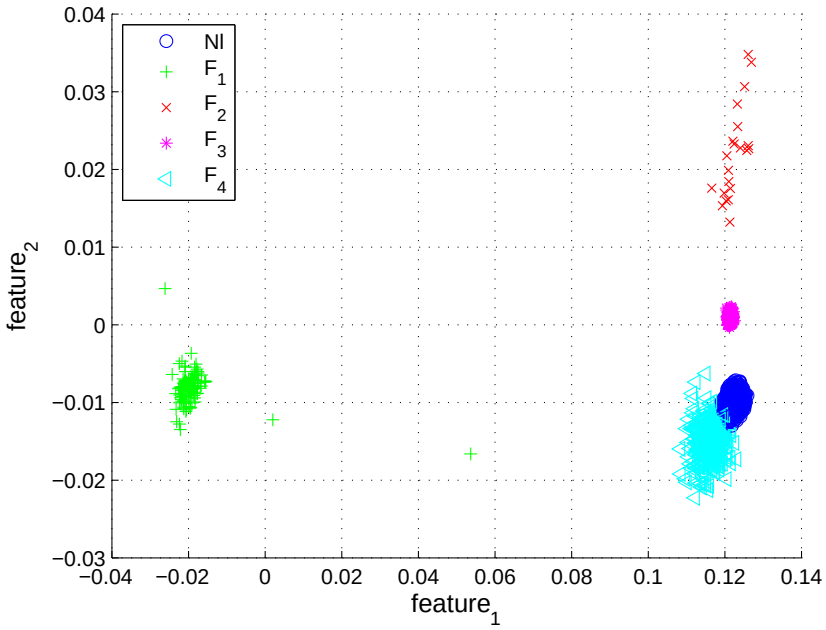

Figure 4-7: Data projected to the 2-dimensional space for 40-cell stack

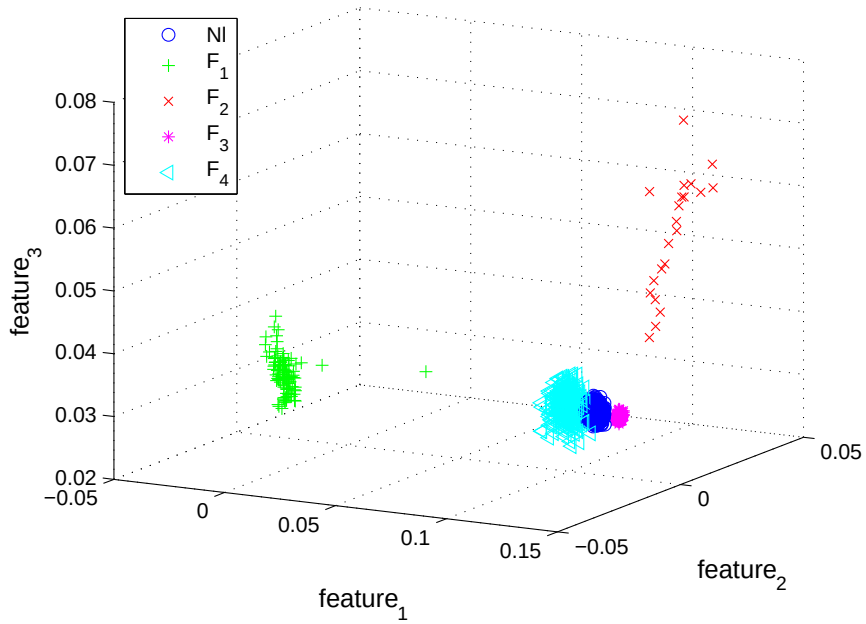

Figure 4-8: Data projected to the 3-dimensional space for 40-cell stack

space that from 2-dimensional feature space. For instance, some overlaps exist between the class F_1 and F_5 in 2-dimensional feature space, and the overlaps decrease in 3-dimensional feature space.

Concerning the choice of the dimension of the feature space, on the one hand, more discriminative information can be preserved in a higher dimensional feature space; On the other hand, the computation cost of performing FDA would increase with the increasing in feature space dimension. In the following section, it will be illustrated that the computation cost of DAGSVM is also correlated to the feature space dimensional number. Hence, the choice of the feature space dimension must be evaluated with the consideration of the DAGSVM stage.

4.2.3 DAGSVM procedure

After FDA, the DAGSVM classification is carried out to classify the generated features into the relevant classes. To implement DAGSVM algorithm, parameter σ in Gaussian kernel and parameter D in (3.56) were regularized via evaluating the di-

agnosis accuracy (DA) of the test dataset[1]. After several attempts, the parameters, with which a relatively higher DA can be obtained, are used to configure the SVMs.

The performance of the classification procedures in the feature spaces of varied dimension numbers was firstly evaluated. The comparative results for the two stacks are summarized in Table 4.2 and 4.3. From the tables, it can be observed that as the feature dimension number increases, the DAs increase for both training data and test data. This means that the higher classification performance could be obtained in the higher feature space. Apart from that, the number of SVs decreases as the dimension number increases. That is to say, some memory space corresponding SVs and their coefficients could be saved, and the computation could be achieved within a shorter time when DAGSVM is carried out in the higher feature space. Hence, it is recommended to set the feature space dimension number at the maximum possible value, i.e. one less than the class number.

Table 4.2: Comparative results of classification in various feature spaces for 8-cell stack

Dimension number	ACR	DA (training data)	DA (test data)	SV number
1	0.7082	0.8034	0.8430	1279
2	0.8807	0.9091	0.9172	754
3	0.9908	0.9282	0.9497	660
4	0.9996	0.9869	0.9858	265
5	1	0.9896	0.9885	230

Table 4.3: Comparative results of classification in various feature spaces for 40-cell stack

Dimension number	ACR	DA (training data)	DA (test data)	SV number
1	0.6777	0.8735	0.6270	1150
2	0.9325	0.9978	0.9235	62
3	0.9764	0.9980	0.9331	58
4	1	0.9987	0.9399	54

[1]DA and EDR defined in the last chapter satisfy $DA + EDR = 1$.

4.3 Results and discussion

From the above analysis, the DAs for test data for the 8-cell stack and 40-cell stack can be satisfying values when the classification is carried out in a relative high feature dimension as given in Table 4.2 and 4.3. Other than the global DAs, the mis-classified points should also be analyzed with more attention. Here, frequently-used criterion in pattern classification, called confusion matrix, is used to evaluate the diagnostic performance more specifically.

Definition 1. A confusion matrix is a specific table layout that allows visualization of the performance of an algorithm, typically a supervised learning one. Each column of the matrix represents the instances in a predicted class, while each row represents the instances in an actual class [96].

From *confusion matrix*, it is easy to see the mis-classification between two classes. The *confusion matrices* of test data sets for the 8-cell stack and the 40-cell stack are summarized in Table 4.4 and 4.5. Here, different from the original definition, each row of the *confusion matrices* represents the diagnosed distribution of the data in an actual class.

Table 4.4: Confusion matrix of the test data after classification for 8-cell stack

		Diagnosed class					
		Nl	F_1	F_2	F_3	F_4	F_5
Actual class	Nl	1.0000	0	0	0	0	0
	F_1	0	0.9163	0	0	0.0628	0.0209
	F_2	0.0399	0	0.9502	0.0100	0	0
	F_3	0	0	0	1	0	0
	F_4	0.0611	0.0056	0	0.0389	0.8944	0
	F_5	0	0	0	0	0.0092	0.9908

From the two tables, it can be observed and analyzed that:

- For both stacks, the mis-classifications happen mostly on the data of class F_4. The mis-classified points are located mostly in the class of Nl and some are classified to the F_3 class. This means F_4 is a fault type that is the most difficult

Table 4.5: Confusion matrix of the test data after classification for 40-cell stack

		Diagnosed class				
		Nl	F_1	F_2	F_3	F_4
Actual class	Nl	0.9479	0	0	0.0059	0.0462
	F_1	0.0323	0.9355	0	0	0.0323
	F_2	0	0	1.0000	0	0
	F_3	0	0	0	0.9956	0.0044
	F_4	0.1486	0	0	0	0.8514

to detect. For instance, in Table 4.5, 4.62% points in the Nl class are mis-classified to the F_4 class, and 14.8% samples in the F_4 class appear in the Nl class. It can be inferred that the faults of stoichiometry variation (referring to F_4) to a certain extent are light faults compared with other types of faults.

- Some mis-classified samples also appear in class F_1, F_2, and F_5. Actually, from our observations, the mis-classification mostly happens at the initial stage of these faults. It could be thought that these samples are located in the transition zone between the normal state and fault state.

- During test data acquisition in classes Nl, F_3, and F_4 supplementary EIS measurements were been realized. These EIS measurements added some current disturbances to the system. With such disturbances, the high classification rates can still be maintained.

For both stacks, when the approach is performed in PC (CPU@2.7 GHz, RAM@8 Go, MATLAB environment), the needed memory is less than 5 kb to save the FDA and SVM models. The performing time is less than 0.5 ms. Hence, the approach is promising for online implementation.

The approach is efficient for detecting and isolating the faults whose data are available to train the diagnosis models. Nevertheless, we should also notice the bottleneck of this diagnostic strategy. For instance, a sample from an unseen failure mode would be mis-classified to one of the known fault classes. Hence, an abundant training dataset, which contains the data from a substantial number of fault classes, is usually necessary for this approach. This is considered as the drawback of the

proposed approach.

4.4 Online implementation in an embedded system

Although the diagnostic strategy is justified to be suitable for PEMFC system FDI by using the data from the real system, the last link of the chain for final online diagnosis is still absent. Actually, to realize the final online diagnosis for PEMFC systems used for both the stationary or mobile applications, the strategy should be implemented in a specified embedded system.

In the framework of project DIAPASON2, the programs of the proposed diagnosis strategy were also integrated in this embedded system, and the synthetic tests were also supposed to be carried out. In this section, the preliminary test results obtained from the embedded system are given.

4.4.1 Embedded system designed for PEMFC system diagnosis

An **embedded system** is a computer system with a dedicated function within a larger mechanical or electrical system, often with real-time computing constraints. It is embedded as part of a complete device often including hardware and mechanical parts [97]. The embedded system is proposed versus general-purpose computer, which is designed for wide-range use.

The structure of a typical embedded system is shown in Fig. 4-9. CPU and memory are considered as the cores of the system. They will respectively determine the computation speed and the capability of data and program storage. In addition to the CPU and memory hierarchy, there are a variety of interfaces that enable the system to measure, manipulate, and otherwise interact with the external environment [98].

Fig. 4-10 shows the embedded system, which was specially designed for the

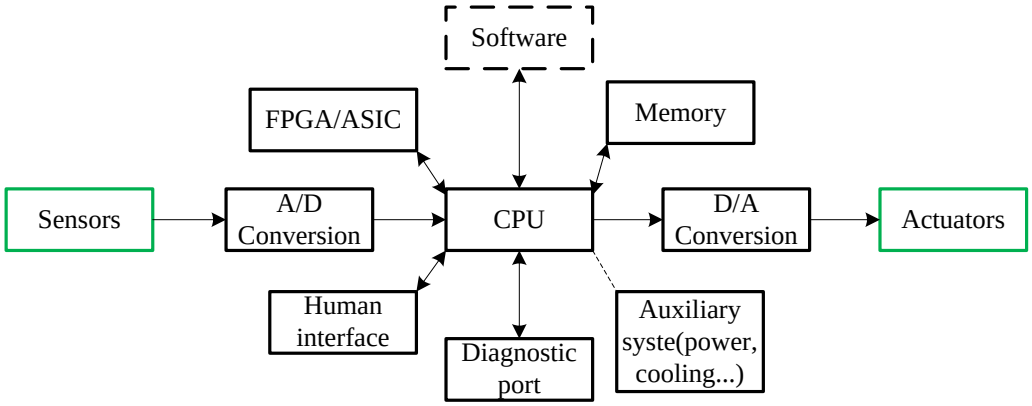

Figure 4-9: Structure of a general embedded system [98]

PEMFC system diagnosis by the project partners. The upper layer shown in the figure can be seen as the "main board" of the system. The main board is equipped with Smartfusion on-chip system developed by Microsemi company. The device integrates an FPGA fabric, ARM Cortex-M3 Processor, and programmable analog circuitry [99]. ARM Cortex-M3 processor is an 100 MHz, 32-bit CPU. The programmable analog circuitry can function as the D/A and A/D conversion blocks. Up to 512 KB flash and 64 KB of SRAM are also equipped inside this integrated device. Another two chips of 16 M memory are also added to the system. With the abundant connecting ports, kinds of communications can be realized with other devices. The other two layers, which are equipped with GMR sensors, are used for measuring individual cell voltages precisely.

4.4.2 Implementation results

4.4.2.1 Online fault diagnosis developing process

As shown in Fig. 4-11, in the framework of the project, the online fault diagnosis developing consists of three steps:

- **Offline verification**: In this stage, the historical data sampled in the experiments of different health states are analyzed using the PC and the software such as Matlab. The objective is to train and verify the methods. Actually, this step is the main focus of this Ph.D. work.

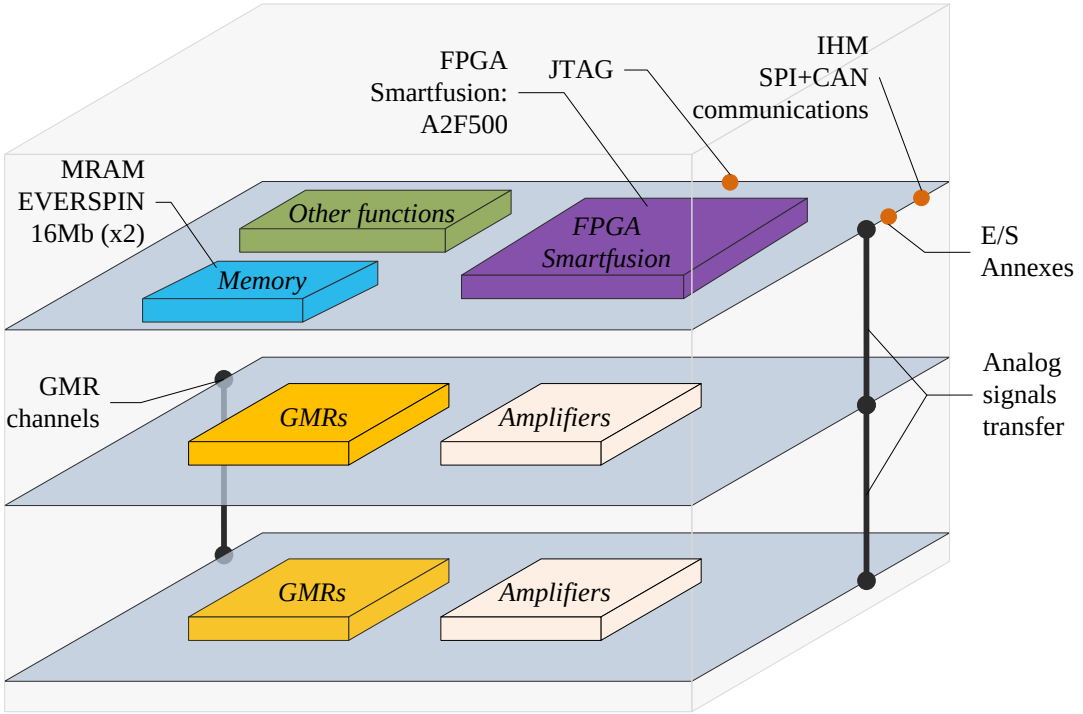

Figure 4-10: Embedded system designed for PEMFC system diagnosis [100]

- **Algorithm integration**: In this step, the programs for performing the diagnosis strategy are coded and burnt into the designed embedded system. The integrated programs are then tested using the historical data. Thus, the obtained results can be compared with the results got from the PC. The objective of this step is to ensure the algorithm can run smoothly in the embedded system. The computation time and occupied memory are also evaluated during this process.

- **Online realization**: After the first two stages, the embedded system, in which the diagnosis strategy is programed, is settled in the real PEMFC system. The tests are carried out using the real-time data. This step is operated just as the real situation. This step is to make sure the different subsystems can cooperate as expectation.

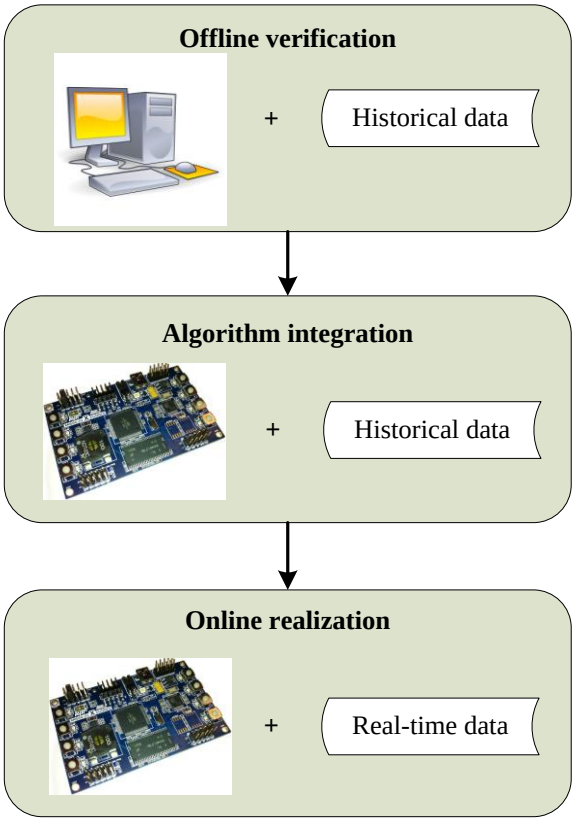

Figure 4-11: Flowchart of online fault diagnosis developing process

4.4.2.2 Algorithm integration test results

The programs of the proposed methods were coded into the embedded system, and the tested were carried out by using the same test database. The obtained results are compared to those obtained from using a PC and Matlab software. As Table 4.6 shows, nearly same results can be obtained by implementing the algorithms in the embedded system and in the PC. The operating time is also acceptable for real time implementation.

Table 4.6: Comparative results from embedded system and from PC

Stack	Class number	Difference ratio (compared to PC & matlab)	Computation time
8-cell stack	6	0	11 ms
40-cell stack	5	0.08%	2.8 ms

Until now, the first two steps shown in the Fig. 4-11 have been finished. The last-step tests are still in process.

4.5 Conclusion

Following the last chapter, the pattern classification based fault diagnosis strategy is tested for the multi-fault FDI of two more stacks. Still, individual cell voltages serve as the original variables for diagnosis. Methods FDA and DAGSVM are employed successively to extract the discriminative features from the raw data and classify the extracted features. FDI is thus achieved. The results show that five concerned faults could be detected and isolated with high accuracy. Moreover, the light computation cost, i.e. needed memory and computing time, makes the approach a promising online multi-fault FDI tool for various stacks. Following that, the embedded system designed for final online implementation is presented, and the preliminary results are given. It is verified that the algorithms are successfully integrated in the embedded system, and the real time capability, such as computation time, is satisfying.

Notice that the capability to recognize an unseen fault type is weak for this strat-

egy, the next chapter will be dedicated to improve the performance in this aspect.

Chapter 5

Pattern classification for diagnosis: novel fault recognition and online adaptation

In the last two chapters, the feature extraction method FDA and the classification method SVM, have been adopted to do FDI for different stacks. The approach provides high diagnosis accuracy and a low computational cost. Nevertheless, some aspects of the approach still need to be improved.

One of the main limits of the conventional classification methods, such as SVM is the impossibility to detect new fault clusters. Actually, the classifiers trained using the pre-existing data can only be used to recognize the known classes. An arbitrary example will be classified into a known class even if it belongs to a new cluster which strongly differs from the samples of known classes. Specifically for PEMFC systems, multiple physical and chemical processes are involved in the fuel cells, and a set of auxiliary components are consisted in the systems. A variety of faults could be encountered on different parts of the systems [15]. It is usually not possible to get the data in all the failure modes at the training stage. The data from unseen failure modes would be always falsely diagnosed in such cases.

Moreover, specifically to the PEMFCs, the behavior in normal operating state is evolutionary when the aging effect is taken into account. For instance, the cell

voltages decrease after a period of time operation. The diagnosis strategy trained initially may gradually lose its efficiency.

To solve the aforementioned problems, in this chapter, a modified data-driven fault diagnosis strategy for PEMFC system is proposed. As in the last two chapters , the individual cell voltages are employed as the original variables for diagnosis, and FDA is used to extract the features for classification. A novel classifier, named *Spherical-Shaped Multiple-class Support Vector Machine* (SSM-SVM) is adopted to classify the features into various classes to fulfill the diagnostic tasks, including the detection and isolation of the known faults and the detection of the potential novel failure modes. Moreover, an online adaptation procedure is proposed to update the diagnosis models in real time.

5.1 Framework of the strategy

The framework of the proposed diagnostic strategy can be summarized in Fig. 5-1. The strategy contains an off-line initial training stage, an on-line performing stage,

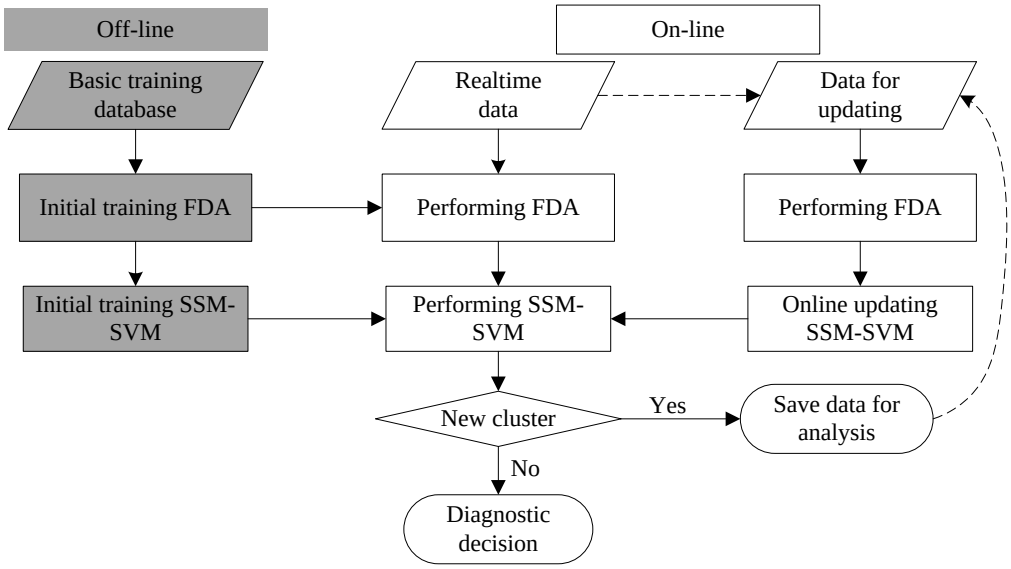

Figure 5-1: Flowchart of the proposed diagnostic strategy

and an online adapting stage. In the off-line training stage, the initial models of FDA and SSM-SVM are trained successively based on the basic training database.

Historical samples of cell voltages, which are distributed in normal class and various fault classes, form the basic training database. Similarly to the strategy given in the last two chapters, the basic training database is composed by labeled samples. The data labeling, which is not shown in Fig. 5-1, is also necessary.

In the on-line performing stage, the real-time sample, i.e. values of cell voltages, is firstly processed by the trained FDA model, through which features can be extracted from raw data. Then, with the aid of trained SSM-SVM model, the features are assigned either to a certain known class to get the diagnostic decision, or to a potential novel failure class.

During the on-line adapting stage, the labeled data for adapting the models are firstly collected. The data can either be prepared from real-time samples or from the potential novel failure class. These data are processed using the trained FDA model. Then, the extracted features will be explored to update the SSM-SVM model.

5.2 FDI and novel fault recognition

5.2.1 Problem mathematical description

Similarly to what is presented previously, the methodology presented in 5.1 section, used to solve the diagnostic problem can be mathematically abstracted as follows. Let $M \in \mathbb{N}$. Suppose that we have a training dataset of N M-dimensional samples $\boldsymbol{x}_n$ ($n \in \mathcal{T} = \{1, \ldots, N\}$), which are distributed in C classes Ω_1, Ω_2, $\ldots$, Ω_C. Sample indexes in ith class are collected as set ω_i. In the sequel, the cardinal of Ω_i (i.e. the sample number in Ω_i) will be denoted by $|\Omega_i|$. The class index of $\boldsymbol{x}_n$ is denoted by h_n, $h_n \in \{1, 2, \ldots, C\}$. FDA and SSM-SVM models are trained based on the training dataset. Through the trained models, a real-time sample $\boldsymbol{x}$ can be classified into a defined class Ω_i, $i = 1, \ldots, C$ or a novel cluster denoted by Ω_{novel}.

The original data are processed firstly using FDA. With the FDA procedure as previously, the original M-dimensional data $\boldsymbol{x}_n$ ($n \in \mathcal{T}$) are projected to L-dimensional space, where the projected data are denoted as $\boldsymbol{z}_n$ ($n \in \mathcal{T}$). The classification pro-

cedure is carried out in the L-dimensional feature space. In the following part, the SSM-SVM procedure is presented.

5.2.2 SSM-SVM

As mentioned in the chapter 3 and chapter 4, the basic SVM was originally designed for binary classification, and to maximize the margin between two class. Through constructing the basic binary SVMs, multi-class SVM classification can be achieved [93]. Although the classifiers based on the binary SVM can classify the data from the known classes, the capability of detecting an unseen cluster seems to be defective. As Fig. 5-2 (a) shows, the bounders among the trained classes, i.e. Class1, Class2, and Class3, can be affirmed by a multi-class classifier based on binary SVM. According to the decision of the trained classifier, an arbitrary sample will be classified into one of the three classes, even if the data are from a novel cluster as it is shown by Fig. 5-2 (b).

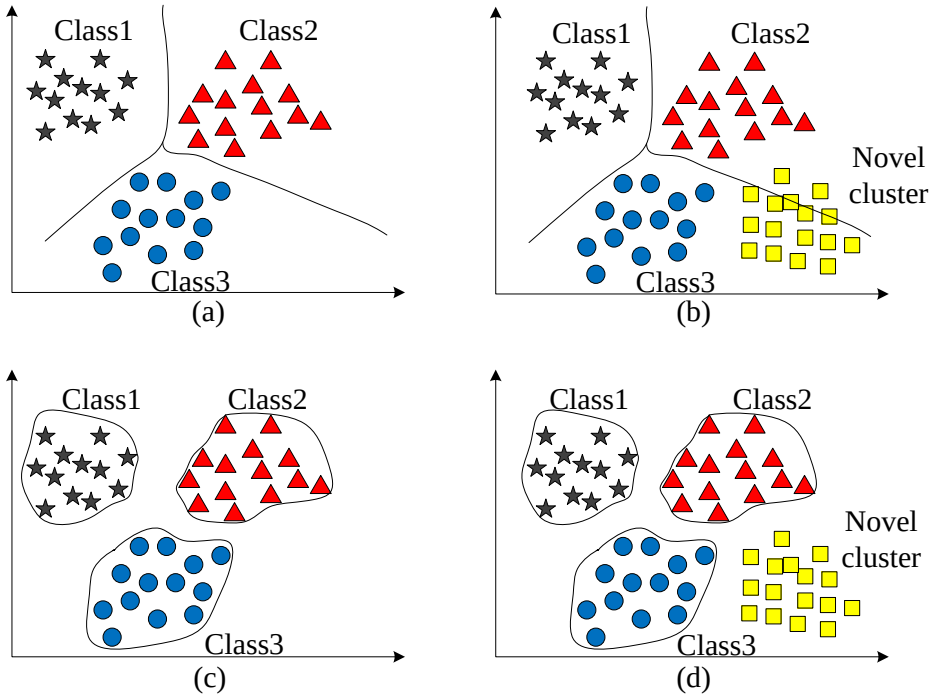

Figure 5-2: Schematic diagrams of conventional binary SVM based multi-class classifier and SSM-SVM.

The authors of [101] proposed classification method SSM-SVM. Different from binary SVM based classifier, the approach finds class-specific spheres that each encloses the samples from one specific class but excludes the ones from other classes. As Fig. 5-2 (c) shows, the closed bounders for all the known classes can be found by training SSM-SVM. Thus, the samples from a novel cluster could be probably detected if they are outside all the closed bounders as it is shown in Fig. 5-2 (d).

Following the FDA step, the training of SSM-SVM is based on the *projected vectors* $\boldsymbol{z}_n$ ($n \in \mathcal{T}$, $\boldsymbol{z}_n \in \mathbb{R}^L$). As shown in Fig. 5-3, to solve the nonlinear classification problem, $\boldsymbol{z}_n$ ($n \in \mathcal{T}$) are firstly projected to a high-dimensional space via a nonlinear transform Φ [101]. Then, the data in each identical class will be enclosed by a sphere, and thus the classification will be achieved using these spheres. Equivalently in the original space, the boundaries among classes are determined consequently.

Take the ith class for example, the method is realized by seeking the sphere with the minimal radius in the high-dimensional space. The sphere encloses all data points in the ith class and leaves the other data points outside it. That is

$$\begin{cases} ||\Phi(\boldsymbol{z}_n) - \boldsymbol{a}_i||^2 \leq R_i^2 + \xi_n^i & \text{if } \boldsymbol{z}_n \in \Omega_i \\ ||\Phi(\boldsymbol{z}_n) - \boldsymbol{a}_i||^2 \geq R_i^2 - \xi_n^i & \text{if } \boldsymbol{z}_n \notin \Omega_i \end{cases} \tag{5.1}$$

where R_i and $\boldsymbol{a}_i$ are the radius and center of the ith sphere respectively, and ξ_n^i, which satisfy $\xi_n^i \geq 0$ ($n \in \mathcal{T}$), are the slack variables corresponding to the training data point $\boldsymbol{z}_n$. The slack variables permit the occurrence of errors. For instance, the data in class i could be outside of the sphere; while the data outside class i could be inside the sphere. The two inequalities in (5.1) are reduced to

$$c_n^i(||\Phi(\boldsymbol{z}_n) - \boldsymbol{a}_i||^2 - R_i^2) - \xi_n^i \leq 0 \text{ and } \xi_n^i \geq 0 \text{ for } n \in \mathcal{T} \tag{5.2}$$

where $c_n^i = 1$ if $\boldsymbol{z}_n \in \omega_i$ and $c_n^i = -1$ if $n \notin \omega_i$. With the constraint conditions of

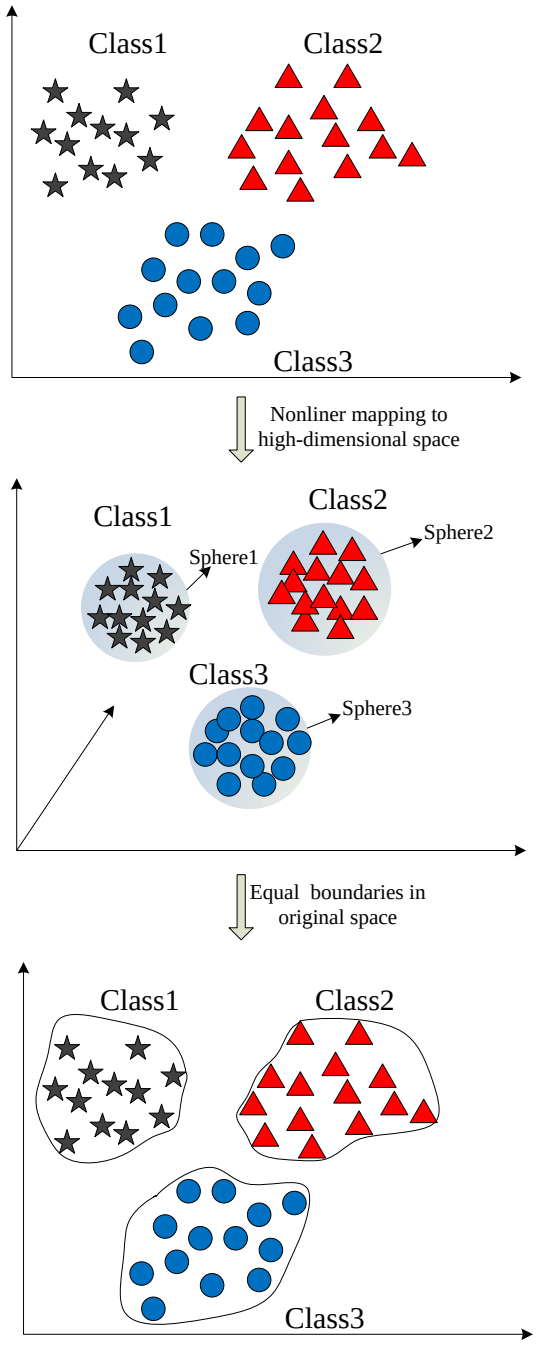

Figure 5-3: Schematic diagram of SSM-SVM

(5.2), this amounts solving the following problem

$$\begin{aligned} &\min_{R_i, \boldsymbol{a}_i}(R_i^2 + D\sum_{n\in\mathcal{T}}\xi_n^i) \\ &s.t. \begin{cases} c_n^i(||\Phi(\boldsymbol{z}_n) - \boldsymbol{a}_i||^2 - R_i^2) - \xi_n^i \leq 0 \\ \xi_n^i \geq 0 \end{cases} \quad \text{for } n \in \mathcal{T} \end{aligned} \tag{5.3}$$

where D is a parameter controlling the penalty of errors [101].

By introducing Lagrange multipliers, we obtain the following dual problem

$$L = R_i^2 + D\sum_{n=1}^{N}\xi_n^i - \sum_{n=1}^{N}\beta_n^i\xi_n^i + \sum_{n=1}^{N}\alpha_n^i(c_n^i(||\Phi(\boldsymbol{z}_n) - \boldsymbol{a}_i||^2) - \xi_n^i) \tag{5.4}$$

where α_n^i $(n \in \mathcal{T})$ and β_n^i $(n \in \mathcal{T})$ are non-negative Lagrange multipliers. Differentiating L with respect to $\boldsymbol{a}_i$, R_i and ξ_n^i and setting the result to zero, we obtain:

$$\frac{\partial L}{\partial R_i} = 0 \rightarrow \sum_{n=1}^{N}\alpha_n^i c_n^i = 1 \tag{5.5}$$

$$\frac{\partial L}{\partial \boldsymbol{a}_i} = 0 \rightarrow \boldsymbol{a}_i = \sum_{n=1}^{N}\alpha_n^i c_n^i \Phi(\boldsymbol{z}_n) \tag{5.6}$$

$$\frac{\partial L}{\partial \xi_n^i} = 0 \rightarrow \alpha_n^i c_n^i + \beta_n^i = D \text{ and } 0 \leq \alpha_n^i \leq D \tag{5.7}$$

Based the above three conditions, the following dual problem is obtained from (5.4):

$$\min\left(\sum_{n,m\in\mathcal{T}}\alpha_n^i c_n^i \alpha_m^i c_m^i \Phi(\boldsymbol{z}_n)\Phi(\boldsymbol{z}_m) - \sum_{n\in\mathcal{T}}\alpha_n^i c_n^i \Phi(\boldsymbol{z}_n)\Phi(\boldsymbol{z}_n)\right) \tag{5.8}$$

subject to

$$\sum_{n\in\mathcal{T}}\alpha_n^i c_n^i = 1 \quad \text{and} \quad 0 \leq \alpha_n^i \leq D \quad \forall n \tag{5.9}$$

Introducing kernel function $k(\boldsymbol{z}_n, \boldsymbol{z}_m) = \Phi(\boldsymbol{z}_n)\Phi(\boldsymbol{z}_m)$, the problem is further transformed to the following dual problem that involves $\{\alpha_n^i\}$, which subjects to (5.9).

$$\begin{aligned} &\min \left(\sum_{n,m \in \mathcal{T}} \alpha_n^i Q_{n,m}^i \alpha_m^i - \sum_{n \in \mathcal{T}} \alpha_n^i c_n^i k(\boldsymbol{z}_n, \boldsymbol{z}_n) \right) \\ &s.t. \sum_{n \in \mathcal{T}} \alpha_n^i c_n^i = 1 \quad \text{and} \quad 0 \leq \alpha_n^i \leq D \quad \forall n \end{aligned} \tag{5.10}$$

where $Q_{n,m}^i = c_n^i c_m^i k(\boldsymbol{z}_n, \boldsymbol{z}_m)$. As stated previously, throughout this chapter, the Gaussian kernel $k(\boldsymbol{z}_n, \boldsymbol{z}_m) = \exp(-||\boldsymbol{z}_n - \boldsymbol{z}_m||^2/\sigma)$ will be used. For $k(\boldsymbol{z}_n, \boldsymbol{z}_n) = 1$, the term $\sum_{n=1}^N \alpha_n^i c_n^i k(\boldsymbol{z}_n, \boldsymbol{z}_n)$ in (5.10) equals to 1.

The training process is to solve the QP (5.10). In this study, an online learning method is used to achieve the training procedure, and the method is stated in detail in the next section.

After solving the problem, the distance from a data point $\boldsymbol{z}$ to the ith sphere center can be expressed by (see [101])

$$d_i^2(\boldsymbol{z}) = ||\Phi(\boldsymbol{z}) - \boldsymbol{a}_i||^2 = 1 - 2 \sum_{n \in \mathcal{T}} \alpha_n^i c_n^i k(\boldsymbol{z}, \boldsymbol{z}_n) + \sum_{n,m \in \mathcal{T}} \alpha_n^i Q_{n,m}^i \alpha_m^i \tag{5.11}$$

The radius R_i is given

$$R_i = ||\Phi(\boldsymbol{z}_n) - \boldsymbol{a}_i|| \quad \text{for some } \boldsymbol{z}_n \text{ such that } \alpha_n^i \in (0, D) \tag{5.12}$$

The reader is referred to [101] for more details for the derivation process of SSM-SVM.

5.2.3 Diagnostic rules

The goal of this subsection is to present the diagnostic rules, including that for novel cluster detection.

Let $F_i : \mathbb{R}_+ \to \mathbb{R}_+$ be a smooth function such that F_i is decreasing and is such that $\lim_{\iota \to \infty} F_i(\iota) = 0$. In the classical approach; i.e. without detection of novel cluster,

a general sample $\boldsymbol{z}$ is allotted to a class using the following criterion:

$$Class(\boldsymbol{z}) = arg \max_i F_i\left(d_i(\boldsymbol{z})\right) \tag{5.13}$$

It should be noted that in this classical approach, the number of classes is fixed and the sample $\boldsymbol{z}$ is associated to a class even if the distances to the different centers are very large.

In this work, it is assumed that the classes are not limited to those defined initially. Furthermore, the fact that the distances from a sample $\boldsymbol{z}$ from the different centers are very large, i.e. $\max F_i\left(d_i(\boldsymbol{z})\right)$ is very small; in a meaning to be defined, can mean the appearance of a novel cluster.

The principle for deciding that a sample belongs to a defined class or a new cluster can be described as follows. For each class Ω_i, $\delta_i \in \mathbb{R}_+$ is considered to denote the threshold from which a sample $\boldsymbol{z}$ is considered to be definitely outside the class. More precisely, it is assumed that $\boldsymbol{z}$ is outside Ω_i if $F_i\left(d_i(\boldsymbol{z})\right) < \delta_i$. The value of threshold can be determined based on calibration dataset and a way to fix its value is the use of the *3-sigma law*:

$$\delta_i = M_i - \frac{3}{|\Omega_i|}\sqrt{\sum_{z_n \in \Omega_i}\left(F_i\left(d_i(\boldsymbol{z})\right) - M_i\right)^2} \tag{5.14}$$

with $M_i = \frac{1}{|\Omega_i|}\sum_{z_n \in \Omega_i} F_i\left(d_i(\boldsymbol{z})\right)$.

Within this approach, the decision rule is defined by

$$Class(\boldsymbol{z}) = \begin{cases} \arg\max_i F_i\left(d_i(\boldsymbol{z})\right) & \text{if } \max F_i(d_i(\boldsymbol{z}) \geq \delta_i \\ \text{novel} \quad \text{if } \max F_i\left(d_i(\boldsymbol{z})\right) < \delta_i \end{cases} \tag{5.15}$$

Note that by considering the threshold given by (5.14), less than 0.15% of the samples in the training dataset are misclassified to the novel class.

As for the function F_i, several expressions are possible. For the implementation

part, the one proposed in [101] is used, as

$$F_i\left(d_i(\boldsymbol{z})\right) = \begin{cases} 0.5\left(\dfrac{1-d_i(\boldsymbol{z})/R_i}{1+\lambda_1 d_i(\boldsymbol{z})/R_i}\right) + 0.5 \text{ if } d_i(\boldsymbol{z}) \leq R_i \\ 0.5\left(\dfrac{1}{1+\lambda_2(d_i(\boldsymbol{z})-R_i)}\right) \text{ otherwise} \end{cases} \tag{5.16}$$

where parameters λ_1 and λ_2 are constants that satisfy $R_i\lambda_2(1+\lambda_1) = 1$.

5.3 Online adaptation method

In [101], the modified SMO method is proposed to solve the QP problem (5.10) so as to train SSM-SVM. This method is known as a *batch training* approach which is performed in one batch. It implies that if more training data arrive subsequently, the SSM-SVM classifier should be retrained from scratch. Since the computational cost of training procedure is much heavier compared to the performing procedure. The *batch training* is considered to be computationally inefficient in this case [102]. As for PEMFC system diagnosis, the degradation related to ageing effect can make the normal class data shift when long-time operation is taken into consideration. The adaptation of the diagnostic strategy is necessary, and the adaptation is supposed to be achieved online. The *batch training* thus can hardly satisfy the requirement of online adaptation.

In [103], an incremental learning method is proposed for training the classic binary SVM. In this method, the solution for $N+1$ training data could be formulated in terms of that for N data and one new data point which can avoid the *batch learning*. In this section, the incremental training method is extended to the training and online adaptation for SSM-SVM without much modification. A procedure is also proposed to further lower the real-time computational cost.

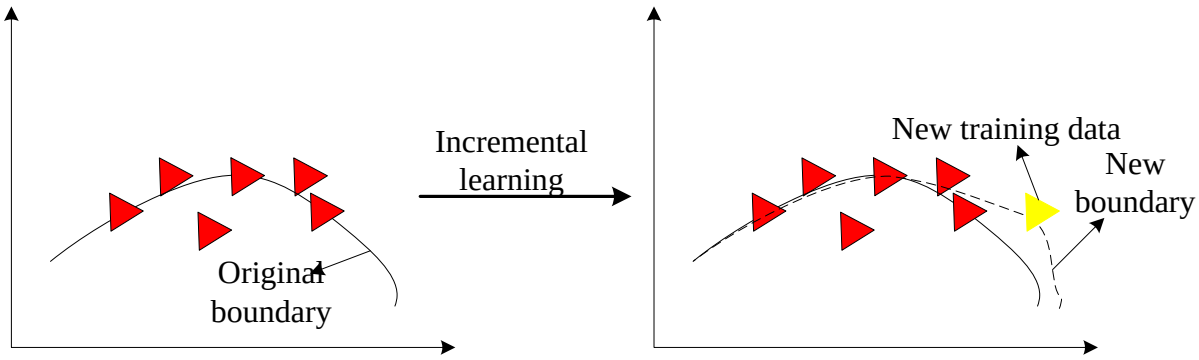

Figure 5-4: Schematic of incremental learning

5.3.1 Incremental learning method for SSM-SVM

By introducing another Lagrange multiplier b_i, the problem (5.10) can be re-expressed as:

$$\min_{0\leq\alpha_n^i,\alpha_m^i\leq D} W_i = \frac{1}{2}\sum_{n,m\in\mathcal{T}} \alpha_n^i Q_{n,m}^i \alpha_m^i + b_i(\sum_{n\in\mathcal{T}} c_n^i \alpha_n^i - 1) \tag{5.17}$$

The goal of the incremental learning is to keep the Kuhn-Tucker (KT) conditions of (5.17) satisfied when a new training sample is added to the current training data. The principle of incremental learning can be shown in Fig. 5-4. When a new training sample is added to the available training dataset, the training result which is expressed as boundary just need to be modified slightly through incremental learning to take in the new sample. Such that the retraining process could be avoided.

5.3.1.1 Incremental procedure

To solve the optimization problem (5.17), we proceed as in [103]. Let g_n^i ($n \in \mathcal{T}$) and h_i be the quantities defined by

$$g_n^i = \frac{\partial W_i}{\partial \alpha_n^i} = \sum_{m\in\mathcal{T}} Q_{n,m}^i \alpha_m + c_n^i b_i \tag{5.18}$$

and

$$h_i = \frac{\partial W_i}{\partial b_i} = \sum_{n\in\mathcal{T}} c_n^i \alpha_n^i - 1 = 0 \tag{5.19}$$

According to the value of g_n^i, the set $\mathcal{T}$ is partitioned into three sets.

$$\begin{aligned}\mathcal{T} &= \mathcal{T}_M^i \cup \mathcal{T}_E^i \cup \mathcal{T}_R^i \\ &= \{n \in \mathcal{T} : g_n^i = 0\} \cup \{n \in \mathcal{T} : g_n^i \leq 0\} \cup \{n \in \mathcal{T} : g_n^i \geq 0\}\end{aligned} \tag{5.20}$$

It should be noted that the solutions for (5.17) (see for instance [103]) are so that

$$\begin{cases} \alpha_n^i = 0 \text{ for } n \in \mathcal{T}_R^i \\ \alpha_n^i \in (0, D) \text{ for } n \in \mathcal{T}_M^i \\ \alpha_n^i = D \text{ for } n \in \mathcal{T}_E^i \end{cases} \tag{5.21}$$

We use $(t_j^M)_{j=1,\ldots,|\mathcal{T}_M^i|}$ as the denotations of the elements of $\mathcal{T}_M^i$, and $(\bar{t}_j^M)_{j=1,\ldots,|\mathcal{T}_E^i \cup \mathcal{T}_R^i|}$ for those of $\mathcal{T}_E^i \cup \mathcal{T}_R^i$.

The matrix $\boldsymbol{P}^i \in \mathbb{R}^{(|\mathcal{T}_M^i|+1)\times(|\mathcal{T}_M^i|+1)}$ which is later used is defined, as

$$\begin{cases} P_{1,1}^i = 0, P_{1,k+1}^i = P_{k+1,1}^i = c_k^i, \text{ and } P_{l+1,k+1}^i = Q_{t_l^M, t_k^M}^i \\ \text{for } k, l \in \{1, \ldots, |\mathcal{T}_M^i|\} \end{cases} \tag{5.22}$$

In what follows, $\mathcal{U}$ will denote the index set of unlearned vectors. Let $\boldsymbol{z}_s$ ($s \in \mathcal{U}$) a new sample to be added to the learned data. Let also $\alpha_s^i = 0$ be the coefficient assigned to $\boldsymbol{z}_s$ and g_s^i the quantity associated to α_s^i and determined using (5.18). If $g_s^i \geq 0$, s will be added to $\mathcal{T}_R^i$ and thus the KT conditions are satisfied. Otherwise, the KT conditions are maintained by varying the *margin vector* coefficients α_n^i ($n \in \mathcal{T}_M^i$) and b_i in response to the perturbation imparted by the incremented new coefficient $\Delta\alpha_s^i$, until the s enters into $\mathcal{T}_E^i$ or $\mathcal{T}_M^i$.

Taking into account the perturbation caused by the incremental step, the coefficient differences $\Delta\alpha_l^i, \Delta g_l^i$ ($l \in \mathcal{T} \cup \{s\}$), and Δb_i are introduced. Besides, for $\iota \in \{\Delta b_i, \Delta\alpha_n^i, \Delta g_n^i; n \in \mathcal{T}\}$, *coefficient sensitivities* $\bar{\iota}$ is defined so that $\iota = \bar{\iota}\Delta\alpha_s^i$.

The KT conditions (5.18) and (5.19) can be expressed differentially, as

$$\Delta g_n^i = \sum_{m \in \mathcal{T}_M^i \cup \{s\}} Q_{n,m}^i \Delta\alpha_m^i + c_n^i \Delta b_i \quad \forall n \in \mathcal{T} \cup \{s\} \tag{5.23}$$

$$\Delta h_i = \sum_{m \in \mathcal{T}_M^i \cup \{s\}} c_m^i \Delta\alpha_m^i = 0 \tag{5.24}$$

For all $n \in \mathcal{T}_M^i$, the condition $g_n^i \equiv 0$ should be maintained. Thus, it can be deduced from (5.23) and (5.24) that

$$\boldsymbol{P}^i \begin{pmatrix} \Delta b_i \\ \Delta\alpha_{t_1^M}^i \\ \vdots \\ \Delta\alpha_{t_{|\mathcal{T}_M^i|}^M}^i \end{pmatrix} = - \begin{pmatrix} c_s^i \\ Q_{t_1^M,s}^i \\ \vdots \\ Q_{t_{|\mathcal{T}_M^i|}^M,s}^i \end{pmatrix} \Delta\alpha_s^i \tag{5.25}$$

Or, in terms of coefficient sensitivities

$$\begin{pmatrix} \bar{b}_i \\ \bar{\alpha}_{t_1^M}^i \\ \vdots \\ \bar{\alpha}_{t_{|\mathcal{T}_M^i|}^M}^i \end{pmatrix} = \bar{\boldsymbol{P}}^i \begin{pmatrix} c_s^i \\ Q_{t_1^M,s}^i \\ \vdots \\ Q_{t_{|\mathcal{T}_M^i|}^M,s}^i \end{pmatrix} \tag{5.26}$$

where $\bar{\boldsymbol{P}}^i = -\{\boldsymbol{P}^i\}^{-1}$. Note that $\bar{\alpha}_n^i \equiv 0$ for all $n \in \mathcal{T}_E^i \cup \mathcal{T}_R^i$.

According to (5.23) and (5.26), it can be deduced that

$$\bar{g}_n^i = \sum_{l \in \mathcal{T}_M^i \cup \{s\}} Q_{n,l}^i \bar{\alpha}_l^i + c_n^i \bar{b}_i, \ \forall n \in \mathcal{T}_E^i \cup \mathcal{T}_R^i \cup \{s\} \tag{5.27}$$

and $\bar{g}_n^i \equiv 0$ for all $n \in \mathcal{T}_M^i$.

From above explanations, it can be seen that $\Delta\alpha_s^i$ can be absorbed by varying α_n^i ($n \in \mathcal{T}_M^i$) and b_i. Meanwhile, g_n^i ($n \notin T_M^i$) vary accordingly. Thus, within several incremental steps, s will be added to category $\mathcal{T}_E^i$ when $\alpha_s^i = D$, or to $\mathcal{T}_M^i$ when $g_s^i = 0$ [103].

As in [103], some procedures in the incremental learning algorithm can be used here without modifications.

5.3.1.2 Upper limit on $\Delta\alpha_s^i$

The composition of sets $\mathcal{T}_M^i$, $\mathcal{T}_E^i$, and $\mathcal{T}_R^i$ can be changed with the change of α_l^i ($l \in \mathcal{T}_M^i \cup \{s\}$) and g_n^i ($n \in \mathcal{T}_E^i \cup \mathcal{T}_R^i \cup \{s\}$). The procedure to determine $\Delta\alpha_s^i$ such that the index of some sample migrates can be utilized here. Table 5.1 lists the possible category changes that can occur during the learning process.

Table 5.1: Bookkeeping conditions

Case	Initial Category	New Category	Condition	$\Delta\alpha_c^i$
1	$\mathcal{U}$	$\mathcal{T}_M^i$	$\bar{g}_n^i > 0$	$\frac{-g_n^i}{\bar{g}_n^i}$
2	$\mathcal{U}$	$\mathcal{T}_E^i$	null	$D - \alpha_n^i$
3	$\mathcal{T}_M^i$	$\mathcal{T}_R^i$	$\bar{\alpha}_n^i < 0$	$\frac{-\alpha_n^i}{\bar{\alpha}_n^i}$
4	$\mathcal{T}_M^i$	$\mathcal{T}_E^i$	$\bar{\alpha}_n^i > 0$	$\frac{D-\alpha_n^i}{\bar{\alpha}_n^i}$
5	$\mathcal{T}_E^i$	$\mathcal{T}_M^i$	$\bar{g}_n^i > 0$	$\frac{-g_n^i}{\bar{g}_n^i}$
6	$\mathcal{T}_R^i$	$\mathcal{T}_M^i$	$\bar{g}_n^i < 0$	$\frac{-g_n^i}{\bar{g}_n^i}$

Once set-to-set migration occurs, which means any condition listed in Table 5.1 happens for one single example, the different sets must be resettled. Therefore, the maximum increment of α_s^i should be determined by comparing the minimum $\Delta\alpha_s^i$ in each category change case, as

$$M_{\Delta\alpha_s^i} = \min_j(\Delta\alpha_{s,j}^i) \tag{5.28}$$

where $\Delta\alpha_{s,j}^i$ is the minimum $\Delta\alpha_s^i$ in category change case j

$$\Delta\alpha_{s,j}^i = \min\{\Delta\alpha_s^i : \text{Case } j\} \quad j = 1, \ldots, 6 \tag{5.29}$$

Make$M_{\Delta\alpha_s^i}$ as the increment of α_s^i, the updating of α_s^i, b_i, α_n^i ($n \in \mathcal{T} \cup \{s\}$), and g_n^i ($n \in \mathcal{T} \cup \{s\}$) can be carried out.

5.3.1.3 Recursive update of the inverse matrix

In the learning process, the composition of the set $\mathcal{T}_M^i$ might change. To account for the new composition of $\mathcal{T}_M^i$, matrix $\bar{\boldsymbol{P}}^i$ must be re-computed. The procedure of

recursive computing the $\bar{\boldsymbol{P}}^i$ proposed in [103] can also be adopted in our case.

Actually, $\bar{\boldsymbol{P}}^i$ can be easily adapted as examples are added or removed from $\mathcal{S}_i$ [103]. When adding an example k to $\mathcal{T}_M^i$, $\bar{\boldsymbol{P}}^i$ expands as

$$\begin{pmatrix} & & & 0 \\ & \bar{\boldsymbol{P}}^i & & \vdots \\ & & & 0 \\ 0 & \dots & 0 & 0 \end{pmatrix} + \frac{1}{\bar{g}_k^i} \begin{pmatrix} \bar{b}_i \\ \bar{\alpha}_{t_1^M}^i \\ \vdots \\ \bar{\alpha}_{t_{|\mathcal{T}_M^i|}^M}^i \\ 1 \end{pmatrix} \left(\bar{b}_i, \bar{\alpha}_{t_1^M}^i, \dots, \bar{\alpha}_{t_{|\mathcal{T}_M^i|}^M}^i, 1 \right) \tag{5.30}$$

By contrary, to remove an example k from $\mathcal{T}_M^i$, $\bar{\boldsymbol{P}}^i$ is contracted as

$$\bar{R}_{n,m}^i \longleftarrow \bar{R}_{n,m}^i - \{\bar{R}_{k,k}^i\}^{-1} \bar{R}_{n,k}^i \bar{R}_{k,m}^i \quad \forall n, m \in \mathcal{T}_M^i \cup \{0\}; n, m \neq k \tag{5.31}$$

where index 0 refers to the $\bar{b}_i$-term.

5.3.1.4 Incremental learning algorithm

The overall incremental procedure for learning the new sample $\boldsymbol{z}_s$ can be summarized as Algorithm 8. The samples in $\mathcal{U}$ can be learned sequentially using the algorithm.

5.3.1.5 Initialization procedure

The KT conditions (5.18) and (5.19) are assumed to be satisfied on $\mathcal{T}$ before carrying out Algorithm 8. However, the conditions are not satisfied initially by default, when the training of a new SSM-SVM classifier is launched. An initial procedure is therefore necessary to make the KT conditions fulfilled for a certain number (N^i) of training samples. The initialization procedure proposed in this study is summarized as Algorithm 9.

Algorithm 8 Incremental SSM-SVM algorithm

Assign $\alpha_s^i = 0$;
Compute g_s^i;
if $g_s^i \geq 0$ **then**
  Add s to $\mathcal{T}_R^i$;
end if
while $g_s^i < 0$ & $\alpha_s^i < D$ **do**
  Compute $M_{\Delta\alpha_s^i}$
  Update $\alpha_s^i + M_{\Delta\alpha_s^i} \rightarrow \alpha_s^i$;
  Compute $\bar{b}_i$;
  Update $b_i + \bar{b}_i M_{\Delta\alpha_s^i} \rightarrow b_i$;
  for $l = 1$ to $|\mathcal{T}_M^i|$ **do**
    Compute $\bar{\alpha}_{t_l^M}^i$;
    Update $\alpha_{t_l^M}^i + \bar{\alpha}_{t_l^M}^i M_{\Delta\alpha_s^i} \rightarrow \alpha_{t_l^M}^i$;
  end for
  for $l = 1$ to $|\mathcal{T}_E^i \cup \mathcal{T}_R^i|$ **do**
    Compute $\bar{g}_{\bar{t}_l^M}^i$;
    Update $g_{\bar{t}_l^M}^i + \bar{g}_{\bar{t}_l^M}^i M_{\Delta\alpha_s^i} \rightarrow \alpha_{\bar{t}_l^M}^i$;
  end for
  Update $\mathcal{T}_M^i$, $\mathcal{T}_E^i$, $\mathcal{T}_R^i$;
  Update $\boldsymbol{P}^i$;
end while

Algorithm 9 Initialization of incremental SSM-SVM

1: Assign $N^i = \lfloor 1/D \rfloor + 1$[1];
2: Select $\boldsymbol{z}_1^i, \ldots \boldsymbol{z}_{N^i}^i$ from Ω_i;
3: Assign $\alpha_1^i = 1 - \lfloor 1/D \rfloor D$;
4: **for** $n = 2$ to N^i **do**
5: Assign $\alpha_n^i = D$;
6: **end for**
7: **for** $n = 1$ to N^i **do**
8: Compute $g_n^i = \sum_{m=1}^{N_{ini}} Q_{n,m}^i \alpha_m^i$;
9: **end for**
10: Assign $b_i = -\max\{g_n^i\}$;
11: **for** $n = 1$ to N^i **do**
12: Update $g_n^i + b_i \rightarrow g_n^i$;
13: **end for**
14: **if** $\arg\max_n g_n^i = 1$ **then**
15: Assign $\mathcal{T}_M^i = \{1\}$, Assign $\mathcal{T}_E^i = \{2, \ldots, N^i\}$;
16: **else**
17: Assign $\mathcal{T}_M^i = \{\arg\max_n g_n^i\}$, $\mathcal{T}_E^i = \{2, \ldots, N^i\} - \{\arg\max_n g_n^i\}$;
18: Assign $s = 1$, go to step 6 of Algorithm 8;
19: **end if**

5.3.2 Improvement of real-time learning performance

It can be noticed that the ith sphere ($\boldsymbol{a}_i$, R_i) is determined by the samples associated to $\mathcal{T}_M^i$ and $\mathcal{T}_E^i$; whereas Algorithm 8 involves the whole set $\mathcal{T}$. Based on the tacit assumption that the sphere surface before incremental training does not move much after incremental procedure, the samples which are associated to $\mathcal{T}_R^i$, meanwhile are far away from the sphere surface have little impact on the training results. Thus, these samples could be discarded to reduce the memory consumption and the computation time. Nevertheless, the potential candidates for $\mathcal{T}_M^i$ and $\mathcal{T}_E^i$ should not be deleted in the deletion process.

In this section, a procedure is proposed to keep the training candidates and to discard the useless ones whose indexes are from $\mathcal{T}_R^i$. The principle of the proposed procedure can be shown in Fig. 5-5. The samples which are nearest to the sphere surface are kept, for they are more promising candidates than others. In order to find

[1]In the algorithm, $\lfloor x \rfloor$ denotes the floor function largest integer not greater than x.

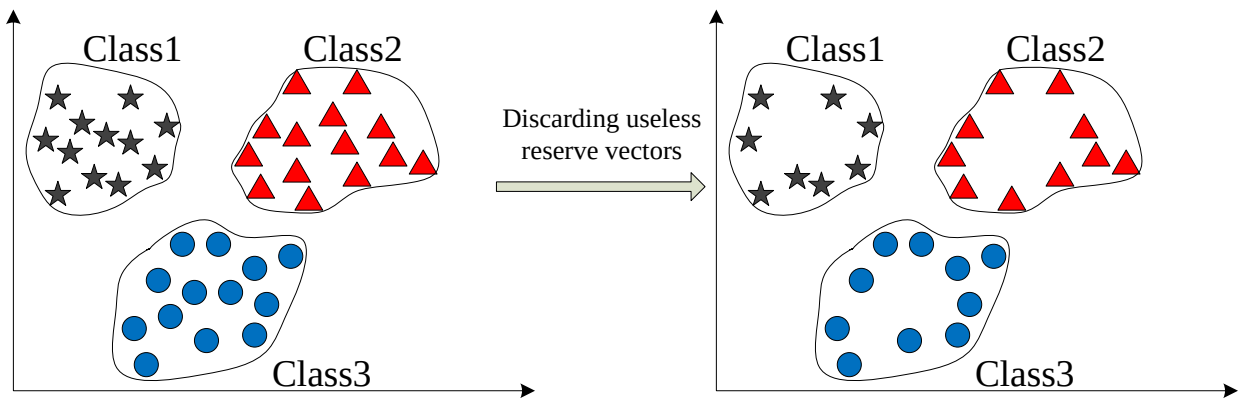

Figure 5-5: Principle of discarding useless data

these samples, the difference of ${d_n^i}^2$ (defined in 5.11) and ${R_i}^2$ is deduced from (5.11), (5.12), (5.6) and (5.18) (see Appendix A.8):

$$|{d_i}^2(\boldsymbol{z}_n) - R_i^2| = 2g_n^i \quad n \in \mathcal{T}_R^i \tag{5.32}$$

Hence, the samples corresponding to the $|\mathcal{T}_R^i|$ smallest g_n^i are kept, while the others are discarded. Here, the maximum $|\mathcal{T}_R^i|$ is set as twice the value $|\mathcal{T}_M^i \cup \mathcal{T}_E^i|$, as:

$$|\mathcal{T}_R^i| = \begin{cases} |\mathcal{T}_R^i|, & \text{if } |\mathcal{T}_R^i| \leq 2|\mathcal{T}_M^i \cup \mathcal{T}_E^i| \\ 2|\mathcal{T}_M^i \cup \mathcal{T}_E^i|, & \text{if } |\mathcal{T}_R^i| > 2|\mathcal{T}_M^i \cup \mathcal{T}_E^i| \end{cases} \tag{5.33}$$

Since $|\mathcal{T}_M^i \cup \mathcal{T}_E^i|$ is usually small, this procedure can confirm the light memory consumption and computation.

5.4 Results and discussion

5.4.1 Experiments and database

The data of 40-cell PEMFC stack mentioned previously were investigated to verify the proposed strategy.

To observe the ageing effects on the performance of fault diagnosis strategy, the experiments in normal state and various faulty states were carried out on the test-

bench. The concerned health states are listed in Table 5.2. Note that the normal tests were carried out at four different time points to take the influence of aging into account. The experiment in each state was repeated several times. Although various physical variables had been sampled and collected from the testbench, only the cell voltages sampled during the experiments were drawn to construct the training dataset and the test dataset. For each state, data from one (or several) experiment(s) were used as training data, while data from others were considered as test data.

Table 5.2: Concerned states (classes)

Health state description	Location	Notation
Nominal operating (time 1)	Whole system	Nl_1
Nominal operating (time 2)	Whole system	Nl_2
Nominal operating (time 3)	Whole system	Nl_3
Nominal operating (time 4)	Whole system	Nl_4
High current pulse or short circuit	Electric circuit	F_1
Stop cooling water	Temperature subsystem	F_2
High air stoichiometry (4)	Air supply subsystem	F_3
Low air stoichiometry (1.4)	Air supply subsystem	F_4

For recalling, the evolution of cell voltages in different states is shown in Fig. 5-6. It should be noted that those for Nl_2, Nl_3, Nl_4 are not given here since they are visually little varied from that of Nl_1. Among them, F_1, F_2 occurred in-between the experiments, while Nl_1, F_3, and F_4 were maintained during the whole corresponding experiments. It could be found that the voltages of different cells have different responses to different health states. Essentially, this character is utilized for fault diagnosis.

5.4.2 Multi-fault detection and isolation

Firstly, the performance of multi-fault detection and isolation was investigated. Four faulty states, namely F_1, F_2, F_3 and F_4, and the normal state at time point 1, namely Nl_1, were taken into consideration. After training FDA, the data of five states were projected to a 4-dimensional *feature space*. Fig. 5-7 shows the first three features of the *projecting vectors*. The samples from different classes are overall isolated from

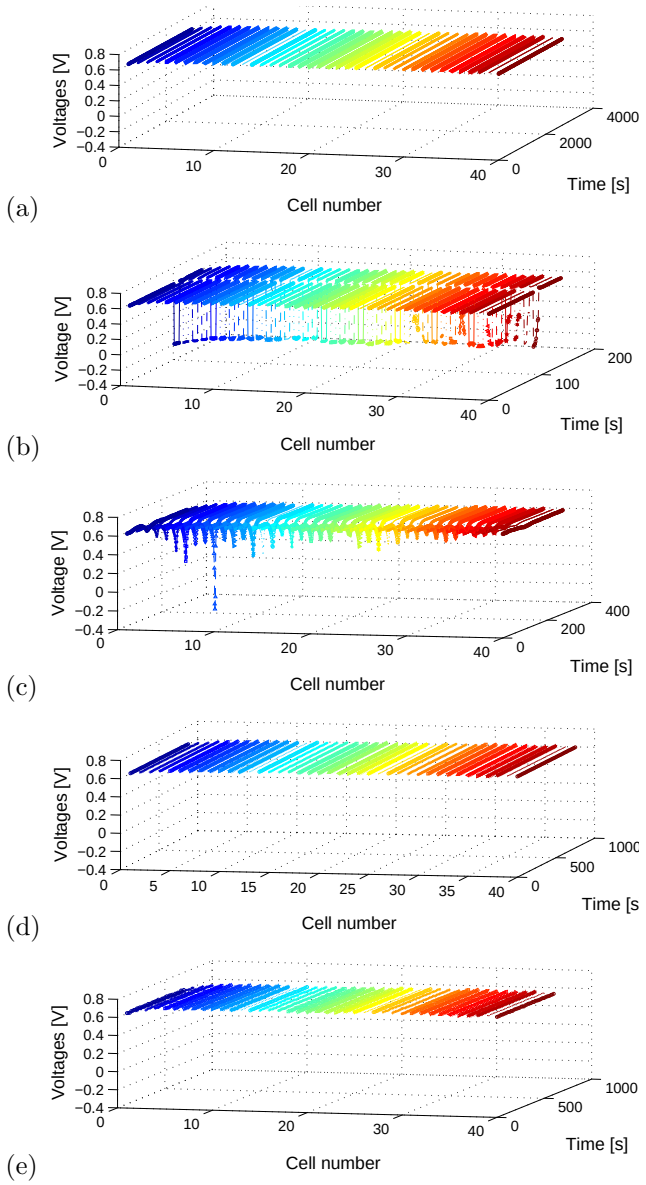

Figure 5-6: Evolution of cell voltages in different states. (a) Nl_1, (b) F_1, (c) F_2, (d) F_3, (e) F_4

the visual point of view.

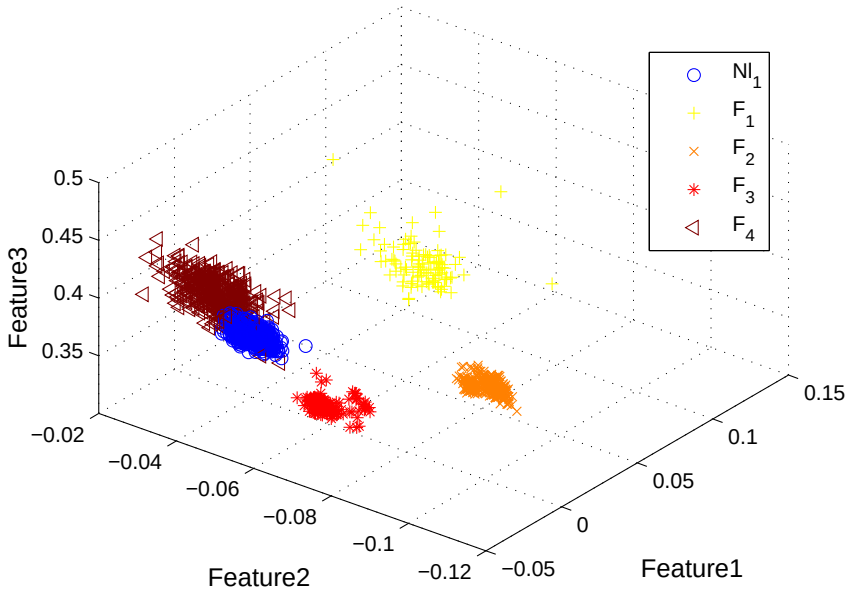

Figure 5-7: First 3 features of the *projecting vectors* from 5 different health states

Following the FDA training process, the SSM-SVM classifier was then trained in the *feature space*. The training process could be considered as the initial training which is offline.

With the trained FDA and SSM-SVM models, the diagnostic accuracy of the test dataset was evaluated. The *confusion matrix*, which allows visualization of the classification performance, is shown in Table 5.3. From the table, it could be seen that the diagnostic accuracy is more than 95% for each class except for class F_4, which is 89.32%. Actually, F_4 is the lightest fault which has some overlaps with the normal state. The overlaps can also be observed from Fig. 5-7. Moreover, as the decision rule given by (5.15) was used, a tiny fraction of samples were misclassified or misdiagnosed to the new fault class. Table 5.4 gives the results without the new fault detection procedure. Comparing the two tables, it could be found that the samples that were misclassified to the new fault class were also mostly misclassified without the new fault detection procedure.

By comparing Table 5.3 and Table 4.5, the performance of strategy FDA plus

SSM-SVM can be compared with that of FDA plus DAGSVM strategy. It can be observed that the former strategy can obtain comparable or even better accuracies in the aspect of multi-fault FDI.

Table 5.3: Confusion matrix (%) with new fault detection

Actual class	Diagnosed class					
	Nl_1	F_1	F_2	F_3	F_4	New fault
Nl_1	97.91	0	0	0.59	1.50	0
F_1	0	96.77	0	0	3.23	0
F_2	0	0	95.24	0	0	4.76
F_3	0	0	0	99.68	0	0.32
F_4	10.00	0	0	0.05	89.32	0.64

Table 5.4: Confusion matrix (%) without new fault detection

Actual class	Diagnosed class				
	Nl_1	F_1	F_2	F_3	F_4
Nl_1	97.91	0	0	0.59	1.50
F_1	0	96.77	0	0	3.23
F_2	0	0	95.24	0	4.76
F_3	0	0	0	99.68	0.32
F_4	10.00	0	0	0.05	89.95

5.4.3 Online adaptation

When the aging effect is taken into account, a performance degradation arises over time. Fig. 5-8 shows the stack voltage sampled at four different time points. A decrease could be observed over time. Since the operating frequency is not homogeneous, the descent speed of stack voltage is varying during the time.

The performance degradation due to the aging effect is usually considered as the normal degradation which is acceptable within certain limits. By using the trained FDA, the data from states Nl_2, Nl_3, Nl_4 can be projected to the *feature space*. As in Fig. 5-7, the first three features of the *projected vectors* in different states are shown in Fig.5-9. It could be seen that the data from normal classes shift over time. The

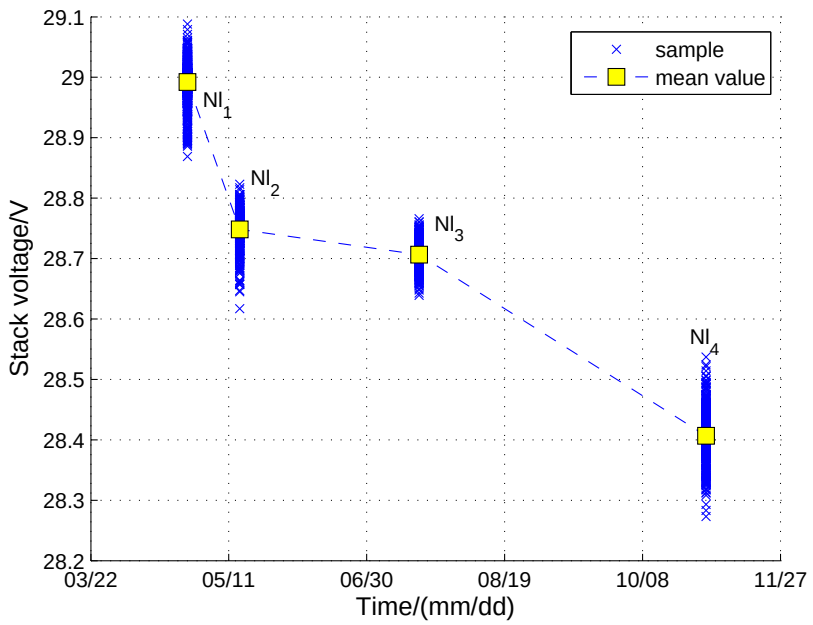

Figure 5-8: Evolution of stack voltage over time

diagnostic models should be updated to avoid the misclassifying of the data in normal functioning, but collected after normal aging, into the classes representing faults.

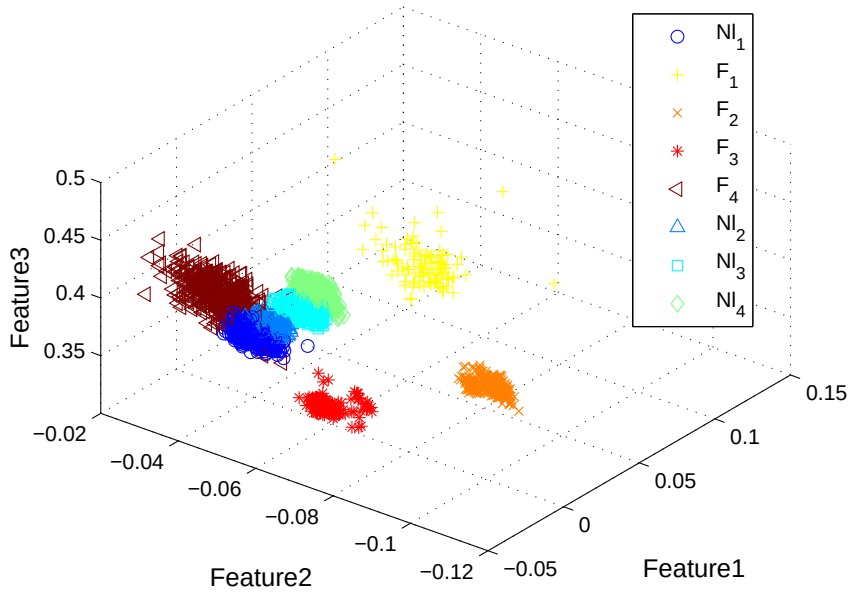

Figure 5-9: First 3 features of the *projecting vectors* from 8 different health states

Here, in order to test the efficiency of the updating procedure, the data from classes Nl_1, Nl_2, Nl_3, Nl_4 were tested by using the diagnostic models that are updated at different times. $Model_1$, $Model_2$, $Model_3$, and $Model_4$ denote the models trained or updated at time 1, time 2, time 3, and time 4. Each model is updated by using the previous model and the current samples. For instance, $Model_3$ is updated by using $Model_2$ and data from Nl_2.

Table 5.5 summarizes the test results. It could be seen that the diagnostic accuracy is low without updating procedure at each time. On the contrary, with updating procedure, the diagnosis accuracy could be improved significantly. Hence, the updating procedure is therefore justified to be useful and efficient.

Table 5.5: Classification accuracy (%) of normal datasets using the models updated at different times

Class	$Model_1$	$Model_2$	$Model_3$	$Model_4$
Nl_1	97.91			
Nl_2	65.50	99.75		
Nl_3	0	0.20	1	
Nl_4	0	0	36.03	1

5.4.4 Detection a novel failure mode

In this subsection, classes Nl_R $(R = 1, \ldots, 4)$ are combined as an unique class denoted by Nl. In order to test the performance of the proposed strategy for detecting novel failure mode, we proposed as follows. Let $j \in \{1, \ldots, 4\}$. Assume that the fault represented by the class F_j was initially an unknown fault. Hence, the initial step dedicated to training was realized with the data that were representative of classes Nl and F_i with $i \in \{1, \ldots, 4\} - \{j\}$. After that, the data from various classes including the ones used in training phase and the unknown class F_j were treated. Table 5.6-5.9 show the confusion matrices for the different values of j.

For all the cases, the probabilities that the data located in the known classes were misclassified to the novel classes, are generally low. It should be noted for the cases where F_1, F_2, and F_3 were considered as novel classes, the probabilities of detection

Table 5.6: Confusion matrix (%) with F_1 as new fault class

Actual class	Diagnosed class				
	Nl	F_2	F_3	F_4	New fault
Nl	98.91	0	0	1.09	0
F_2	0	95.24	0	0	4.76
F_3	0	0	99.00	0	1
F_4	6.77	0	0	93.23	0
New fault	3.23	0	0	0	96.77

Table 5.7: Confusion matrix (%) with F_2 as new fault class

Actual class	Diagnosed class				
	Nl	F_1	F_3	F_4	New fault
Nl	94.95	0	0	4.32	0.73
F_1	3.32	83.87	0	0	12.9
F_3	0	0	99.00	0	1.00
F_4	8.55	0	0	90.36	1.09
New fault	0	0	0	0	100

Table 5.8: Confusion matrix (%) with F_3 as new fault class

Actual class	Diagnosed class				
	Nl	F_1	F_2	F_4	New fault
Nl	94.68	0	0	4.68	0.64
F_1	3.23	90.32	0	0	6.45
F_2	0	0	95.24	0	4.76
F_4	9.73	0	0	89.45	0.82
New fault	0.12	0	0	4.52	95.36

Table 5.9: Confusion matrix (%) with F_4 as new fault class

Actual class	Diagnosed class				
	Nl	F_1	F_2	F_3	New fault
Nl	99.59	0	0	0	0.41
F_1	3.23	96.77	0	0	0
F_2	0	0	95.24	0	4.76
F_3	0	0	0	99.16	0.84
New fault	46.91	13.23	0	0	39.86

the novel class are more than 95%. However, for the case where F_4 was considered as novel class, the probability is only equal to 39.86%, which is a low level. It can be deduced that it is relatively difficult to recognize the data in the novel class when they are too close to the known classes.

5.4.5 Real-time capability

In order to implement the proposed approach online in an embedded system, the computational cost should be evaluated carefully. In this study, the computational cost of the two online procedures (i.e. performing process and updating process), were evaluated from the perspectives of occupied memory and computing time. The tests were carried out under a 64-bit Matlab 2010b environment with 2.7-GHz CPU and 8 G RAM. The results are summarized in Table 5.10. Note that $Model_1$ is the initial model that was trained off-line.

Table 5.10: Occupied memory and computing time

	$Model_1$	$Model_2$	$Model_3$	$Model_4$
Occupied memory	30.4 kb	125 kb	125 kb	125 kb
Performing time	0.49 ms	0.53 ms	0.56 ms	0.53 ms
Updating time		2.93 ms	3.98 ms	5.32 ms

It could be found that the updating time is longer than the performing time, and is thus the main part of the computing burden. To our knowledge, the diagnostic period of 1 s could satisfy the requirements of diagnosis for most PEMFC systems, and memory equipped by most embedded systems can achieve the storage task easily. Hence, the proposed strategy is suitable for online implementation.

5.5 Conclusion

In this chapter, a novel data-driven diagnostic strategy is proposed for PEMFC systems. The FDA and SSM-SVM methods are used successively to extract the features from individual cell voltages, and to classify the extracted features to different classes

corresponding to the known health states and the potential novel failure mode. By the incremental learning of SSM-SVM, the online adaptation of diagnostic approach is realized.

The test results for a 40-cell PEMFC stack show that, different faults can be detected and isolated with a high accuracy, and the data from the potential novel failure modes can be recognized in most cases. Using an online adaptation procedure, the diagnostic approach can be adapted over the operating time, and diagnostic performance can be maintained. Moreover, the computational cost is justified to be suitable for online implementation.

Chapter 6

Partially model-based methodology for data-driven diagnosis

In the previous chapters, the diagnostic strategies, which are based on classification techniques, are investigated. Although encouraging results are obtained by using these methodologies, it should still be noticed that the essential bottlenecks hidden inside these classification methods still exist. Such as, the classification based strategies suffer from robustness from unseen data; it is hard to sample a completed dataset when the system operate in dynamic processes. For instance, when the normal state is mentioned, only the operations near to nominal operating point are taken into consideration tacitly in the previous three chapters. By contrary, the diagnostic strategy relying on a dynamic model, such as state space model, can usually do better in these aspects. In addition, a lot of well established diagnostic model based methods could be applied for an analytical model. The only thing lacked is an suitable model. We can say that there are advantages and disadvantages existing in both model-based and data-driven diagnosis. Hence, a proper combination of them seems to be attractive. Such a combined diagnosis strategy can proceed from data to diagnosis in three stages: first, the dynamic model is identified from the historical data; second, the diagnosis strategy is designed based on the identified model; third, the online diagnosis is carried out using the designed strategy.

Recently, authors of [104] proposed a FDI design scheme, in which *parity vectors*

can be identified from the process data with the aid of SIM (subspace identification method), and then used for a model-based fault diagnosis design. The attractive advantages of these methods are that, the well-established model-based fault diagnosis tools can be adopted; the sophisticated modeling work can be avoided. This chapter is dedicated to adopt this partially model-based data-driven diagnosis strategy for PEMFC system diagnosis. Additionally, some modifications are proposed to improve the performance of this strategy.

6.1 Background knowledge

In this section, a model structure called ***linear time invariant (LTI)*** state space model, which is mostly used in automatic control and model-based fault diagnosis will be recalled. Specific to this model structure, a model based fault detection technique and a model identification method will be reviewed generally. The background knowledge mentioned in this section will be used to develop the diagnosis strategy in the next sections.

6.1.1 Model description

Suppose that a process data set including process input and output records is available. These data can be represented by a discrete LTI state-space model, as[1][2]

$$\begin{aligned} \boldsymbol{x}(k+1) &= \boldsymbol{A}\boldsymbol{x}(k) + \boldsymbol{B}\boldsymbol{u}(k) + \boldsymbol{w}(k) \\ \boldsymbol{y}(k) &= \boldsymbol{C}\boldsymbol{x}(k) + \boldsymbol{D}\boldsymbol{u}(k) + \boldsymbol{v}(k) \end{aligned} \tag{6.1}$$

with

$$\boldsymbol{E}\left\{\begin{pmatrix}\boldsymbol{w}(p)\\ \boldsymbol{v}(q)\end{pmatrix}\begin{pmatrix}\boldsymbol{w}(p) & \boldsymbol{v}(q)\end{pmatrix}\right\} = \begin{pmatrix}\boldsymbol{Q} & \boldsymbol{S}\\ \boldsymbol{S}^T & \boldsymbol{R}\end{pmatrix}\delta_{pq} \tag{6.2}$$

[1] $\boldsymbol{E}$ denotes the expected value operator, δ_{pq} the Kronecker delta.

[2] The symbols used in this chapter are defined independently. To avoid confusion, they will be defined locally and will not be listed in the nomenclature table.

where $\boldsymbol{u}(k) \in \mathbb{R}^l$, $\boldsymbol{y}(k) \in \mathbb{R}^m$, and $\boldsymbol{x}(k) \in \mathbb{R}^n$ are input, output and state variables. $\boldsymbol{w}(k) \in \mathbb{R}^n$, $\boldsymbol{v}(k) \in \mathbb{R}^m$ are zero-mean, normal distributed white noises. $\boldsymbol{Q} \in \mathbb{R}^{n\times n}$, $\boldsymbol{S} \in \mathbb{R}^{n\times m}$ and $\boldsymbol{R} \in \mathbb{R}^{m\times m}$ are the covariance matrices of the noise sequence $\boldsymbol{w}(k)$ and $\boldsymbol{v}(k)$.

Many industrial processes can be described very accurately by this type of model even though this model seems to be restricted. It is also found that complex behaviors of system can be captured by choosing the high enough system order n [105]. Moreover the state space representation is the only model that is convenient to work with in computer aided control system design [105]. Actually, the model-based fault diagnosis theory is also established and developed based on this kind of model.

6.1.2 Parity space model based fault diagnosis

Figure 6-1: Schematic of parity space based fault detection

As mentioned in chapter 1, various model-based fault diagnosis methods have been developed, such as observer based diagnostic ones, parity space based ones. Among them, the parity space based schemes firstly proposed by the authors of [106], have received much attention. The design of parity relation based residual generator can be achieved in a straightforward manner.

From (6.1), the system output can be recursively expressed as follows:

$$\boldsymbol{y}(k-s) = \boldsymbol{C}\boldsymbol{x}(k-s) + \boldsymbol{D}\boldsymbol{u}(k-s) + \boldsymbol{v}(k-s) \tag{6.3}$$

$$\begin{aligned}\boldsymbol{y}(k-s+1) =& \boldsymbol{C}\boldsymbol{x}(k-s+1) + \boldsymbol{D}\boldsymbol{u}(k-s+1) + \boldsymbol{v}(k-s+1)\\ =& \boldsymbol{C}\boldsymbol{A}\boldsymbol{x}(k-s) + \boldsymbol{C}\boldsymbol{B}\boldsymbol{u}(k-s) + \boldsymbol{C}\boldsymbol{w}(k-s)\\ &+ \boldsymbol{D}\boldsymbol{u}(k-s+1) + \boldsymbol{v}(k-s+1)\end{aligned} \tag{6.4}$$

Repeating this procedure, we can obtain

$$\begin{aligned}\boldsymbol{y}(k) =& \boldsymbol{C}\boldsymbol{A}^{s}\boldsymbol{x}(k-s) + \boldsymbol{C}\boldsymbol{A}^{s-1}\boldsymbol{B}\boldsymbol{u}(k-s) + \cdots + \boldsymbol{C}\boldsymbol{B}\boldsymbol{u}(k-1) + \boldsymbol{D}\boldsymbol{u}_k \\ &+ \boldsymbol{C}\boldsymbol{A}^{s-1}\boldsymbol{w}(k-s) + \cdots + \boldsymbol{C}\boldsymbol{w}(k-1) + \boldsymbol{v}(k)\end{aligned} \tag{6.5}$$

We can further rewrite the above equations in a compactly form, as

$$\boldsymbol{y}_s(k) = \boldsymbol{\Gamma}_s\boldsymbol{x}(k-s) + \boldsymbol{H}_{s,u}\boldsymbol{u}_s(k) + \boldsymbol{H}_{s,w}\boldsymbol{w}_s(k) + \boldsymbol{v}_s(k) \tag{6.6}$$

where

$$\boldsymbol{y}_s(k) = \begin{bmatrix} \boldsymbol{y}(k-s) \\ \boldsymbol{y}(k-s+1) \\ \vdots \\ \boldsymbol{y}(k) \end{bmatrix}$$

s is the order of the *parity space*, $\boldsymbol{u}_s(k)$, $\boldsymbol{w}_s(k)$, and $\boldsymbol{v}_s(k)$ are defined similarly. $\boldsymbol{\Gamma}_s$, $\boldsymbol{H}_{s,u}$, and $\boldsymbol{H}_{s,w}$ are defined

$$\boldsymbol{\Gamma}_s = \begin{bmatrix} \boldsymbol{C} \\ \boldsymbol{C}\boldsymbol{A} \\ \vdots \\ \boldsymbol{C}\boldsymbol{A}^{s} \end{bmatrix} \in \mathbb{R}^{m(s+1)\times n}$$

$$\boldsymbol{H}_{s,u} = \begin{bmatrix} \boldsymbol{D} & 0 & \dots & 0 \\ \boldsymbol{C}\boldsymbol{B} & \boldsymbol{D} & \dots & 0 \\ \vdots & \ddots & \ddots & \vdots \\ \boldsymbol{C}\boldsymbol{A}^{s-1}\boldsymbol{B} & \dots & \boldsymbol{C}\boldsymbol{B} & \boldsymbol{D} \end{bmatrix} \in \mathbb{R}^{m(s+1)\times l(s+1)}$$

$$\boldsymbol{H}_{s,w} = \begin{bmatrix} 0 & 0 & \dots & 0 \\ \boldsymbol{C} & 0 & \dots & 0 \\ \vdots & \ddots & \ddots & \vdots \\ \boldsymbol{C}\boldsymbol{A}^{s-1} & \dots & \boldsymbol{C} & 0 \end{bmatrix} \in \mathbb{R}^{m(s+1)\times n(s+1)}$$

Assume that $(\boldsymbol{C}, \boldsymbol{A})$ is observable, for $s > n$, $rank(\boldsymbol{\Gamma}_s) = n$. This ensures that there exists at least a row vector $\boldsymbol{\alpha}_s$:

$$\boldsymbol{\alpha}_s \boldsymbol{\Gamma}_s = 0 \tag{6.7}$$

Vectors satisfying (6.7) are called *parity vectors*, the set of which,

$$\boldsymbol{P}_s = \{\boldsymbol{\alpha}_s | \boldsymbol{\alpha}_s \boldsymbol{\Gamma}_s = 0\} \tag{6.8}$$

is called the *parity space*. It can be easily found that the rank of *parity space* is $(s+1)m - n$.

A parity relation based residual generator can be constructed as

$$r(k) = \boldsymbol{\alpha}_s \left(\boldsymbol{y}_s(k) - \boldsymbol{H}_{u,s}(k)\boldsymbol{u}_s(k)\right) = \boldsymbol{\alpha}_s \left(\boldsymbol{H}_{s,w}\boldsymbol{w}_s(k) + \boldsymbol{v}_s(k)\right) \tag{6.9}$$

The value of $r(k)$ should be zero when the disturbances and noises are zero. Notice that, the *parity space* is usually multi-dimensional, and the number of the residuals are equal to the dimensional number of *parity space*. Hence, for a sample $(\boldsymbol{u}_s(k), \boldsymbol{y}_s(k))$, the multiple residuals could be formulated by a *residual vector* $\boldsymbol{r}(k)$.

Followed by *residual evaluation* procedure, fault detection could be realized. In this study, the *residual evaluation* is achieved by using the following decision rule:

$$R = ||\boldsymbol{r}(k)||^2 \begin{cases} \leq Th & \text{Fault free} \\ > Th & \text{Fault} \end{cases} \tag{6.10}$$

where Th is the pre-defined threshold.

Normally, for the detection design of a given model, the parameters to be designed are the *parity vectors*; whereas for the case that the model is not available, which is the case in this work, both $\boldsymbol{\alpha}_s$ and $\boldsymbol{\alpha}_s \boldsymbol{H}_{u,s}$ are needed.

Algorithm 10 Parity space model-based fault detection

Design:

1: Obtain the system LTI state space model.
2: Initial parity relation order s.
3: Form matrices $\boldsymbol{\Gamma}_s$, $\boldsymbol{H}_{u,s}$.
4: Find the null space of $\boldsymbol{\Gamma}_s^T$, i.e. the set of *parity vectors* $\boldsymbol{P}_s$.

Perform:

1: Calculate the residuals according to (6.9) and using the obtained *parity vectors*.
2: Carry out fault detection according to (6.10).

6.1.3 Subspace model identification method

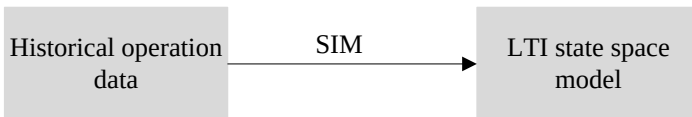

Figure 6-2: Objective of the model identification

For some industrial systems, such as PEMFC systems, it is hard to obtain the LTI state space models based on the first principles in practice [25]. System identification is the field of modeling dynamics systems from experimental data [107]. Among the available system identification methods, subspace algorithms are an important class of algorithms for identifying LTI state-space models [108]. Compared with other model identification methods, SIMs possess the attractive advantages. First, they are intrinsically robust from a numerical point of view. Second, SIMs are also non-iterative procedures such that local minima and convergence problems can be avoided. Additionally, they may also be converted into an adaptive version of model identification [107].

The main mathematical problem of SIM is stated as following:

> Given input and output historical samples $\boldsymbol{u}_1, \boldsymbol{u}_2, \ldots, \boldsymbol{u}_{N_s}$, $\boldsymbol{y}_1, \boldsymbol{y}_2, \ldots, \boldsymbol{y}_{N_s}$, find an appropriate order n and the system matrices $\boldsymbol{A}$, $\boldsymbol{B}$, $\boldsymbol{C}$, $\boldsymbol{D}$, $\boldsymbol{Q}$, $\boldsymbol{R}$, $\boldsymbol{S}$.

The name 'subspace' reflects the fact that linear models can be obtained from row and column spaces of certain matrices, calculated from input-output data [105].

Several basic SIM algorithms have been proposed in the literature [109] [110] [111]. In [112], theses basic SIM algorithms are unified as singular value decomposition task with different of some matrix with different weighting. Developing from these basic algorithms, a SIM method via PCA procedure is proposed in [113]. This method is certified to have better performance at solving error in variable (EIV) problem. Authors in [114] further proposed an *orthogonal projection* SIM approach, which is able to significantly improve the model accuracy [115]. Since the performance of the method seems to be superior to a number of existing, this method will be presented in the follows and partly used for fault diagnosis.

To present the methodologies conveniently, we define

$$\boldsymbol{z}(k) = \begin{bmatrix} \boldsymbol{y}(k) \\ \boldsymbol{u}(k) \end{bmatrix} \tag{6.11}$$

By introducing integers s_p and s_f with $s_p, s_f > n$, the past and future vectors are defined as

$$\boldsymbol{y}_p(k) = \begin{bmatrix} \boldsymbol{y}(k-s_p) \\ \boldsymbol{y}(k-s_p+1) \\ \vdots \\ \boldsymbol{y}(k-1) \end{bmatrix} \in \mathbb{R}^{ms_p} \tag{6.12}$$

$\boldsymbol{u}_p(k)$, $\boldsymbol{z}_p(k)$, $\boldsymbol{w}_p(k)$ and $\boldsymbol{v}_p(k)$ are defined similarly;

$$\boldsymbol{y}_f(k) = \begin{bmatrix} \boldsymbol{y}(k) \\ \boldsymbol{y}(k+1) \\ \vdots \\ \boldsymbol{y}(k+s_f-1) \end{bmatrix} \in \mathbb{R}^{ms_f} \tag{6.13}$$

$\boldsymbol{u}_f(k)$, $\boldsymbol{z}_f(k)$, $\boldsymbol{w}_f(k)$ and $\boldsymbol{v}_f(k)$ are defined similarly.

The corresponding matrices are defined as

$$\boldsymbol{Y}(k) = \Big[\boldsymbol{y}(k), \boldsymbol{y}(k+1), \ldots, \boldsymbol{y}(k+N-1)\Big] \in \mathbb{R}^{m\times N} \tag{6.14}$$

where N is a pre-set positive integer, $\boldsymbol{U}(k)$, $\boldsymbol{Z}(k)$, $\boldsymbol{W}(k)$ and $\boldsymbol{V}(k)$ are defined similarly;

$$\boldsymbol{Y}_f = \begin{bmatrix} \boldsymbol{Y}(k) \\ \boldsymbol{Y}(k+1) \\ \vdots \\ \boldsymbol{Y}(k+s_f-1) \end{bmatrix} \in \mathbb{R}^{ms_f \times N} \tag{6.15}$$

$\boldsymbol{U}_f$, $\boldsymbol{Z}_f$, $\boldsymbol{W}_f$ and $\boldsymbol{V}_f$ are defined similarly.

$$\boldsymbol{Y}_p = \begin{bmatrix} \boldsymbol{Y}(k-s_p) \\ \boldsymbol{Y}(k-s_p+1) \\ \vdots \\ \boldsymbol{Y}(k-1) \end{bmatrix} \in \mathbb{R}^{ms_p \times N} \tag{6.16}$$

$\boldsymbol{U}_p$, $\boldsymbol{Z}_p$, $\boldsymbol{W}_p$ and $\boldsymbol{V}_p$ are defined similarly. To sufficiently use the sample, N is set as $N_s - s_f - s_p + 1$ and k is set at $s_p + 1$.

Similar to (6.6), by iterating (6.1), we can obtain

$$\boldsymbol{Y}_f = \boldsymbol{\Gamma}_{s_f-1}\boldsymbol{X}(k) + \boldsymbol{H}_{s_f-1,u}\boldsymbol{U}_f + \boldsymbol{H}_{s_f-1,w}\boldsymbol{W}_f + \boldsymbol{V}_f \tag{6.17}$$

where $\boldsymbol{\Gamma}_{s_f-1}$, $\boldsymbol{H}_{s_f-1,u}$, and $\boldsymbol{H}_{s_f-1,w}$ are defined as $\boldsymbol{\Gamma}_s$, $\boldsymbol{H}_{s,u}$, and $\boldsymbol{H}_{s,w}$ with s replaced by $s_f - 1$. The essential system information is contained in the *extended observability matrix* $\boldsymbol{\Gamma}_{s_f-1}$ from which the system matrices are drawn [105].

6.1.3.1 Identification of the intermediate matrices

To get $\boldsymbol{\Gamma}_{s_f-1}$, we recall the definition of *orthogonal projection*: The orthogonal projection of the row space of $\boldsymbol{A}$ onto the row space of $\boldsymbol{B}$ is denoted by $\boldsymbol{A}/\boldsymbol{B}$ and can be calculated through

$$\boldsymbol{A}/\boldsymbol{B} = \boldsymbol{A}\boldsymbol{B}^{\dagger}\boldsymbol{B} \tag{6.18}$$

where $\boldsymbol{B}^{\dagger}$ is the pseudo inverse of $\boldsymbol{B}$, which can be expressed $\boldsymbol{B}^T(\boldsymbol{B}\boldsymbol{B}^T)^{-1}$[3].

[3]Here $\boldsymbol{B}$ is a full row rank matrix, and the its row number is less than its column number.

Equation (6.17) can be rewritten as

$$\begin{aligned} \boldsymbol{Y}_f - \boldsymbol{H}_{s_f-1,u}\boldsymbol{U}_f &= [\boldsymbol{I}| - \boldsymbol{H}_{s_f-1,u}]\boldsymbol{Z}_f \\ &= \boldsymbol{\Gamma}_{s_f-1}\boldsymbol{X}(k) + \boldsymbol{H}_{s_f-1,w}\boldsymbol{W}_f + \boldsymbol{V}_f \end{aligned} \tag{6.19}$$

By projecting the left and right sides of (6.19) to the row space of $\boldsymbol{Z}_p$, we can obtain

$$[\boldsymbol{I}| - \boldsymbol{H}_{s_f-1,u}]\boldsymbol{Z}_f/\boldsymbol{Z}_p = \boldsymbol{\Gamma}_{s_f-1}\boldsymbol{X}(k)/\boldsymbol{Z}_p + \boldsymbol{H}_{s_f-1,w}\boldsymbol{W}_f/\boldsymbol{Z}_p + \boldsymbol{V}_f/\boldsymbol{Z}_p \tag{6.20}$$

The noise of the future is independent with the past input and output matrix $\boldsymbol{Z}_p$. The last two terms of the right side of (6.20), namely $\boldsymbol{H}_{s_f-1,w}\boldsymbol{W}_f/\boldsymbol{Z}_p$ and $\boldsymbol{V}_f/\boldsymbol{Z}_p$, are orthogonal projections of the future disturbances (white noise) onto the row space of the the past input and output matrix $\boldsymbol{Z}_p$, which should be zeros [114]. Hence,

$$[\boldsymbol{I}| - \boldsymbol{H}_{s_f-1,u}]\boldsymbol{Z}_f/\boldsymbol{Z}_p = \boldsymbol{\Gamma}_{s_f-1}\boldsymbol{X}(k)/\boldsymbol{Z}_p \tag{6.21}$$

Now multiplying both sides of (6.21) by orthogonal column space of $\boldsymbol{\Gamma}_{s_f-1}$, denoted by $\boldsymbol{\Gamma}^{\perp}_{s_f-1}$,

$$(\boldsymbol{\Gamma}^{\perp}_{s_f-1})^T[\boldsymbol{I}| - \boldsymbol{H}_{s_f-1,u}]\boldsymbol{Z}_f/\boldsymbol{Z}_p = 0 \tag{6.22}$$

Perform Singular Value Decomposition (SVD) of $\boldsymbol{Z}_f/\boldsymbol{Z}_p$ as

$$\boldsymbol{Z}_f/\boldsymbol{Z}_p = \begin{bmatrix} \boldsymbol{U}_1 & \boldsymbol{U}_2 \end{bmatrix} \begin{bmatrix} \boldsymbol{\Sigma}_{z,1} & 0 \\ 0 & \boldsymbol{\Sigma}_{z,2} \end{bmatrix} \begin{bmatrix} \boldsymbol{V}_1^T \\ \boldsymbol{V}_2^T \end{bmatrix} \tag{6.23}$$

where $\boldsymbol{\Sigma}_{z,2} \approx 0$. In theory, the rank of $\boldsymbol{Z}_f/\boldsymbol{Z}_p$ should be $s_f l + n$, of which the proof can be found in [113].

In practice, $\boldsymbol{Z}_f/\boldsymbol{Z}_p$ is not strictly singular and one has to determine its rank. The rank determination is equivalent to the determination of system order n. In [115], the optimal order of the model will be the one which minimize a criteria named AIC (Akaike Information Criterion). The details are provided in Appendix A.7 [113]. And

s_f and s_p is assigned $n+1$ empirically [113].

With (6.23), we can easily find the orthogonal column space of $\boldsymbol{Z}_f/\boldsymbol{Z}_p$ is $\boldsymbol{U}_2$, therefore

$$\left[(\boldsymbol{\Gamma}_{s_f-1}^{\perp})^T[\boldsymbol{I}| - \boldsymbol{H}_{s_f-1,u}]\right]^T = \boldsymbol{U}_2\boldsymbol{M} \tag{6.24}$$

where $\boldsymbol{M} \in \mathbb{R}^{(ms_f-n)\times(ms_f-n)}$ is any constant non-singular matrix. Here it is set as a unit matrix.

$$\boldsymbol{U}_2\boldsymbol{M} = \begin{bmatrix} \boldsymbol{U}_{2,y} \\ \boldsymbol{U}_{2,u} \end{bmatrix} \tag{6.25}$$

where $\boldsymbol{U}_{2,y}$ is the first $s_f m$ rows of $\boldsymbol{U}_2\boldsymbol{M}$; From (6.24) and (6.25)

$$\boldsymbol{\Gamma}_{s_f-1}^{\perp} = \boldsymbol{U}_{2,y} \tag{6.26}$$

$$-(\boldsymbol{H}_{s_f-1,u})^T\boldsymbol{\Gamma}_{s_f-1}^{\perp} = \boldsymbol{U}_{2,u}^T \tag{6.27}$$

Therefore,

$$\boldsymbol{\Gamma}_{s_f-1} = (\boldsymbol{U}_{2,y})^{\perp} \tag{6.28}$$

$$-(\boldsymbol{U}_{2,y})^T\boldsymbol{H}_{s_f-1,u} = \boldsymbol{U}_{2,u}^T \tag{6.29}$$

6.1.3.2 Identification of system matrices

In the follows, the system matrices $\boldsymbol{A}$, $\boldsymbol{B}$, $\boldsymbol{C}$, and $\boldsymbol{D}$ will be identified from the obtained $\boldsymbol{\Gamma}_{s_f-1}$, and $\boldsymbol{H}_{s_f-1,u}$. Actually, this procedure is presented in some published books or papers. Here, we refer [105] for more details.

Algorithm 11 Orthogonal projection SIM

1: Obtain historical samples $\boldsymbol{u}_1, \boldsymbol{u}_2, \ldots, \boldsymbol{u}_{N_s}$, $\boldsymbol{y}_1, \boldsymbol{y}_2, \ldots, \boldsymbol{y}_{N_s}$.
2: Initial system order n, and parameter s_f, s_p.
3: Construct matrix $\boldsymbol{Z}_f$ and $\boldsymbol{Z}_p$, and further $\boldsymbol{Z}_f/\boldsymbol{Z}_p$.
4: Perform SVD decomposition of $\boldsymbol{Z}_f/\boldsymbol{Z}_p$ as (6.23), and obtain $\boldsymbol{U}_2$.
5: Calculate $\boldsymbol{\Gamma}_{s_f-1}$ and $\boldsymbol{H}_{s_f-1,u}$ according to (6.28) and (6.29).
6: Get system matrices $\boldsymbol{A}$, $\boldsymbol{B}$, $\boldsymbol{C}$, and $\boldsymbol{D}$ using the procedure proposed in [105].

6.2 Description of the diagnostic strategy

Recently, authors of [104] proposed a FDI design scheme, in which *parity vectors* can be identified from the process data with the aid of SIM, and then used for a model-based fault diagnosis design. The attractive advantages of these methods are that, the well-established model-based fault diagnosis tools can be adopted; the sophisticated modeling work can be avoided. In this section, this idea is adopted to the PEMFC system diagnosis design. Specifically, the orthogonal projection SIM and parity space based diagnosis method, which are aforementioned, are combined to realize the fault detection in dynamic process. Moreover, fault isolation is achieved through classification in residual space.

6.2.1 Fault detection

Figure 6-3: Parity space designed from data

Observing equations (6.6) and (6.17), it is notice that $\boldsymbol{\Gamma}_s$ and $\boldsymbol{\Gamma}_{s_f-1}$ would be equal, if we make $s = s_f - 1$. It is also the case for $\boldsymbol{H}_{s,u}$ and $\boldsymbol{H}_{s_f-1,u}$. Thus, the row vector of $(\boldsymbol{\Gamma}^{\perp}_{s_f-1})^T$ can be seen as the a set of *parity vector* $\boldsymbol{\alpha}_s$, and the corresponding row vector of $(\boldsymbol{\Gamma}^{\perp}_{s_f-1})^T\boldsymbol{H}_{s_f-1,u}$ can be seen as a set of $\boldsymbol{\alpha}_s\boldsymbol{H}_{u,s}$. Hence, the problem of *parity space* identification is transferred to seeking $(\boldsymbol{\Gamma}^{\perp}_{s_f-1})^T[\boldsymbol{I}| - \boldsymbol{H}_{s_f-1,u}]$, which should equal to the orthogonal column space of $\boldsymbol{Z}_f/\boldsymbol{Z}_p$. Consequently, each row vector of $\boldsymbol{U}^T_{2,y}$ and $\boldsymbol{U}^T_{2,u}$ can be considered as $\boldsymbol{\alpha}_s$ and $\boldsymbol{\alpha}_s\boldsymbol{H}_{u,s}$ with $s = s_f - 1$. The *parity space* dimension is $ms_f - n$. Until now, it is found that the parity space can be drawn directly from the historical data which originally used for model identification. The residual computation given in (6.9) can be re-expressed as

$$\boldsymbol{r}(k) = \boldsymbol{U}_{2,y}^T \boldsymbol{y}_s(k) - \boldsymbol{U}_{2,u}^T \boldsymbol{u}_s(k) = \boldsymbol{U}_2^T \begin{pmatrix} \boldsymbol{y}_s(k) \\ \boldsymbol{u}_s(k) \end{pmatrix} \tag{6.30}$$

with $s = s_f - 1$. Thus, the parity space based fault detection procedure is designed directly from the data without a model. The procedure can be summarized in Algorithm 12.

Algorithm 12 Data-driven parity space fault detection procedure

1: Obtain historical samples $\boldsymbol{u}_1, \boldsymbol{u}_2, \ldots, \boldsymbol{u}_{N_s}$, $\boldsymbol{y}_1, \boldsymbol{y}_2, \ldots, \boldsymbol{y}_{N_s}$.
2: Initial system order n, and parameter s_f, s_p.
3: Construct matrix $\boldsymbol{Z}_f$ and $\boldsymbol{Z}_p$, and further $\boldsymbol{Z}_f/\boldsymbol{Z}_p$.
4: Perform SVD decomposition of $\boldsymbol{Z}_f/\boldsymbol{Z}_p$ as (6.23), and obtain $\boldsymbol{U}_2$.

Perform:

1: Calculate the residuals according to (6.30) and using the obtained *parity vectors*.

2: Carry out fault detection according to (6.10).

Remarks:

- As a whole SIM operation, the system matrices $\boldsymbol{A}$, $\boldsymbol{B}$, $\boldsymbol{C}$, $\boldsymbol{D}$ should be extracted from the estimated $\boldsymbol{\Gamma}_{s_f-1}^{\perp}$ and $\boldsymbol{H}_{s_f-1,u}$, although it is not necessary in our case.
- The data for *parity space* identification are collected from routine normal operation rather than a system identification plant test [116].
- It must be remembered that the states identified using these techniques do not have necessary a physical meaning. The different subspace identification techniques available in the literature also differ in the manner in which the basis of the state space is estimated [105].

6.2.2 Fault isolation in residual space

From last subsection, it is known that we can construct a $ms_f - n$ dimension *parity space*. Thus, a residual space of identical dimension can be generated, and fault detection can be achieved by checking the generated residuals. However, the fault isolation is still absent. It is reasonable and convincing that the magnitudes and signs

of residuals differ for different faults. Consequently, fault isolation can be realized by carrying out a classification procedure in residual space, when the data sets of concerning faults are available in hand.

Generally, the data from fault experiments could be considered as those for training the classifier. However, the data in normal and faulty states are usually mixed in one experimental dataset. A procedure is therefore needed and extract the fault data and peel those in normal state. As shown in Fig. 6-4, the residuals of the data sampled from the historical fault experiments are calculated and checked. Only the residuals which are diagnosed as fault ones are saved for training use. In addition, it should be emphasized that the knowledge of the concerned faults should be necessary.

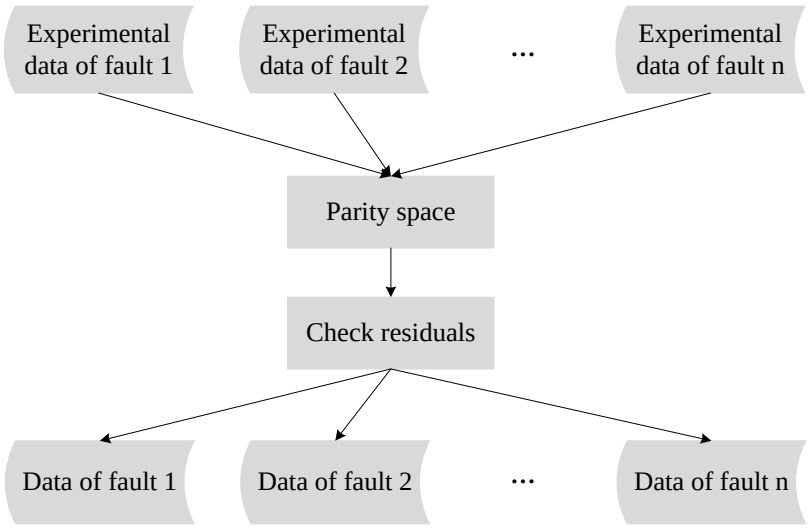

Figure 6-4: Procedure of fault data preparation

In this study, the classification method DAGSVM presented in chapter 4 is used in consideration of its superior performance.

6.2.3 Overall framework of the strategy

The approach contains off-line and on-line operations. As shown in Fig. 6-5, in the off-line part, *parity space* is identified from normal process data, and the multi-class SVM is trained with the faulty data. In the on-line diagnostic stage, the fault

detection and isolation procedures for realtime data can be realized with the obtained *parity space* and trained multi-class SVM. Notice that, the faulty data for training multi-class SVM is usually filtered from normal data with the aid of the *parity space*.

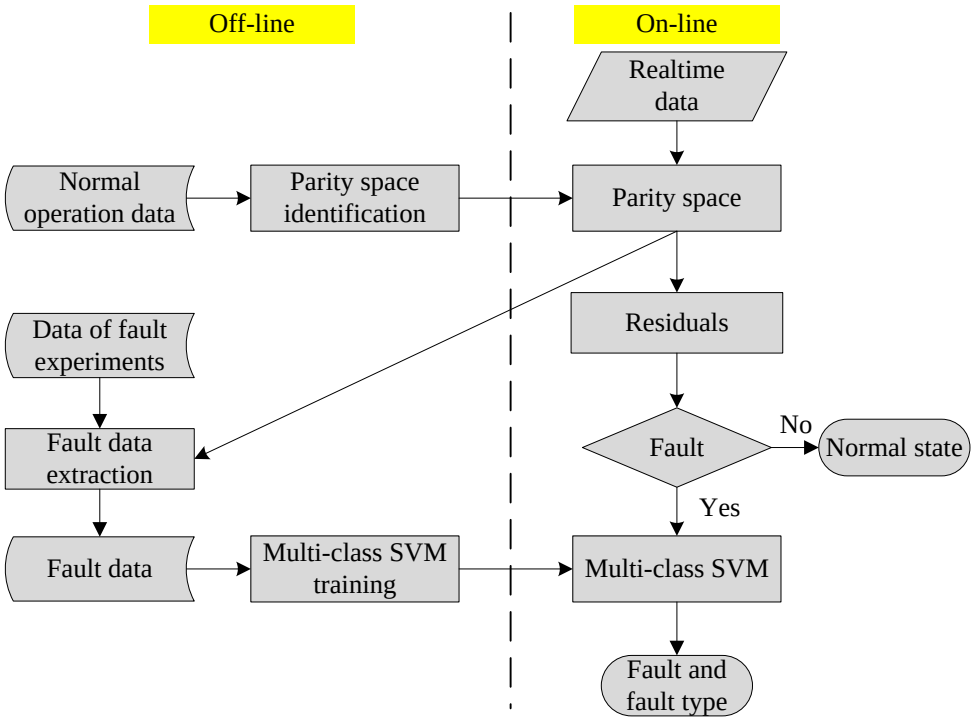

Figure 6-5: Flow chart of the diagnosis strategy

6.3 Application of PEMFC diagnosis

6.3.1 Experiments and data acquisition

The experimental data from 40-cell stack were used to verify the diagnostic strategy. The experiments of normal state and various fault states were carried out in our test bench. The input and output data were measured and saved with the sample frequency of 1 Hz. The data from fault-free state were used to identify the *parity vectors*. The data from faulty experiments were firstly used to verify the *parity space* based fault detection, and then used for training and testing of DAGSVM based fault isolation. In order to carry out the approach, 8 variables, including pressures of

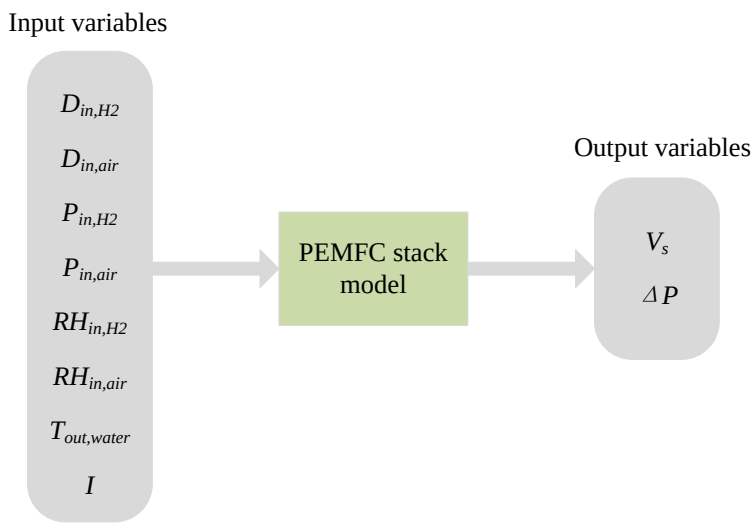

Figure 6-6: Input and output variables used for fault diagnosis strategy

input air and hydrogen ($P_{in,air}$, P_{in,H_2}), flow rates of input air and hydrogen ($D_{in,air}$, D_{in,H_2}), relative humidity of input air and hydrogen ($RH_{in,air}$, RH_{in,H_2}), current (I), and stack temperature (considered as temperature of cooling water outlet $T_{out,water}$), are selected as input variables. 2 output variables are stack voltage (V_s), and pressure drop of input air and output air (ΔP). Hence, as shown in Fig. 6-6, the input variable number $l = 8$ and the output variable number $m = 2$.

The data from fault-free state were used to identify the *parity vectors*. To realize the FDI in dynamic process, the database should not only includes the normal data sampled at or near to the nominal operating point, but also includes that sampled from the normal dynamic operating states. Concerning the considered PEMFC system, the routine dynamic processes consist of the system starting and stopping, and varying load current gradually in safe range, for instance the polarization test.

Four representative faults are presented in 2.2.2. Each faulty experiment was repeated several times. Data from one experiment are used for training the classifier DAGSVM; while data from other experiments are used for test.

6.4 Results and discussion

6.4.1 Parity space identification

The profiles of different input and output variables in normal dynamic states are shown respectively in Fig. 6-7 and Fig. 6-8. The parity space was identified based on these data. Note that to cover the normal dynamic states as completed as possible, the data sampled from two different experiments were joint together. So there will be a noncontinuous point in between these data sequences.

Firstly, the dimensional number of *parity space* $ms_f - n$, or equally the system order n should be determined. The AIC values are shown in Fig. 6-9 for cases of system order from 1 to 15. So the system order n is considered to be 2 in the study. s_f and s_p were assigned 3 accordingly. The dimension *parity space* is $ms_f - n = 4$.

By using aforementioned *parity space* identification procedure, 4 *parity vectors* were obtained. The residuals corresponding to these *parity vectors* were calculated using (6.9) and denoted by r_1, r_2, r_3 and r_4 in figures 6-10-6-14. The residuals and the corresponding R in normal state are shown in Fig. 6-10. It can be seen that the residuals in normal state are mostly near to zero. Since data from two normal experiments were jointed together to identify the *parity space*, a strike can be observed in the joining together of the two data sets (at about 5000 s).

After the *parity space* identification step, $\boldsymbol{U}_2^T$ (shown in (6.30)), which consists of the parity vectors ${\boldsymbol{\Gamma}_{s_f-1}^{\perp}}^T$ and ${\boldsymbol{\Gamma}_{s_f-1}^{\perp}}^T \boldsymbol{H}_{s_f-1,u}$, are identified.

6.4.2 Fault detection

In the fault detection procedure, (6.30) and (6.10) were used to decide whether the faults happened. Here the threshold Th was set to 1 to insure 99.9% of normal data is justified in to the normal state. The residuals and R in faulty experiments are shown in Fig. 6-11 to 6-12. These figures depict that the faults F_1 and F_2 occurred in a session of the experiments. It is noticed that the detected starting point and ending point of fault periods are not exactly the same as those of the fault operating periods.

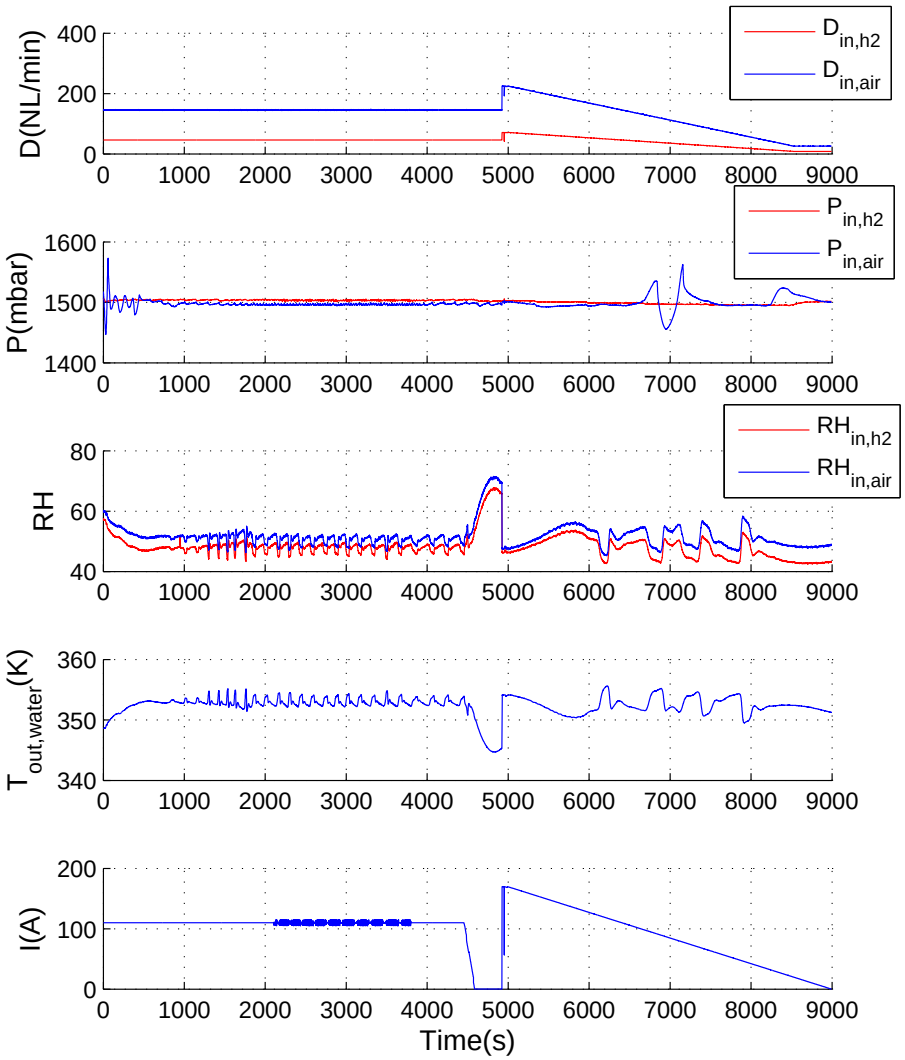

Figure 6-7: Input variables in normal operating state

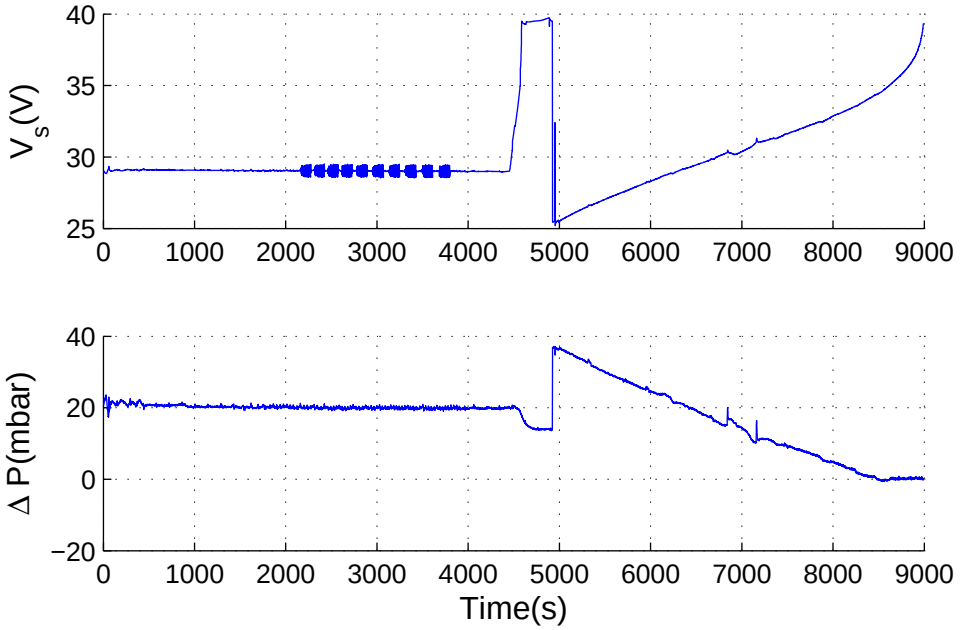

Figure 6-8: Output variables in normal operating state

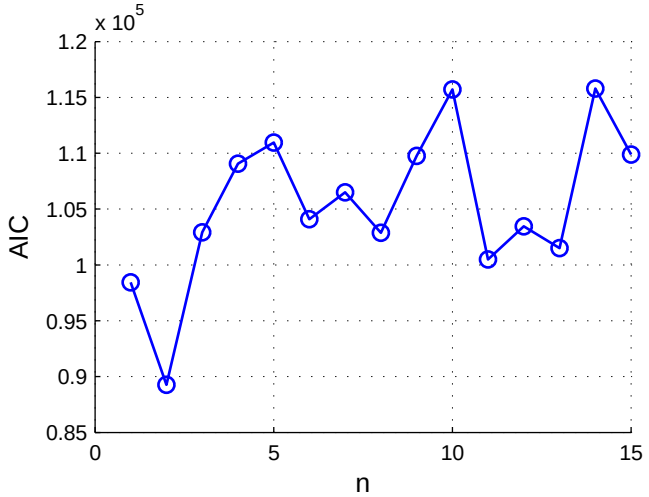

Figure 6-9: Values of AIC for different system order

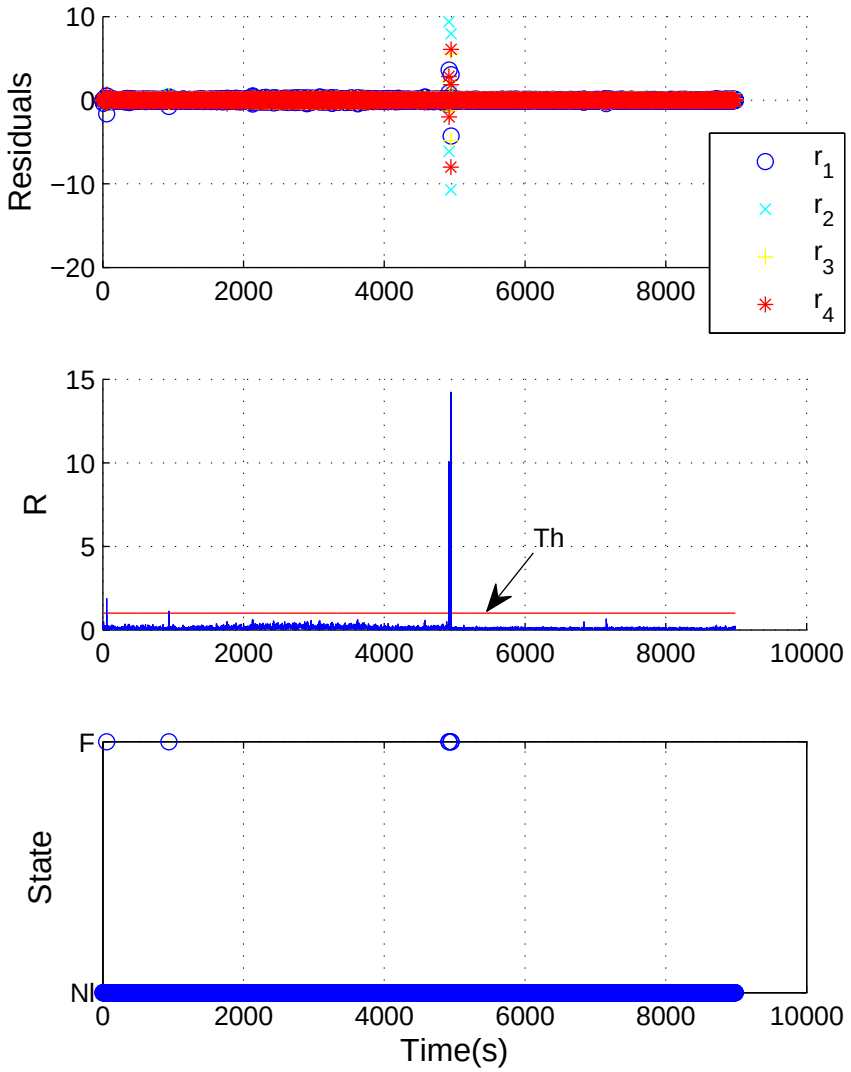

Figure 6-10: Residuals and R in normal state

For F_3 and F_4, the faults could be maintained in the stable states. In Fig. 6-13, F_3 was emerged from the beginning by setting $S_c = 4$, and aggravated by increasing S_c to 5 after some time (namely, about 1300s). It can be inferred that the severity of fault can be somehow reflected through the magnitude of the parameter R. In Fig. 6-14, F_4 was brought after a period of normal operating.

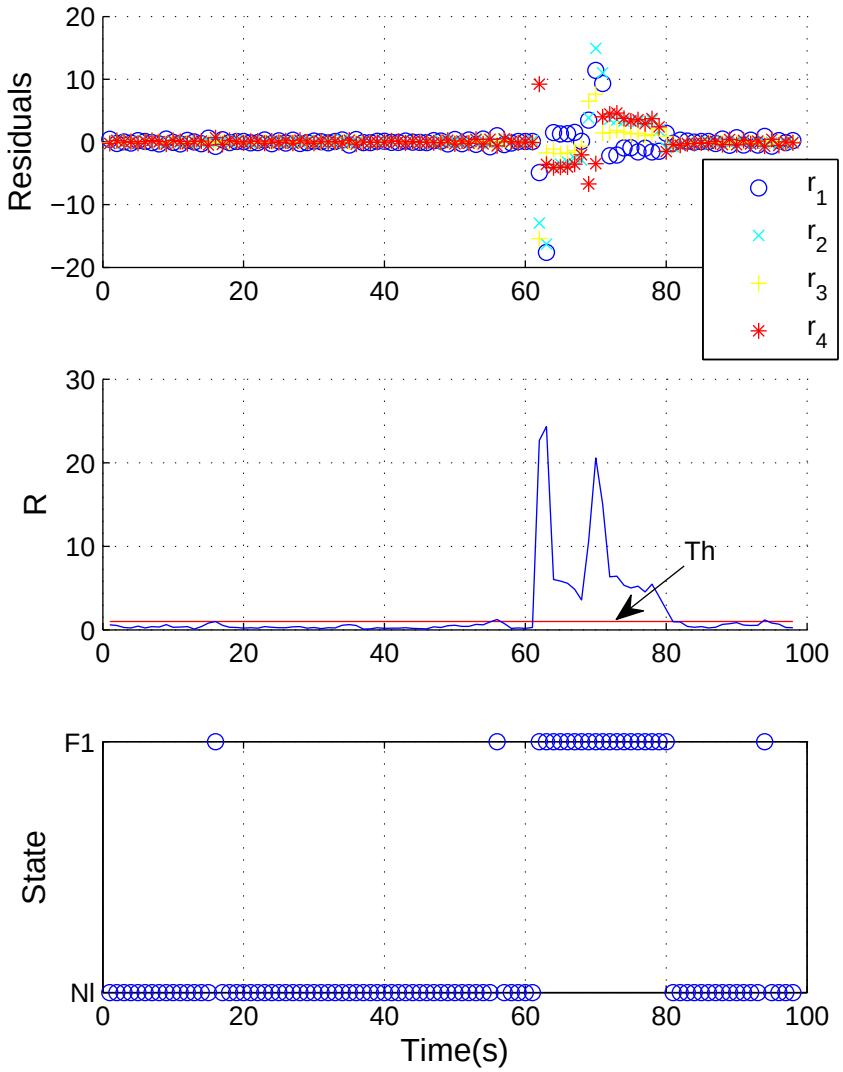

Figure 6-11: Residuals and R in the experiment of F_1 fault

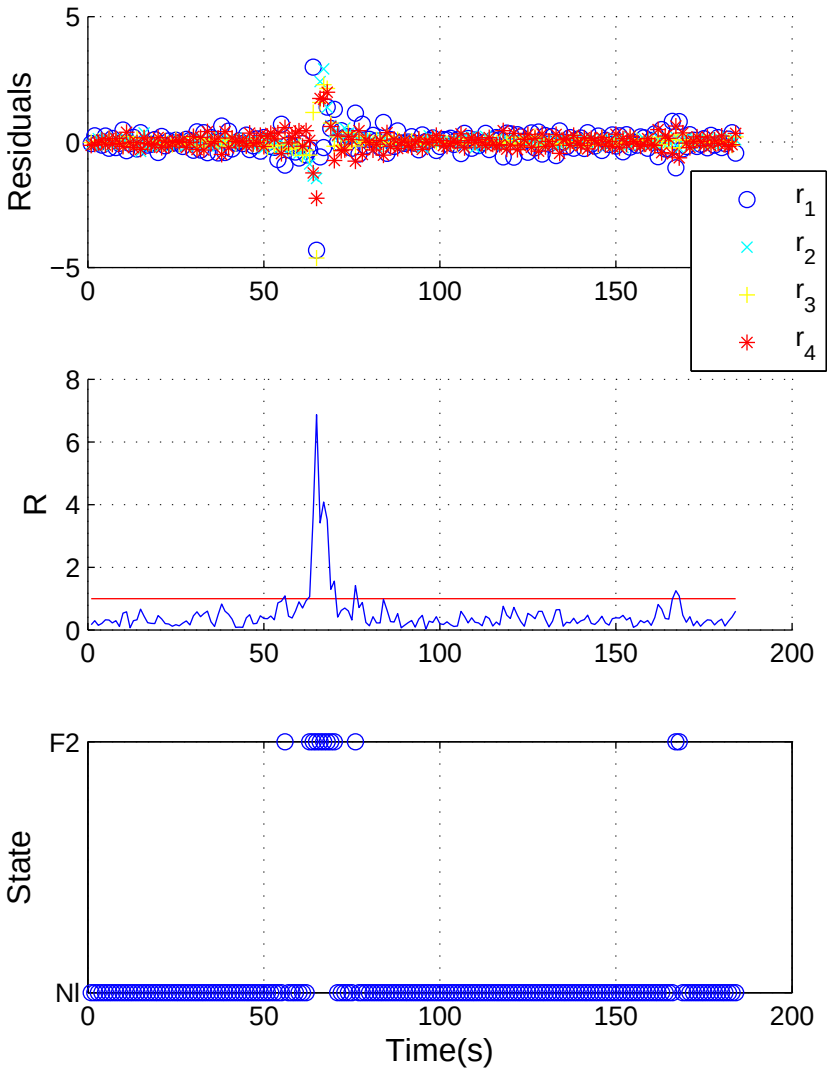

Figure 6-12: Residuals and R in the experiment of F_2 fault

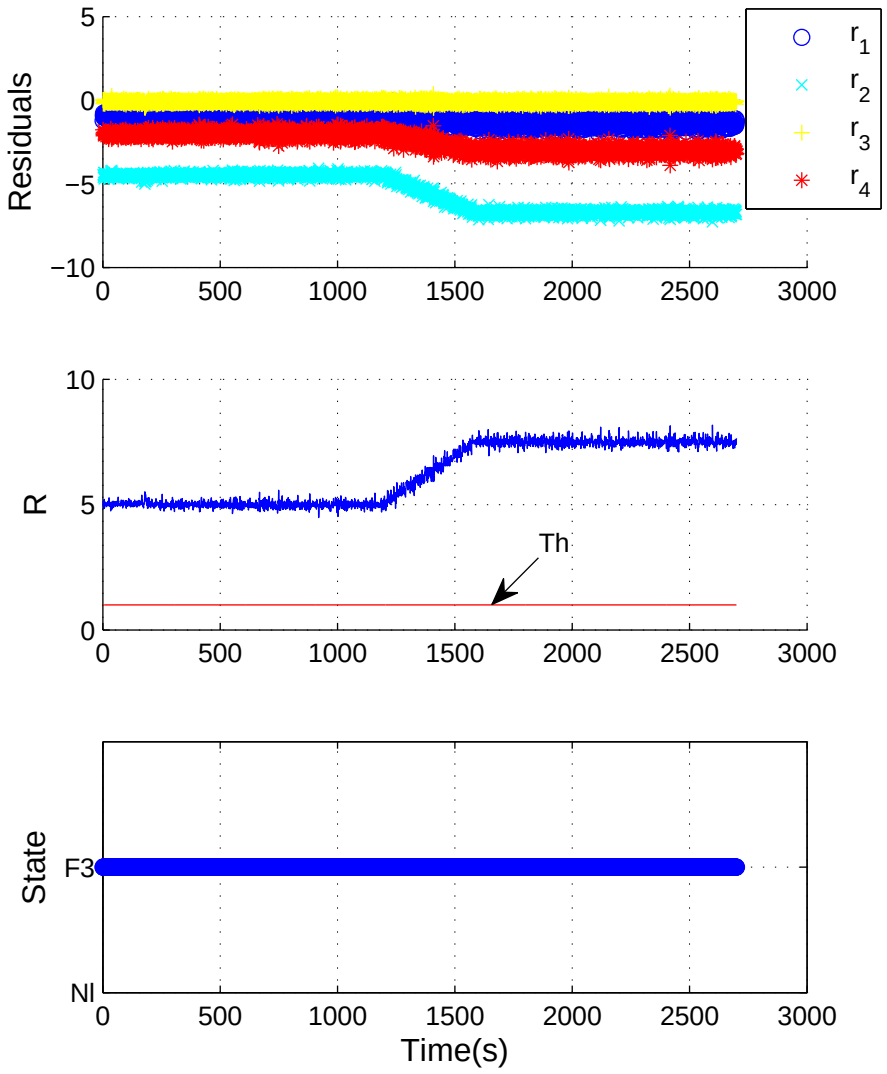

Figure 6-13: Residuals and R in the experiment of F_3 fault

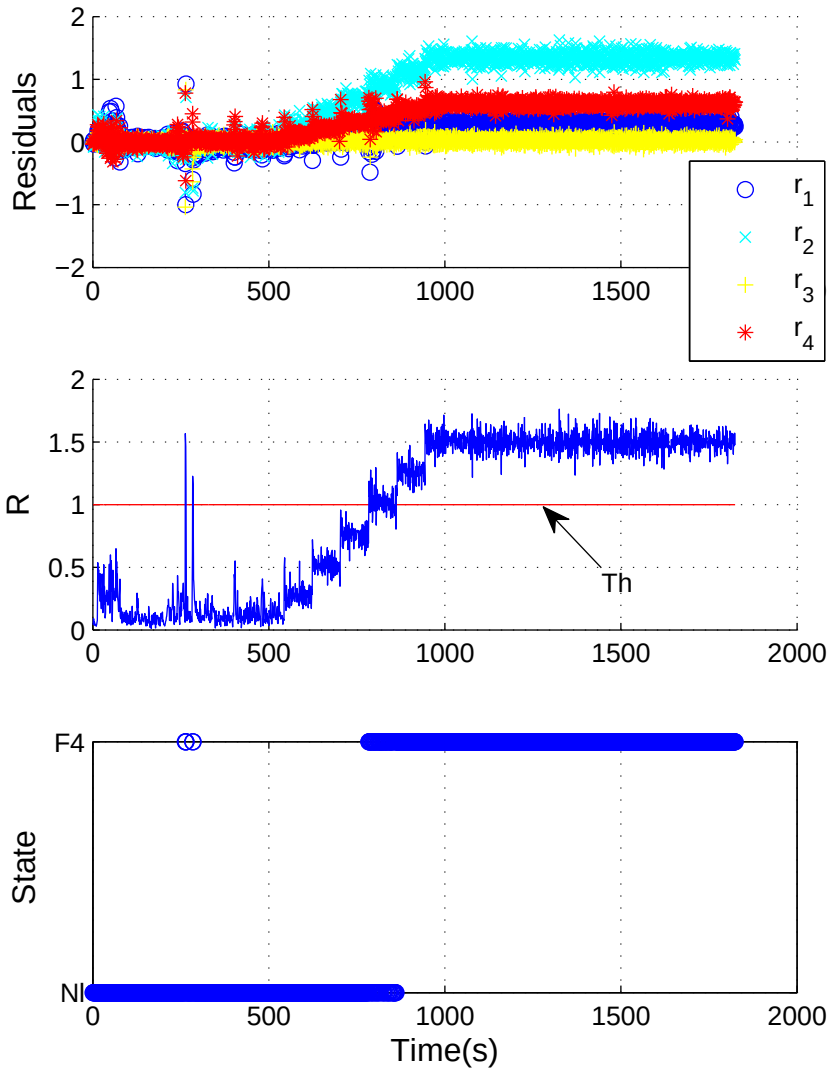

Figure 6-14: Residuals and R in the experiment of F_4 fault

6.4.3 Fault isolation

After faults are detected, fault isolation should be taken into account. The samples, whose R values are greater than threshold, were selected from various faulty data sets. Since the faults were deliberately caused, the faulty data can be labeled into four fault classes. The labeled samples were used to train and test the DAGSVM. For each fault case, the data from one corresponding experiment were used for training, while that from other experiments were used for testing. On the basis of our results, the fault isolation accuracy is 100% for both training data and testing data, which verify the good fault isolation capability of DAGSVM classification.

Compared with the diagnostic strategies proposed in previous chapters, more variables need to be measured. Undoubtedly, more information of faults can be extracted from these variables. That is why the 100% fault isolation rate can be obtained.

Concerning the computation cost of the strategy, the multiplication times for online detection procedure, which is related to (6.30), is $O((s_f m - n)s_f(m + l))$. In our case, it is considered to be sufficiently light for online implementation. As for fault isolation process, DAGSVM has been justified to be suitable for online implementation. Hence, globally, the whole diagnostic procedure is suitable for online implementation in an embedded system.

6.5 Conclusion

A partial model data-driven strategy is proposed to address PEMFC diagnosis problems, especially for the applications with high dynamic processes. With the aid of an orthogonal projection SIM approach, *parity space* can be identified from normal process data. With the *parity vectors*, fault detection can be realized. DAGSVM is used for the following fault isolation procedure. The diagnostic results of a 40-cell stack show that the 4 concerned faults can be detected and isolated with a high accuracy.

It should emphasized that a number of variables which can impacts the performance of PEMFC system should be measured. On the one hand, this would certainly increase the overall cost of the system, and also probably increase the system size.

On the other hand, in some cases, these measurements seems to be necessary for the system control objectives for some applications. It is still an open issue that which measurements should be equipped for a specific practice system.

Conclusion and Perspectives

To promote the utilization and commercialization of fuel cell technologies, the durability have to be improved. Towards this target, the primary objective of this thesis is to design data-driven diagnosis strategy for PEMFC systems.

The main contributions of this dissertation can be summarized as follows.

1. The water indicator W, which is calculated using the measured values of the air pressure drop and the air flow rate, is proposed to describe the quantity of water inside the fuel cell stack. Combining with statistical analysis, the experimental data can be labeled by comparing the values of water indicator to the thresholds.

2. The strategy based on pattern recognition tools are designed. The diagnostic procedure is realized by classifying the features that are extracted from the vectors constructed by individual cell voltages. Individual cell voltages are chosen as original variables for diagnosis. Representative feature extraction methods: PCA, FDA, KPCA, KFDA, and classification methods: GMM, kNN, SVM, are employed and compared from the point of view of diagnosis precision and computation cost. Concerning the diagnosis of water management faults, the test results for a 20-cell stack show that FDA and SVM have higher performance and less computation costs compared with other methods.

3. To verify the generality of the diagnosis strategy based on pattern classification, FDI of multiple types of faults for different PEMFC stacks is studied. To further decrease the performing time, the multi-class SVM named DAGSVM is adopted. Experimental data, which cover five fault types of two stacks, are investigated. The results show that five concerned faults could be detected and

isolated with high accuracy. The light computation cost still highlights the strategy in multiple fault diagnosis.

4. The proposed pattern classification based diagnosis algorithms were successfully integrated to the embedded system specially designed for PEMFC system diagnosis. The preliminary results shows that the real time capability, such as computation time, can be maintained.

5. To detect the unseen fault types, a novel data-driven diagnostic strategy is proposed for PEMFC systems. By using the classification method SSM-SVM instead of the traditional classifiers, both the known health states and the potential novel failure mode can be recognized. The test results for a 40-cell PEMFC stack show that, different faults can be detected and isolated with a high accuracy, and the data from the potential novel failure modes can be recognized in most cases.

6. Through the incremental learning of SSM-SVM, the online adaptation of diagnostic approach is realized. The test results for a 40-cell PEMFC stack show that the diagnostic approach can be adapted over the operating time, and diagnostic performance can be maintained. Moreover, the computational cost is justified to be suitable for online implementation.

7. A partial model data-driven strategy is proposed to address the diagnosis problem for PEMFC systems with high dynamic processes. With the aid of an orthogonal projection SIM approach, *parity space* can be identified from normal process data. Fault detection can be further realized. Moreover, fault isolation is realized by carrying out classification in the residual space. The diagnostic results of a 40-cell stack show that the concerned faults can be detected and isolated with a high accuracy.

A summary of related research directions, which deserve future investigation, is concluded here.

1. To complete the developing process of the online diagnosis strategy, online tests of the designed embedded integrated with the proposed strategy are in process.

2. The evolution of the current demand on a cycle of real application should be emulated in the PEMFC system. The proposed fault diagnosis strategies will be tested and adapted in such cases.

3. For the partial model based diagnosis strategy, in order to model and diagnosis the nonlinear profiles of PEMFC systems, LPV model can be used instead of LTI model. Hence, much more work should be done in the aspects of LPV model identification, and LPV model based fault diagnosis for PEMFC systems.

4. The fault diagnosis could be combined with the control strategy. To our knowledge, the research of this aspect is just started. More efforts should be made to the fault tolerance control for the PEMFC systems.

Bibliography

[1] (2013) Website: International Energy Outlook 2013. [Online]. Available: http://www.eia.gov/forecasts/ieo/

[2] (2012) Website: Fuel Cell Technologies Office Multi-Year Research, Development and Demonstration Plan. [Online]. Available: http://www1.eere.energy.gov/hydrogenandfuelcells/mypp/

[3] R. Khurmi and R. Sedha, *Materials Science*. S. Chand Limited, 2008.

[4] (2011) Website: The Department of Energy Hydrogen and Fuel Cells Program Plan. [Online]. Available: http://www.hydrogen.energy.gov/pdfs/program_plan2011.pdf

[5] J. Larminie and A. Dicks, *Fuel Cell Systems Explained*. J. Wiley, 2003.

[6] G. T. Services, "Fuel cell handbook (seventh edition)," 2004.

[7] N. Yousfi-Steiner, P. Moçotéguy, D. Candusso, D. Hissel, A. Hernandez, and A. Aslanides, "A review on PEM voltage degradation associated with water management: Impacts, influent factors and characterization," *Journal of Power Sources*, vol. 183, no. 1, pp. 260 – 274, 2008.

[8] (2006) Website: Future Energies: Part of the Fuel Cell Networks. [Online]. Available: http://www.futureenergies.com/modules.php?op=modload&name=News&file=article&sid=959

[9] P. Corbo, F. Migliardini, and O. Veneri, *Hydrogen fuel cells for road vehicles*. Springer, 2011.

[10] N. Sammes, *Fuel cell technology: reaching towards commercialization*. Springer, 2006.

[11] Website: Honda mobile. [Online]. Available: http://automobiles.honda.com/

[12] (2013) Website: The Fuel Cell Industry Review 2013. [Online]. Available: http://www.fuelcelltoday.com/analysis/analyst-views/2013/13-10-09-the-fuel-cell-industry-review-2013

[13] (2013) Website: Fuel Cell Technical Team Roadmap. [Online]. Available: http://www1.eere.energy.gov/vehiclesandfuels/pdfs/program/fctt_roadmap_june2013.pdf

[14] (2012) Website: DOE Hydrogen and Fuel Cells Program: Annual Report 2012. [Online]. Available: http://www.hydrogen.energy.gov/annual_progress12.html

[15] J. Wu, X. Zi, J. J. Martin, H. Wang, J. Zhang, J. Shen, S. Wu, and W. Merida, "A review of PEM fuel cell durability : Degradation mechanisms and mitigation strategies," *Journal of Power Sources*, vol. 184, pp. 104–119, 2008.

[16] X. Cheng, Z. Shi, N. Glass, L. Zhang, J. Zhang, D. Song, Z.-s. Liu, H. Wang, and J. Shen, "A review of PEM hydrogen fuel cell contamination : Impacts , mechanisms , and mitigation," *Journal of Power Sources*, vol. 165, pp. 739–756, 2007.

[17] N. Yousfi-Steiner, P. Moçotéguy, D. Candusso, and D. Hissel, "A review on polymer electrolyte membrane fuel cell catalyst degradation and starvation issues : Causes , consequences and diagnostic for mitigation," *Journal of Power Sources*, vol. 194, pp. 130–145, 2009.

[18] M. Santarelli, M. Torchio, M. Cali, and V. Giaretto, "Experimental analysis of cathode flow stoichiometry on the electrical performance of a PEMFC stack," *International Journal of Hydrogen Energy*, vol. 32, no. 6, pp. 710–716, May 2007.

[19] A. Niknezhadi, M. Allué-Fantova, C. Kunusch, and C. Ocampo-Martínez, "Design and implementation of LQR/LQG strategies for oxygen stoichiometry control in PEM fuel cells based systems," *Journal of Power Sources*, vol. 196, no. 9, pp. 4277–4282, May 2011.

[20] S. Wasterlain, D. Candusso, D. Hissel, F. Harel, P. Bergman, P. Menard, and M. Anwar, "Study of temperature , air dew point temperature and reactant flow effects on proton exchange membrane fuel cell performances using electrochemical spectroscopy and voltammetry techniques," *Journal of Power Sources*, vol. 195, pp. 984–993, 2010.

[21] W.-M. Yan, C.-Y. Chen, S.-C. Mei, C.-Y. Soong, and F. Chen, "Effects of operating conditions on cell performance of PEM fuel cells with conventional or interdigitated flow field," *Journal of Power Sources*, vol. 162, no. 2, pp. 1157 – 1164, 2006, special issue including selected papers from the International Power Sources Symposium 2005 together with regular papers.

[22] H. Wang, H. Li, and X. Yuan, *PEM Fuel Cell Failure Mode Analysis*, ser. PEM Fuel Cell Durability Handbook. Taylor & Francis, 2011.

[23] R. E. Silva, F. Harel, S. Jemeï, R. Gouriveau, D. Hissel, L. Boulon *et al.*, "Proton exchange membrane fuel cell operation and degradation in short-circuit,"

in *International Conference on Fundamentals and Development of Fuel Cells (FDFC 2013)*, 2013.

[24] S. X. Ding, *Model-based fault diagnosis techniques.* Springer, 2008, vol. 2013.

[25] S. Yin, "Data-driven design of fault diagnosis systems," Ph.D. dissertation, Universität Duisburg-Essen, Fakultät für Ingenieurwissenschaften» Ingenieurwissenschaften-Campus Duisburg» Abteilung Elektrotechnik und Informationstechnik» Automatisierung und komplexe Systeme, 2012.

[26] V. Venkatasubramanian, R. Rengaswamy, K. Yin, and S. N. Kavuri, "A review of process fault detection and diagnosis: Part i: Quantitative model-based methods," *Computers & Chemical Engineering*, vol. 27, no. 3, pp. 293 – 311, 2003.

[27] R. Isermann, *Fault-diagnosis applications.* Springer, 2011.

[28] G. Tian, I. Endichi, D. Candusso, F. Harel, D. Hissel, and J.-m. Kauffmann, "Diagnosis methods dedicated to the localisation of failed cells within PEMFC stacks," *Journal of Power Sources*, vol. 182, pp. 449–461, 2008.

[29] R. Petrone, Z. Zheng, D. Hissel, M. Péra, C. Pianese, M. Sorrentino, M. Becherif, and N. Yousfi-Steiner, "A review on model-based diagnosis methodologies for PEMFCs," *International Journal of Hydrogen Energy*, vol. 38, no. 17, pp. 7077–7091, Jun. 2013.

[30] Z. Zheng, R. Petrone, M. Péra, D. Hissel, M. Becherif, C. Pianese, N. Yousfi Steiner, and M. Sorrentino, "A review on non-model based diagnosis methodologies for PEM fuel cell stacks and systems," *International Journal of Hydrogen Energy*, vol. 38, no. 21, pp. 8914–8926, Jul. 2013.

[31] A. Hernandez, D. Hissel, and R. Outbib, "Modeling and Fault Diagnosis of a Polymer Electrolyte Fuel Cell Using Electrical Equivalent Analysis," *IEEE Transaction on Energy Conversion*, vol. 25, no. 1, pp. 148–160, 2010.

[32] S. De Lira, V. Puig, and J. Quevedo, "Robust LPV model-based sensor fault diagnosis and estimation for a PEM fuel cell system," in *Control and Fault-Tolerant Systems (SysTol), 2010 Conference on*, Oct 2010, pp. 819–824.

[33] S. De Lira, V. Puig, J. Quevedo, and A. Husar, "LPV observer design for pem fuel cell system: Application to fault detection," *Journal of Power Sources*, vol. 196, no. 9, pp. 4298–4305, 2011.

[34] Q. Yang, A. Aitouche, and B. O. Bouamama, "Fault detection and isolation of PEM fuel cell system by analytical redundancy," *18th Mediterranean Conference on Control and Automation, MED'10*, pp. 1371–1376, Jun. 2010.

[35] D. Hissel, D. Candusso, and F. Harel, "Fuzzy-Clustering Durability Diagnosis of Polymer Electrolyte Fuel Cells Dedicated to Transportation Applications," *IEEE Transactions on Vehicular Technology*, vol. 56, no. 5, pp. 2414–2420, 2007.

[36] N. Yousfi-Steiner, D. Hissel, P. Moçotéguy, and D. Candusso, "Diagnosis of polymer electrolyte fuel cells failure modes (flooding & drying out) by neural networks modeling," *International Journal of Hydrogen Energy*, vol. 36, no. 4, pp. 3067–3075, Feb. 2011.

[37] D. Hissel, M. C. Péra, and J. M. Kauffmann, "Diagnosis of automotive fuel cell power generators," *Journal of Power Sources*, vol. 128, no. 2, pp. 239–246, 2004.

[38] Y. Vural, D. B. Ingham, and M. Pourkashanian, "Performance prediction of a proton exchange membrane fuel cell using the ANFIS model," *International Journal of Hydrogen Energy*, vol. 34, no. 22, pp. 9181–9187, Nov. 2009.

[39] S. Jemeï, D. Hissel, M.-C. Péra, and J.-M. Kauffmann, "A new modeling approach of embedded fuel-cell power generators based on artificial neural network," *Industrial Electronics, IEEE Transactions on*, vol. 55, no. 1, pp. 437–447, Jan 2008.

[40] K.-Y. Chang, "The optimal design for PEMFC modeling based on Taguchi method and genetic algorithm neural networks," *International Journal of Hydrogen Energy*, vol. 36, no. 21, pp. 13 683 – 13 694, 2011, 2010 Asian/APEC BioH2.

[41] Z.-D. Zhong, X.-J. Zhu, and G.-Y. Cao, "Modeling a PEMFC by a support vector machine," *Journal of Power Sources*, vol. 160, no. 1, pp. 293 – 298, 2006.

[42] Z.-D. Zhong, X.-J. Zhu, G.-Y. Cao, and J.-H. Shi, "A hybrid multi-variable experimental model for a PEMFC," *Journal of Power Sources*, vol. 164, no. 2, pp. 746 – 751, 2007.

[43] A. Narjiss, D. Depernet, D. Candusso, F. Gustin, and D. Hissel, "Online diagnosis of pem fuel cell," in *Power Electronics and Motion Control Conference, 2008. EPE-PEMC 2008. 13th*, Sept 2008, pp. 734–739.

[44] X. Yuan, H. Wang, J. C. Sun, and J. Zhang, "AC impedance technique in PEM fuel cell diagnosis - A review," *International Journal of Hydrogen Energy*, vol. 32, pp. 4365 – 4380, 2007.

[45] B. Wahdame, L. Girardot, D. Hissel, F. Harel, X. François, D. Candusso, M. Péra, and L. Dumercy, "Impact of power converter current ripple on the durability of a fuel cell stack," in *Industrial Electronics, 2008. ISIE 2008. IEEE International Symposium on*, June 2008, pp. 1495–1500.

[46] S. Wasterlain, D. Candusso, F. Harel, D. Hissel, and X. Franc, "Development of new test instruments and protocols for the diagnostic of fuel cell stacks," *Journal of Power Sources*, vol. 196, pp. 5325–5333, 2011.

[47] (2014) Website: D-CODE project homepage. [Online]. Available: https://dcode.eifer.uni-karlsruhe.de/

[48] G. Tian, S. Wasterlain, D. Candusso, F. Harel, D. Hissel, and X. François, "Identification of failed cells inside PEMFC stacks in two cases: Anode/cathode crossover and anode/cooling compartment leak," *International Journal of Hydrogen Energy*, vol. 35, no. 7, pp. 2772–2776, Apr. 2010.

[49] J. Hua, J. Li, M. Ouyang, L. Lu, and L. Xu, "Proton exchange membrane fuel cell system diagnosis based on the multivariate statistical method," *International Journal of Hydrogen Energy*, pp. 1–10, 2011.

[50] V. Venkatasubramanian, R. Rengaswamy, S. N. Kavuri, and K. Yin, "A review of process fault detection and diagnosis: Part iii: Process history based methods," *Computers & Chemical Engineering*, vol. 27, no. 3, pp. 327 – 346, 2003.

[51] J. Kim, I. Lee, Y. Tak, and B. Cho, "State-of-health diagnosis based on hamming neural network using output voltage pattern recognition for a PEM fuel cell ," *International Journal of Hydrogen Energy*, vol. 37, no. 5, pp. 4280 – 4289, 2012.

[52] Z. Zheng, R. Petrone, M. Péra, D. Hissel, M. Becherif, and C. Pianese, "Diagnosis of a commercial PEM fuel cell stack via incomplete spectra and fuzzy clustering," *IECON 2013 - 39th Annual Conference of the IEEE Industrial Electronics Society*, pp. 1595–1600, Nov. 2013.

[53] L. Alberto, M. Riascos, M. G. Simoes, and P. E. Miyagi, "On-line fault diagnostic system for proton exchange membrane fuel cells," *Journal of Power Sources*, vol. 175, pp. 419–429, 2008.

[54] S. Wasterlain, D. Candusso, F. Harel, X. François, and D. Hissel, "Diagnosis of a fuel cell stack using electrochemical impedance spectroscopy and bayesian networks," in *Vehicle Power and Propulsion Conference (VPPC), 2010 IEEE*, 2010, pp. 1–6.

[55] J. Chen and B. Zhou, "Diagnosis of PEM fuel cell stack dynamic behaviors," *Journal of Power Sources*, vol. 177, no. 1, pp. 83 – 95, 2008.

[56] N. Yousfi-Steiner, D. Hissel, P. Moçotéguy, and D. Candusso, "Non intrusive diagnosis of polymer electrolyte fuel cells by wavelet packet transform," *International Journal of Hydrogen Energy*, vol. 36, no. 1, pp. 740–746, Jan. 2011.

[57] D. Benouioua, D. Candusso, F. Harel, and L. Oukhellou, "Fuel cell diagnosis method based on multifractal analysis of stack voltage signal," *International Journal of Hydrogen Energy*, vol. 33, no. 0, pp. 1–10, Dec. 2013.

[58] J. Dong and M. Verhaegen, "Data driven fault detection and isolation of a wind turbine benchmark," in *Proceedings of IFAC World Congress*, vol. 2, 2011, pp. 7086–7091.

[59] S. X. Ding, *Model-Based Fault Diagnosis Techniques: Design Schemes, Algorithms and Tools*, 2nd ed. Springer, 2013.

[60] D. Candusso, A. De Bernardinis, M.-C. Péra, F. Harel, X. François, D. Hissel, G. Coquery, and J.-M. Kauffmann, "Fuel cell operation under degraded working modes and study of diode by-pass circuit dedicated to multi-stack association," *Energy Conversion and Management*, vol. 49, no. 4, pp. 880–895, Apr. 2008.

[61] D. Candusso, F. Harel, a. Debernardinis, X. Francois, M. Péra, D. Hissel, P. Schott, G. Coquery, and J. Kauffmann, "Characterisation and modelling of a 5kW PEMFC for transportation applications," *International Journal of Hydrogen Energy*, vol. 31, no. 8, pp. 1019–1030, Jul. 2006.

[62] M. Hinaje, S. Raël, J.-P. Caron, and B. Davat, "An innovating application of PEM fuel cell: Current source controlled by hydrogen supply," *International Journal of Hydrogen Energy*, vol. 37, no. 17, pp. 12 481 – 12 488, 2012, 12th CHEC.

[63] S. Giurgea, R. Tirnovan, D. Hissel, and R. Outbib, "An analysis of fluidic voltage statistical correlation for a diagnosis of PEM fuel cell flooding," *International Journal of Hydrogen Energy*, vol. 38, no. 11, pp. 4689–4696, Apr. 2013.

[64] N. Wagner and E. Gülzow, "Change of electrochemical impedance spectra (EIS) with time during CO-poisoning of the Pt-anode in a membrane fuel cell," *Journal of Power Sources*, vol. 127, no. 1-2, pp. 341–347, Mar. 2004.

[65] P. Rodatz, F. Buchi, C. Onder, and L. Guzzella, "Operational aspects of a large PEFC stack under practical conditions ," *Journal of Power Sources*, vol. 128, no. 2, pp. 208 – 217, 2004.

[66] Y. Wang, S. Basu, and C.-Y. Wang, "Modeling two-phase flow in PEM fuel cell channels ," *Journal of Power Sources*, vol. 179, no. 2, pp. 603 – 617, 2008.

[67] K. Ito, K. Ashikaga, H. Masuda, T. Oshima, Y. Kakimoto, and K. Sasaki, "Estimation of flooding in PEMFC gas diffusion layer by differential pressure measurement," *Journal of Power Sources*, vol. 175, no. 2, pp. 732 – 738, 2008.

[68] Q. P. He, S. J. Qin, and J. Wang, "A new fault diagnosis method using fault directions in fisher discriminant analysis," *AIChE Journal*, vol. 51, no. 2, pp. 555–571, 2005.

[69] R. Tirnovan and S. Giurgea, "Efficiency improvement of a PEMFC power source by optimization of the air management ," *International Journal of Hydrogen Energy*, vol. 37, no. 9, pp. 7745 – 7756, 2012.

[70] H. Lilliefors, "On the kolmogorov-smirnov test for normality with mean and variance unknown," *Journal of the American Statistical Association*, vol. 62, no. 318, pp. 399–402, 1967.

[71] P. Wu and W. Little, "Measurement of the heat transfer characteristics of gas flow in fine channel heat exchangers used for microminiature refrigerators," *Cryogenics*, vol. 24, no. 8, pp. 415 – 420, 1984.

[72] R. Duda, P. Hart, and D. Stork, *Pattern Classification*. Wiley, 2001.

[73] C. M. Bishop, *Pattern Recognition and Machine Learning*. New York: Springer, 2006.

[74] K. Fukunaga, *Introduction to statistical pattern recognition*, 2nd ed. Academic Press, 1990.

[75] T. Cover, "Geometrical and statistical properties of systems of linear inequalities with applications in pattern recognition," *Electronic Computers, IEEE Transactions on*, vol. EC-14, no. 3, pp. 326–334, 1965.

[76] C. Campbell, "Kernel methods: a survey of current techniques ," *Neurocomputing*, vol. 48, no. 1 - 4, pp. 63 – 84, 2002.

[77] J. Lee, C. Yoo, S. W. Choi, P. A. Vanrolleghem, and I. Lee, "Nonlinear process monitoring using kernel principal component analysis," *Chemical Engineering Science*, vol. 59, no. 1, pp. 223–234, Jan. 2004.

[78] Vapnik, *The Nature of Statistical Learning Theory*, 1st ed. Springer Verlag, New York, 1995.

[79] N. C. John Shawe-Taylor, *Kernel Methods for Pattern Analysis*, 1st ed. Cambridge University Press, 2004.

[80] A. J. Smola, B. Schölkopf, and K. R. Müller, "The connection between regularization operators and support vector kernels." *Neural networks : the official journal of the International Neural Network Society*, vol. 11, no. 4, pp. 637–649, Jun. 1998.

[81] H. G. Hiden, M. J. Willis, M. Tham, and G. Montague, "Non-linear principal components analysis using genetic programming," *Computers & chemical engineering*, vol. 23, no. 3, pp. 413–425, 1999.

[82] K.-P. Wu and S.-D. Wang, "Choosing the kernel parameters for support vector machines by the inter-cluster distance in the feature space ," *Pattern Recognition*, vol. 42, no. 5, pp. 710 – 717, 2009.

[83] S. Mahadevan and S. L. Shah, "Fault detection and diagnosis in process data using one-class support vector machines," *Journal of Process Control*, vol. 19, no. 10, pp. 1627–1639, Dec. 2009.

[84] J. Yang, Z. Jin, J. yu Yang, D. Zhang, and A. F. Frangi, "Essence of kernel Fisher discriminant: KPCA plus LDA," *Pattern Recognition*, vol. 37, no. 10, pp. 2097 – 2100, 2004.

[85] G. Baudat and F. Anouar, "Generalized discriminant analysis using a kernel approach," *Neural computation*, vol. 12, no. 10, pp. 2385–2404, 2000.

[86] Z.-B. Zhu and Z.-H. Song, "Fault diagnosis based on imbalance modified kernel Fisher discriminant analysis ," *Chemical Engineering Research and Design*, vol. 88, no. 8, pp. 936 – 951, 2010.

[87] L. Cao, K. Chua, W. Chong, H. Lee, and Q. Gu, "A comparison of PCA, KPCA and ICA for dimensionality reduction in support vector machine," *Neurocomputing*, vol. 55, no. 1, pp. 321 – 336, 2003.

[88] T. Koski and J. M. Noble, *Bayesian Networks: An Introduction.* Wiley, 2009.

[89] G. McLachlan and D. Peel, *Finite Mixture Models.* New York: Wiley, 2004.

[90] N. S. Altman, "An introduction to kernel and nearest-neighbor nonparametric regression," *The American Statistician*, vol. 46, no. 3, pp. 175–185, 1992.

[91] J. C. Platt, "Sequential Minimal Optimization : A Fast Algorithm for Training Support Vector Machines," *Technical Report MSR-TR-98-14, Microsoft Research*, pp. 1–21, 1998.

[92] D. Mining, K. Discovery, B. Laboratories, and L. Technologies, "A Tutorial on Support Vector Machines for Pattern Recognition," *Knowledge Creation Diffusion Utilization*, vol. 167, pp. 121–167, 1998.

[93] C.-W. Hsu and C.-J. Lin, "A comparison of methods for multiclass support vector machines," *Neural Networks, IEEE Transactions on*, vol. 13, no. 2, pp. 415–425, 2002.

[94] L. Maria, R. Baccarini, V. Vieira, and B. R. D. Menezes, "Expert Systems with Applications SVM practical industrial application for mechanical faults diagnostic," *Expert Systems With Applications*, vol. 38, no. 6, pp. 6980–6984, 2011.

[95] J. C. Platt, M. Way, and J. Shawe-taylor, "Large Margin DAGs for Multiclass Classification," *Analysis*, vol. 12, pp. 547–553, 2000.

[96] S. V. Stehman, "Selecting and interpreting measures of thematic classification accuracy," *Remote Sensing of Environment*, vol. 62, no. 1, pp. 77 – 89, 1997.

[97] S. Heath, *Embedded Systems Design.* Elsevier Science, 2002.

[98] P. Koopman, "Embedded system design issues (the rest of the story)," in *Computer Design: VLSI in Computers and Processors, 1996. ICCD'96. Proceedings., 1996 IEEE International Conference on.* IEEE, 1996, pp. 310–317.

[99] Website: Smartfusion introduction. [Online]. Available: http://www.microsemi.com/products/fpga-soc/soc-fpga/smartfusion

[100] A. GIRAUD, "Embedded smart sensors for measurement and diagnosis of measurement and diagnosis of multicells pemfc," June 2012, report - project DIAPASON.

[101] P. Y. Hao and Y. H. Lin, "A new multi-class support vector machine with multi-sphere in the feature space," in *Proceedings of the 20th international conference on Industrial, engineering, and other applications of applied intelligent systems*, ser. IEA/AIE'07. Berlin, Heidelberg: Springer-Verlag, 2007, pp. 756–765.

[102] S. Nikitidis, N. Nikolaidis, and I. Pitas, "Multiplicative update rules for incremental training of multiclass support vector machines," *Pattern Recognition*, vol. 45, no. 5, pp. 1838 – 1852, 2012.

[103] G. Cauwenberghs and T. Poggio, "Incremental and decremental support vector machine learning," in *Advances in Neural Information Processing Systems (NIPS*2000)*, vol. 13. MIT Press, 2001.

[104] S. Ding, P. Zhang, a. Naik, E. Ding, and B. Huang, "Subspace method aided data-driven design of fault detection and isolation systems," *Journal of Process Control*, vol. 19, no. 9, pp. 1496–1510, Oct. 2009.

[105] P. van Overschee and L. de Moor, *Subspace identification for linear systems: theory, implementation, applications*. Kluwer Academic Publishers, 1996, no. 1.

[106] E. Chow and A. S. Willsky, "Analytical redundancy and the design of robust failure detection systems," *Automatic Control, IEEE Transactions on*, vol. 29, no. 7, pp. 603–614, 1984.

[107] B. Huang and R. Kadali, *Dynamic modeling, predictive control and performance monitoring*. Springer, 2008.

[108] H. Palanthandalam-Madapusi, S. Lacy, J. Hoagg, and D. Bernstein, "Subspace-based identification for linear and nonlinear systems," *Proceedings of the 2005, American Control Conference, 2005.*, pp. 2320–2334, 2005.

[109] P. V. Overschee and B. D. Moor, "N4sid: Subspace algorithms for the identification of combined deterministic-stochastic systems," *Automatica*, vol. 30, no. 1, pp. 75 – 93, 1994, special issue on statistical signal processing and control.

[110] M. Verhaegen and P. Dewilde, "Subspace model identification part 1. the output-error state-space model identification class of algorithms," *International journal of control*, vol. 56, no. 5, pp. 1187–1210, 1992.

[111] W. E. Larimore, "System identification, reduced-order filtering and modeling via canonical variate analysis," in *American Control Conference, 1983*. IEEE, 1983, pp. 445–451.

[112] P. Van Overschee and B. De Moor, "A unifying theorem for three subspace system identification algorithms," *Automatica*, vol. 31, no. 12, pp. 1853–1864, 1995.

[113] J. Wang and S. Qin, "A new subspace identification approach based on principal component analysis," *Journal of Process Control*, vol. 12, no. 8, pp. 841 – 855, 2002.

[114] B. Huang, S. X. Ding, and S. Qin, "Closed-loop subspace identification: an orthogonal projection approach," *Journal of Process Control*, vol. 15, no. 1, pp. 53–66, Feb. 2005.

[115] J. Wang and S. J. Qin, "Closed-loop subspace identification using the parity space," *Automatica*, vol. 42, no. 2, pp. 315 – 320, 2006.

[116] S. J. Qin, "Survey on data-driven industrial process monitoring and diagnosis," *Annual Reviews in Control*, vol. 36, no. 2, pp. 220–234, Dec. 2012.

[117] D. Reynolds, "Gaussian mixture models," *Encyclopedia of Biometrics*, pp. 659–663, 2009.

Appendix A

Derivation processes of some methodologies

A.1 Formulation of KPCA

From equation (3.28), we can obtain

$$\lambda\langle\Phi(\boldsymbol{v}_k), \boldsymbol{w}\rangle = \langle\Phi(\boldsymbol{v}_k), \boldsymbol{C}\boldsymbol{w}\rangle, k = 1, \ldots, N \tag{A.1}$$

Substitute (3.30) to the left side of (A.1), it is obtained that

$$\lambda\langle\Phi(\boldsymbol{v}_k), \boldsymbol{w}\rangle = \lambda \sum_{n=1}^{N} \alpha_n \langle\Phi(\boldsymbol{v}_k), \Phi(\boldsymbol{v}_n)\rangle \tag{A.2}$$

Substitute (3.30) and (3.27) to the right side of (A.1), it is obtained that

$$\begin{aligned}\langle\Phi(\boldsymbol{v}_k), \boldsymbol{C}\boldsymbol{w}\rangle &= \langle\Phi(\boldsymbol{v}_k), \frac{1}{N}\sum_{n=1}^{N} \alpha_n \sum_{m=1}^{N} \Phi(\boldsymbol{v}_m)\Phi(\boldsymbol{v}_m)^T\Phi(\boldsymbol{v}_n)\rangle \\ &= \frac{1}{N}\sum_{n=1}^{N} \alpha_n \langle\Phi(\boldsymbol{v}_k), \sum_{m=1}^{N} \Phi(\boldsymbol{v}_m)\rangle\langle\Phi(\boldsymbol{v}_m), \Phi(\boldsymbol{v}_n)\rangle\end{aligned} \tag{A.3}$$

With the definition of kernel matrix as (3.32), the right side of (A.2) can be expressed as

$$\lambda \sum_{n=1}^{N} \alpha_n \langle \Phi(\boldsymbol{v}_k), \Phi(\boldsymbol{v}_n) \rangle = \lambda \sum_{n=1}^{N} \alpha_n k_{kn} \tag{A.4}$$

The right side of (A.3) can be expressed as

$$\frac{1}{N} \sum_{n=1}^{N} \alpha_n \langle \Phi(\boldsymbol{v}_k), \sum_{m=1}^{N} \Phi(\boldsymbol{v}_m) \rangle \langle \Phi(\boldsymbol{v}_m), \Phi(\boldsymbol{v}_n) \rangle = \frac{1}{N} \sum_{n=1}^{N} \alpha_n \sum_{m=1}^{N} k_{km} k_{mn} \tag{A.5}$$

(A.4) and (A.5) can be extensionally expressed as $\lambda \boldsymbol{K} \boldsymbol{\alpha}$ and $(1/N)\boldsymbol{K}^2 \boldsymbol{\alpha}$ with consideration of all the cases of $k = 1, \ldots, N$. Thus, we further obtain

$$\lambda N \boldsymbol{K} \boldsymbol{\alpha} = \boldsymbol{K}^2 \boldsymbol{\alpha} \tag{A.6}$$

to find the solution of (A.6), we solve the eigenvalue problem (3.31).

A.2 Centering in high-dimension space

The vectors $\{\Phi(\boldsymbol{v}_n)\}$ in high-dimension space $\mathbb{F}$ are centered as

$$\tilde{\Phi}(\boldsymbol{v}_n) = \Phi(\boldsymbol{v}_n) - \frac{1}{N}\sum_{n=1}^{N}\Phi(\boldsymbol{v}_n) \tag{A.7}$$

and we define covariance matrix and $\tilde{\boldsymbol{K}}_{nm} = \langle\tilde{\Phi}(\boldsymbol{v}_n), \tilde{\Phi}(\boldsymbol{v}_m)\rangle$. The eigenvalue problem (3.31) is converted to

$$\tilde{\lambda} N \tilde{\boldsymbol{K}}\tilde{\boldsymbol{\alpha}} = \tilde{\boldsymbol{K}}\tilde{\boldsymbol{\alpha}} \tag{A.8}$$

where $\tilde{\boldsymbol{\alpha}}$ is the expansion coefficients of eigenvector (in $\mathbb{F}$) in terms of $\tilde{\Phi}(\boldsymbol{v}_n)$, $\tilde{\boldsymbol{w}} = \sum_{n=1}^{N}\tilde{\alpha}_n\tilde{\Phi}(x_n)$. As we do not have the centered data $\{\tilde{\Phi}(x_n)\}$, it is hard to compute $\tilde{\boldsymbol{K}}$; however, we can use $\boldsymbol{K}$ to express $\tilde{\boldsymbol{K}}$

$$\begin{aligned}
\tilde{\boldsymbol{K}}_{nm} &= \Big\langle \big(\Phi(\boldsymbol{v}_n) - \frac{1}{N}\sum_{n=k}^{N}\Phi(\boldsymbol{v}_k)\big), \big(\Phi(\boldsymbol{v}_m) - \frac{1}{N}\sum_{k=1}^{N}\Phi(\boldsymbol{v}_k)\big)\Big\rangle \\
&= \boldsymbol{K}_{nm} - \frac{1}{N}\sum_{k=1}^{N}1_{nk}\boldsymbol{K}_{km} - \frac{1}{N}\sum_{k=1}^{N}\boldsymbol{K}_{nk}1_{km} + \frac{1}{N^2}\sum_{k,j=1}^{N}1_{nk}\boldsymbol{K}_{kj}1_{jm} \\
&= \boldsymbol{K} - \mathbf{1}_N\boldsymbol{K} - \boldsymbol{K}\mathbf{1}_N + \mathbf{1}_N\boldsymbol{K}\mathbf{1}_N
\end{aligned} \tag{A.9}$$

where $1_{nm} = 1$ for all n, m, $\mathbf{1}_N$ is a $N \times N$ matrix with all terms are $1/N$.

A.3 Formulation of KFDA

From (3.37) and (3.30), we can obtain

$$\begin{aligned} \boldsymbol{S}_t^{\Phi}\boldsymbol{w} &= \sum_{i=1}^{C}\sum_{k=1}^{N_i}\Phi(\boldsymbol{v}_{ik})\Phi(\boldsymbol{v}_{ik})^T\sum_{p=1}^{C}\sum_{q=1}^{N_p}\alpha_{pq}\Phi(\boldsymbol{v}_{pq}) \\ &= \sum_{p=1}^{C}\sum_{q=1}^{N_p}\alpha_{pq}\sum_{i=1}^{C}\sum_{k=1}^{N_i}\Phi(\boldsymbol{v}_{ik})\langle\Phi(\boldsymbol{v}_{ik}),\Phi(\boldsymbol{v}_{pq})\rangle \end{aligned} \tag{A.10}$$

Make Fisher criterion (3.35) equal to λ,

$$\begin{aligned} \lambda\Phi(\boldsymbol{v}_{ij})^T\boldsymbol{S}_t^{\Phi}\boldsymbol{w} &= \lambda\sum_{p=1}^{C}\sum_{q=1}^{N_p}\alpha_{pq}\Phi(\boldsymbol{v}_{ij})^T\sum_{i=1}^{C}\sum_{k=1}^{N_i}\Phi(\boldsymbol{v}_{ik})\langle\Phi(\boldsymbol{v}_{ik}),\Phi(\boldsymbol{v}_{pq})\rangle \\ &= \lambda\sum_{p=1}^{C}\sum_{q=1}^{N_p}\alpha_{pq}\sum_{i=1}^{C}\sum_{k=1}^{N_i}\langle\Phi(\boldsymbol{v}_{ij}),\Phi(\boldsymbol{v}_{ik})\rangle\langle\Phi(\boldsymbol{v}_{ik}),\Phi(\boldsymbol{v}_{pq})\rangle \end{aligned} \tag{A.11}$$

Using this formula for all class i and for all its element j we get:

$$\lambda[\Phi(\boldsymbol{v}_{11})^T;\ldots,\Phi(\boldsymbol{v}_{1N_1})^T;\ldots;\Phi(\boldsymbol{v}_{ij});\ldots;\Phi(\boldsymbol{v}_{C1})^T;\ldots;\Phi(\boldsymbol{v}_{N_C})^T]\boldsymbol{S}_t^{\Phi}\boldsymbol{w} = \lambda\boldsymbol{K}\boldsymbol{K}\boldsymbol{\alpha} \tag{A.12}$$

From (3.36) and (3.30), we can obtain

$$\begin{aligned} \boldsymbol{S}_b^{\Phi}\boldsymbol{w} &= \sum_{i=1}^{C}N_i\Big[\frac{1}{N_i}\sum_{k=1}^{N_i}\Phi(\boldsymbol{v}_{ik})\Big]\Big[\frac{1}{N_i}\sum_{k=1}^{N_i}\Phi(\boldsymbol{v}_{ik})\Big]^T\sum_{p=1}^{C}\sum_{q=1}^{N_p}\alpha_{pq}\Phi(\boldsymbol{v}_{pq}) \\ &= \sum_{p=1}^{C}\sum_{q=1}^{N_p}\alpha_{pq}\sum_{i=1}^{C}\frac{1}{N_i}\sum_{k=1}^{N_i}\Phi(\boldsymbol{v}_{ik})\big\langle\Phi(\boldsymbol{v}_{ik}),\Phi(\boldsymbol{v}_{pq})\big\rangle \end{aligned} \tag{A.13}$$

Multiplied with $\Phi(\boldsymbol{v}_{ij})^T$, we obtain

$$\Phi(\boldsymbol{v}_{ij})^T\boldsymbol{S}_b^{\Phi}\boldsymbol{w} = \sum_{p=1}^{C}\sum_{q=1}^{N_p}\alpha_{pq}\sum_{i=1}^{C}\frac{1}{N_i}\sum_{k=1}^{N_i}\big\langle\Phi(\boldsymbol{v}_{ij}),\Phi(\boldsymbol{v}_{ik})\big\rangle\big\langle\Phi(\boldsymbol{v}_{ik}),\Phi(\boldsymbol{v}_{pq})\big\rangle \tag{A.14}$$

Using this formula for all class i and for all its element j we get:

$$\left[\Phi(\boldsymbol{v}_{11})^T; \ldots; \Phi(\boldsymbol{v}_{1N_1})^T; \ldots; \Phi(\boldsymbol{v}_{ij}); \ldots; \Phi(\boldsymbol{v}_{C1})^T; \ldots; \Phi(\boldsymbol{v}_{CN_C})^T\right] \boldsymbol{S}_b^{\Phi} \boldsymbol{w} = \boldsymbol{K}\boldsymbol{W}\boldsymbol{K}\boldsymbol{\alpha} \tag{A.15}$$

Combining (A.12) and (A.15) we deduce that

$$\lambda \boldsymbol{K}\boldsymbol{K}\boldsymbol{\alpha} = \boldsymbol{K}\boldsymbol{W}\boldsymbol{K}\boldsymbol{\alpha} \tag{A.16}$$

which is left multiplied by $\boldsymbol{\alpha}^T$ to obtain (3.38).

A.4 Proof of EM process

EM is developed from the most popular and well-established method is maximum likelihood (ML) estimation. The aim of ML estimation is to find the model parameters $\zeta_i,\ i = 1, \ldots, C$ which maximize the likelihood of the GMM given the training data. Taking the ith class as example, the GMM likelihood can be written as

$$p(Z_i|\zeta_i) = \prod_{n=1}^{N_i} p(\boldsymbol{z}_{in}|\zeta_i) \tag{A.17}$$

Unfortunately, direct maximization of this equation is not possible. However, ML parameter estimation can be realized using EM algorithm. The basic idea of the EM algorithm is, beginning with an initial model ζ_i, to estimate a new model $\hat{\zeta}_i$, such that $p(Z_i|\hat{\zeta}_i) \geq p(Z_i|\zeta_i)$.

On each EM iteration, the expectation step is to compute *posterior probability* for each data point. The *posterior probability* for component c_j is given by

$$p(c_j|\boldsymbol{z}_{in}, \zeta_i) = \frac{p(c_j)p(\boldsymbol{z}_{in}|c_j, \zeta_i)}{p(\boldsymbol{z}_{in}|\zeta_i)} = \frac{p(c_j)p(\boldsymbol{z}_{in}|c_j, \zeta_i)}{\sum_{j=1}^{R_i} p(\boldsymbol{z}_{in}|c_j, \zeta_i)} \tag{A.18}$$

The maximization step is to update the parameter set ζ_i based on the expectation step result. The the following formulas are used to guarantee monotonic increase of (A.17) [117]:

$$\hat{\boldsymbol{\mu}}_j = \frac{\sum_{n=1}^{N_i} p(c_j|\boldsymbol{z}_{in}, \zeta_i)\boldsymbol{z}_{in}}{\sum_{n=1}^{N_i} p(c_j|\boldsymbol{z}_{in}, \zeta_i)} \tag{A.19}$$

$$p(\hat{c}_j) = \frac{1}{N_i}\sum_{n=1}^{N_i} p(c_j|\boldsymbol{z}_{in}, \zeta_i) \tag{A.20}$$

$$\hat{\Sigma}_j = \frac{\sum_{n=1}^{N_i} p(c_j|\boldsymbol{z}_{in}, \zeta_i)[(\boldsymbol{z}_{in} - \hat{\boldsymbol{\mu}}_j)(\boldsymbol{z}_{in} - \hat{\boldsymbol{\mu}}_j)^T]}{\sum_{n=1}^{N_i} p(c_j|\boldsymbol{z}_{in}, \zeta_i)} \tag{A.21}$$

After iterations, the parameter set ζ_i can be obtained.

A.5 Extension linear separable SVM to nonlinear non-separable case

In SVM methodology, kernel function is also used to solve the nonlinear classification problem. Suppose we first mapped the data to some high dimension space using a nonlinear mapping Φ, after that the previous procedures are carried out, (3.53) can be converted to

$$\tilde{L}(\boldsymbol{a}) = \frac{1}{2}\sum_{n=1}^{N}\sum_{m=1}^{N} a_n a_m g_n g_m \langle \Phi(\boldsymbol{z}_n), \Phi(\boldsymbol{z}_m)\rangle - \sum_{n=1}^{N} a_n \tag{A.22}$$

By introducing kernel function, this can be expressed as follow

$$\tilde{L}(\boldsymbol{a}) = \sum_{n=1}^{N} a_n - \frac{1}{2}\sum_{n=1}^{N}\sum_{m=1}^{N} a_n a_m g_n g_m k(\boldsymbol{z}_n, \boldsymbol{z}_m) \tag{A.23}$$

In order to classify new data point $\boldsymbol{x}$ using the trained model, the sign of $y(\boldsymbol{x})$ is evaluated.

We have discussed the situation in which data in space $\Phi(\boldsymbol{x})$ is linear separable, however, the class-condition distributions may overlap in practice. Therefore, a way is needed to modify SVM to allow some training data points to be misclassified. A penalty variable is used to do this.

The penalty will increase with distance from the misclassified points from boundary. To make the penalty a linear function of this distance, slack variable $\xi_n \geq 0$ is introduced, where $n = 1, \ldots, N$. $\xi_n = 0$, for data inside or on the correct margin boundary and $\xi_n = |g_n - y(\boldsymbol{z}_n)|$ for other data. Thus, data points which satisfy $0 < \xi_n \leq 1$ lie inside the margin, but on the correct side of the decision boundary, and those data points for which $\xi_n > 1$ lie on the wrong side of the decision boundary. The classification constrains (3.48) are then replaced by

$$g_n(\boldsymbol{w}\boldsymbol{z}_n - b) \geq 1 - \xi_n \tag{A.24}$$

Our goal is now to maximize the margin while softly penalizing points that lie on the wrong side of the decision boundary, therefore the problem is converted to minimize

$$D\sum_{n=1}^{N}\xi_n + \frac{1}{2}||\boldsymbol{w}||^2 \tag{A.25}$$

where the parameter $D > 0$ controls the trade-off between the slack variable penalty and the margin. In the limit $D \to \infty$, the earlier SVM for separable data will be recovered. In order to minimize (A.25) subject to the constraints (A.24) and $\xi_n \geq 0$, the corresponding Lagrange function is given by

$$L(\boldsymbol{w}, b, \boldsymbol{a}) = \frac{1}{2}||\boldsymbol{w}||^2 + D\sum_{n=1}^{N}\xi_n - \sum_{n=1}^{N} a_n[y_n(\boldsymbol{w}\boldsymbol{z}_n - b) - 1 + \xi_n] - \sum_{n=1}^{N}\mu_n\xi_n \tag{A.26}$$

where $a_n \geq 0$ and $\mu_n \geq 0$ are Lagrange multipliers, setting the derivative of $L(\boldsymbol{w}, b, \boldsymbol{a})$ with respect to $\boldsymbol{w}$, b and $\{\xi_n\}$ equal to zero, we obtain the folowing the condition other than (3.51) and (3.52)

$$a_n = D - \mu_n \tag{A.27}$$

Using these results to eliminate $\boldsymbol{w}$, b and $\{\xi_n\}$ from the Lagrange function, the dual Lagrange function is given as (3.54), which is identical to the separable case. Considering $\mu_n > 0$, the constraints are given as (3.55) and (3.56).

Until now, the problem is converted to a quadratic programming (QP) problem as (3.54) with constraints (3.55) and (3.56)

A.6 SMO training

SMO is a simple algorithm that can quickly solve the SVM QP problem (3.54). SMO decomposes the overall QP problem into QP sub-problems. There are two components to SMO: an analytic method for solving for the two Lagrange multipliers, and a heuristic for choosing which multipliers to optimize.

A.6.1 Solving for two Lagrange multipliers

Taking Lagrange multipliers a_1 and a_2 as example, because there are only two multipliers, the constraints of the problem can be easily be displayed in two dimensions. To satisfy the bound constraints (3.56) and the linear equality constraints (3.55), the low limit and high limit of term a_2, denoted as $a_{2,l}$ and $a_{2,h}$, can be obtained, as

$$\begin{cases} a_{2,l} = \max(0, a_2 - a_1),\ a_{2,h} = \min(D, a_2 - a_1 + D) \text{ if } g_1 \neq g_2 \\ a_{2,l} = \max(0, a_2 + a_1 + D),\ a_{2,h} = \min(D, a_2 + a_1) \text{ if } g_1 = g_2 \end{cases} \tag{A.28}$$

The second derivative of the objective function with respect to a_2 can be expressed as:

$$\eta = k(\boldsymbol{z}_1, \boldsymbol{z}_1) + k(\boldsymbol{z}_2, \boldsymbol{z}_2) - 2k(\boldsymbol{z}_1, \boldsymbol{z}_2) \tag{A.29}$$

which is greater or equal to zero. Thus, the minimum could be computed, and the optimal new a_2 is expressed as

$$a_2^{new} = a_2 + \frac{g_2(E_2 - E_1)}{\eta} \tag{A.30}$$

where E_n is the error on nth training sample, which can be expressed as

$$E_n = \sum_{m=1}^{N_1+N_2} a_m g_m k(\boldsymbol{z}_m, \boldsymbol{z}_n) + b - g_n \tag{A.31}$$

Taking the constraints (A.28) into account, a_2 is further expressed as

$$a_2^{new} = \begin{cases} a_{2,l} & \text{if } a_2 < a_{2,l} \\ a_2^{new} & \text{if } a_2^{2,l} \leq a_2 \leq a_{2,h} \\ a_{2,h} & \text{if } a_2 > a_{2,h} \end{cases} \tag{A.32}$$

New a_1 can be deduced, as

$$a_1^{new} = a_1 + g_1 g_2 (a_2 - a_2^{new}) \tag{A.33}$$

New b is calculated, as

$$b_{new} = b_{new,1} + b_{new,2} \tag{A.34}$$

where

$$b_{new,1} = E_1 + g_1(a_1^{new} - a_1)k(\boldsymbol{z}_1, \boldsymbol{z}_1) + g_1(a_1^{new} - a_1)k(\boldsymbol{z}_1, \boldsymbol{z}_2) + b$$

and

$$b_{new,2} = E_2 + g_2(a_2^{new} - a_2)k(\boldsymbol{z}_2, \boldsymbol{z}_2) + g_1(a_1^{new} - a_1)k(\boldsymbol{z}_1, \boldsymbol{z}_2) + b$$

A.6.2 Choosing multipliers to optimize

The KKT conditions of problem (3.54) with its constrains are

$$\begin{cases} a_n = 0 \Leftrightarrow (\sum_{m=1}^{N_1+N_2} a_m g_m k(\boldsymbol{z}_m, \boldsymbol{z}_n) + b) g_n \geq 1 \\ 0 < a_n < D \Leftrightarrow (\sum_{m=1}^{N_1+N_2} a_m g_m k(\boldsymbol{z}_m, \boldsymbol{z}_n) + b) g_n = 1 \quad \forall n \\ a_n = D \Leftrightarrow (\sum_{m=1}^{N_1+N_2} a_m g_m k(\boldsymbol{z}_m, \boldsymbol{z}_n) + b) g_n \leq 1 \end{cases} \tag{A.35}$$

There are the methods used to choose the first and the second multipliers respectively. To choose the first one, the entire training set and the examples whose Lagrange multipliers are neither 0 nor D are checked in turn against the KKT conditions and

violating examples are drawn. Once the first multiplier is chosen, the second one is chosen with respect the maximization of $|E_1 - E_2|$. The choosing procedure is terminated until the entire training dataset obeys the KKT conditions.

More details of algorithm SMO and the pseudo-code can be found in [91].

A.7 Determination of system order

Given a set of system order n, the system model order is the one which makes the following AIC minimum.

$$AIC(n) = N\left(m(1+2\pi) + \log(|\boldsymbol{\Sigma}_n|)\right) + 2\delta_n M_n \tag{A.36}$$

where

$$|\boldsymbol{\Sigma}_n| = \frac{1}{N}\sum_{k}^{N}(\boldsymbol{y}(k) - \hat{\boldsymbol{y}}(k))(\boldsymbol{y}(k) - \hat{\boldsymbol{y}}(k))^T \tag{A.37}$$

$$M_n = 2nm + \frac{m(m+1)}{2} + nl + ml \tag{A.38}$$

$$\delta_n = \frac{N}{N - (\frac{M_n}{m} - \frac{m+1}{2})} \tag{A.39}$$

In [113], it is proven that the prediction error can be expressed as

$$\boldsymbol{y}(k) - \hat{\boldsymbol{y}}(k) = (\boldsymbol{U}_2\boldsymbol{U}_2^T\boldsymbol{\Xi})^{\dagger}\boldsymbol{z}_f(k - s_f + 1) \tag{A.40}$$

where

$$\boldsymbol{\Xi} = \begin{pmatrix} \mathbf{0}_{(s_f-1)m\times m} \\ \boldsymbol{I}_m \\ \mathbf{0}_{s_f l\times m} \end{pmatrix} \tag{A.41}$$

$\mathbf{0}_{p\times q}$ is $p \times q$ zero matrix, $\boldsymbol{I}_m$ is $m \times m$ identity matrix.

A.8 Proof of (5.32)

According to (5.11) and (5.12), the left side of (5.32) can be expressed

$$|{d_i}^2(\boldsymbol{z}_n) - R_i^2| = |-2\Phi(\boldsymbol{z}_n)\boldsymbol{a}_i + 2\Phi(\boldsymbol{z}_l)\boldsymbol{a}_i| \; l \in \mathcal{T}_M^i \tag{A.42}$$

Substituting (5.6) and taking into account (5.18), we obtain

$$\begin{aligned} \Phi(\boldsymbol{z}_l)\boldsymbol{a}_i &= \Phi(\boldsymbol{z}_l)\sum_{m\in\mathcal{T}} c_m^i \alpha_m^i \Phi(\boldsymbol{z}_m) = \frac{\sum_{m\in\mathcal{T}} Q_{m,l}^i}{c_l^i} \\ &= \frac{g_l^i - c_l^i b_i}{c_l^i} = \frac{0 - c_l^i b_i}{c_l^i} = -b_i \end{aligned} \tag{A.43}$$

Substituting (A.43) and (5.6), and taking into account (5.18), the right side of (A.42) can be expressed by

$$\begin{aligned} &|-2\Phi(\boldsymbol{z}_n)\sum_{m\in\mathcal{T}} c_m^i \alpha_m^i \Phi(\boldsymbol{z}_m) - 2b_i| \\ &= 2|\sum_{m\in\mathcal{T}} Q_{m,n} + c_n^i b_i| = 2|g_n^i| = 2g_n^i \quad n \in \mathcal{T}_R^i \end{aligned} \tag{A.44}$$

Personal publications

Journal articles

1. **Zhongliang LI**, Rachid OUTBIB, Daniel HISSEL, Stefan GIURGEA (2014), "Data-driven diagnosis of PEM fuel cell: A comparative study", **Control Engineering Practice** (DOI: 10.1016/j.conengprac.2014.02.019).

2. **Zhongliang LI**, Stefan GIURGEA, Rachid OUTBIB, Daniel HISSEL (2014), "Online Diagnosis of PEMFC by Combining Support Vector Machine and Fluidic Model", **Fuel Cells – from Fundamentals to Systems** (DOI: 10.1002/fuce.201300197).

3. **Zhongliang LI**, Rachid OUTBIB, Stefan GIURGEA, Daniel HISSEL, Yongdong LI (2014), "Fault detection and isolation for Polymer Electrolyte Membrane Fuel Cell system by analyzing cell voltage generated space", **Journal of Power Sources** (under review).

4. **Zhongliang LI**, Rachid OUTBIB, Daniel HISSEL, Stefan GIURGEA, "Diagnosis for PEMFC system: a data-driven approach with the capabilities of online adaptation and novel fault detection", **IEEE Trans. on Industrial Electronics** (under review).

Conference Papers

1. **Zhongliang LI**, Rachid OUTBIB, Daniel HISSEL, Stefan GIURGEA, "Diagnosis of PEMFC by using statistical analysis", The 6th international conference on Integrated Modeling and Analysis in Applied Control and Automation (**IMAACA**) 2012, Vienna, 2012 (oral).

2. **Zhongliang LI**, Stefan GIURGEA, Rachid OUTBIB, Daniel HISSEL, "Online Diagnosis of PEMFC by Combining Support Vector Machine and Fluidic Model", Fondamentals to Developments of Fuel Cells conference (**FDFC**) 2013, Karlsruhe, 2013 (poster).

3. **Zhongliang Li**, Rachid Outbib, Daniel HISSEL, Giurgea, Stefan GIURGEA, "Online diagnosis of PEMFC by analyzing individual cell voltages", European Control Conference (**ECC**) 2013, Zürich, pp.2439,2444, 17-19 July 2013 (oral).

4. **Zhongliang LI**, Stefan GIURGEA, Rachid OUTBIB, Daniel HISSEL, "Fault detection and isolation of PEMFC system: a classification approach", International Discussion on Hydrogen Energy and Applications (**IDHEA**) 2014, Nantes, 2014 (oral).

5. **Zhongliang LI**, Rachid OUTBIB, Daniel HISSEL, Stefan GIURGEA, "Diagnosis of PEMFC by using data-driven parity space strategy", European Control Conference (**ECC**) 2014, Strasbourg, 2014 (oral).

6. **Zhongliang LI**, Stefan GIURGEA, Rachid OUTBIB, Daniel HISSEL, "Fault diagnosis and novel fault type detection for PEMFC system based on Spherical-Shaped Multiple-class Support Vector Machine", IEEE International Conference on Advanced Intelligent Mechatronics (**AIM**) 2014, Besançon, 2014 (oral).